

GENE REGULATORY NETWORKS IN PARKINSON'S DISEASE

Juan Manuel Barba Reyes

Thesis Supervisor

Ana Belén Muñoz Manchado

Doctoral Program

Biomolecules and Biomedicine

Cadiz, 2026

“Todo ser humano, si se lo propone,
puede ser escultor de su propio cerebro”

Santiago Ramón y Cajal

Funding

The authors acknowledge support from grants PID2019-109046GA-I00, PID2022-136526OB-I00 by MICIU/AEI/10.13039/501100011033 and ERDF/EU (to Ana Belén Muñoz Manchado and 2019-FPI to Juan Manuel Barba Reyes). RyC program RYC-2017–22594 and CNS2024-154925 by MICIU/AEI/10.13039/501100011033 ESF Investing in your future (to Ana Belén Muñoz Manchado)

Contents

1. Abstract **12**
2. Resumen **14**
3. List of Abbreviations **16**
4. Introduction **24**
4.1. Parkinson’s Disease 24
4.1.1. Definition and Brief History 24
4.1.2. Etiology and Risk Factors 24
4.1.3. Epidemiology 27
4.1.4. Classical physiopathological mechanisms 28
4.1.5. Brain circuits involved in PD. Special focus on Basal Ganglia 29
4.1.6. Clinical Presentation and Diagnosis 31
4.1.7. Prognosis and Disease Course 33
4.2. Glial Cells in PD 34
4.2.1. Oligodendrocytes 34
4.2.2. Oligodendrocytes in PD 35
4.2.3. Oligodendrocytes Precursor Cells (OPCs) 37
4.2.4. Oligodendrocytes Precursor Cells (OPCs) in PD 38
4.2.5. Astrocytes 38
4.2.6. Astrocytes in PD 39
4.2.7. Microglia 42
4.2.8. Microglia in EP 43
4.2.9. Glia-Glia Crosstalk: a network of dysfunction 45
4.2.10. Glial Network as a Novel Therapeutic Target 46
4.3. Single-cell RNA Sequencing 47
4.3.1. Bulk versus single-cell RNA sequencing 47
4.3.2. Single-nuclei RNA sequencing in Parkinson’s Disease 50
4.4. Spatial Transcriptomics 51
4.4.1. Applications in Neuroscience: Mapping the Brain's Complex Architecture 53
4.4.2. Applying ST to Parkinson’s Disease 53
4.4.3. Current Challenges and Future Directions 54
5. Justification **56**
6. Hypotheses and Objectives **58**
6.1. General hypotheses 58
6.2. General objectives 58
6.3. Specific aims 58
7. Material and Methods **59**
7.1. Human Tissue 59
7.2. Tissue Dissociation 59
7.3. Fluorescent-activated nuclei sorting (FANS) 60
7.4. Library preparation 61
7.5. Illumina sequencing 62
7.6. snRNA-seq Data Analysis 62

7.6.1. Pre-Processing 62
7.6.2. Quality control 62
7.6.3. Glia and non-neuronal detection 63
7.6.4. Subclustering of glial and non-neuronal populations 64
7.6.5. Hierarchical analysis 65
7.6.6. Compositional analysis 65
7.6.7. Module analysis 65
7.6.8. Differential expression analysis 66
7.6.9. KEGG PD analysis 66
7.6.10. Transcription factors analysis 67
7.6.11. Cells Interaction Analysis 67
7.6.12. UPR signaling analysis 68
7.6.13. Braak Lewy Body Staging Analysis 68
7.6.14. Correlations between glial subpopulations and Lewy Body quantifications 68
7.6.15. Correlations between PDAO-1/PDAO-2/MOLA ratio and MBP quantifications 69
7.6.16. Differential expression analysis and comparison between donor groups and PD 69
7.6.17. Functional Enrichment Analysis 70
7.6.18. GSEA superpathways 70
7.6.19. Trajectory Analysis 71
7.6.20. Factor Analysis 71
7.7. Immunohistochemistry with peroxidase-DAB method 71
7.8. Immunohistochemistry images analysis and quantification 72
7.9. Spatial transcriptomics data generation 72
7.9.1. Spatial transcriptomics platform 72
7.9.2. Gene panel design 72
7.9.3. Experimental workflow 73
7.10. Spatial transcriptomics data analysis 73
7.10.1. Segmentation, data preprocessing and cell type identification 73
7.10.2. Gene module analysis using Hotspot 74
7.10.3. Niche identification 74
7.10.4. Identification of spatially-variable genes 75
8. Results 76
8.1. Transcriptional and spatial remodeling of oligodendrocyte lineage cells in the dorsal striatum in Parkinson's Disease 76
8.1.1. A high-resolution atlas of the oligodendrocyte lineage 76
8.1.2. Transcriptional heterogeneity and stress signaling 80
8.1.3. Functional decoding: from transcriptome to phenotype 84
8.1.4. Oligodendrocyte differentiation trajectory and PD-associated alterations 87
8.1.5. Collapse of the signaling infrastructure 90
8.1.6. Spatial validation 93
8.2. Astrocyte heterogeneity and disease-associated states in Parkinson's Disease 95
8.2.1. Cellular heterogeneity of astrocytes and SVZ-derived populations in the human dorsal striatum 95
8.2.2. Reactive astrocyte expansion and stress-driven transcriptional reprogramming in PD 97

8.2.3. Disease-driven astrocyte state transitions from A0 to AR1 and AR2 99
8.3. Microglial activation states and neuroimmune remodeling in the parkinsonian dorsal striatum 101
8.3.1. Single-nucleus transcriptomics reveals multiple microglial states in the human dorsal striatum 101
8.4. Braak Lewy Body stage-dependent remodeling and coordinated glial programs in Parkinson's Disease 105
8.5. Supplementary Information 111
8.5.1. Supplementary Figures 111
8.5.2. Supplementary Tables 118
9. Discussion 120
9.1. Overview and conceptual framework 120
9.2. Oligodendrocyte lineage dysfunction: stress and failed maturation 120
9.3. Astrocyte reactivity in the parkinsonian striatum: between stress and inflammation 122
9.4. Microglial States in the PD Striatum: from Surveillance to Chronic Stress 124
9.5. Braak Lewy Body Stage-Dependent Glial Dynamics and the Two Endophenotypes of PD 125
10. Conclusions 128
11. References 129
12. Acknowledgements 159
13. Appendix 160
13.1. Publications 160

1. Abstract

Parkinson's disease (PD) has historically been understood as a primarily neuronal disorder, but growing evidence makes clear that glial cell dysfunction plays an active role in driving neurodegeneration. This doctoral thesis presents a high-resolution transcriptomic and spatial atlas of glial cells in the human dorsal striatum, covering both caudate nucleus and putamen, with the aim of deciphering their contribution to PD pathogenesis. By combining single-nucleus RNA sequencing (snRNA-seq) with image-based spatial transcriptomics (Xenium platform), we analyzed postmortem samples from 56 donors (36 with PD and 20 neurologically healthy controls), profiling over 270,000 glial nuclei.

The analysis revealed a profound pathological remodeling across all three major glial lineages. In oligodendrocytes, which represent the most abundant glial population, we identified 15 transcriptionally distinct subpopulations, among which several disease-specific states emerged (PDAO-1, PDAO-2, PDAO-3, and PDAOPCs). These disease-associated states change their homeostatic myelinating function in favor of survival under proteostatic stress, as reflected by strong upregulation of heat shock proteins. This functional deviation disrupts normal maturation trajectories, collapses the adhesion signaling required for axonal contact, and correlates directly with alterations in myelination, as demonstrated by reduced MBP immunoreactivity in striatal tissue. In astrocytes and microglia, the results are equally striking. The homeostatic astrocyte population (A0) declines in favor of two divergent reactive phenotypes in PD patients: AR1, defined by proteostatic stress adaptation, and AR2, characterized by overt neuroinflammation and metabolic stress. In parallel, microglia shift away from their homeostatic surveillance state (MH) toward disease-associated phenotypes including phagocytically and metabolically exhausted DAM cells, markedly pro-inflammatory M1 states, and a heat-shock-protein-enriched stress phenotype (MH-HSP).

Perhaps the most conceptually significant finding concerns how this cellular remodeling unfolds across disease progression. Stratification by Braak Lewy body stage revealed that PD does not follow a single glial pathological trajectory. Instead, the data point to the existence of two mutually exclusive reactive programs across patients: an inflammatory/reactive program, dominated by AR2 astrocytes and M1 microglia, and a proteostatic stress program defined by the unfolded protein response (UPR), with predominance of AR1 astrocytes, MH-HSP microglia, and PDAO oligodendrocytes. Different subjects appear to engage preferentially one or the other of these programs, which challenges the traditional view of PD as a disease with a single, uniform glial progression.

Taken together, this thesis demonstrates that PD triggers a coordinated dysfunction of the entire glial network in the dorsal striatum, altering cells that should be protective into amplifiers of tissue damage. The identification of two clearly distinct glial profiles (reactive and UPR programs) reframes our understanding of neurodegeneration at the cellular level. Beyond that, it lays the conceptual groundwork for future patient stratification based on biofluid biomarkers, opening a realistic path toward personalized therapeutic strategies that could modify disease course by targeting the specific glial dysfunctions driving each patient's pathology.

2. Resumen

La enfermedad de Parkinson (EP) se ha definido históricamente como un trastorno neuronal. Sin embargo, numerosos estudios han evidenciado alteraciones de las células gliales en la EP, teniendo estas células un papel activo en la neurodegeneración. Esta tesis doctoral presenta un atlas transcriptómico y espacial de alta resolución de las células gliales en el estriado dorsal humano, abarcando tanto el núcleo caudado como el putamen, con el objetivo de determinar su contribución al desarrollo de la EP. Mediante la combinación de secuenciación de ARN de núcleo único (snRNA-seq) con transcriptómica espacial (Xenium), se analizaron muestras postmortem de 56 sujetos (36 con EP y 20 controles sanos), obteniendo aproximadamente 270.000 células gliales.

El análisis de estas células reveló una remodelación patológica en los tres principales linajes gliales. En los oligodendrocitos, que representan la población glial más abundante, se identificaron 15 subpoblaciones transcripcionalmente distintas, entre las cuales encontramos varios estados específicos de la enfermedad (PDAO-1, PDAO-2, PDAO-3 y PDAOPCs). Estos estados asociados a la enfermedad modifican su función homeostática de mielinización a cambio de sobrevivir, para lo que aumentan las herramientas de estrés proteostático, que se refleja en una marcada sobreexpresión de proteínas de choque térmico. Esta desviación funcional interrumpe las trayectorias normales de maduración, alteran los procesos de adhesión necesarios para el contacto axonal y se correlaciona directamente con alteraciones en la mielinización, tal como demuestra la reducción de la proteína MBP en el tejido estriatal. En astrocitos y microglía, los resultados son igualmente llamativos. La población astrocítica homeostática (A0) disminuye en los pacientes con EP en favor de dos fenotipos reactivos divergentes: AR1, definido por la adaptación al estrés proteostático, y AR2, caracterizado por una marcada neuroinflamación y estrés metabólico. En paralelo, la microglía abandona su estado de vigilancia homeostática (MH) hacia fenotipos asociados a la enfermedad, incluyendo células denominadas DAM, con agotamiento fagocítico y metabólico, estados marcadamente proinflamatorios en M1 y un fenotipo de estrés enriquecido en proteínas de choque térmico (MH-HSP).

No obstante, el hallazgo conceptualmente más relevante tiene que ver con cómo esta remodelación celular se desarrolla a lo largo de la progresión de la enfermedad. La estratificación por estadios de Braak, basada en cuerpos de Lewy, reveló que la EP no sigue una única trayectoria patológica glial. En contraposición, nuestros datos apuntan a la existencia de dos programas reactivos mutuamente excluyentes entre los pacientes: un programa inflamatorio o reactivo, dominado por astrocitos AR2 y microglía M1, y un programa de estrés proteostático definido por la respuesta a proteínas mal plegadas (UPR), con predominio de astrocitos AR1, microglía MH-HSP y oligodendrocitos PDAO. Los pacientes en nuestro estudio parecen activar preferentemente uno u otro de estos programas, lo

que cuestiona la visión tradicional de la EP como una enfermedad con una progresión glial única y uniforme.

En conjunto, esta tesis demuestra que la EP genera una alteración coordinada de toda la red glial en el estriado dorsal, transformando células que deberían ser protectoras en amplificadoras del daño tisular. La identificación de dos perfiles gliales claramente diferenciados (programa reactivo y programa UPR) replantea nuestra comprensión de la neurodegeneración a nivel celular. Además, asentamos las bases conceptuales para una futura estratificación de pacientes basada en biomarcadores en biofluidos, abriendo un camino realista hacia estrategias terapéuticas personalizadas que podrían modificar el curso de la enfermedad actuando sobre las disfunciones gliales específicas que impulsan la patología de cada paciente.

3. List of Abbreviations

A0 - Homeostatic astrocytes 0

ABCA9 - ATP-binding cassette subfamily A member 9

ACTN2 - Actinin-Alpha 2

AD - Alzheimer's disease

ADAMTSL3 - ADAMTS-like protein 3

AGTR1 - Angiotensin II receptor type 1

ALDH1L1 - Aldehyde dehydrogenase 1 family member L1

ANGPT2 - Angiopoietin 2

ANGPL12 - Angiopoietin Like 2

ANGPTL4 - Angiopoietin Like 4

ANK3 - Ankyrin 3

APOC1 - Apolipoprotein C1

APOE - Apolipoprotein E

APP - Amyloid precursor protein

AQP4 - Aquaporin 4

AR1 / AR2 - Reactive astrocytes 1 and 2

ARHGAP24 - Rho GTPase-activating protein 24

ARP - Astrocyte-restricted precursors

ATP5F1E - ATP synthase F1 subunit epsilon

MT-ATP6 - Mitochondrially encoded ATP synthase membrane subunit 6

BAG3 - BAG cochaperone 3

BCL6 - BCL6 transcription repressor

BG - Basal ganglia

BICC1 - BicC family RNA binding protein 1

BIN1 - Bridging integrator 1

BMPR2 - Bone morphogenetic protein receptor type 2

BNIP3L - BCL2 interacting protein 3-like

C1QC - Complement C1q C chain

CABLES1 - Cdk5 And Abl Enzyme Substrate 1

CACNA1A - Calcium Voltage-Gated Channel Subunit Alpha1 A

CADM - Cell adhesion molecule

CCDC153 - Dynein Regulatory Complex Subunit 12 Homolog

CCDC85A - Coiled-Coil Domain Containing 85A

CCL2 - C-C Motif Chemokine Ligand 2

CCND2 - Cyclin D2

CCT3 - Chaperonin Containing TCP1 Subunit 3

CD14 - CD14 Molecule

CD163 - CD163 Molecule

CD3D - CD3 Delta Subunit Of T-Cell Receptor Complex

CD3E - CD3 Epsilon Subunit Of T-Cell Receptor Complex

CD3G - CD3 Gamma Subunit Of T-Cell Receptor Complex

CD44 - CD44 Molecule

CD63 - CD63 Molecule

CD81 - Cluster of differentiation markers (cell surface and immune markers)

CDH1 - Cadherin 1

CDH20 - Cadherin 20

cDNA - Complementary DNA

CEBPB - CCAAT Enhancer Binding Protein Beta

CEBPD - CCAAT Enhancer Binding Protein Delta

CFTR - CF Transmembrane Conductance Regulator

CHI3L1 - Chitinase 3 Like 1

CHRNA10 - Cholinergic Receptor Nicotinic Alpha 10 Subunit

CLDN5 - Claudin 5

CLR - Centered log-ratio

CN - Caudate nucleus

CNS - Central nervous system

CNTN1 - Contactin 1

CNTN2 - Contactin 2

COL12A1 - Collagen Type XII Alpha 1 Chain

COL6A6 - Collagen Type VI Alpha 6 Chain

COPG2 - Coat Protein Complex I Subunit Gamma 2

COPs - Committed oligodendrocyte precursor cells

COX7C - Cytochrome c oxidase subunit 7C

CPT1A - Carnitine palmitoyltransferase 1A

CRYAB - Crystallin Alpha B

CSF1R - Colony-stimulating factor 1 receptor

CTNNA2 - Catenin alpha 2

CTSD - Cathepsin D

CTSL - Cathepsin L

CX3CR1 - C-X3-C Motif Chemokine Receptor 1

DAAM2 - Dishevelled Associated Activator Of Morphogenesis 2

DAB - Diaminobenzidine

DAM - Disease-associated microglia

DAP12 - DNAX-activation protein 12

DAT - Dopamine transporter

DBNDD2 - Dysbindin domain-containing protein 2

DDIT3 - DNA damage-inducible transcript 3

DDIT4 - DNA damage-inducible transcript 4

DEGs - Differentially expressed genes

DJ-1 (PARK7) - Parkinsonism Associated Deglycase

DNAJA1 - DnaJ Heat Shock Protein Family (Hsp40) Member A1

DNAJB1 - DnaJ Heat Shock Protein Family (Hsp40) Member B1

DNAJB6 - DnaJ Heat Shock Protein Family (Hsp40) Member B6

DOCK4 - Dedicator of cytokinesis 4

DSCAML1 - DS Cell Adhesion Molecule Like 1

ECM - Extracellular matrix

ECM2 - Extracellular matrix protein 2

EGR1 - Early growth response 1

ELN - Elastin

PD - Parkinson's disease

ERBB4 - Erb-b2 receptor tyrosine kinase 4

ET - Extratelencephalic

ETV5 - ETS variant transcription factor 5

FANS - Fluorescence-activated nuclei sorting

FCGR3A - Fc gamma receptor IIIa

FDR - False discovery rate

FKBP5 - FKBP Prolyl Isomerase 5

FN1 - Fibronectin 1

FOS - Fos Proto-Oncogene, AP-1 Transcription Factor Subunit

FOXJ1 - Forkhead box J1

FTH1 - Ferritin Heavy Chain 1

FTL - Ferritin Light Chain

GABRG1 - Gamma-Aminobutyric Acid Type A Receptor Subunit Gamma1

GABRR2 - Gamma-Aminobutyric Acid Type A Receptor Subunit Rho2

GARS - Glycyl-tRNA synthetase

GBA - Glucosylceramidase Beta

GBA1 - Glucosylceramidase Beta 1

GCN - Graph convolutional network

GFAP - Glial fibrillary acidic protein

GJA1 - Gap junction protein alpha 1

GLIS3 - GLIS family zinc finger 3

GPC5 - Glypican 5

GPe - Globus pallidus external segment

GPi - Globus pallidus internal segment

GPNMB - Glycoprotein Nmb

GPR17 - G protein-coupled receptor 17

GRIA1 - Glutamate Ionotropic Receptor AMPA Type Subunit 1

GRIA2 - Glutamate Ionotropic Receptor AMPA Type Subunit 2

GRIA3 - Glutamate Ionotropic Receptor AMPA Type Subunit 3

GRID2 - Glutamate Ionotropic Receptor Delta Type Subunit 2

GRM5 - Glutamate Metabotropic Receptor 5

GSEA - Gene set enrichment analysis

H&Y - Hoehn and Yahr scale

HES4 - Hes Family BHLH Transcription Factor 4

HES5 - Hes Family BHLH Transcription Factor 5

HIF1A-AS3 - HIF1A antisense RNA 3

HILPDA - Hypoxia-inducible lipid droplet-associated

HSPA1A - Heat Shock Protein Family A (Hsp70) Member 1A

HSPA1B - Heat Shock Protein Family A (Hsp70) Member 1B

HSPA4L - Heat Shock Protein Family A (Hsp70) Member 4 Like

HSPA5 - Heat Shock Protein Family A (Hsp70) Member 5

HSPA8 - Heat Shock Protein Family A (Hsp70) Member 8

HSPB1 - Heat Shock Protein Family B (Small) Member 1

HSPD1 - Heat Shock Protein Family D (Hsp60) Member 1

HSPE1 - Heat Shock Protein Family E (Hsp10) Member 1

HSPH1 - Heat Shock Protein Family H (Hsp110) Member 1

HSP90AA1 - Heat Shock Protein 90 Alpha Family Class A Member 1

HSP90AB1 - Heat Shock Protein 90 Alpha Family Class B Member 1

HSP90B1 - Heat Shock Protein 90 Beta Family Member 1

HSPR - Heat shock protein response

HVGs - Highly variable genes

IGF1 - Insulin-like growth factor 1

IKZF2 - Ikaros family zinc finger 2

IL-1α / IL-1β (IL1B) - Interleukin 1 alpha and beta

IL13RA1 - Interleukin 13 receptor subunit alpha 1

IL7 - Interleukin 7

IFNGR2 - Interferon gamma receptor 2

IRF1 - Interferon Regulatory Factor 1

IRF7 - Interferon Regulatory Factor 7

IRF8 - Interferon Regulatory Factor 8

IT - Intratelencephalic

JUNB - JunB Proto-Oncogene, AP-1 Transcription Factor Subunit

KAZN - Kazrin, Periplakin Interacting Protein

KCNIP1 - Potassium Voltage-Gated Channel Interacting Protein 1

KCNIP4 - Potassium Voltage-Gated Channel Interacting Protein 4

KIT - KIT Proto-Oncogene, Receptor Tyrosine Kinase

KITLG - KIT ligand

KNN - K-nearest neighbors

LAMA2 - Laminin Subunit Alpha 2

LAMA4 - Laminin Subunit Alpha 4

LB - Lewy body

LNs - Lewy neurites

LGR5 - Leucine Rich Repeat Containing G Protein-Coupled Receptor 5

LHX6 - LIM homeobox 6

LRRK2 - Leucine-rich repeat kinase 2

LUZP2 - Leucine zipper protein 2

M1 - Microglia-1

MAG - Myelin-associated glycoprotein

MBP - Myelin basic protein

MDS-UPDRS - Movement Disorder Society Unified Parkinson's Disease Rating Scale

MDGA2 - MAM domain-containing glycosylphosphatidylinositol anchor 2

MERTK - MER proto-oncogene tyrosine kinase

MH - Homeostatic microglia

MH-HSP - Heat shock protein-enriched stress-associated microglia

MGLL - Monoglyceride lipase

MMP24 - Matrix metallopeptidase 24

MOBP - Myelin-associated oligodendrocyte basic protein

MOLs - Mature oligodendrocytes

MRC1 - Mannose receptor C-type 1

MSA-P - Multiple system atrophy of parkinsonian type

MSNs - Medium spiny neurons

MT1X - Metallothionein 1X

MT2A - Metallothionein 2A

MT3 - Metallothionein 3

MT-ND3 - Mitochondrially Encoded NADH:Ubiquinone Oxidoreductase Core Subunit 3

NAMPT - Nicotinamide phosphoribosyltransferase

NAV3 - Neuron navigator 3

NCAM - Neural cell adhesion molecule

NDUFS5 - NADH:Ubiquinone Oxidoreductase Subunit S5

NDUFS6 - NADH:Ubiquinone Oxidoreductase Subunit S6

NFKBIZ - NF-kappa-B inhibitor zeta

NGEF - Neuronal Guanine Nucleotide Exchange Factor

NLGN1 - Neuroligin 1

NMS - Non-motor symptoms

NR4A2 - Nuclear receptor subfamily 4 group A member 2

NRXN1 - Neurexin 1

NTRK2 - Neurotrophic receptor tyrosine kinase 2

OL - Oligodendrocyte

OPALIN - Oligodendrocytic myelin paranodal and inner loop protein

OPCs - Oligodendrocyte precursor cells

OSM - Oncostatin M

P2RY12 - Purinergic receptor P2Y12

PARK7 - Parkinsonism Associated Deglycase

PCA - Principal component analysis

PDA - Parkinson's disease-associated

PDAOPCs - Parkinson's disease-associated oligodendrocyte precursor cells

PDD - Parkinson's disease dementia

PDE1B - Phosphodiesterase 1B

PDGFRA - Platelet-derived growth factor receptor alpha

PDK4 - Pyruvate dehydrogenase kinase 4

PE - Phycoerythrin

PECAM1 - Platelet and endothelial cell adhesion molecule 1

PELI1 - Pellino E3 ubiquitin protein ligase 1

PFKFB3 - 6-phosphofructo-2-kinase/fructose-2,6-biphosphatase 3

PIGD - Postural instability and gait difficulty

PINK1 - PTEN-induced kinase 1

PLP1 - Proteolipid protein 1

PNS - Peripheral nervous system

PPARG - Peroxisome proliferator-activated receptor gamma

PRDM1 - PR/SET domain 1

PROCR - Protein C receptor

PTPRC - Protein tyrosine phosphatase receptor type C

Pu - Putamen

QDPR - Quinoid dihydropteridine reductase

RBD - REM sleep behavior disorder

RBFOX1 - RNA-binding fox protein 1

RERG - Ras-related and estrogen-regulated growth inhibitor (A0 marker)

RGS6 - Regulator of G protein signaling 6

RIT2 - Ras-like without CAAX 2

ROBO2 - Roundabout guidance receptor 2

ROIs - Regions of interest

ROS - Reactive oxygen species

RPL / RPS - Ribosomal protein families (large and small subunits)

RUNX1 - RUNX family transcription factor 1

RYR2 - Ryanodine receptor 2

RYR3 - Ryanodine receptor 3

S100B - S100 calcium-binding protein B

scCODA - Single-cell compositional data analysis

SELENOM - Selenoprotein M

SEMA3D - Semaphorin 3D

SERPINE1 - Serpin family E member 1

SFRP2 - Secreted frizzled-related protein 2

SLC11A1 / SLC13A4 / SLC14A1 / SLC1A2 / SLC1A5 / SLC2A3 / SLC2A5 / SLC5A11 / SLC7A10 - Solute carrier transporter families

SNAP23 - Synaptosomal-associated protein 23

SNCA - Alpha-synuclein

snRNA-seq - Single-nucleus RNA sequencing

SNc / SNpc - Substantia nigra pars compacta

SNr - Substantia nigra pars reticulata

SOD1 / SOD2 - Superoxide dismutases 1 and 2

SOX11 - SRY-box transcription factor 11

SPARC - Secreted protein acidic and rich in cysteine (osteonectin)

SPP1 - Secreted phosphoprotein 1 (osteopontin)

SRGAP3 - SLIT-ROBO Rho GTPase-activating protein 3

ST - Spatial transcriptomics

STIP1 - Stress-induced phosphoprotein 1

STN - Subthalamic nucleus

SVGs - Spatially variable genes

SVZCs - Subventricular zone cells

SYNDIG1 - Synapse differentiation-inducing gene protein 1

TCF7L1 - Transcription factor 7-like 1

TD - Tremor-dominant

TET1 - Tet methylcytosine dioxygenase 1

TH - Tyrosine hydroxylase

TMEM163 - Transmembrane protein 163

TNF-α - Tumor necrosis factor alpha

TSC22D3 - TSC22 domain family member 3

ULK1 - Unc-51-like autophagy activating kinase 1

UMI - Unique molecular identifier

UPR - Unfolded protein response

VCAN - Versican

VPS35 - Vacuolar protein sorting-associated protein 35

WARS - Tryptophanyl-tRNA synthetase

WIF1 - Wnt inhibitory factor 1

WM - White matter

WMAs - White matter astrocytes

ZFPM2 - Zinc finger protein FOG family member 2

α-syn - Alpha-synuclein

4. Introduction

4.1. Parkinson’s Disease

4.1.1. Definition and Brief History

Parkinson's disease (PD) is a chronic and progressive neurodegenerative disorder, currently ranked as the second most common after Alzheimer's disease (Poewe et al., 2017). The clinical presentation is heterogeneous, with patients showing varying combinations of motor and non-motor symptoms, which involves many challenges for diagnosis and management (GBD 2016 Parkinson’s Disease Collaborators, 2018; Jankovic, 2008).

The disease was first formally described by James Parkinson in 1817 (Parkinson, 2002). Working from observations of just six individuals, he identified what are still recognized as cardinal features: resting tremor, which he described as "involuntary tremulous motion, with lessened muscular power, in parts not in action," slowness of movement, and a characteristic forward-leaning, propulsive gait. He believed cognition was preserved, something that is largely accurate in early stages, though not as the disease progresses (Parkinson, 2002; Poewe et al., 2017).

Later in the 19th century, Jean-Martin Charcot added considerably to this disorder. He drew a clearer boundary between PD and other conditions causing tremor, such as multiple sclerosis, established rigidity as a defining feature, and drew attention to symptoms that were not strictly motor in nature. In addition, he formally introduced the name "Parkinson's disease" (Jankovic, 2008).

The 20th century changed things fundamentally. In 1912, Frederic Lewy identified intracytoplasmic protein deposits, now called Lewy bodies, which remain one of the main neuropathological markers used to confirm PD diagnosis post-mortem (Dickson, 2012; Kalia & Lang, 2015). On the neurochemical side, Arvid Carlsson's work establishing dopamine as a neurotransmitter (Carlsson, 1993) gave Oleh Hornykiewicz the conceptual tools he needed: dopamine was severely depleted in the striatum of PD patients (Fahn, 2008). Consequently, Levodopa came out directly. Introduced in the late 1960s, it remains the most effective symptomatic treatment available (Fahn, 2008; Kalia & Lang, 2015).

4.1.2. Etiology and Risk Factors

The etiology of PD remains unclear in the majority of cases. Around 90-95% are classified as idiopathic or sporadic, meaning no identifiable single cause can be established (Kalia & Lang, 2015). Current evidence suggests sporadic PD has a multifactorial origin, due to interactions between an

individual's genetic background and environmental exposures accumulated over a lifetime, rather than a discrete triggering event (Ascherio & Schwarzschild, 2016; Poewe et al., 2017).

A smaller subset of patients (5-10%), carry high-penetrance mutations in single genes that are sufficient to cause the disease (Kalia & Lang, 2015). These monogenic forms are uncommon, but they have been very informative for understanding PD pathophysiology. The first PD-linked gene discovered was SNCA (encoding alpha-synuclein), with related autosomal dominant mutations. Another gene is LRRK2 (Leucine-Rich Repeat Kinase 2), which accounts for the largest share of autosomal dominant cases (Poewe et al., 2017). Recessive forms, typically associated with early-onset forms of the disease, involve Parkin, PINK1, and DJ-1, all of which play roles in mitochondrial quality control (Kalia & Lang, 2015) (Table 1).

At a population level, GWAS have catalogued numerous common variants that individually confer small increases in PD risk, but whose aggregate effect on susceptibility is considerable (Nalls et al., 2019; Poewe et al., 2017). GBA variants are also important in PD risk, as although they are not directly causal in the monogenic sense, they raise lifetime PD risk by five- to sevenfold and are associated with more rapid cognitive deterioration after disease onset (A. H. V. Schapira, 2015) (Table 1).

The single strongest non-genetic risk factor is age, with prevalence increasing after 60 (Poewe et al., 2017). Several environmental exposures have been consistently associated with elevated PD risk, particularly the pesticides paraquat, rotenone and the industrial solvent trichloroethylene (Ascherio & Schwarzschild, 2016; Tanner et al., 2011). Head trauma has also been proposed as a contributing factor, though the evidence is less uniform (Marras et al., 2014). On the other hand, regular caffeine consumption and tobacco smoking both show inverse associations with PD incidence (Ascherio & Schwarzschild, 2016; Poewe et al., 2017). Higher physical activity levels have also been repeatedly linked to reduced PD risk (Ascherio & Schwarzschild, 2016).

Gene	Protein	Frequency in PD	Pathogenic Variants*
Autosomal Dominant			
SNCA	Alpha-synuclein	<<1%	A30P, E46K, H50Q, G51D, A53T
LRRK2	Leucine-rich repeat kinase 2	~3%	G2019S, I2020T, R1441C, R1441G, R1441H, N1437H, Y1699C
VPS35	Vacuolar protein sorting-associated protein 35	<1%	D620N
Autosomal Recessive			
Parkin	Parkin	~1%	R42P, V65E, K211N, C212Y, T415N, C431F, C441R, T240R, R275W, G430D
PINK1	PTEN induced putative kinase 1	<1%	G309D, Q456X, L347P, G411S, W437X, M261I
DJ-1	Protein deglycase DJ-1	< <1%	L166P, A104T
Risk Factor			
GBA1	Glucocerebrosidase	5-15%	E326K, N370S, L444P, D140H, T369M
LRRK2	Leucine-rich repeat kinase 2	5–10%	G2385R
GWAS risk variant	Intergenic variant (i.e., non-protein-coding)	~50%	rs6658353

Table 1. Overview of PD-associated genetic variants. Adapted from Bogers *et al* (Bogers et al., 2023). *Only a subset of known pathogenic variants is shown for each gene, as most genes carry several to dozens of documented variants. GBA1 is an exception, with over 400 pathogenic variants identified to date.

4.1.3. Epidemiology

PD is currently the fastest-growing neurological disorder worldwide, a distinction that has brought increasing attention from a global public health perspective (GBD 2016 Parkinson's Disease Collaborators, 2018). Understanding the scale of this growth, its geographic distribution, and the factors driving it has become a central concern in the field.

The numbers are substantial. GBD analyses documented that the total number of people living with PD more than doubled between 1990 and 2016, rising from approximately 2.5 million to 6.1 million (GBD 2016 Parkinson's Disease Collaborators, 2018). More recent epidemiological work confirms this upward trend and suggests the rate of increase may have accelerated over the past two decades (J. Zhu et al., 2024). The burden is not distributed uniformly. Prevalence and incidence differ across regions, ethnic groups, and sexes, which implies that the drivers of this increase are not acting homogeneously across the global population (Ben-Shlomo et al., 2024; Dorsey et al., 2018).

Future projections are not encouraging. Estimates based on GBD 2021 data indicate that the global burden will grow considerably further by 2050 (Su et al., 2025). Population aging is consistently identified as the primary driver of this projected increase, which is unsurprising given how steeply PD risk rises after age 60 (Dorsey et al., 2018; Su et al., 2025). A persistent sex difference is also well established: men show higher PD rates than women across decades of epidemiological data, and this disparity remains poorly understood mechanistically (Ben-Shlomo et al., 2024).

These epidemiological patterns also reflect broader socioeconomic gradients. A meta-analysis of historical trends found higher PD prevalence in countries with greater Socio-Demographic Index and Human Development Index scores, pointing toward industrialization as a contributing factor (J. Zhu et al., 2024). This fits with what is known about PD's multifactorial etiology. Industrial and agricultural development has introduced environmental exposures, such as pesticides and industrial solvents, that are already established risk factors in the literature (Ascherio & Schwarzschild, 2016; Ben-Shlomo et al., 2024). Their cumulative contribution to the global burden of PD is likely underestimated.

4.1.4. Classical physiopathological mechanisms

The two defining pathological features of PD are well established: selective loss of dopaminergic neurons in the substantia nigra pars compacta (SNpc), and the presence of intracellular protein aggregates of α-synuclein, known as Lewy bodies (Kalia & Lang, 2015; Poewe et al., 2017; Spillantini et al., 1997) (Figure 1). When dopaminergic neurons die, striatal dopamine levels drop sharply, disrupting basal ganglia motor circuits and generating the characteristic motor features of the disease (Jankovic, 2008). Alpha-synuclein (α-syn) stands at the center of this process (Poewe et al., 2017). α-syn is a soluble presynaptic protein that participates in synaptic vesicle dynamics and

neurotransmitter release. However, in PD, it misfolds, progressing from monomers to oligomers, and finally to insoluble fibrils that pack into Lewy bodies (Kalia & Lang, 2015). The oligomeric intermediates are thought to be particularly harmful. They disrupt membranes, impair proteostasis, and can transfer between cells in a prion-like manner, seeding aggregation in healthy neurons (Frost & Diamond, 2010; Luk et al., 2012). This propagation capacity is the basis of the Braak Lewy Body (LB) staging hypothesis: PD pathology is proposed to begin in the dorsal motor nucleus of the vagus or the olfactory bulb and spread upward in a predictable pattern, reaching the SNpc and, in later stages, the cortex (Braak et al., 2003) (Figure 1).

Why SNpc dopaminergic neurons are particularly vulnerable remains an active area of investigation, though mitochondrial dysfunction and oxidative stress are consistently implicated (Kalia & Lang, 2015; Poewe et al., 2017). Reduced Complex I activity in the mitochondrial electron transport chain is one of the most reproducible findings in PD tissue, as it limits ATP production and increases reactive oxygen species (ROS) (A. H. V. Schapira, 2015). Mutations in PINK1 and Parkin, both required for mitophagy, create this problem by impairing the clearance of damaged mitochondria. The result is accumulation of dysfunctional mitochondria, increased ROS, and eventual activation of apoptotic pathways (Youle & Narendra, 2011) (Figure 1).

Lysosomal dysfunction is another major contributor (A. H. V. Schapira, 2015). Under normal conditions, the lysosomal pathway degrades misfolded α-syn; when it fails, aggregates build up and further impair lysosomal function, a feedback cycle that reduces proteostasis (Kalia & Lang, 2015; A. H. V. Schapira, 2015). GBA mutations decrease the activity of the lysosomal enzyme glucocerebrosidase and represent the strongest known genetic risk factor for sporadic PD, illustrating this mechanism directly (Poewe et al., 2017) (Figure 1).

Early descriptions of PD treated it as a neuronal disease, but that view has been revised considerably. PD progresses within a multicellular environment shaped by chronic neuroinflammation, and this inflammation is not simply a downstream consequence of neuronal death, it appears to actively drive it (Arena et al., 2022; Hirsch & Hunot, 2009; Poewe et al., 2017; Tansey et al., 2022). Single-nucleus RNA sequencing (snRNA-seq) has clarified some of the cellular players here. Microglia frequently shift into a disease-associated state, releasing pro-inflammatory cytokines and ROS in response to extracellular α-syn (Hirsch & Hunot, 2009; Sanchez-Guajardo et al., 2013). The NLRP3 inflammasome, activated by α-syn, amplifies this cascade further (Liang et al., 2025; Menu & Vince, 2011). Astrocytes, meanwhile, adopt an A1-like reactive phenotype, losing their homeostatic and metabolic support functions and instead releasing factors that worsen dopaminergic neuronal damage (Liddelow et al., 2017; Poewe et al., 2017; Yun et al., 2018). Oligodendrocytes and their precursor cells (OPCs) are also affected; snRNA-seq data show widespread transcriptional disruption in these

populations, pointing to impaired myelination and reduced metabolic support as additional factors in axonal degeneration and neuronal vulnerability (Agarwal et al., 2020; Bae et al., 2023).

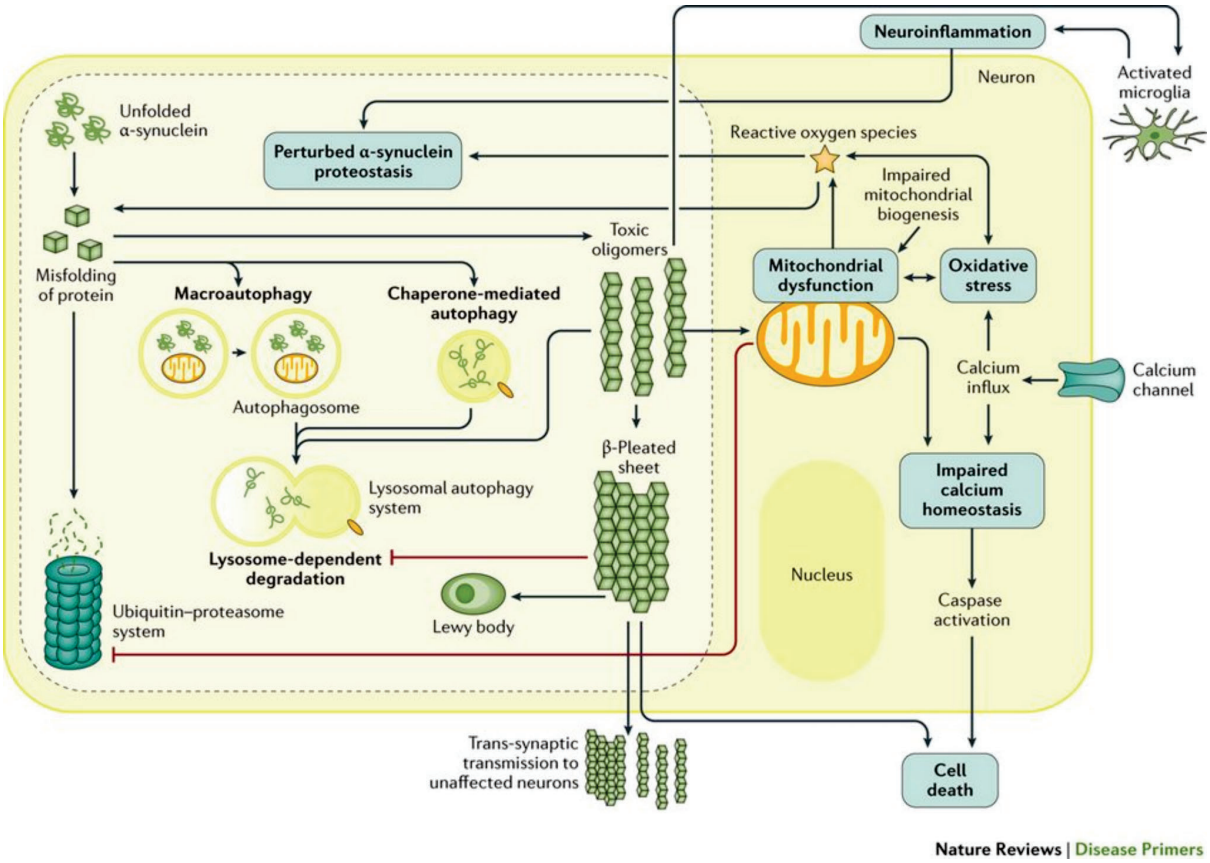

Figure 1. Overview of the key molecular pathways involved in PD pathogenesis and their interactions. Modified from Poewe *et al* (Poewe et al., 2017).

4.1.5. Brain circuits involved in PD. Special focus on Basal Ganglia

The motor symptoms of PD are best understood in the context of basal ganglia (BG) circuitry. The BG consist of several interconnected subcortical nuclei: the dorsal striatum (caudate nucleus, CN, and putamen, Pu), the ventral striatum (nucleus accumbens and olfactory tubercle), the external and internal segments of the globus pallidus (GPe and GPi), the subthalamic nucleus (STN), and the substantia nigra, which divides into the pars compacta (SNc) and pars reticulata (SNr). Each of these structures contributes differently to motor regulation (Kalia & Lang, 2015). Together, they form looping circuits that receive excitatory cortical inputs, process them through successive BG areas, and return outputs to the cortex via the thalamus. This is known as corticostriato-thalamo-cortical pathways (Alexander et al., 1986). Multiple loops exist, some related to cognitive or limbic functions, but the motor loop is the one whose disruption is most clinically evident in PD (Jankovic, 2008) (Figure 2).

The striatum is the main input structure of the BG, receiving glutamatergic projections from cortical areas (Poewe et al., 2017). Output from the BG goes through the GPi and SNr, which maintain tonic GABAergic inhibition over thalamic neurons that in turn modulate motor cortical activity. In this way, the BG continuously regulates the balance between facilitation of intended movements and suppression of competing ones. Two anatomically and functionally distinct pathways, originating from separate striatal populations of GABAergic medium spiny neurons (MSNs) defined by their dopamine receptor expression, are responsible for this regulation: the direct and indirect pathways (Albin et al., 1989). D1 receptor-expressing MSNs form the direct pathway, projecting monosynaptically to the GPi/SNr. Their activation inhibits GPi/SNr output, disinhibiting thalamic neurons and facilitating cortical motor activity (DeLong, 1990; Kalia & Lang, 2015). D2-expressing MSNs, by contrast, form the indirect pathway, which routes polysynaptically through the GPe and STN before reaching the GPi/SNr. When D2-MSNs are active, they inhibit the GPe, which releases the STN from tonic inhibition; the resulting increase in STN excitatory drive to the GPi/SNr strengthens thalamic inhibition and suppresses unwanted movements (Albin et al., 1989; Bergman et al., 1990; DeLong, 1990) (Figure 2).

Under normal conditions, dopamine released from SNc terminals modulates both pathways simultaneously, potentiating D1-MSN activity to favour direct pathway activation, while suppressing D2-MSN activity to attenuate indirect pathway throughput (Poewe et al., 2017). The net result is a BG output state that permits smooth voluntary movement (Figure 2).

In PD, progressive SNc degeneration causes marked striatal dopamine depletion (Kalia & Lang, 2015). D1-MSNs, deprived of dopaminergic facilitation, become hypoactive, weakening the direct pathway. D2-MSNs, released from dopaminergic suppression, become hyperactive, amplifying indirect pathway drive. Both changes push in the same direction: excessive GPi/SNr activation and disproportionate thalamic inhibition (DeLong, 1990; Jankovic, 2008). The downstream effect is a reduced thalamocortical excitation, which manifests clinically as bradykinesia and rigidity (Poewe et al., 2017). Beyond these rate-based changes, the classical model has been refined over the years. Dopamine depletion also generates abnormal oscillatory synchronisation across BG-cortical networks, most notably in the beta frequency band (roughly 13–30 Hz). This pathological beta synchrony creates an anti-kinetic network state that interferes with the initiation and execution of movement, and its magnitude correlates with the degree of bradykinesia and rigidity (C. Hammond et al., 2007; Little & Brown, 2014) (Figure 2).

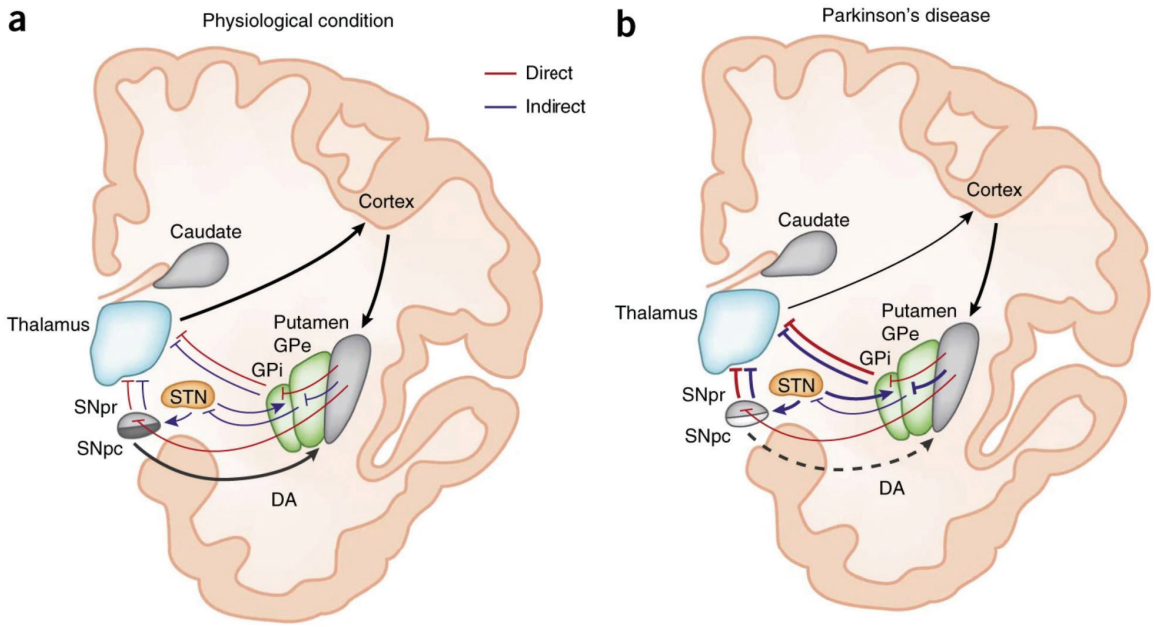

Figure 2. Basal Ganglia Circuit Imbalance in Parkinson's Disease. Modified from Calabresi *et al* (Calabresi et al., 2014).

4.1.6. Clinical Presentation and Diagnosis

The clinical presentation of PD is heterogeneous, but diagnosis still depends on identifying a core set of motor signs. It has become clear over the years that these motor features represent only a part of the problem, as PD also carries a wide range of non-motor symptoms, many of which appear before any visible motor change and contribute substantially to overall disease burden (Chaudhuri et al., 2006).

Cardinal Motor Presentation and Clinical Diagnosis

In PD, parkinsonism is the diagnostic starting point. It is defined as bradykinesia accompanied by at least one of the following: resting tremor or rigidity (Postuma et al., 2015). Symptoms typically begin unilaterally before involving both sides, an asymmetric onset that often helps differentiate PD from other parkinsonian syndromes (Jankovic, 2008).

Bradykinesia is the most essential diagnostic feature. It is more than simple slowness. The defining characteristic is a progressive decrease in movement amplitude during repetitive tasks (Postuma et al., 2015). In practice, this shows up as reduced arm swing, a shuffling gait, difficulty with fine motor tasks like buttoning clothes, and micrographia (Jankovic, 2008; Kalia & Lang, 2015). Resting tremor, though not required for diagnosis, is the most recognizable feature to patients and families (Jankovic, 2008).

Rigidity manifests as increased muscle tone during passive movement, detecting either a smooth, constant resistance or a ratcheted quality (Kalia & Lang, 2015). Postural instability tends to emerge later and becomes a major contributor to falls as the disease advances (Jankovic, 2008).

It is important to note that PD remains a clinical diagnosis, despite the advances in neuroimaging and biomarker research in the last decades. The current MDS criteria require parkinsonism as the essential first step (Postuma et al., 2015). A diagnosis of "clinically established PD" requires the absence of exclusionary features: early prominent dementia, cerebellar signs, and others, together with supportive evidence, of which a robust and sustained levodopa response carries the most diagnostic weight (Kalia & Lang, 2015; Postuma et al., 2015). When uncertainty persists, dopamine transporter (DAT) imaging can help confirm a presynaptic dopaminergic deficit (Poewe et al., 2017).

Non-Motor and Prodromal Presentation

PD is now understood as a multisystem disorder. Its non-motor symptoms (NMS) affect nearly every domain of daily life and, for many patients, prove more disabling than the motor syndrome (Chaudhuri et al., 2006; Kalia & Lang, 2015). A significant number of these symptoms appear during the prodromal phase, before parkinsonism is clinically detectable (Berg et al., 2015; Postuma et al., 2015). Hyposmia and chronic constipation are among the most consistent early markers (Kalia & Lang, 2015). REM sleep behavior disorder (RBD) is one of the strongest prodromal predictors of synucleinopathy and can precede motor symptoms by years to decades (Postuma et al., 2015; Schenck et al., 2013).

As PD progresses, the non-motor burden expands. Autonomic dysfunction becomes more prevalent, including orthostatic hypotension, urinary urgency, and excessive sweating (Jankovic, 2008). Depression and anxiety often appear early and are frequently underrecognized (Kalia & Lang, 2015). Cognitive impairment follows a slower trajectory, typically beginning with executive dysfunction before advancing, in some cases, to Parkinson's disease dementia (PDD) (Degirmenci et al., 2023; Emre et al., 2007). Visual hallucinations are the most common form of psychosis in advanced disease (Kalia & Lang, 2015).

Disease Staging and Assessment

To assess progression in PD, the Hoehn and Yahr (H&Y) scale remains a standard clinical staging tool (Hoehn & Yahr, 1967), providing a broad overview across five stages:

- Stage 1: Unilateral involvement only.
- Stage 2: Bilateral involvement without postural instability.
- Stage 3: Mild-to-moderate bilateral disease with some postural instability but preserved independence.
- Stage 4: Severe disability; patient can still walk or stand unaided.
- Stage 5: Wheelchair-bound or bedridden without assistance.

The H&Y scale is simple and quick but captures only a fraction of PD's complexity (Jankovic, 2008). For more granular assessment, particularly in research, the MDS-UPDRS is the accepted standard (Goetz et al., 2008). It covers four domains:

- Part I: Non-motor experiences of daily living (cognition, mood, sleep, pain).
- Part II: Motor experiences of daily living (speech, dressing, freezing).
- Part III: Clinician-rated motor examination (tremor, rigidity, bradykinesia).
- Part IV: Motor complications (dyskinesias, “off” periods).

This multidimensional structure makes it suited for tracking both symptom evolution and treatment response across the full range of PD manifestations (Poewe et al., 2017).

4.1.7. Prognosis and Disease Course

PD is by definition a progressive neurodegenerative condition, but the rate and pattern of that progression differ considerably between patients (Kalia & Lang, 2015; Poewe et al., 2017). This variability is one of the features that makes long-term management challenging for both patients and clinicians. PD is not a terminal diagnosis. Mortality rates tend to track those of age-matched controls for roughly the first decade after diagnosis, diverging more significantly as accumulated disability increases (Hely et al., 2008; Poewe et al., 2017).

Early disease is often characterized by a period of good symptomatic control. Motor features typically respond well to dopaminergic therapy, especially levodopa (Kalia & Lang, 2015). This window does not last indefinitely. As nigrostriatal degeneration advances, most patients develop motor complications: dyskinesias and response fluctuations in which medication effects disappear before the next dose is due (Kalia & Lang, 2015; Olanow et al., 2009). Long-term follow-up data from the Sydney Multicenter Study illustrate just how prevalent these problems become. By 15 years from diagnosis, non-levodopa-responsive features dominate the clinical picture (Hely et al., 2008).

Later stages are increasingly shaped by symptoms that dopaminergic therapy does not adequately address (Jankovic, 2008). Axial motor problems, such as postural instability, freezing of gait, or dysarthria, become more prominent and are a major source of falls and functional decline. Non-motor burden also grows substantially: autonomic dysfunction, neuropsychiatric symptoms, and cognitive impairment become the leading contributors to disability in advanced disease (Kalia & Lang, 2015).

The onset of PDD marks a significant transition point, associated with greater caregiver burden and higher mortality (Degirmenci et al., 2023; Emre et al., 2007).

Certain clinical features at diagnosis carry prognostic weight. For example, tremor-dominant (TD) presentation is generally associated with slower motor progression and less cognitive involvement. Patients with the postural instability and gait difficulty (PIGD) subtype tend to deteriorate faster, respond less robustly to dopaminergic drugs, and are at higher risk for early dementia (Jankovic, 2008; Poewe et al., 2017). Older age at onset, GBA mutations, and early non-motor features are additional markers of a more aggressive disease course (Halliday et al., 2011; Poewe et al., 2017; A. H. V. Schapira, 2015).

4.2. Glial Cells in PD

Glial cells make up the non-neuronal component of the nervous system. For a long time they were treated as a scaffolding that gives structural support to neurons, but that view has changed considerably over the past few decades. We now know that glia participate in neural development, circuit regulation, and tissue protection, and their dysfunction is increasingly linked to neurological disease (Barres, 2008; Jäkel & Dimou, 2017; Lago-Baldaia et al., 2020). The group itself is not uniform. In the CNS the main populations are astrocytes, microglia, oligodendrocytes, and OPCs; in the PNS, Schwann cells take on comparable roles.

4.2.1. Oligodendrocytes

Myelination is one of the most recognizable contributions glial cells make to nervous system function. Myelin allows fast neural communication. Axons wrapped in this lipid-rich sheath conduct action potentials more efficiently than unmyelinated ones, not because the signal travels faster along the membrane, but because it jumps between gaps in the sheath called nodes of Ranvier rather than propagating continuously (Hartline & Colman, 2007; Nave & Werner, 2014; Rasband & Peles, 2015). That saltatory conduction is also metabolically cheaper, which matters in an organ that consumes a disproportionate share of the body's energy budget (Nave & Werner, 2014).

Who builds the myelin depends on where the axon is. In the CNS, oligodendrocytes do it. A single cell can extend processes to multiple axons simultaneously, producing dozens of myelin segments from one cell body. This level of multi-axon coverage has no equivalent in the PNS, where each Schwann cell handles only one segment (Nave & Werner, 2014).

Beyond wrapping axons, oligodendrocytes actively support the axons they contact. They transfer metabolites (lactate and pyruvate) directly into the axonal compartment through monocarboxylate transporters, providing a local energy supply that is independent of astrocytic input (Funfschilling et

al., 2012). This turns out to be critical: mice in which oligodendrocytes cannot perform glycolytic support develop axonal degeneration even when myelin structure appears intact, which separates the trophic function from the insulating one. Oligodendrocytes also help regulate axonal diameter and cytoskeletal organization, influencing conduction properties (Nave & Werner, 2014).

4.2.2. Oligodendrocytes in PD

PD research has been dominated for decades by a fairly narrow focus: dopaminergic neuron loss in the substantia nigra. That framing is not wrong, but it is increasingly looking incomplete. Evidence from transcriptomics, epigenomics, and postmortem tissue profiling is pointing toward glial cells, not only as reactive bystanders to neuronal death, but as active contributors to the disease process from early stages (Errea & Rodriguez-Oroz, 2021; Hirsch & Hunot, 2009; Tansey et al., 2022). While microglia and astrocytes have long been implicated in this process (Glass et al., 2010; Ouchi et al., 2005), oligodendrocytes have only recently entered the picture (Adams et al., 2024; Bryois et al., 2020; Salazar Campos et al., 2025).

Single-cell epigenomic mapping of PD risk loci has shown that a substantial fraction of causal variants do not overlap in regulatory elements active in neurons. Instead, they fall in enhancers that are selectively active in oligodendrocytes (Bryois et al., 2020; Corces et al., 2020; A. J. Lee et al., 2023). That is not the result you would expect if oligodendrocytes were simply collateral damage from dying neurons, suggesting that something is going wrong in the oligodendrocyte lineage itself, possibly before any significant neuronal loss has occurred (Reynolds et al., 2019).

One of the canonical pathological hallmarks of PD is α-syn aggregation and it has historically been studied almost entirely in neurons. There is growing evidence for what some have started calling an oligodendrocytopathy: α-syn accumulation within oligodendrocytes that triggers its own distinct pathological cascade (Ettle et al., 2016; Rohan et al., 2016; Salazar Campos et al., 2025).

Single-cell sequencing of human midbrain tissue has captured this directly, showing substantial glial activation alongside the expected neuronal changes (Smajić et al., 2022). Inside oligodendrocytes, α-syn aggregates provoke a cellular stress response that is particularly damaging. Oligodendrocytes are metabolically expensive to run, because sustaining myelin sheaths across dozens of axon segments demands continuous energy output (Philips & Rothstein, 2017; Salazar Campos et al., 2025) (Figure 3). When α-syn disrupts that metabolic machinery, the cell can no longer maintain myelin integrity (Azevedo et al., 2022; Richter-Landsberg & Leyk, 2013).

The consequences of that failure extend beyond the oligodendrocyte itself. An axon that loses its myelin sheath loses more than electrical insulation, it also loses the trophic support that the oligodendrocyte was providing through metabolite transfer. That combination renders axons

vulnerable to degeneration independently of what is happening to the neuronal cell body, and there is an argument that this axonal deterioration precedes and contributes to neuronal death rather than following from it (Errea & Rodriguez-Oroz, 2021; Ettle et al., 2016; Nave, 2010; Salazar Campos et al., 2025) (Figure 3).

Spatial omics and single-cell studies in the striatum have confirmed that oligodendrocytes and astrocytes in PD tissue carry disease-specific transcriptional signatures, and they are not generic stress responses, but changes that map onto PD genetic risk loci and neuroinflammatory pathways (Bryois et al., 2020; A. J. Lee et al., 2023; Xu et al., 2023).

High-resolution, cell-type-specific profiling technologies have substantially changed how neurodegeneration is understood. In AD, they revealed discrete disease-associated subtypes of astrocytes and oligodendrocytes with distinct molecular signatures, some driving pathology and some apparently conferring resilience (Mathys et al., 2019a, 2019b; Sadick et al., 2022). The same analytical approach applied to PD is producing comparably complex results.

Oligodendrocytes are now implicated across multiple levels of PD pathogenesis simultaneously: as cells with genetic susceptibility, as sites of α-syn accumulation, and as the origin of functional failures that feed into both axonal degeneration and neuroinflammation (Adams et al., 2024; Corces et al., 2020; Errea & Rodriguez-Oroz, 2021; Smajić et al., 2022; Xu et al., 2023). Whether they are better described as initiators or amplifiers of disease probably depends on which genetic subtype of PD is being considered, and that distinction has not been resolved yet (Salazar Campos et al., 2025).

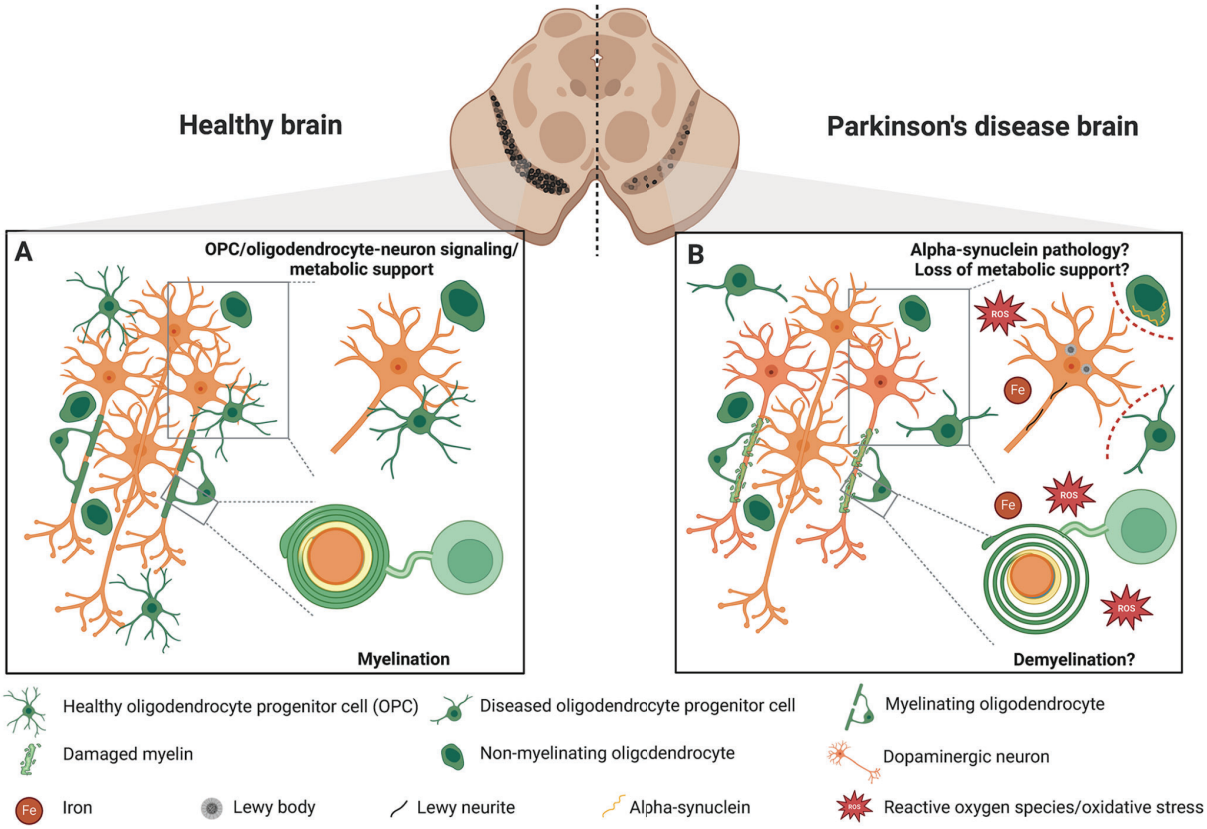

Figure 3. Myelination, metabolic support, and oligodendrocyte dysfunction in Parkinson's Disease. Modified from Salazar-Campos *et al* (Salazar Campos et al., 2025).

4.2.3. Oligodendrocytes Precursor Cells (OPCs)

OPCs, also called NG2-glia, are not an inactive reserve that remains on standby to act. Their processes are in constant motion, sampling the local environment, and the cells themselves divide regularly even in healthy tissue (Dehestani et al., 2024; Nishiyama et al., 2009; Viganò & Dimou, 2016). Under normal conditions their main output is new oligodendrocytes, which feed into the ongoing remodeling of myelin that occurs in response to neural activity and experience (myelin plasticity) (Fields, 2015; Richardson et al., 2011).

When myelin is damaged, OPCs respond. They migrate toward the lesion, proliferate, and differentiate into myelinating oligodendrocytes that can restore the sheath around demyelinated axons (Franklin & Ffrench-Constant, 2017; Nishiyama et al., 2009). In diseases like multiple sclerosis this remyelination process does occur, at least early on, and axonal conduction recovers (Fancy et al., 2011; Kuhlmann et al., 2008). The problem is that remyelination often fails in chronic lesions, and why OPC differentiation stalls in that context despite the cells being present is one of the more actively studied questions in the field (Franklin & Ffrench-Constant, 2017; May et al., 2014).

4.2.4. Oligodendrocytes Precursor Cells (OPCs) in PD

Demyelination in PD is not just the loss of mature oligodendrocytes. OPCs replace oligodendrocyte populations when damage occurs, but they are compromised by the disease process (Akay et al., 2021; Dehestani et al., 2024; Nishiyama et al., 2009). In healthy tissue these cells are not inactive, they divide, migrate, and differentiate in response to myelin damage, functioning as a local repair system that turns over continuously even in the adult brain (Figure 3).

In PD the repair capacity breaks down. α-syn accumulation appears to be toxic to the OPC lineage, not by killing the cells outright, but by arresting them at an immature stage where they cannot complete differentiation into functional myelinating oligodendrocytes (Azevedo et al., 2022; May et al., 2014) (Figure 3). Single-nucleus transcriptomic data from human PD midbrain tissue has captured a population of OPCs that are transcriptionally activated but stuck, unable to progress along their normal differentiation trajectory (Agarwal et al., 2020; Smajić et al., 2022).

The result is a deficit operating at two levels at the same time. Mature oligodendrocytes are degenerating, and the mechanism that would normally replace them is blocked by the same proteinopathy driving that degeneration. Axons lose both their myelin sheath and their metabolic support, with no endogenous cells supporting repair (Dehestani et al., 2024; Ettle et al., 2016; Salazar Campos et al., 2025). Whether restoring OPC differentiation capacity could slow that process is an open question.

4.2.5. Astrocytes

Astrocytes are the most abundant glial cells in the CNS. Each cell extends a dense array of processes that make contact with neurons, blood vessels, and neighboring glia, influencing multiple aspects of neural activity at once (Sofroniew & Vinters, 2010; Zhou et al., 2019).

Their role at the synapse is perhaps the best studied. Astrocytic processes wrap around pre- and postsynaptic terminals, and the resulting structure is referred to as the tripartite synapse (Araque et al., 1999; Eroglu & Barres, 2010). From there, astrocytes buffer extracellular ion concentrations and clear glutamate from the cleft through specific membrane transporters. This removal step matters more than it might initially seem: when glutamate accumulates, signals are prolonged and neurons become vulnerable to excitotoxic damage (Mahmoud et al., 2019; Verkhratsky & Nedergaard, 2018).

Astrocytes also cover the metabolic side of neuronal activity. Glucose taken up from the bloodstream is converted to lactate inside the astrocyte and then transferred to neurons, which use it as fuel. This is the basis of the astrocyte-neuron lactate shuttle, a mechanism that keeps energy-demanding circuits

running under normal physiological conditions (Bélanger et al., 2011; Pellerin & Magistretti, 1994; Verkhratsky & Nedergaard, 2018).

On the vascular side, astrocytic end-feet wrap around CNS blood vessels and help maintain the tight junctions between endothelial cells that form the blood-brain barrier (Abbott et al., 2006; Stackhouse & Mishra, 2021). This physical contact, combined with paracrine signaling toward endothelial cells, limits the entry of circulating toxins, pathogens, and other potentially harmful molecules into neural tissue (Alvarez et al., 2011; Verkhratsky & Nedergaard, 2018). However, after CNS injury the situation changes, and astrocytes undergo reactive astrogliosis. This means they hypertrophy, shift their gene expression profile, and over time contribute to glial scar formation around the damaged area (Escartin et al., 2021; Sofroniew & Vinters, 2010). The scar contains the damage and stabilizes the local environment, but it also creates a barrier that axons have difficulty crossing, complicating regeneration and synaptic repair (Burda & Sofroniew, 2014; Jäkel & Dimou, 2017; Silver & Miller, 2004).

4.2.6. Astrocytes in PD

The idea that astrocytes are passive bystanders in neurodegenerative processes is no longer a reality. In PD specifically, they are now understood to actively shape the disease environment by amplifying neuroinflammatory signals, facilitating protein spread, and influencing neuronal survival in ways that are not simply reactive (Booth et al., 2017; Iovino et al., 2020; Sonninen et al., 2020). Whether they are better described as early drivers of pathology or late amplifiers depends on the stage and context (Booth et al., 2017; K. Li et al., 2019; Wakabayashi et al., 2000).

Under normal circumstances, astrocytes are efficient at clearing misfolded proteins from the extracellular space. When neurons release α-syn, astrocytes take it up as part of their ordinary housekeeping (Lindström et al., 2017; Tsunemi et al., 2020). The problem is that misfolded α-syn resists normal degradation. It accumulates in lysosomes, progressively impairing the same clearance machinery the astrocyte depends on to process it (Iovino et al., 2020; Sonninen et al., 2020). Lewy body-like inclusions have been identified in astrocytes in postmortem PD tissue, which suggests this is not an experimental artifact and it happens in the disease itself (Lindström et al., 2017; Wakabayashi et al., 2000).

Once they cross that threshold, the downstream effects become more severe. Mitochondrial function becomes altered, decreasing ATP availability the cell needs to run protein degradation pathways (Braidy et al., 2013; Lindström et al., 2017). Autophagy and the ubiquitin-proteasome system both decline, and damaged proteins accumulate rather than getting cleared. Thus, what started as an attempt to protect the surrounding tissue ends with an astrocyte that is metabolically compromised,

transcriptionally reactive, and now releasing pro-inflammatory signals that worsen the environment for nearby neurons (Booth et al., 2017; Sonninen et al., 2020; Yun et al., 2018) (Figure 4). The transition from supportive to harmful is not a switch, it appears to be a gradual failure, which makes it harder to identify a clear therapeutic target.

Reactive astrogliosis is not a binary switch. When the CNS is exposed to injury, inflammation, or accumulating α-syn, astrocytes undergo a graded response with changes in gene expression, morphology, and function that vary considerably depending on the nature and severity of the triggering insult (Escartin et al., 2021; Sofroniew & Vinters, 2010). In acute settings this response is broadly protective. In PD, it tends to become maladaptive over time (Booth et al., 2017; K. Li et al., 2019) (Figure 4).

Part of what goes wrong is the loss of glutamate buffering. Reactive astrocytes in PD show reduced expression of glutamate transporters, which allows glutamate to accumulate at synapses and exposes nearby neurons to excitotoxic damage (Iovino et al., 2020; J. Wang et al., 2020) (Figure 4). Metabolic support, represented by lactate export to neurons, decreases. This is particularly problematic in the dopaminergic circuits of the midbrain that are already under energetic stress (Sonninen et al., 2020).

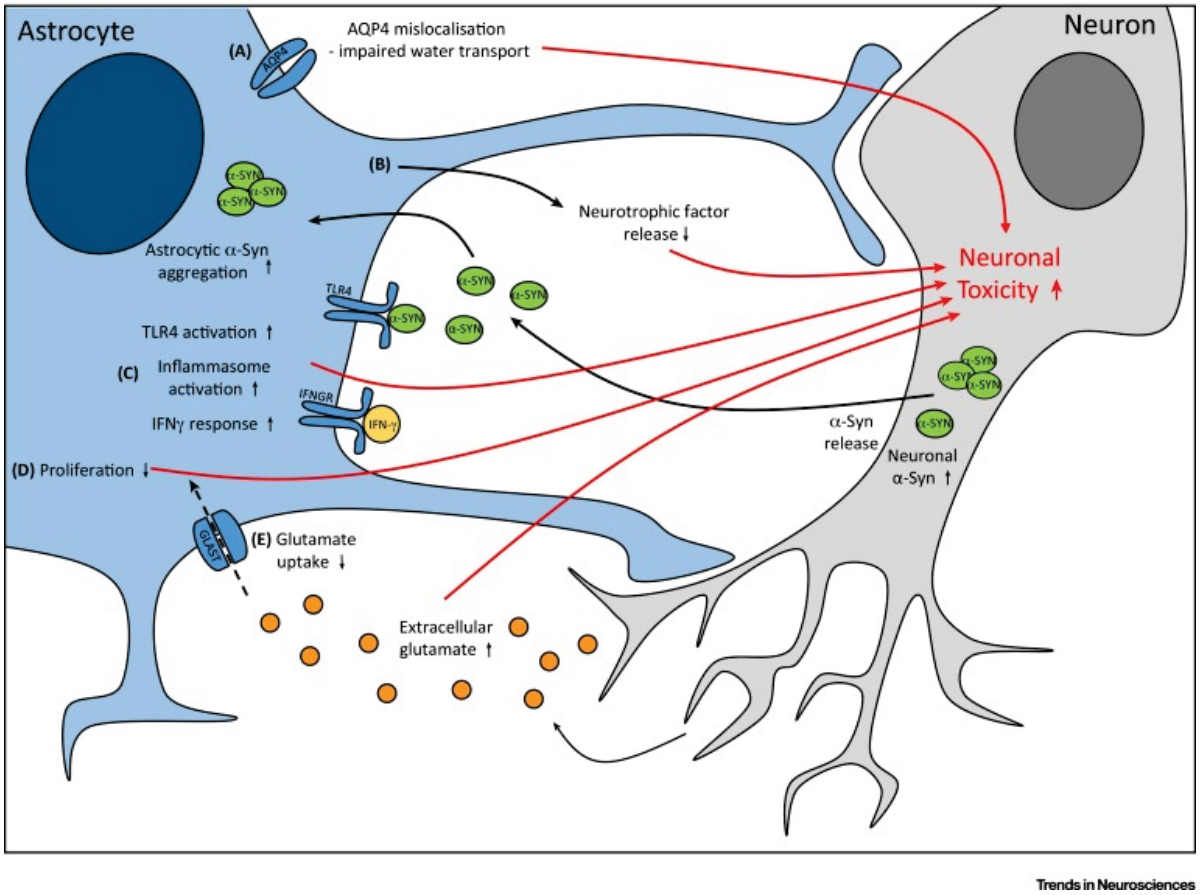

Figure 4. Mechanisms of astrocyte dysfunction contributing to neuronal toxicity. Modified from Booth *et al* (Booth et al., 2017).

In addition, inflammatory signaling from activated microglia can push astrocytes into the defined A1-like state (Liddelow et al., 2017). A1 astrocytes actively release neurotoxic factors rather than simply failing to provide support. In the striatum, the emergence of this phenotype has been linked not just to motor symptoms like bradykinesia but to non-motor pain features including allodynia, which patients often report early in the disease course, sometimes before diagnosis (K. Chen et al., 2023; Yun et al., 2018; H. Zhang et al., 2021). That the same cell-state shift might underlie both motor and sensory symptoms is an interesting convergence that has not been fully resolved mechanistically.

Thinking about astrocytic dysfunction as purely secondary to neuronal injury is probably wrong. Several PD-associated genetic variants are highly expressed in astrocytes and produce cell-autonomous dysfunction, meaning that astrocytes do not need alterations in neuron to be altered, it can initiate pathology on its own (S. Kim et al., 2023; Sonninen et al., 2020). GBA mutations are the clearest example. GBA encodes glucocerebrosidase, a lysosomal enzyme, and loss-of-function mutations directly impair proteolytic capacity in astrocytes. The consequence is intracellular α-syn accumulation and a shift toward reactive, maladaptive states that precede any obvious neuronal pathology (Iovino et al., 2020; S. Kim et al., 2023; Mazzulli et al., 2011).

LRRK2 mutations produce a different but overlapping picture. Gain-of-function variants increase inflammatory signaling while simultaneously suppressing glutamate uptake. These two effects compound each other and accelerate neurodegeneration through both excitotoxic and inflammatory routes (Bailey & Cookson, 2024; Booth et al., 2017; S. Kim et al., 2023; Sonninen et al., 2020). That a single genetic variant can dysregulate multiple astrocyte functions at the same time probably explains why LRRK2 mutations produce such clinically penetrant disease.

Astrocytes are not a uniform population. Single-cell and spatial transcriptomic studies have made this assumption evident. Astrocyte molecular identity varies substantially depending on brain region, and those regional differences appear functionally meaningful rather than casuality (Bayraktar et al., 2020; Endo et al., 2022; Lozzi et al., 2020; Zeisel et al., 2018). In the context of PD, this matters because it offers a potential explanation for why dopaminergic neurons in the midbrain and striatum are selectively vulnerable while other regions are not as affected.

Single-nucleus and multiomic profiling of postmortem PD tissue has identified transcriptomic changes in striatal astrocytes that are distinct from what is seen in Alzheimer's disease, with disease-specific shifts rather than a generic neurodegeneration signature (Smajić et al., 2022; Xu et al., 2023). This mirrors work in the AD field, where particular astrocyte subtypes have been linked to disease progression rather than astrocytes as a whole (Mathys et al., 2019a; Sadick et al., 2022;

Serrano-Pozo et al., 2024). In PD midbrain tissue specifically, the transcriptional changes in astrocytes involve genes associated with PD genetic risk and neuroinflammatory pathways, suggesting these cells are not simply aging or responding generically to a deteriorating environment, but undergoing disease-specific alterations (Adams et al., 2024; Smajić et al., 2022). However, the origin of those subtype-specific changes, and whether targeting them therapeutically is feasible, remains open.

4.2.7. Microglia

Microglia represent the resident immune cells of the CNS. One thing that sets microglia apart from every other CNS glial cell is where they come from. Astrocytes, oligodendrocytes, and OPCs are all neural tube derivatives, while Microglia originate from yolk sac progenitors and seed the brain parenchyma during early embryogenesis, after which the population sustains itself through local proliferation with minimal input from circulating monocytes (Alliot et al., 1999; Ginhoux et al., 2010; Prinz et al., 2021).

Their morphology in healthy tissue is distinctive: small soma, long thin branching processes which move constantly. Two-photon imaging made this visible: in the brain, microglial processes extend and retract on a scale of minutes, sampling the surrounding parenchyma without any obvious triggering event (Davalos et al., 2005; Nimmerjahn et al., 2005).

When something is out of balance (a dying cell, a pathogen, an aggregated protein), microglia detect it through damage- and pathogen-associated receptors and shift toward an activated state (Colonna & Butovsky, 2017; Prinz et al., 2021). Processes retract, the soma enlarges, and phagocytic clearance of debris begins (Sierra et al., 2014). In PD research this matters because aggregated α-synuclein can trigger that response before neuronal loss is detectable, raising unresolved questions about whether early microglial activation is protective, harmful, or both depending on context.

During brain development microglia also prune synapses. Weak or rarely used synaptic terminals get tagged with complement proteins and phagocytosed (Paolicelli et al., 2011; Schafer et al., 2012). Animals where this is experimentally disrupted end up with too many synaptic connections and poor circuit function, meaning this is active circuit sculpting. Whether the same mechanism runs in the adult brain and contributes to plasticity is suggested in previous studies (Prinz et al., 2021).

In disease the whole picture shifts. Across Alzheimer's, Parkinson's, ALS and others, microglial activation does not resolve, it persists. Chronically activated microglia release TNF-α, IL-1β, reactive oxygen species, and nitric oxide at levels that damage neurons (Boche et al., 2013; Heneka et al., 2015; Prinz et al., 2021). Instead of protecting the tissue, Microglia becomes harmful. Single-cell

transcriptomics has since shown that microglia exist across a spectrum of states rather than a simple activated/resting binary, and some of those states appear specific to particular diseases.

4.2.8. Microglia in EP

Microglia are the CNS resident immune cells, but as discussed earlier, their origin sets them apart from every other immune cell in the body. They derive from yolk sac progenitors during embryogenesis, making them a distinct myeloid lineage that is established in the brain before the blood-brain barrier closes (Ginhoux et al., 2010; Prinz et al., 2021; Sun & Jiang, 2024). In healthy tissue they are never truly inactive; their processes sample the local environment continuously, enforcing homeostasis without obvious triggering. In PD, that same vigilance becomes part of the problem. Microglia transition from surveillance to active participation in pathology, implicated at multiple stages from early initiation through symptomatic progression (K. Chen et al., 2023).

For a long time the relationship between microglia and PD was framed almost entirely as neuroinflammation, understanding it as a response to dying neurons rather than a contributor to their death. A PET imaging study by Ouchi *et al* (Ouchi et al., 2005) complicated that view. Microglial activation was detectable early, and its magnitude correlated with dopamine terminal loss rather than simply following it (Liu et al., 2022; Ouchi et al., 2005). That timing matters because it shifts microglia, becoming a potential driver.

The framework historically used to describe this was the M1/M2 model, or microglia as either neurotoxic or neuroprotective (Guo et al., 2022; Ransohoff, 2016). In PD the idea was that microglia were stuck in a chronic M1-like state, continuously releasing TNF-α, IL-1β, and other cytokines that accelerated neuronal death (K. Chen et al., 2023; Trainor et al., 2024) (Figure 5). That model was useful for a while, but it is now considered too simple, for reasons discussed below.

The interaction between microglia and α-syn is where the pathology gets self-reinforcing. Extracellular α-syn released by damaged neurons acts as a danger signal that triggers microglial activation (Glass et al., 2010; Y. Li et al., 2021; Pike et al., 2021). Microglia attempt to phagocytose it, but the problem is that aggregated α-syn resists lysosomal degradation. It accumulates intralysosomally, eventually causing membrane rupture and inflammasome activation, which dramatically amplifies the inflammatory output (Arena et al., 2022; Codolo et al., 2013; Gao et al., 2023) (Figure 5). More inflammation means more neuronal damage, which releases more α-syn, which activates more microglia. This loop was demonstrated by experimental models in which microglia are forced to overexpress α-syn. Microglia develops the phagocytic exhaustion and oxidative stress enough to kill dopaminergic neurons independently of any pre-existing neuronal

pathology (Bido et al., 2021; Gordon et al., 2018). Thus, microglial dysfunction alone, without an altered neuron to respond to, can initiate degeneration.

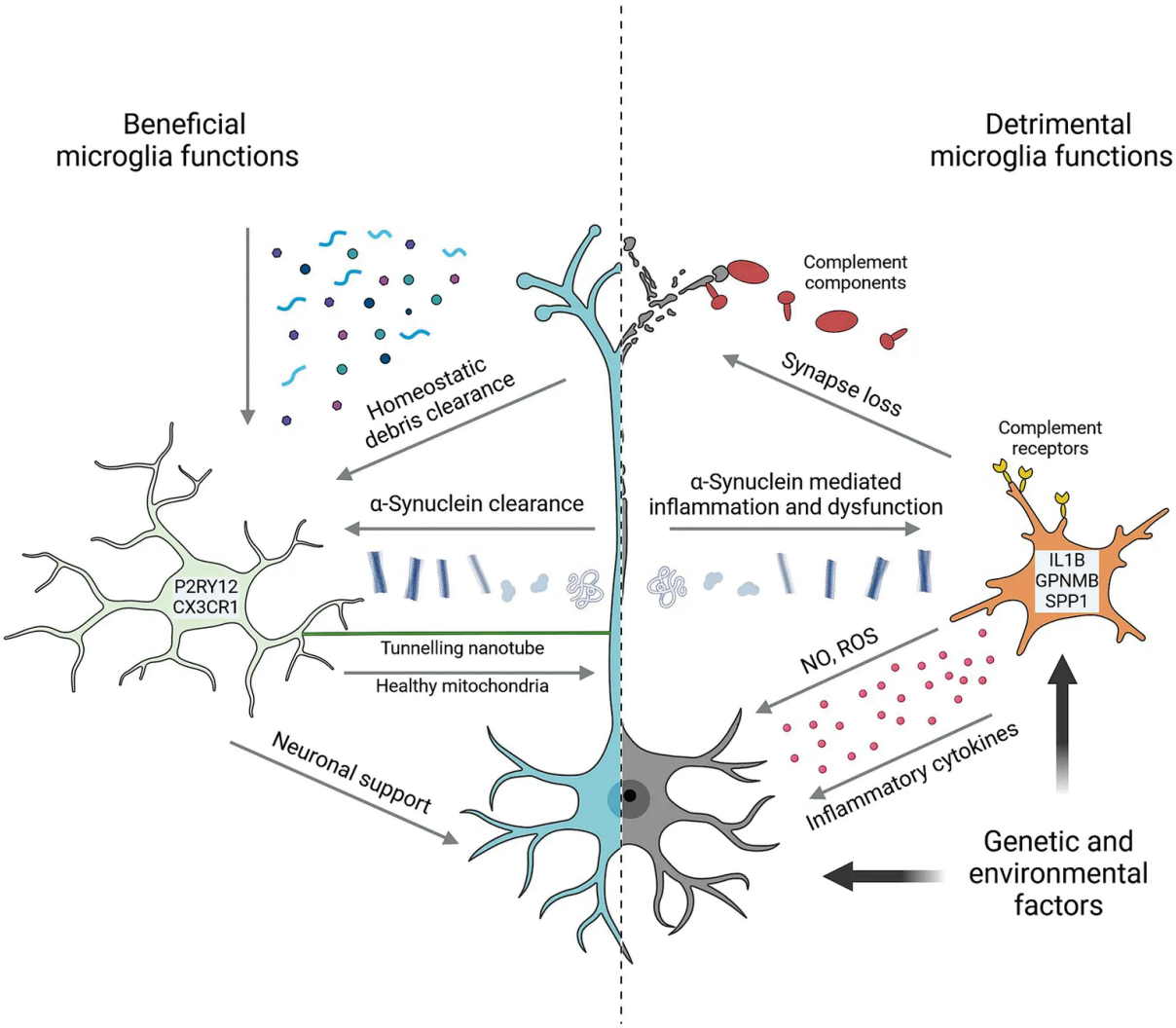

Figure 5. Dual Roles of Microglia in Neuronal Support and Neurodegeneration. Modified from Trainor *et al* (Trainor et al., 2024).

Single-cell transcriptomics has largely abandoned the M1/M2 concept. Microglia do not occupy two states, they show a continuous, multidimensional landscape of phenotypes that shifts with brain region, age, metabolic context, and disease stage (T. R. Hammond et al., 2019; Masuda et al., 2020; Ransohoff, 2016). This heterogeneity represents a fundamental organizational feature of the microglial population (Dadwal & Heneka, 2024; Hasel et al., 2023; Olah et al., 2020; Sankowski et al., 2024; Yaqubi et al., 2023).

In neurodegeneration, a specific response state has been identified: Disease-Associated Microglia, or DAM. It was first characterized in Alzheimer's disease (Gao et al., 2023; Keren-Shaul et al., 2017). DAM is not simply a more activated version of homeostatic microglia. They have a distinct transcriptional profile, and functionally they are not uniform. Some subtypes appear oriented toward myelin clearance, others toward protein aggregate removal (Dadwal & Heneka, 2024; Sankowski et al., 2024). Whether DAM are protective, harmful, or context-dependent is still not known.

Moreover, the recently published Human Microglia Atlas (Martins-Ferreira et al., 2025) provides a more systematic view of this landscape across diseases. Its relevance to PD is that microglial molecular signatures in PD are distinguishable from those in other neurological conditions. That disease-specificity is what has pushed the field away from broad anti-inflammatory strategies toward something more targeted: identifying which specific microglial states drive pathology and intervening selectively (Paolicelli et al., 2022; Vecchiarelli & Tremblay, 2023).

4.2.9. Glia-Glia Crosstalk: a network of dysfunction

Although it is important to characterize each glial cell type, looking at them in isolation also misses information. Astrocytes, microglia, and oligodendrocytes do not operate independently, they are in constant communication, allowing the normal functioning of the CNS (Colonna & Butovsky, 2017; Jäkel & Dimou, 2017). In PD, that regulatory network becomes actively dysregulated, and the interactions between cell types start amplifying pathology rather than suppressing it (Kędzia et al., 2026; Y. S. Kim et al., 2020) (Figure 6).

The microglia-astrocyte axis seems to be the main altered interaction. Pathological α-syn triggers microglia to release a specific combination of signals, such as IL-1α, TNF, and C1q, that transforms astrocytes in the surrounding from a homeostatic to an A1-like neurotoxic state (Liddelow et al., 2017; Yun et al., 2018) (Figure 6). That transition matters because A1 astrocytes do not just stop being supportive, they actively secrete factors that damage neurons and mature oligodendrocytes (K. Chen et al., 2023; Trainor et al., 2024). Thus, the two cell types end up locked in a loop.

Oligodendrocytes are involved in this dysregulation as well. Inflammatory microglia attack myelin directly, generating debris that feeds back into the neuroinflammatory environment (Errea & Rodriguez-Oroz, 2021). At the same time, the neurotoxic factors released by A1 astrocytes impair OPC differentiation, blocking the repair response that would partially compensate for oligodendrocyte loss (Liddelow et al., 2017; S. Zhang et al., 2025). Although neuronal loss remains the principal cause of the motor and cognitive deficits in patients, the conditions driving that loss, including chronic neuroinflammation, progressive demyelination or excitotoxicity, are being maintained and amplified by glial dysfunction (Colonna & Butovsky, 2017; Kędzia et al., 2026; Y. S. Kim et al., 2020). A

treatment strategy focused on protecting dopaminergic neurons is then addressing the outcome rather than the process.

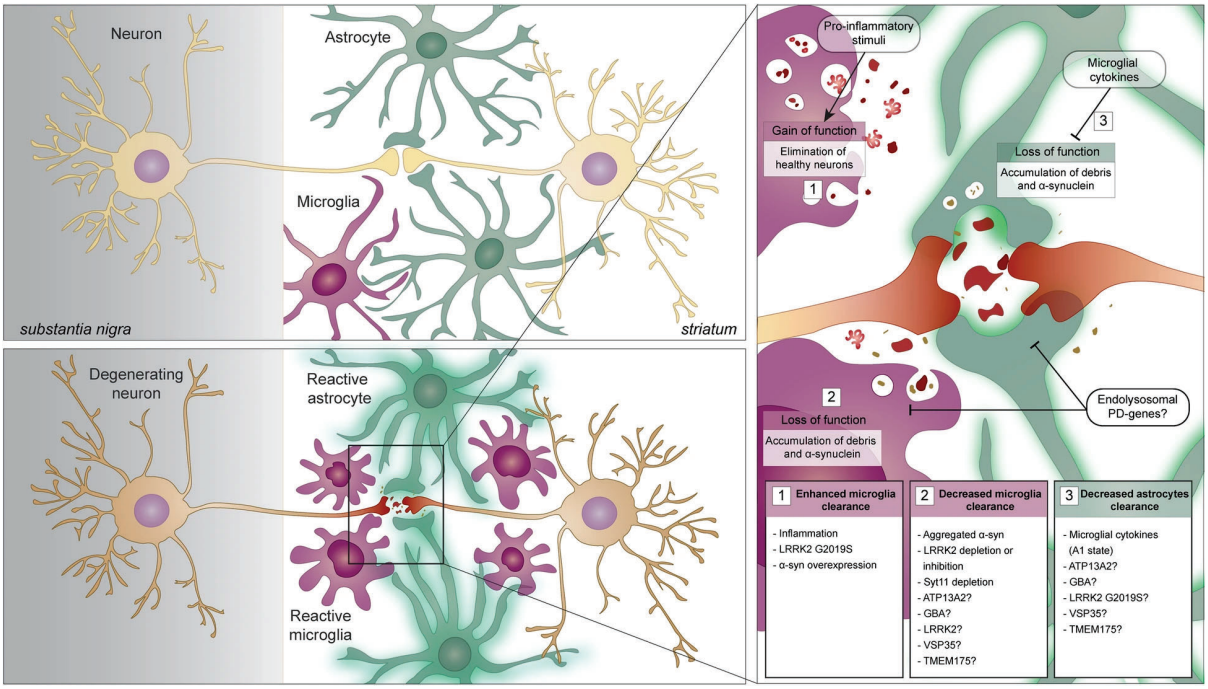

Figure 6. Glial Phagocytosis in Health and Its Dysregulation in Parkinson's Disease. Modified from Tremblay *et al* (Tremblay et al., 2019).

4.2.10. Glial Network as a Novel Therapeutic Target

The standard pharmacological approach in PD has not changed much in decades. Dopamine replacement through levodopa and its derivatives remains the main strategy of treatment, and it works, at least for motor symptoms and at least for a while (Connolly & Lang, 2014). However, it does not slow the underlying disease. The pathology continues while symptoms are managed, and that is increasingly hard to justify given what is now known about glial contributions to disease progression (Vishnumukkala et al., 2025).

If chronic neuroinflammation, failed remyelination, and disrupted glial communication are actively driving neurodegeneration, then the relevant therapeutic targets are not only dopaminergic neurons, also glial cells and signaling networks upstream of neuronal death. That reorientation is what is based on this thesis.

Broad-spectrum anti-inflammatory strategies have largely failed in PD clinical trials, probably because they were not too refined, suppressing beneficial microglial functions alongside harmful ones (Athauda & Foltynie, 2015). However, advances in techniques' resolution, such as single-cell and spatial omics, allow the field to distinguish between specific microglial states, which opens the

possibility of reprogramming particular populations toward phagocytic, homeostatic behavior rather than simply suppressing microglial activity altogether (Gao et al., 2023; Keren-Shaul et al., 2017). Whether that is achievable pharmacologically in humans is not yet known, but the conceptual basis is more solid than it was.

A parallel effort targets the microglia-astrocyte axis. Blocking the specific signals (IL-1α, TNF, C1q) that drive A1 astrocyte conversion is one approach that has shown promise in preclinical models (Liddelow et al., 2017). Then, if neurotoxic astrocyte states are induced by microglial signaling rather than being cell-autonomous, interrupting that signal might preserve astrocyte homeostatic function without needing to alter astrocytes directly.

The OPC differentiation block is perhaps the most therapeutically concrete target of the three. Drugs capable of overcoming the metabolic arrest that prevents OPCs from completing differentiation into myelinating oligodendrocytes have been identified, and some are already in development for other demyelinating conditions (Cole et al., 2017; Mei et al., 2014). Repurposing that work toward PD is not very clear, as the OPC dysfunction in PD occurs in a different inflammatory context than in multiple sclerosis, but the mechanistic overlap is enough to try new avenues of therapies.

However, none of these approaches are close to clinical translation. The targets are better defined than they were five years ago, and the rationale for pursuing them is stronger than it has ever been. But the distance between a compelling disease mechanism and an effective drug remains large, and PD has a history of preclinical findings that did not survive contact with human trials (Athauda & Foltynie, 2015). Thus, these glial alterations offer a set of targets that address the process driving neurodegeneration rather than its downstream consequences.

4.3. Single-cell RNA Sequencing

4.3.1. Bulk versus single-cell RNA sequencing

Brain regions affected in PD are not uniform tissues. The dorsal striatum is a structurally complex region composed of multiple neuronal subtypes, dense glial populations, and two anatomically and functionally distinct subdivisions (CN and Pu), each of which may respond differently to the dopaminergic denervation that defines PD. Bulk RNA sequencing, which dominated the field for decades, cannot resolve any of that, as it produces an averaged transcriptomic signal across all cell types in the homogenate that does not reflect any individual cell population and, in a heterogeneous tissue, does not reflect most of them accurately (Trapnell, 2015). The same limitation applies to other PD-relevant regions, including the substantia nigra pars compacta, where dopaminergic neurons,

GABAergic neurons, and multiple glial phenotypes sit in close proximity, each with distinct molecular identities (Poulin et al., 2014).

The practical consequence for PD research is significant. In the striatum, because neurons largely survive the early and middle stages of the disease, the dominant transcriptional shifts in PD reflect glial responses to dopaminergic denervation rather than neuronal loss, but bulk sequencing cannot resolve which glial populations are responding, in what way, or whether CN and Pu are doing so differently. The signal from each subpopulation is averaged together and the cell-type-specific information is lost. A similar problem exists in the substantia nigra, where the selectively vulnerable dopaminergic neurons are a numerical minority: their transcriptomic signature is statistically submerged below the signal from more abundant cell types, particularly glia (Hrvatin et al., 2018).

There is a second, related problem shared across both regions. Bulk sequencing cannot distinguish between a change in gene expression and a change in cellular composition. If a PD sample shows reduced expression of a neuronal marker relative to controls, that could mean neurons are downregulating that gene, or it could simply mean there are fewer neurons in the sample due to cell death. The two interpretations have completely different implications, and bulk data cannot separate them (Hrvatin et al., 2018; Trapnell, 2015). In the striatum, where compositional shifts are subtler than in the nigra, this ambiguity is particularly difficult to resolve without single-cell resolution.

Single-cell RNA sequencing (scRNA-seq) addressed a fundamental resolution problem that bulk methods could not solve. With this technique, a whole-transcriptome analysis from a single mammalian cell was possible. It was established by Tang and colleagues in 2009, but for several years the method remained low-throughput and technically demanding (Tang et al., 2009). Scaling it to thousands of cells simultaneously required a different physical approach.

That came with droplet-based microfluidics. The core idea is to isolate individual cells inside nanoliter-scale aqueous droplets, each containing a bead coated with capture oligonucleotides (Klein et al., 2015; Macosko et al., 2015). Each droplet functions as an independent reaction chamber: the cell is lysed inside it, and its mRNA is captured by the bead before it can degrade or mix with RNA from neighboring cells. Platforms built on this principle, including the widely adopted 10x Genomics Chromium system, made the technology accessible enough to become routine (Zheng et al., 2017) (Figure 7).

The barcoding strategy makes the data interpretable. Every bead carries a unique cell barcode, which tags all transcripts originating from that cell, and each individual RNA molecule receives a unique molecular identifier (UMI) at the point of capture (Islam et al., 2014). The UMI is what allows PCR amplification bias to be corrected during analysis, because each original molecule is uniquely labeled

and copies generated during amplification can be collapsed back to a single count. Without that correction, highly amplified transcripts would dominate the data regardless of their actual abundance in the cell.

After sequencing, the barcoded reads are computationally demultiplexed (sorted by cell of origin), and the result is a gene expression matrix where each row is a cell and each column is a gene. From that matrix, cells are clustered by transcriptomic similarity, and clusters are assigned to cell types based on known marker genes. In a heterogeneous tissue like the dorsal striatum, this approach can simultaneously resolve Medium Spiny Neuron subtypes, Interneuron subtypes, distinct glial states, and rare transitional populations that would be entirely invisible in bulk data, something previously done in midbrain (Poulin et al., 2014; Smajić et al., 2022).

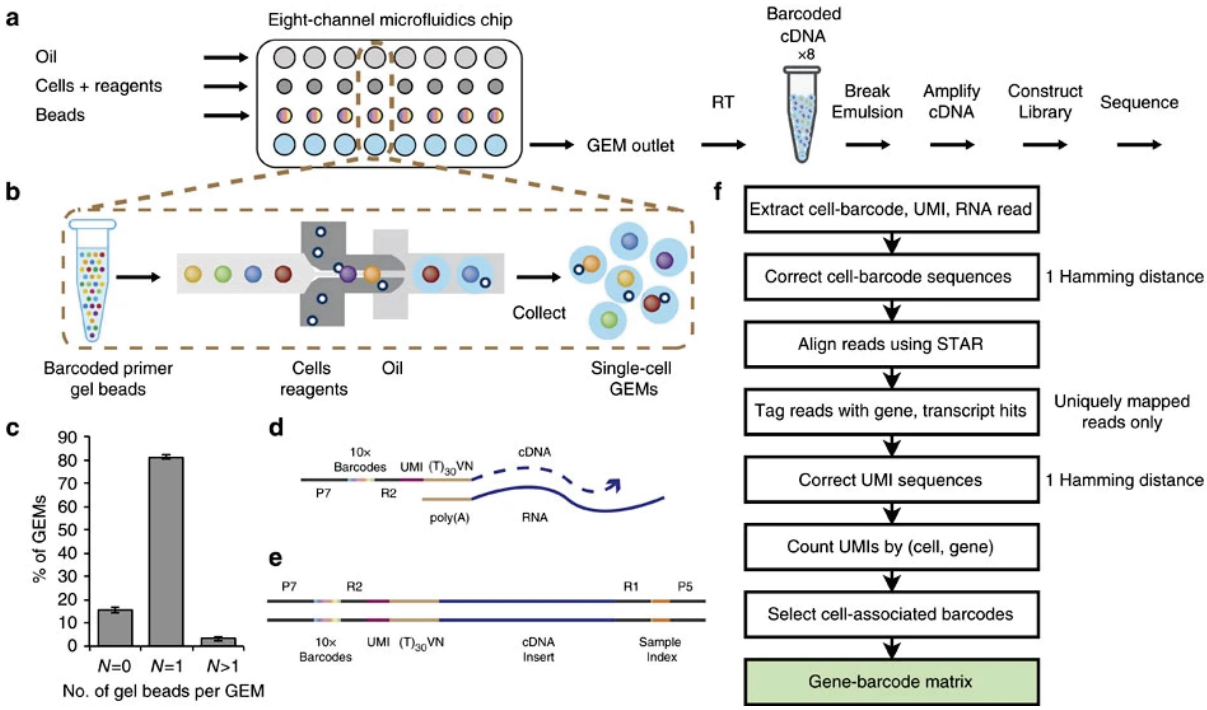

Figure 7. Overview of the 10x Genomics scRNA-seq platform: GEM Generation, Barcoding, and Data Processing. Modified from Zheng *et al* (Zheng et al., 2017).

Translating scRNA-seq to human neuropathology ran into a basic practical problem. The technique requires fresh, dissociated cells in viable suspension. However, postmortem human tissue, which is what most human neuropathology studies depend on, has to be maintained frozen. Enzymatic dissociation protocols designed for fresh tissue perform poorly on frozen samples, and a lot of neurons are lost in the process (Habib et al., 2017). Then, what survives the dissociation is not a representative sample of the original tissue. Smaller, more resilient cell types, such as glia, are overrepresented, and neurons which it is known are most relevant to disease are systematically underrepresented.

snRNA-seq avoids this by targeting the nucleus rather than the intact cell (Grindberg et al., 2013). Nuclei are mechanically robust, they tolerate freeze-thaw cycles without the structural failure that destroys whole cells, and they can be isolated from frozen tissue by mechanical homogenization rather than enzymatic digestion (Lake et al., 2019). That fix makes the approach compatible with biobank postmortem material in a way that whole-cell methods are not.

The obvious concern is whether nuclear RNA is a reliable source for whole-cell transcriptomes. It mostly is. Validation studies comparing nuclear and whole-cell profiles from matched samples show high concordance for cell type identification and gene expression patterns, with the main limitation being a reduced capture of cytoplasmic transcripts (Ding et al., 2020; Habib et al., 2017). For the purposes of cell type classification and disease-associated transcriptional shifts, snRNA-seq has demonstrated to be enough, and it is now the standard approach for human brain transcriptomics.

4.3.2. Single-nuclei RNA sequencing in Parkinson's Disease

Applied to PD, sc/snRNA-seq has not just improved resolution, it has changed the questions that can be asked. The traditional framework treated the disease as dopaminergic neuron loss plus secondary glial reactions, but what the data actually shows is more complicated and interesting.

Dopaminergic neurons in the substantia nigra are not a uniform population. Kamath *et al.* (Kamath et al., 2022) provided some of the clearest evidence for this, identifying a discrete subpopulation marked by AGTR1 expression that shows selective depletion in PD tissue compared to controls (Kamath et al., 2022). Martirosyan *et al.* (Martirosyan et al., 2024) replicated the subtype-specific vulnerability pattern, and Wang et al. (Q. Wang et al., 2024) identified a distinct RIT2-positive cluster with similar selective loss. Smajić et al. (Smajić et al., 2022) added more mechanistically information: rather than simply dying, some neurons appear to enter a transcriptionally distinct intermediate state, one in with altered gene expression.

As we have explained, the pathology is not confined to neurons. Smajić *et al.* (Smajić et al., 2022) documented reactive transcriptional shifts across the glial compartment of the PD midbrain, and similar findings have emerged from other regions. In the prefrontal cortex, Zhu *et al.* (B. Zhu et al., 2024) found evidence of T cell infiltration alongside alterations in metabolic coupling between neurons and astrocytes. Christodoulou *et al.* (Christodoulou et al., 2023) mapped failures in protein folding machinery across multiple cell types. And as discussed earlier, epigenomic profiling has established that PD GWAS risk loci are enriched in regulatory elements active in oligodendrocytes rather than neurons (Bryois et al., 2020; Corces et al., 2020), which makes it harder to argue that glial involvement is purely secondary.

Single-cell approaches have also changed what can be learned from experimental models. Transcriptomic analysis of PD mouse models and iPSC-derived neurons has identified activation of integrated stress response genes (DDIT4), as an early molecular event (Jiang et al., 2025), and disruption of Gi/o-GIRK synaptic signaling has been mapped at cellular resolution in ways that bulk methods could not resolve (Fernandes et al., 2020; E.-K. Lee et al., 2025). In the microglial compartment, a Cd74-positive subpopulation has been identified that appears to actively promote neuronal loss rather than simply responding to it (Kambey et al., 2023). On the therapeutic side, single-cell profiling of stem cell grafts has made it possible to verify cellular composition before transplantation by checking that the graft actually contains the intended cell types in the intended proportions, which had not previously been possible (Tiklová et al., 2020).

4.4. Spatial Transcriptomics

scRNA-seq helped to solve one problem but it created another. By dissociating tissue into individual cells, scRNA-seq produces a high-resolution dataset of cell types, but due to dissociation this process lacks the information of where each cell was (K. H. Chen et al., 2015).

That loss matters more in the brain than in most tissues. Neural function depends on adjacency, layered organization, and local signaling between specific cell populations. A neuron's transcriptional state is shaped in part by what it is next to it, what it is connected to, and what molecular signals it is exposed to in its immediate microenvironment. None of that survives the dissociation process (K. H. Chen et al., 2015).

In PD, the defining pathological interrogation is the selective vulnerability: why a specific dopaminergic neuron subpopulation in the substantia nigra degenerates while physically adjacent populations do not. That is, basically, a spatial question, a question about neighborhood and local exposure. But spatial context is equally relevant downstream. The dorsal striatum, as the primary target of the nigrostriatal projections that degenerate in PD, is where the functional consequences of that loss are expressed, and understanding how glial cells respond to denervation within specific striatal microenvironments requires knowing not just what those cells express, but where they are located relative to each other and to the white matter bundles, vascular structures, and ventricular borders that define the tissue architecture. Dissociated snRNA-seq, regardless of how many cells it profiles or how deeply it sequences them, is structurally incapable of answering this.

Spatial transcriptomics addresses this question directly. Rather than extracting cells from their tissue context, ST anchors transcriptomic measurements to physical coordinates on a tissue section, so each gene expression profile comes tagged with the x,y position it came from. The result is not a catalog of

cell types but a map: molecular identity and spatial organization is captured simultaneously, layered on top of the histological architecture that dissociation-based methods discard.

Two technically distinct approaches have been developed in parallel, each making different equilibrium between spatial resolution and transcriptomic coverage.

The spatial transcriptomics origin traces back to Ståhl et al. (Ståhl et al., 2016), whose foundational experiment was conceptually simple: a glass slide printed with an array of oligonucleotide capture probes, each bearing a unique positional barcode. Tissue is placed on the slide and permeabilized, mRNA diffuses down and is captured at whatever spot it lands on, and sequencing then reads both the transcript identity and its positional tag. The limitation of the original implementation was resolution, because spots of roughly 100 μm capture the mRNA of multiple cells and average their signals together, reintroducing some of the same heterogeneity problem that scRNA-seq was meant to solve. Subsequent bead-based platforms, particularly Slide-seq (Rodriques et al., 2019), reduced capture area to approximately 10 μm, bringing resolution close to the single-cell level without fully reaching it.

The imaging-based lineage took a different route. Rather than extracting RNA and sequencing it, methods like MERFISH (K. H. Chen et al., 2015) and seqFISH (Shah et al., 2016) detect transcripts directly in the tissue section using fluorescent in situ hybridization. The key innovation is combinatorial labeling across sequential rounds of imaging. Each round adds information, and the combination of signals across rounds produces a unique optical barcode for each RNA species. This achieves subcellular spatial resolution and preserves the physical relationship between transcripts and cellular compartments. The disadvantage is transcriptomic selectiveness: imaging-based methods typically profile a predefined gene panel rather than the whole transcriptome, though panel sizes have grown substantially (K. H. Chen et al., 2015; Marco Salas et al., 2025) (Figure 8).

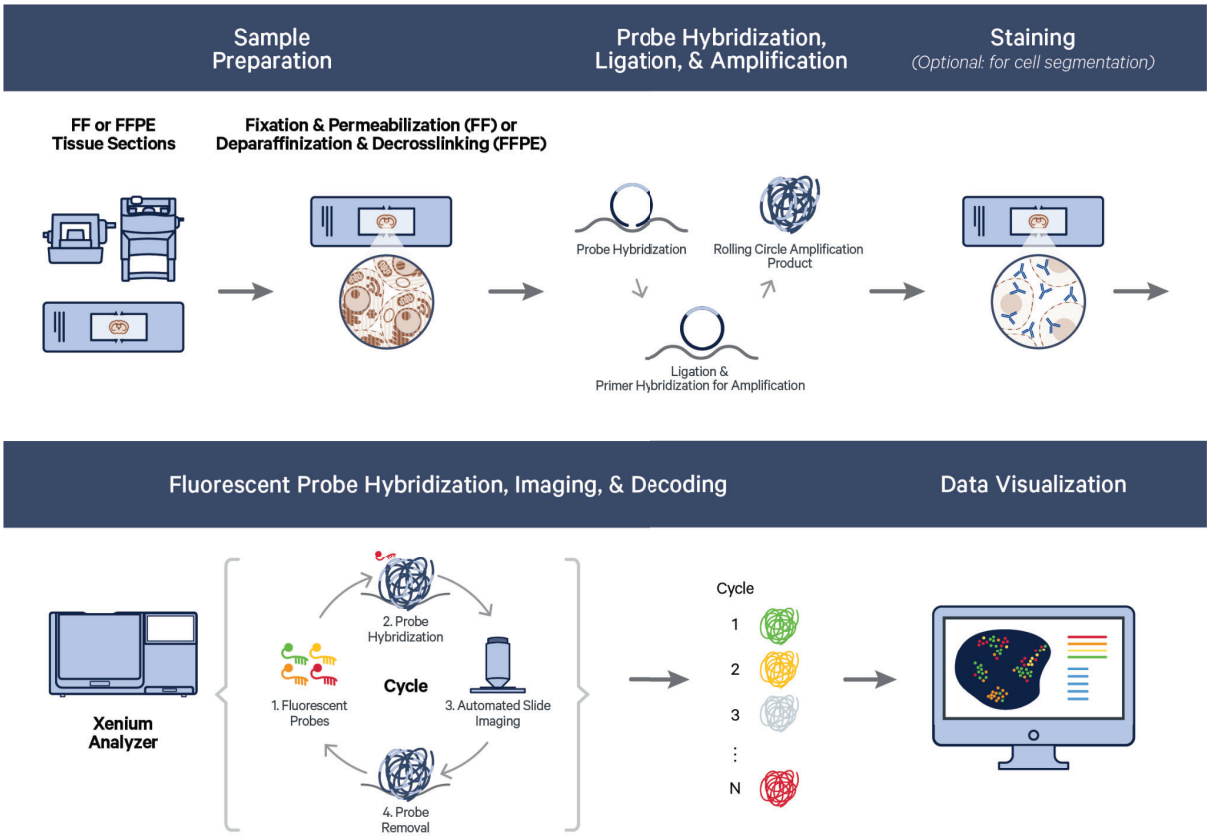

Figure 8. Xenium spatial transcriptomics workflow: from tissue preparation to high-resolution 3D transcript mapping. Modified from 10X website (*Overview of Xenium Algorithms | Official 10x Genomics Support*, n.d.)

4.4.1. Applications in Neuroscience: Mapping the Brain's Complex Architecture

The brain is where spatial context matters most, and some of the most compelling early demonstrations of ST used neural tissue. Shah et al. (Shah et al., 2016) used seqFISH to map the laminar organization of the hippocampus at the level of individual transcripts. More recently, Ma *et al.* (Ma et al., 2024) adapted the high-resolution Xenium platform for use on fixed frozen brain sections, which is significant because it makes the technology compatible with standard biobank postmortem material rather than requiring fresh tissue.

4.4.2. Applying ST to Parkinson's Disease

The core pathological questions in PD are fundamentally spatial ones. Why do dopaminergic neurons in the SNc die while adjacent populations in the VTA survive? How is glial dysfunction distributed across tissue microenvironments? Does α-syn pathology propagate in spatially organized patterns, or does it spread without spatial logic? Dissociation-based sequencing could not answer any of these directly. ST can, at least in principle, and the first wave of studies applying it to PD tissue is beginning to produce results that are difficult to obtain any other way.

The selective vulnerability problem has been approached spatially with some interesting results. Using ST, researchers have mapped close to twenty molecularly distinct dopaminergic subtypes in the midbrain, and the spatial position of each subtype correlates with how early it is lost in disease (Gaertner et al., n.d.). This suggests that vulnerability is not just a matter of molecular identity in isolation but is shaped by local context.

In a study using the Xenium platform, Horan-Portelance *et al*. (Horan-Portelance et al., 2024) found significant discrepancies between their spatial data and established models of disease. In the neocortex, for example, while previous studies predicted that L5 IT (intratelencephalic) neurons were the most vulnerable, the spatial data showed that L5 ET (extratelencephalic) neurons actually developed the most frequent and severe pathology. A similar flip occurred in the hippocampus; while CA2/3 is typically thought of as the most vulnerable subfield in Lewy body diseases, this study found that CA1 neurons developed pathology approximately twice as often as those in CA2/3.

Spatial transcriptomic profiling of post-mortem SNpc tissue from PD and MSA-P patients has revealed that, while both conditions share a core pattern of downregulated ribosomal protein synthesis, their transcriptional signatures diverge in several important ways (Shin et al., 2025). Immune and inflammatory pathways, mitochondrial electron transport, and autophagy-related genes were more broadly suppressed in MSA-P than in PD, possibly reflecting a longer-term adaptation to more pronounced neuroinflammatory activity in that condition. A notable topographic finding in MSA-P was the selective enrichment of antigen presentation pathways in the dorsomedial quadrant of the SNpc, a pattern absent in PD. In both diseases, amyloid precursor protein (APP) emerged as the most significant hub gene in network propagation analysis, downregulated in the SNpc relative to controls, a finding the authors interpret as potentially linked to synucleinopathy mechanisms independent of amyloid pathology.

4.4.3. Current Challenges and Future Directions

It is important to understand these approaches have their limitations. The field is technically immature in ways that matter for reproducibility and interpretation. Platforms differ in capture efficiency, gene coverage, and spatial resolution. Analytical pipelines are not standardized, and the datasets generated are large enough to create computational bottlenecks. It is because of this that efforts are underway to establish workflows based on best practices and assess which outcomes are valid across all platforms and processing procedures (Marco Salas et al., 2025).

The direction the field is moving is toward multimodal integration by computationally combining ST spatial maps with the transcriptomic depth of snRNA-seq to get both dimensions simultaneously.

Whether that integration can be done robustly at scale, and what new biological questions it will open up in PD specifically, is where the methodological frontier currently sits.

5. Justification

PD is currently the fastest-growing neurodegenerative disorder worldwide, driven by aging populations and environmental factors. Prevalence is rising, and with it the economics and healthcare of managing a chronic, progressive neurological condition. Despite decades of research and the refinement of dopaminergic replacement therapies (levodopa and dopamine agonists), available treatments remain symptomatic. They compensate for dopamine loss but do not slow the degeneration of the nigrostriatal tract. That therapeutic ceiling reflects, at least in part, a conceptual limitation: PD research has been built almost entirely around neurons.

The focus has been centered on the selective loss of dopaminergic neurons in the SNpc and the aggregation of α-syn into Lewy bodies. That foundation was necessary, but it has also limited the view of PD pathogenesis. Neurons do not function in isolation. The brain is an interdependent system in which glial cells constitute the majority of cells and regulate neuronal environment: metabolism, immune surveillance, synaptic maintenance, and ion homeostasis. Treating neurons as the unit of analysis while treating glia as background is, at this point, difficult to justify.

Oligodendrocytes are perhaps the least studied glial population in PD, yet recent evidence suggests their involvement may be more consequential than previously appreciated. Their primary role is to myelinate axons and provide metabolic support to neurons through the transfer of lactate and other substrates, a function that is particularly relevant for the long, energy-demanding axons of nigrostriatal dopaminergic neurons (Nave & Werner, 2014). Bulk and single-nucleus transcriptomic analyses of PD post-mortem tissue consistently show widespread gene expression changes in oligodendrocytes and their precursor cells (OPCs), including disruption of pathways related to myelin maintenance, lipid metabolism, and axonal support (Agarwal et al., 2020; Bae et al., 2023). Impaired OPC differentiation reduces the capacity for myelin repair (Dehestani et al., 2024), and loss of oligodendrocyte-derived metabolic support likely increases axonal vulnerability to the bioenergetic stress that already characterizes the parkinsonian SNpc. Notably, LRRK2 shows preferential expression in oligodendrocytes and OPCs rather than in neurons across multiple single-nucleus datasets (Bae et al., 2023; Martirosyan et al., 2024; Smajić et al., 2022), which raises the possibility that LRRK2-associated pathology may partly operate through this cell type.

Astrocyte dysfunction adds another layer. These cells supply lactate to neurons, buffer extracellular glutamate, and maintain the metabolic conditions that energy-demanding dopaminergic neurons depend on. In PD, there is an initial defensive response which becomes maladaptive over time (also known as reactive astrogliosis). Glutamate transporter expression drops, synaptic glutamate accumulates, and finally it converges in excitotoxic damage to downstream neurons (Iovino et al.,

2020). In addition, inflammatory signals from activated microglia can induce an A1-like neurotoxic phenotype in astrocytes, causing them to release factors directly harmful to neurons and oligodendrocytes rather than supporting them (Liddelow et al., 2017; Yun et al., 2018). Genetics reinforces these findings. GBA and LRRK2, two major PD risk genes, are highly expressed in astrocytes. GBA mutations impair lysosomal function in astrocytes, reducing α-syn clearance and thus accumulating misfolded proteins (S. Kim et al., 2023; Mazzulli et al., 2011). Moreover, LRRK2 dysfunction disrupts mitochondrial respiration, reducing the metabolic support astrocytes provide to neighboring dopaminergic neurons (Booth et al., 2017; Sonninen et al., 2020). These are not secondary effects, they are cell-autonomous failures in glial biology driven by the same genetic variants that increase PD risk.

The first glial population to attract attention in PD was microglia. Under normal conditions they maintain the homeostasis in the parenchyma, clearing debris and refining synaptic architecture. In PD, misfolded α-syn acts as a chronic pathological stimulus. Rather than clearing these aggregates efficiently, microglia undergo phagocytic exhaustion. Lysosomal overload triggers NLRP3 inflammasome activation, and the cell transitions to a chronically pro-inflammatory state (Boche et al., 2013; Dadwal & Heneka, 2024). Although we had the classical M1/M2 classification, single-cell transcriptomics has shown that it does not capture microglial heterogeneity. Disease-associated microglial states in PD carry distinct transcriptional signatures from those described in Alzheimer's disease, and these cells appear to actively contribute to neuronal death through ROS and cytokine secretion rather than simply responding to it (Colonna & Butovsky, 2017; Prinz et al., 2021).

These findings suggest that neuronal death in PD may be, in part, a consequence of glial dysfunction and not the primary and unique event. If that is the case, therapies aimed at protecting neurons while the glial environment remains pathological are intervening too late. The upstream targets, such as alterations in oligodendrocytes and myelination, lysosomal function in astrocytes, and inflammatory state transitions in microglia, are where disease modification may actually be achievable. Defining those targets with cell-type and state-level resolution is the central rationale for this thesis.

6. Hypotheses and Objectives

6.1. Hypotheses

Beyond the well-characterized loss of dopaminergic input to the striatum in PD, we hypothesize that the dorsal striatum, both CN and Pu, undergo cellular and molecular responses to that deficit, involving active glial participation, which would become a key determinant of the functional alterations observed in PD striatum. Whether glial alterations drive neurodegeneration, amplify it, or both, is a question this thesis works toward.

6.2. General objectives

This doctoral thesis studies the contribution of glial cells in neurodegenerative processes in the context of PD in the dorsal striatum (CN and Pu). We combined snRNA-seq, spatial transcriptomics, and immunohistochemical validation to capture different axes of biological information, obtaining both molecular depth and spatial context. The aim is to resolve the different glial types (oligodendrocytes, OPCs, astrocytes, and microglia) into transcriptionally distinct states, identifying disease-associated subpopulations within each lineage, and characterize how their differentiation trajectories, gene regulatory networks and intercellular communication are disrupted in PD.

6.3. Specific objectives

1) Identify glial subpopulations and their disease-associated states in the parkinsonian dorsal striatum.

2) Characterize the molecular pathways dysregulated within those disease-associated states.

3) Link the transcriptional changes determined in 2, to the structural and functional deterioration of striatal circuits and anatomy.

7. Material and Methods

7.1. Human Tissue

This study is based on the systematic analysis of well-characterized postmortem human brain tissue. Donors were selected through careful review of both clinical documentation and neuropathological assessment to ensure diagnostic accuracy. The cohort comprises individuals with neuropathologically confirmed PD as well as control donors without clinical or histopathological evidence of neurodegenerative disorders. Tissue acquisition was made possible through collaboration with three established brain banks: Human Brain and Spinal Fluid Resource Center (Los Angeles, CA, USA), Parkinson's UK Brain Bank (London, UK), and Massachusetts Alzheimer's Disease Research Center (Massachusets, MA, USA). To ensure anatomical consistency across cases, we performed standardized dissections of CN and Pu, sampling coronal sections at the level of the nucleus accumbens. The control cohort included 20 individuals (Pu: n = 20; CN: n = 18) spanning a broad adult age range, from 25 to over 90 years. The PD cohort comprised 36 donors (Pu: n = 35; CN: n = 34), all aged between 60 and over 90 years. All tissue was obtained under approved ethical protocols, with written informed consent provided by donors or their next of kin. Study procedures were reviewed and authorized by the respective Institutional Review Boards. Detailed clinical information is provided in Supplementary Table 1.

One important demographic feature of the cohort needs consideration. PD shows a well-documented male predominance, which was reflected in the available donor pool. As a result, it was not possible to obtain a perfectly sex-balanced cohort. The final dataset includes 16 female and 40 male donors (Control: 6 females/14 males; PD: 10 females/26 males). Although this distribution reflects the epidemiology of the disease, it limits our ability to rigorously evaluate sex as an independent biological variable. Consequently, while sex was accounted for in the analytical design when appropriate, the study is not powered to draw definitive conclusions regarding sex-specific transcriptional differences.

7.2. Tissue Dissociation

Nuclei were extracted from fresh-frozen human brain specimens using a modified version of a protocol originally developed by the Allen Institute for Brain Science (https://www.protocols.io/view/isolation-of-nuclei-from-adult-human-brain-tissue-eq2lyd1nqlx9/v2), adapted here to for the specific characteristics of our samples. To preserve RNA integrity, all procedures were conducted at 4°C and with nuclease-free reagents.

Briefly, 100-150 mg of tissue was thawed on ice and transferred into 2 mL of pre-chilled homogenization buffer. The buffer consisted of 10 mM Tris (pH 8.0), 250 mM sucrose, 25 mM KCl, 5 mM $MgCl_2$, and 0.1 mM DTT, supplemented with protease inhibitor cocktail (1×, 50× stock in 100% ethanol, G6521, Promega) and 0.2 U/μL RNasin Plus (N2615, Promega), as well as 0.1% Triton X-100 to facilitate membrane disruption while maintaining nuclear integrity. Mechanical dissociation was performed using a glass Dounce homogenizer, applying sequential strokes with loose and tight pestles to achieve effective but controlled tissue disruption (357538, Wheaton). The homogenate was sequentially filtered through 70 μm and 30 μm strainers to remove large debris, and the volume was adjusted to 6 mL with an additional buffer.

The filtrate was centrifuged at 900 × g for 10 minutes to pellet nuclei. After carefully aspirating the supernatant, leaving a minimal residual volume to avoid disturbing the pellet, nuclei were gently resuspended in a homogenization buffer. For further purification, the suspension was mixed 1:1 with 50% iodixanol (OptiPrep Density Gradient Medium, D1556, Sigma) prepared in 60 mM Tris (pH 8), 250 mM sucrose, 150 mM KCl, and 30 mM $MgCl_2$) and layered over a 29% iodixanol cushion prepared in a high-sucrose Tris-based solution. Density gradient centrifugation was performed at 13,500 × g for 20 minutes, allowing intact nuclei to sediment while reducing contamination from cellular debris and myelin. The resulting pellet was resuspended in cold blocking buffer containing PBS, 1% BSA, and 0.2 U/μL RNasin Plus, and adjusted to a final volume of 500 μL for downstream sorting.

To enable selective exclusion of neuronal nuclei, samples were incubated on ice with a PE-conjugated anti-NeuN antibody (1:500, Millimark mouse anti-NeuN PE conjugated, FCMAB317PE, Merck) for 30 minutes in the dark. Following incubation, nuclei were pelleted at 400 × g for 5 minutes, resuspended in blocking buffer, and filtered through a 20 μm mesh immediately prior to fluorescence-activated nuclei sorting (FANS). DAPI (0.1 mg/mL, D3571, Invitrogen) was added just before sorting to label intact nuclei and exclude debris or damaged material.

We had particular care throughout the procedure to maintain efficient dissociation with preservation of nuclear structure.

7.3. Fluorescent-activated nuclei sorting (FANS)

Fluorescence-activated nuclei sorting (FANS) was performed at 4°C using either a BD FACSAria Fusion or a BD FACSAria III instrument. To preserve fluorescence signal integrity, samples were protected from light throughout the sorting procedure. Nuclei were gated based on DAPI fluorescence, marking intact nuclei, and phycoerythrin (PE) signal corresponding to NeuN

immunolabeling. This strategy enabled the resolution of two distinct nuclear populations: NeuN-positive ($NeuN^+$) neuronal nuclei and NeuN-negative ($NeuN^-$) non-neuronal nuclei.

Each fraction was collected into tubes preloaded with 50 µL of cold blocking buffer to stabilize the nuclei immediately upon sorting. Sorting proceeded until approximately 200,000 nuclei were obtained per fraction. Following collection, nuclei were concentrated by centrifugation at 400 × g for 4 minutes. The supernatant was carefully removed, leaving a small residual volume (approximately 30 µL) to avoid disturbing the pellet and to facilitate gentle resuspension. From this point onward, sorted nuclei were maintained on ice to preserve structural integrity and RNA quality in preparation for downstream molecular analyses.

7.4. Library preparation

Complementary DNA (cDNA) libraries were generated from sorted nuclei using the Chromium Next GEM Single Cell 3′ Reagent Kit v3.1 (PN-1000268, 10X Genomics), following the manufacturer's recommendations with minor practical adjustments. Prior to library preparation, nuclei were manually counted and diluted to a final concentration between 200 and 1,700 nuclei/µL. Careful estimation at this stage was essential to optimize encapsulation efficiency and minimize doublet formation.

Reverse transcription and barcoding were carried out according to the 10X Genomics protocol (CG000204 Rev D). Nuclei were partitioned using the Chromium Next GEM Chip G (PN-1000120). Depending on the experimental design, neuronal ($NeuN^+$) and non-neuronal ($NeuN^-$) fractions were either loaded separately, targeting a recovery of approximately 5,000 nuclei per lane, or combined prior to loading. For mixed preparations, nuclei were pooled at a 70:30 ratio ($NeuN^+$:$NeuN^-$), with an expected recovery of 5,000-7,000 nuclei per reaction. Subsequent cDNA amplification and library construction were completed using the Single Index Kit T Set A (PN-1000213), in accordance with the manufacturer's instructions.

Library quality was evaluated prior to sequencing through two complementary approaches. Fragment size distribution was assessed using the Agilent High Sensitivity DNA Kit (5067-4626, Agilent Technologies), ensuring the expected cDNA profile. Library concentration was quantified with the KAPA Library Quantification Kit (2700098952, Roche) to confirm accurate molarity for sequencing. Together, these quality control steps verified the structural integrity and concentration of the libraries, providing confidence in their suitability for downstream high-throughput sequencing.

7.5. Illumina sequencing

Following indexing, individual libraries were multiplexed to optimize sequencing capacity. When targeting a recovery of approximately 5,000 nuclei per sample, up to 19 libraries were pooled per

sequencing run; for experiments aiming at 7,000 nuclei, pools included up to 16 samples to maintain adequate read depth per cell.

Sequencing was performed on an Illumina NovaSeq 6000 platform using an S4-200 (v1.5) flow cell distributed across eight lanes. The run configuration followed a 28-8-0-91 base pair layout, in accordance with the technical specifications of the 10X Genomics 3′ gene expression protocol, ensuring proper capture of cell barcodes, unique molecular identifiers, and transcript reads.

All sequencing was carried out by the National Genomics Infrastructure, which provided standardized high-throughput sequencing services and quality-controlled data delivery.

7.6. snRNA-seq Data Analysis

7.6.1. Pre-Processing

Raw base call files generated from snRNA-seq were processed into gene-by-cell count matrices using the Cell Ranger software (v3.0.0, 10x Genomics). Sequencing reads were aligned to the human reference genome hg38 (GRCh38.p5; NCBI accession GCA_000001405.20) to generate transcript counts for downstream analyses.

Because our material was derived from isolated nuclei rather than whole cells, the alignment workflow was configured to retain both exonic and intronic reads. This adjustment is particularly important in single-nucleus datasets, where a substantial fraction of transcripts remains unspliced and localized within the nucleus. By incorporating intronic signals into the quantification step, we aimed to more faithfully capture the nuclear transcriptome and thereby obtain a more accurate representation of gene expression across cell types.

7.6.2. Quality control

Initial processing of the snRNA-seq dataset focused on the identification and removal of potential doublets. We applied Scrublet (Wolock et al., 2019) independently to each sample, running 100 iterations per dataset with a fixed random seed and automated thresholding to ensure consistency. Nuclei flagged as doublets in more than 10% of iterations were excluded from further analysis, reducing the potential of retaining artifactual cell profiles.

We next implemented quality control filters based on the distribution of unique molecular identifiers (UMIs) and detected gene counts. Nuclei with fewer than 500 UMIs or fewer than 1,200 detected genes were removed, as these profiles typically reflect low-quality or damaged nuclei. At the opposite extreme, nuclei exceeding 250,000 UMIs or 15,000 genes were excluded to minimize the inclusion of potential multiplets. Additionally, nuclei in which mitochondrial transcripts accounted for more than

10% of total reads were discarded, given that elevated mitochondrial content often indicates compromised integrity.

To further refine the dataset, we modeled the relationship between log-transformed UMI counts and gene counts using a second-degree polynomial regression. Nuclei deviating from the predicted curve by more than 2,000 counts were classified as outliers and removed, as these profiles were unlikely to represent biologically real transcriptional states. Recognizing that some doublets (particularly those formed by nuclei from distinct cell types) may avoid detection by global metrics, we conducted an additional layer of screening based on canonical marker expression. For major brain cell classes, including neurons, astrocytes, microglia, and oligodendrocytes we calculated a cell-type score for each nucleus derived from the average expression of established marker genes. Because these scores exhibited bimodal distributions, we fitted Gaussian mixture models to distinguish true single-cell identities from ambiguous profiles. A stringent cutoff was defined as the mean of the lower component plus four standard deviations. Nuclei exceeding this threshold for more than one cell class were considered likely doublets and removed.

Finally, to confirm regional specificity, we examined the expression of striatal marker genes described in the Allen Brain Atlas. Nuclei expressing markers characteristic of adjacent regions, such as the claustrum or amygdala, were excluded from this analysis.

7.6.3. Glia and non-neuronal detection

Because this study centers on glial and other non-neuronal populations, our analytical workflow started with a clear separation of these cells from neuronal subtypes. After library size normalization, we identified 2,500 highly variable genes (HVGs), which were used to capture the principal axes of transcriptional heterogeneity for downstream analyses.

We next performed principal component analysis (PCA) and retained the top 15 principal components, which together accounted for the most informative sources of variation in the dataset. To reduce potential batch effects introduced by differences in sample origin or processing, we applied Harmony-based integration prior to neighborhood graph construction. Using the corrected embeddings, a k-nearest neighbor graph (k = 15) was generated in Scanpy (Wolf et al., 2018), and a two-dimensional UMAP representation was computed to visualize the global cellular landscape.

We performed unsupervised clustering using the Louvain algorithm, allowing transcriptionally distinct groups to join without prior assumptions. Clusters were then annotated through the expression of established lineage markers. Oligodendrocyte precursor cells (OPCs) were identified by *PDGFRA* and *VCAN* expression, while mature oligodendrocytes expressed canonical myelin genes such as *MBP* and

PLP1. Astrocytes were defined by markers including *GFAP, ALDH1L1*, and *S100B*; Microglia by *CSF1R, CX3CR1*, and *P2RY12*; and Perivascular Macrophages by *CD163* and *MRC1*. Additional populations were annotated as follows: Ependymal Cells (*FOXJ1, CCDC153*), Vascular Cells (*CLDN5, PECAM1*), Fibroblasts (*ABCA9, BICC1, COL12A1*), Lymphocytes (*PTPRC* and T cell-associated genes *CD3D, CD3G, CD3E*), medium spiny neurons (*NGEF, PDE1B*), and interneurons (*LHX6*).

Following this systematic annotation, neuronal clusters were excluded, and the dataset was subsetted to retain glial and other non-neuronal populations. This curated atlas served as the foundation for all subsequent analyses.

7.6.4. Subclustering of glial and non-neuronal populations

To determine the heterogeneity within each glial and non-neuronal lineage, we applied a unified subclustering strategy across all major cell classes. After defining broad populations, such as astrocytes, microglia, vascular-associated cells, and lymphocytes, we independently reanalyzed each class to uncover finer transcriptional structure. For every subset, we selected the 2,000 most variable genes to capture within-lineage diversity and performed principal component analysis, keeping the first 15 components as the basis for downstream clustering.

Because samples originated from multiple sequencing runs, we corrected for potential batch effects within each class using Harmony. The corrected embeddings were used to construct neighborhood graphs, and clusters were identified using the Louvain algorithm. We initiated clustering at a base resolution of 0.2 and adjusted this parameter as needed for each lineage to balance granularity with interpretability. When inspection of marker expression suggested that a cluster included biologically distinct groups, we performed iterative subclustering to further refine those populations.

Subcluster identities were determined through differential gene expression analysis using the scanpy.tl.rank_genes_groups function with a Wilcoxon rank-sum test. Candidate marker genes were selected based on a log fold change greater than 0.5 and an adjusted p-value below 0.05. These genes were then studied manually to assign biologically meaningful annotations to each subpopulation.

7.6.5. Hierarchical analysis

To explore the transcriptional relationships among identified subpopulations, we constructed hierarchical representations of cluster similarity using the scanpy.tl.dendrogram function within the Scanpy (Wolf et al., 2018) framework. Similarity between clusters was quantified by calculating Pearson correlation coefficients derived from their average gene expression profiles, providing a measure of how closely related the transcriptional programs were across groups.

For hierarchical clustering, we applied the complete linkage method, meaning that the distance between two clusters is defined by the greatest dissimilarity between their respective elements when forming higher-order groupings. This approach offers a conservative view of cluster relationships, emphasizing separation between transcriptionally distinct populations while preserving meaningful structural organization in the data.

7.6.6. Compositional analysis

When comparing changes in subpopulation abundance across conditions, we accounted for the compositional nature of single-cell data. Because the proportions of all cell types within a sample must sum to 100%, interpreting raw percentages directly can be misleading and may introduce spurious associations. For astrocyte and microglial subpopulations, we applied a centered log-ratio (CLR) transformation to the subpopulation proportions prior to statistical testing. This approach expresses each subpopulation relative to the geometric mean of all populations within the same sample, normalizing the data and allowing more reliable comparisons between conditions. Differences between groups were then assessed using the Mann-Whitney U test.

For oligodendrocyte subpopulations, the larger number of subpopulations identified made simultaneous pairwise testing unreliable, as the CLR + Mann-Whitney approach does not account for dependencies introduced when testing multiple subpopulations at once. We therefore used single-cell compositional data analysis (scCODA), a Bayesian model specifically designed for compositional data from snRNA-seq experiments (Büttner et al., 2021). By jointly modeling all subpopulations simultaneously, scCODA handles the inherent dependencies in compositional data and provides better control over false discoveries when the number of categories being compared is large.

7.6.7. Module analysis

To identify coordinated gene expression programs within glial subpopulations, we applied the Hotspot (DeTomaso & Yosef, 2021) algorithm to all the populations. This method detects groups of co-expressed genes by taking advantage of structured patterns in single-nucleus transcriptomic data, helping to obtain gene sets that are likely involved in shared biological functions.

We ran the analysis using default settings and limited the input to the top 10,000 highly variable genes (HVGs) for each lineage. Focusing on these genes helps reduce background noise and keeps the analysis centered on the most informative signals in the dataset. With this approach, we aimed to define gene modules that capture functional diversity within populations, and to gain information of the molecular programs underlying their behavior in disease.

7.6.8. Differential expression analysis

To explore transcriptional changes linked to PD, we ran a differential expression analysis separately for each main class, comparing PD samples with controls. At this stage, we treated each cell type as a whole rather than splitting them into subpopulations, with the goal of capturing broad, disease-related shifts across the entire lineage.

Gene expression differences were computed using the sc.tl.rank_genes_groups function in Scanpy (Wolf et al., 2018), applying the Wilcoxon rank-sum test to contrast nuclei annotated as PD versus Control. We controlled for multiple testing using the Benjamini-Hochberg correction. Based on statistical significance and effect size, genes were classified as either upregulated or downregulated in PD.

To better understand the biological context of these changes, we then compared the differentially expressed genes with previously defined marker sets for each subpopulation. This step allowed us to see whether PD-related transcriptional changes tend to align with particular cellular states. By combining global differential expression with subpopulation-specific signatures, we aimed to distinguish between widespread lineage-level effects and changes driven by specific reactive or functionally distinct subgroups.

7.6.9. KEGG PD analysis

The goal of this analysis was to assess whether PD-associated genes show preferential activity in particular subpopulations. To ensure that the results reflected disease-relevant biology, we restricted the analysis to nuclei derived from PD samples. This approach allowed us to examine how PD-related transcriptional programs are distributed across glial states within a pathological context.

We began by compiling a set of PD-associated genes from the KEGG database. Using the sc.tl.score_genes function in Scanpy, we calculated a module score for each cell, which captures the aggregate expression of the KEGG PD gene set. In this way, each cell was assigned a quantitative value reflecting the extent to which it expresses a PD-related transcriptional signature.

To evaluate whether specific subpopulations were enriched for this signature, we compared the scores of each cluster against all remaining cells using a one-versus-rest approach. Differences were assessed with the Wilcoxon rank-sum test, and we also computed mean scores and log fold changes for each comparison. To account for multiple testing, p-values were adjusted using the Benjamini-Hochberg false discovery rate (FDR) method. This workflow enabled us to identify the glial subpopulations most strongly associated with PD-related gene expression patterns.

7.6.10. Transcription factors analysis

Gene regulatory network activity was inferred using the SCENIC workflow (Van de Sande et al., 2020). In brief, this approach identifies regulons (sets of transcription factors and their predicted target genes), and then estimates their activity at the single-cell level using the AUCell algorithm. The resulting activity scores were stored as an AUC matrix within the AnnData object, and all downstream analyses were based on these regulon activity values rather than raw gene expression.

To explore how regulatory programs relate to different biological responses (Control-like, UPR, and Reactive), cells were grouped according to their annotated glial subpopulations. For each group, regulon activity was compared against appropriate reference populations using pairwise statistical tests. Regulons showing significant increases in activity were identified and ranked based on their effect sizes.

We approached this analysis from two complementary angles. First, to identify response-shared regulons, we looked for regulons that were consistently upregulated across subpopulations belonging to the same response category. This was done by intersecting the sets of significant regulons across those subpopulations, with the aim of capturing common regulatory programs linked to a given biological response, regardless of cell type. Second, to define subpopulation-specific regulons, we compared each subpopulation with closely related groups within the same lineage. Regulons were considered specific if they were significantly enriched in one subpopulation but not in others. This allowed us to highlight regulatory signatures associated with distinct cellular identities or state transitions.

7.6.11. Cells Interaction Analysis

Cell-cell communication between glial subpopulations was inferred using the LIANA framework (Dimitrov et al., 2024). Rather than relying on a single ligand-receptor resource, we applied the rank_aggregate method, which combines evidence across multiple databases into a consensus interaction score, improving the robustness of the estimates. The analysis was run on the full single-nucleus glial and non-neuronal dataset using subpopulation annotations, with a minimum expression proportion threshold of 0.3 and a minimum of 100 cells per interacting group. Differential expression was assessed using the Wilcoxon rank-sum test.

From the resulting interaction table, we focused specifically on bidirectional signaling between AR2 astrocytes and M1 microglia, restricting the analysis to interactions where one subpopulation acted as the ligand-expressing cell and the other as the receptor-expressing cell, and retaining both directions separately to preserve signaling directionality. Interaction scores were averaged across observations to obtain mean ligand-receptor scores and mean specificity ranks per ligand-receptor pair. To focus on

high-confidence interactions with biological relevance, we applied stringent filtering based on both score and specificity rank thresholds. The filtered interaction set was then used for visualization and interpretation of the asymmetric signaling patterns between these two reactive glial states.

7.6.12. UPR signaling analysis

To assess UPR activation across glial subpopulations, we examined the expression of marker genes from each of the three canonical UPR branches: IRE1α (*XBP1, TRAF2, MAPK8, MAPK14*), ATF6 (*ATF6, MBTPS1, MBTPS2*), and PERK (*EIF2AK3, EIF2S1, ATF4*). Expression was visualized using dot plots generated with Scanpy across eleven subpopulations: A0, AR1, AR2, MH, MH-HSP, M1, MOL-A, PDAO-1, PDAO-2, OPCs-A, and PDAOPCs. In these plots, dot size reflects the proportion of cells within each subpopulation expressing a given gene, and color intensity indicates the mean expression level among expressing cells.

7.6.13. Braak Lewy Body Staging Analysis

To examine how glial subpopulation composition shifts across Braak LB stages, we applied a centered log-ratio (CLR) transformation at the subject level. Stage-level summaries were obtained by averaging subject-level CLR values within each Braak LB stage. Subpopulation-stage combinations represented by fewer than two donors were excluded to avoid estimates driven by individual subjects. For visualization, CLR values were optionally z-scored across stages for each subpopulation to facilitate comparison of relative enrichment and decreased trends.

7.6.14. Correlations between glial subpopulations and Lewy Body quantifications

To examine the relationship between glial subpopulation abundance and α-synuclein pathological load, we restricted this analysis to donors for whom quantitative immunohistochemical measures of Lewy body density (LBs/Area) were available, as previously reported in Barba-Reyes *et al* (Barba-Reyes et al., 2025). Analyses were conducted separately for CN and Pu, and donors contributing fewer than 50 nuclei in a given region were excluded to ensure reliable compositional estimates.

For each remaining donor, cell counts per subpopulation were converted to proportions of the total nuclei recovered from that region and subsequently CLR-transformed as described above. Spearman rank correlations were then calculated between the CLR-transformed abundance of each subpopulation and the corresponding regional Lewy body density, independently for CN and Pu. The analysis was restricted to a predefined set of disease-relevant subpopulations: A0, AR1, AR2, MH, MH-HSP, M1, DAM, OPCs-A, PDAOPCs, MOL-A, PDAO-1, PDAO-2, and PDAO-3.

7.6.15. Correlations between PDAO-1/PDAO-2/MOLA ratio and MBP quantifications

To explore whether the abundance of PD-associated oligodendrocyte subpopulations (PDAO-1, PDAO-2, and MOL-A) correlated with MBP protein levels, the dataset was first filtered to retain only samples with complete data across all variables of interest. Subpopulation abundance was expressed as the percentage of cells per sample belonging to each subpopulation, and samples contributing fewer than five cells to a given subpopulation were excluded to avoid unreliable estimates. Spearman correlation was then used to test the following relationships: PDAO-1 percentage vs. MBP intensity, PDAO-2 percentage vs. MBP intensity, and MOL-A percentage vs. MBP intensity.

7.6.16. Differential expression analysis and comparison between donor groups and PD

To determine how much of the PD transcriptional signature is driven by the multicellular programs identified in each donor group, we performed cell-type-specific differential expression analysis using Scanpy's rank_genes_groups function with the Wilcoxon rank-sum test.

Two complementary comparisons were carried out. First, donor group-specific comparisons were performed by testing UPR-high and Reactive donors separately against homeostatic donors as a reference, deliberately excluding cells from the reciprocal PD-associated donor group in each comparison to keep the reference population clean. Second, a standard PD versus control comparison was performed across all donors. Genes were considered differentially expressed at an adjusted p-value below 0.05 and a minimum expression prevalence of 10% in the tested population. To capture the range of transcriptional effect sizes, significant DEGs were divided into four fold-change tiers based on absolute log2 fold-change: Tier 1 (≥2.0), Tier 2 (1.0-2.0), Tier 3 (0.5-1.0), and Tier 4 (0.25-0.5). Results were visualized as stacked bar charts with upregulated and downregulated genes on opposing axes, color-coded by tier.

Transcriptional overlap between donor groups and disease condition was assessed using three-way Venn diagrams generated with the matplotlib-venn library, computed separately for each cell type. Before this analysis, potential pseudogenes and non-coding transcripts identified by prefixes including *AC, AL, LINC, AP*, and *AF* were removed. Gene sharing was evaluated using a dual-threshold strategy: a candidate gene universe was first defined using a stringent significance and fold-change threshold in at least one condition, and the presence of those genes in remaining conditions was then assessed using a relaxed threshold, allowing detection of consistent directional changes even when effect sizes differed across groups.

Cross-cell-type gene sharing within each condition was examined using UpSet plots generated with the upsetplot library, applying the same dual-threshold logic described above. For each comparison, UPR-high, Reactive, or PD, a candidate gene set was established at the strict threshold and

cross-referenced across all other cell types at the relaxed threshold. Only intersections containing more than ten genes were included in the final visualizations.

7.6.17. Functional Enrichment Analysis

To explore the biological functions associated with both shared and unique gene sets across donor groups, we carried out gene set enrichment analysis (GSEA) (Subramanian et al., 2005)using the GSEApy library (v1.1+). For each cell type, differentially expressed genes had been previously organized into seven categories based on their overlap: genes specific to PD, Reactive, or UPR states, as well as those shared between these conditions (e.g., PD + Reactive, PD + UPR, and genes common to all three). These groupings were defined by intersecting gene lists generated under both stringent and more relaxed selection criteria.

Enrichment analysis was performed against the GO Biological Process 2023 database. For each category containing at least five genes, we selected the top three most significant terms, based on adjusted p-values, to build a representative set of pathways for each cell type. The results were then visualized using comparative dot plots, where dot size indicates the gene ratio (the proportion of genes overlapping with a given GO term) and color intensity reflects the level of significance, expressed as −log10 of the adjusted p-value.

7.6.18. GSEA superpathways

GSEA outputs from all pairwise comparisons were processed in Python to consolidate redundant pathways and summarize enrichment patterns across contrasts. For each merged pathway group, summary statistics were computed, including mean normalized enrichment score (NES), average false discovery rate (FDR), and gene coverage. To assess similarity between pathways, Jaccard indices were calculated from gene set overlaps, adapting an approach originally implemented in R by Noori et al. (https://github.com/ayushnoori/brainstorm), and hierarchically clustered using average linkage with a similarity threshold of 0.8. Each resulting cluster was characterized by aggregated statistics and gene content. The ten clusters with the highest and lowest mean NES values were annotated manually; the remaining clusters were labeled using KeyBERT (initialized with the allenai-specter model) for unsupervised keyword extraction, selecting the two top-ranked n-gram phrases (1-3 words per phrase) from pathway names as descriptors for each superpathway.

7.6.19. Trajectory Analysis

Differentiation trajectories within the oligodendroglial lineage were mapped using two complementary approaches. The first, StaVia (Stassen et al., 2024), was selected for its ability to integrate spatial and transcriptional information through higher-order random walks, which allows it to trace lineage paths and capture intermediate cell states that simpler methods may miss. The run_VIA function was used with otherwise default settings, adjusting only the k-nearest neighbors

(KNN) parameter to 15 to keep this consistent with the rest of the analysis. The second method, Slingshot (Street et al., 2018), takes a different angle. It identifies developmental lineages by connecting clusters in a way that models continuous maturation rather than discrete transitions, making it well suited for capturing the gradual progression from precursor to mature oligodendrocyte. Slingshot was run entirely with default parameters. Using both methods in parallel allowed cross-validation of the inferred trajectories, with agreement between them providing greater confidence in the lineage structure identified.

7.6.20. Factor Analysis

To identify genes associated with oligodendroglial differentiation, factor analysis was applied to pseudotime-ordered gene expression data using the scikit-learn Python package. Factor analysis decomposes observed gene expression patterns into a smaller set of underlying latent variables (factors) that capture the main sources of variability in the data while reducing the contribution of noise. Input data were normalized and scaled before running the analysis to ensure comparability across genes. The resulting factors were then interpreted in terms of the gene sets loading most strongly onto them, allowing us to identify coherent gene expression programs associated with distinct phases of the differentiation trajectory rather than selecting individual genes in isolation.

7.7. Immunohistochemistry with peroxidase-DAB method

Eight-µm-thick formalin-fixed paraffin-embedded sections from the striatum (contralateral to samples used for sn-RNA-seq and spatial transcriptomics) at the level of the nucleus accumbens were immunostained in a Leica BOND RX fully automated research stainer using the BOND kit (Leica Biosystems, DS9800). Primary antibodies and concentrations were as follows: mouse anti-α-syn clone LB509 (Thermo Fisher Scientific Cat# 18–0215, RRID:AB_2925241, 1:200), mouse anti-myelin basic protein (MBP) amino acids 129–138 clone 1 (Millipore Cat# MAB382, RRID:AB_94971, 1:250), and rabbit anti-tyrosine hydroxylase (TH) polyclonal (Cell Signaling Technology Cat# 2792, RRID:AB_2303165, 1:100). The immunohistochemistry protocol included bake and dewax steps, a 20-min-long heat-induced epitope retrieval (with ER2 solution for α-syn and with ER1 solution for MBP and TH), and hematoxylin counterstaining. Sections were coverslipped with Permount mounting media and whole-slide images were obtained under the 40 × objective (numerical aperture 0.95, resolution 0.17 µm/pixel) of an Olympus VS120 virtual slide scanner (Olympus, Tokyo, Japan).

7.8. Immunohistochemistry images analysis and quantification

All slide images were processed and analyzed using QuPath (version 0.4.3). Quantitative analysis focused on detecting intensity features related to MBP, as well as identifying the density of TH-positive projections from the SNpc to the dorsal striatum and α-synuclein aggregations (Lewy bodies/neurites, LBs/LNs). For each image, random regions of interest (ROIs) were selected within

CN and Pu. TH-positive projections and α-synuclein aggregation detection was performed independently using QuPath's pixel classifier tool. Five representative samples were chosen, and within each sample, the classifier was trained using 25 TH-positive and α-syn-positive annotations and 25 TH-negative or α-syn-negative annotations, resulting in a total of 125 TH-positive and 125 TH-negative annotations, and 125 α-syn-positive and 125 α-syn-negative annotations for classification.

The data obtained from MBP intensity measurements, TH projections quantification, and α-syn aggregate quantifications were further analyzed using the SciPy Python library. A two-sample t test was applied to determine the T and p values for each brain region and condition. For MBP analysis, the mean of diaminobenzidine (DAB) intensity per pixel within the selected ROIs was used as the metric for quantification. TH differences were assessed by comparing the percentage of positive TH annotations, calculated as the area of TH-positive measurements, divided by the total area analyzed (μm2). Similarly, α-syn differences were quantified based on the proportion of α-syn-positive regions relative to the total area (mm2) examined in Pu or CN, respectively. In addition, Spearman's rank correlation analysis was performed to explore relationships between various feature pairs across different regions and experimental conditions.

7.9. Spatial transcriptomics data generation

7.9.1. Spatial transcriptomics platform

Spatial transcriptomic profiling was performed using the Xenium *in situ* platform (10X Genomics), which allows RNA detection at subcellular resolution within intact tissue sections. The overall approach follows previously described workflows (Barba-Reyes et al., 2025; Garma et al., 2024).

7.9.2. Gene panel design

Xenium relies on targeted oligonucleotide probes to quantify gene expression from a predefined panel. In this study, we used a base panel of 266 genes from the Xenium Human Brain Gene Expression Panel. To this, we added 100 genes selected from our own snRNA-seq dataset, generating a customized panel (Xenium Custom Gene Expression Panel 51–100, Z3DREH, PN-1000561, 10x Genomics).

7.9.3. Experimental workflow

Frozen tissue blocks from human donors (N = 4; including CN and Pu) were retrieved from −80 °C storage and transferred on dry ice to a cryostat (CryoStar NX70, Thermo Scientific). Samples were embedded in Tissue-Tek O.C.T. Compound (4583, Sakura), mounted on the specimen holder, and equilibrated at −20 °C for approximately 5 minutes. Sections of 10 μm thickness were then cut and placed directly onto the imaging area of precooled Xenium slides (12 × 24 mm, PN-3000941, 10x

Genomics). To ensure proper adhesion, the back of the slide was briefly warmed with gentle pressure and immediately refrozen on the cryobar. Slides were kept cold throughout the process and stored at -80 °C after sectioning.

Subsequent processing steps, including probe hybridization, ligation, and rolling circle amplification, were carried out at the in situ Sequencing Infrastructure Unit (Science for Life Laboratory, Stockholm), following the manufacturer's protocol (CG000582 Rev E, 10x Genomics). A chemical quenching step was included to reduce background fluorescence. Imaging, signal decoding, and data acquisition were performed using the Xenium Analyzer (10X Genomics).

7.10. Spatial transcriptomics data analysis

7.10.1. Segmentation, data preprocessing and cell type identification

Xenium datasets provide spatial coordinates for every detected transcript, which allows direct mapping of gene expression within tissue sections. As a first step, individual cells were delineated and their transcriptomic profiles reconstructed. We used the default Xenium nuclear-based segmentation, which offers a conservative definition of cell boundaries and helps reduce incorrect assignment of transcripts between neighboring cells.

The resulting cell-by-gene matrices were processed using Scanpy. Low-quality cells were removed by excluding those with fewer than 50 total counts or fewer than 5 detected genes. After filtering, the data were normalized to total counts, log-transformed, and scaled prior to downstream analysis.

To explore the structure of the dataset, we performed principal component analysis (PCA) followed by construction of a neighborhood graph (n_neighbors = 10, n_pcs = 30). This was used to generate a UMAP embedding for visualization. Cell populations were identified using Leiden clustering at a resolution of 2.0. Clusters were then manually annotated based on known marker gene expression patterns together with their spatial localization, using an external reference as guidance.

For higher-resolution analysis, each major cell class was further subclustered. These subpopulations were also manually annotated, allowing a more detailed characterization of cellular heterogeneity within the tissue.

7.10.2. Gene module analysis using Hotspot

The resulting cell-by-gene matrices were analyzed using Scanpy (Wolf et al., 2018). Low-quality cells were filtered out by removing those with fewer than 50 total counts or fewer than 5 detected genes. The remaining data were normalized to total counts, log-transformed, and scaled before proceeding with downstream analyses.

To identify coordinated gene programs within the Xenium data, we applied the Hotspot algorithm. We began by fitting a Depth-Adjusted Negative Binomial (DANB) model to account for differences in sequencing depth and technical variability, using total UMI counts per cell for normalization. A KNN graph was then constructed in PCA space (k = 20) to define each cell's local neighborhood.

We next assessed gene expression patterns by calculating local autocorrelation (Geary's C) across the KNN graph, allowing us to detect genes with non-random spatial or local structure. Genes passing an FDR threshold of 0.05 were retained for further analysis. A local gene-gene correlation matrix was then computed to capture relationships between genes within these neighborhoods.

Gene modules were defined by clustering this matrix, requiring a minimum of five genes per module and applying a clustering FDR cutoff of 0.01. For each module, we calculated a per-cell score reflecting the combined expression of its member genes. These module scores were added back to the dataset and used to explore how different biological programs are distributed across cells and regions. Finally, modules were manually annotated based on their gene composition and their expression patterns across the dataset, facilitating biological interpretation.

7.10.3. Niche identification

To define spatially organized cellular niches across samples, we used NicheCompass. This approach integrates spatial transcriptomic information by learning a latent representation of the data through a graph convolutional network (GCN). During model construction, we incorporated categorical variables such as sample identity to account for potential batch or replicate effects.

The model was trained for 400 epochs, with regularization applied to improve the identification of niches driven by ligand–receptor interactions. Once the latent space was obtained, cells were grouped using the Leiden clustering algorithm at a resolution of 0.2. The resulting clusters were then interpreted as distinct spatial niches and annotated based on their location within the tissue and their underlying cellular composition.

7.10.4. Identification of spatially-variable genes

To detect spatially variable genes (SVGs), we carried out a spatial autocorrelation analysis on a per-sample basis using Squidpy (Palla et al., 2022). As our analysis focused specifically on grey matter, we first restricted each dataset to cells assigned to grey matter domains during the spatial domain annotation step.

Cell-cell neighborhoods were then defined using Delaunay triangulation, which provides a spatially informed connectivity structure. Within each sample, we computed Moran's I statistic for every gene to evaluate the presence of global spatial patterns in expression. Statistical significance was assessed through 100 permutations per gene.

To ensure reliable estimates, only samples containing at least 50 cells were included in the analysis. Finally, Moran's I values and corresponding p-values were combined across samples, allowing us to compare spatial gene expression patterns across conditions in a consistent manner.

8. Results

8.1. Transcriptional and spatial remodeling of oligodendrocyte lineage cells in the dorsal striatum in Parkinson's Disease

8.1.1. A high-resolution atlas of the oligodendrocyte lineage

To delineate the cellular architecture of the human striatum in PD, we analyzed postmortem tissue from a cohort of 56 individuals, including 20 neurologically healthy controls and 36 donors with neuropathologically confirmed PD (Figure 9A). We combined snRNA-seq with spatial transcriptomics using the Xenium platform, the latter applied to a subset of 24 subjects (12 controls and 12 PD cases) with a customized 366-gene panel (Figure 9A; see Material and Methods). For each individual included in the spatial transcriptomics analysis, both CN and Pu were analyzed, enabling direct comparison between these two principal striatal regions.

After rigorous quality control and filtering (see Material and Methods), the snRNA-seq dataset comprised approximately 600,000 high-quality nuclei. Of these, ~270,000 were classified as glial cells, forming the foundation of a comprehensive striatal glial atlas (Figure 9B). The overall cellular composition closely mirrored the known structural organization of the striatum. Oligodendrocytes represented the largest fraction (~56%), followed by astrocytes (~16%), oligodendrocyte precursor cells (OPCs; ~13%), and microglia (~9%). In addition to these major glial classes, we detected less abundant but biologically relevant populations, including vascular-associated cells (~1%) and lymphocytes (~0.4%) (Figure 9B, 9C, Table 2). Although numerically small, these two last populations contribute to the neurovascular and immune landscape of the striatum and were retained to preserve a more complete representation of the striatal cellular composition.

Population	Region			
	Caudate		Putamen	
	Condition			
	Control	PD	Control	PD
Oligodendrocytes	49,70%	52,90%	60,80%	60,40%
Astrocytes	18,40%	18,70%	16,70%	9,80%
OPCs	14,30%	11,80%	11,40%	14,60%
Microglia	8,20%	8,80%	7,20%	11,20%
Ependymal Cells	5,60%	4,20%	-	-
Vascular Cells	1,70%	1,00%	0,90%	1,10%
Fibroblasts	18,40%	1,10%	0,60%	0,70%
Perivascular Macrophages	0,80%	1,20%	0,80%	1,40%
Lymphocytes	0,30%	0,40%	0,30%	0,60%

Table 2. Proportion of cells associated with the distinct populations identified in each region and condition.

Cellular diversity was similarly captured in the spatial transcriptomics dataset, where expression profiles were obtained from 2,337,697 cells spanning 12 major cell classes (Figure 9E). Across both datasets, consistent subpopulations were identified within each cell class (Figure 9D), with substantial heterogeneity across glial and other non-neuronal populations. The relative distribution of these cell classes was comparable across both striatal regions and across Braak LB stages (Figure 9D).

Given the structural heterogeneity of the dorsal striatum, NicheCompass (Birk et al., 2025) was applied to delineate tissue domains (Figure. 1E-F; see Material and Methods). Two dominant domains were identified across samples: gray matter, accounting for 72.1% of cells and characterized by neuronal enrichment (Figure 9G), and white matter, representing 19.0% of cells and predominantly populated by glial cells, particularly oligodendrocytes (Figure 9G). Beyond these two major compartments, additional domains were detected corresponding to vasculature (5.1%), the lateral ventricle (2.8%) (Figure 9E-F), and a small number of sample-specific structures present at low frequency (<0.5%), including non-striatal gray matter and D1D2-rich regions. White matter regions showed the expected spatial organization, appearing both as a surrounding border and as interspersed bundles within the gray matter (Figure 9E). Vascular structures, enriched in immune and vascular cell types, were also embedded within the striatal gray matter. The lateral ventricle, identified by

ependymal cell markers, was detected at the gray matter boundary in a subset of samples restricted to the CN (Figure 9E-F), in line with anatomical expectation (Scelsi et al., 2020).

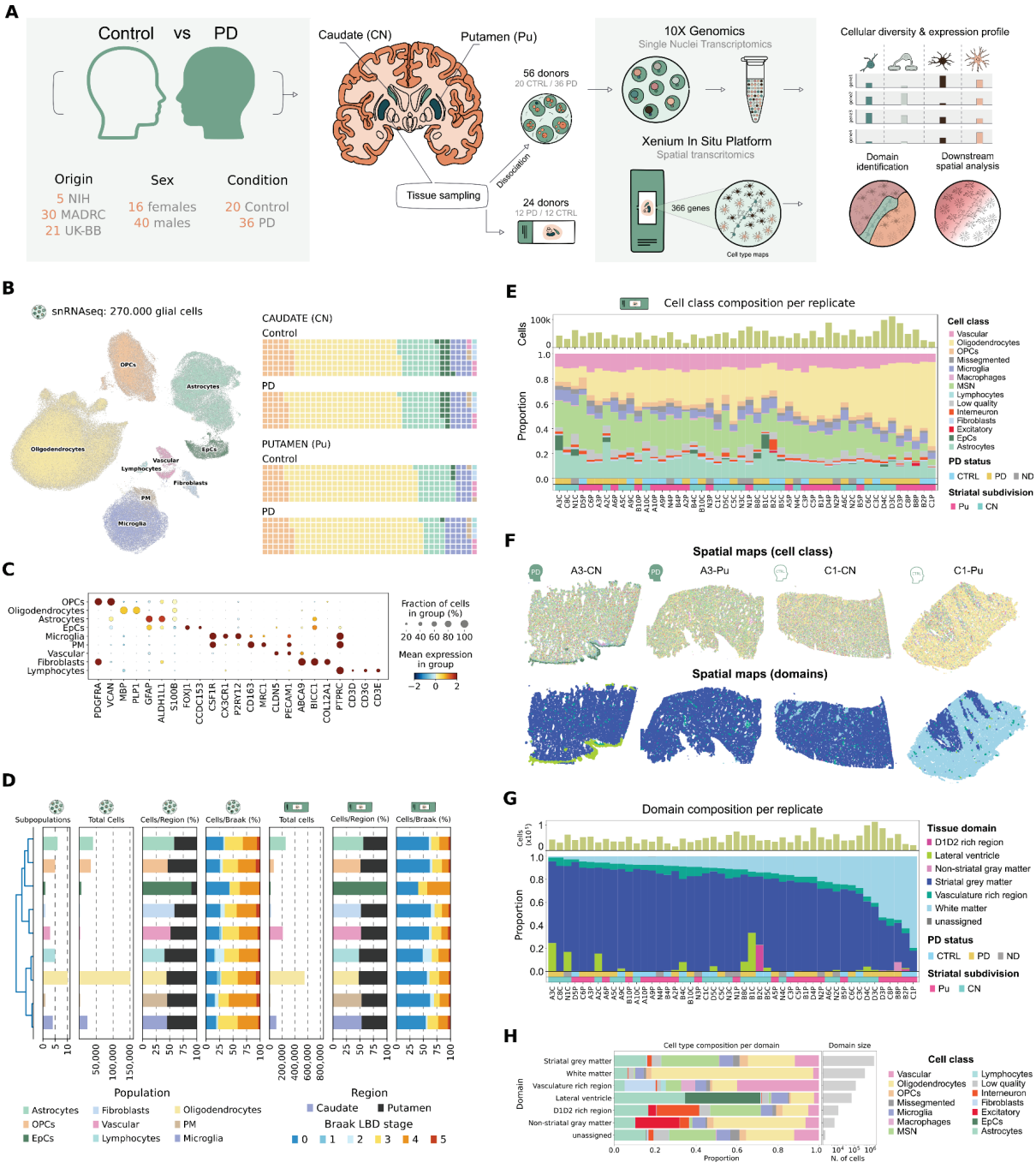

Figure 9. A. Schematic representation of the human samples used in this study and the different approaches carried out (single-nuclei RNA-seq and Spatial Transcriptomics). **B.** UMAP (Left) representing glial and non-neuronal populations with the different distributions per Region and Condition (Right). **C.** Dotplot to identify classical markers from previously defined populations. **D.** Barplots related to Populations identified, from left to right: number of subpopulations identified in each main population, number of cells in single-nuclei dataset after quality control, proportion of these cells related to CN or Pu, proportion of cells related to each Braak LB stage, number of cells in spatial transcriptomics data, proportion of cells related to CN or Pu and proportion of cells related to each Braak LB stage in spatial transcriptomics. **E.** Distribution of snRNA-seq

identified populations in spatial transcriptomics data per Subject and Region. **F.** Representation of domains identified in our data in the tissue slides from CN or Pu **G.** Frequencies of each domain per Subject and Region in spatial transcriptomics data. **H.** Distribution of glial and non-neuronal populations in each domain in spatial data. snRNAseq symbol indicates data from snRNAseq; spatial transcriptomics symbol indicates data from spatial transcriptomics approach.

Apart from the single-nuclei and spatial transcriptomics landscape, we also verified the pathological context of our samples, specifically the striatal denervation from the degeneration of substantia nigra dopaminergic projections and the presence of Lewy pathology (Lewy bodies/neurites). To do this, we performed immunohistochemical staining for tyrosine hydroxylase (TH) and α-synuclein (α-syn) on contralateral sections of dorsal striatum from a subset of donors where formalin-fixed, paraffin-embedded tissue was available (MADRC controls: α-syn N=10, TH N=8; PD donors: N=8 for both) (Figure 10A).

In Pu of PD cases, TH immunoreactivity decreased compared to controls (Control: 1.66 ± 0.58 SEM; PD: 0.21 ± 0.05 SEM; p = 0.027, t = 2.47). Also, α-syn immunoreactivity significantly increased (Control: 0.004 ± 0.0017; PD: 0.01 ± 0.002; p = 0.035, t = 2.31) (Figure 10A). These results validate our cohort, confirming both the severe denervation of TH-positive dopaminergic terminals and the pathological load of aggregated α-syn that defines PD.

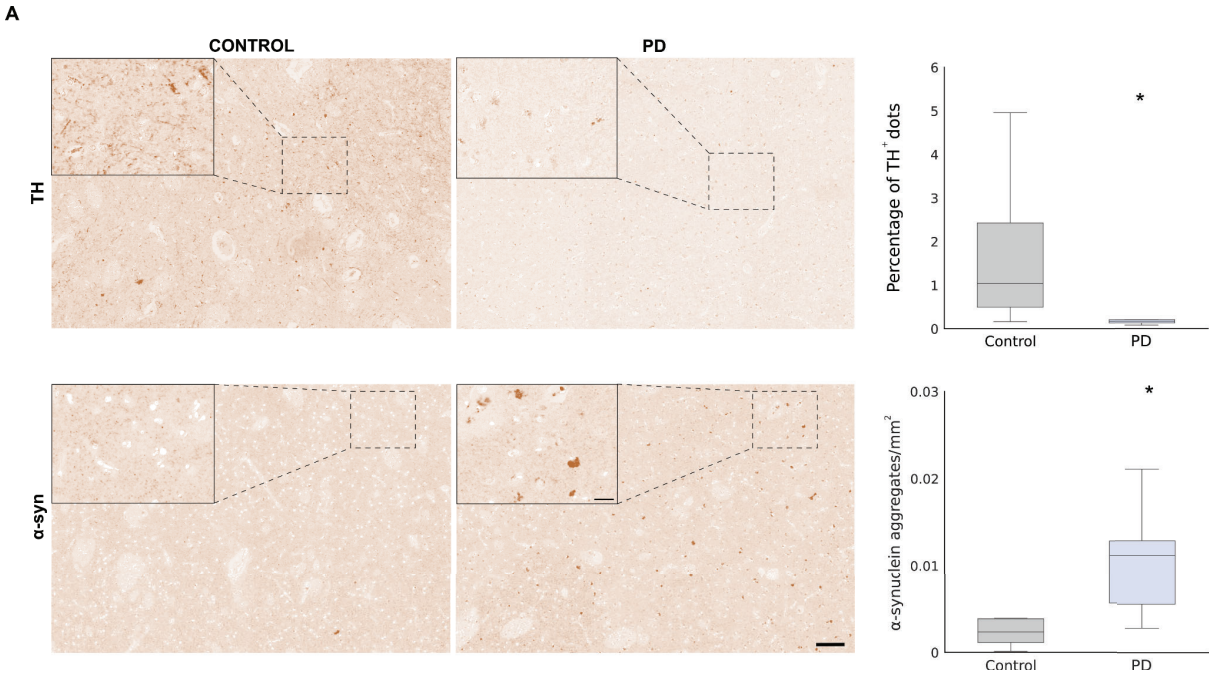

Figure 10. A. Representative sections of control and PD after TH (top) or α-syn (bottom) immunohistochemistry. Representation of Control and PD tissues along barplots showing TH (top) and LBs (bottom) between Conditions. * Highlight significant differences with a p-value < 0.05.

8.1.2. Transcriptional heterogeneity and stress signaling

Our first objective was to decode the molecular perturbations and gene regulatory networks that drive dysfunction within the oligodendrocyte (OL) lineage in the Parkinsonian dorsal striatum. To achieve this, we isolated the previously identified OLs to obtain a massive transcriptomic dataset comprising approximately 200,000 nuclei associated with the OL lineage (Figure 11A, 11B). This dataset represents, the most comprehensive transcriptomic atlas of striatal oligodendroglia generated to date, to our knowledge

After applying rigorous quality control filters (Supplementary Figure 1), unsupervised clustering resolved the lineage into four primary categories. We identified Oligodendrocyte Progenitor Cells (OPCs) via *VCAN* expression, Committed OPCs (COPs) via *GPR17*, and Mature Oligodendrocytes (MOLs) via *MBP* (Supplementary Figure 1). We further stratified the MOL population based on the differential expression of *OPALIN* versus *SLC5A11* (Figure 11B). Importantly, we detected all major classes across both control and PD groups, as well as in both striatal regions (Figure 11A; Supplementary Figure 2). Subsequent high-resolution clustering allowed us to profile 15 transcriptionally distinct cell states. Several of these subpopulations were significantly enriched in PD samples, which made us classify them as PD-associated (PDA) clusters (Figure 11B, 11C).

- OPC lineage: we resolved four subgroups, including canonical **OPCs (A, C, D)** and a specific **PDA-OPC** cluster defined by *VCAN, MT3*, and *CD81* (Figure 11C, 11D).
- MOL lineage: among the *OPALIN*-positive cells, we distinguished five subpopulations (**MOL-A, MOL-B, MOL-F**) and two disease-specific states: **PDAO-1** (*DBNDD2*/*FTL*/*HSPA1A*) and **PDAO-2** (*CTNNA2*/*ARHGAP24*). Similarly, the *SLC5A11*-positive fraction contained a specific **PDAO-3** cluster (*ACTN2*/*MT-ND3*) (Figure 11C, 11D).

Interestingly, these transcriptional groups do not appear to represent rigid, separated subtypes. Instead, the data suggest they form a continuous spectrum. This seems to reflect dynamic variations in cellular maturation, metabolic demand, or functional specialization. This continuum is especially evident within the mature oligodendrocyte population, where most subpopulations share canonical markers and are differentiated primarily by the magnitude of gene expression more than by unique, exclusive markers.

Once these transcriptionally distinct subpopulations were identified, we deciphered their molecular identity through differential expression analysis (Figure 11C). PD-enriched clusters, specifically PDAOPCs and the PDAO-1, 2, and 3 populations are defined by a high amount of molecular chaperones. The transcriptomic signature is dominated by the HSP70 and HSP90 families (*HSPA1A,*

HSPB1, HSP90AB1, HSPA1B, HSPA8, HSP90AA1, HSPA5), alongside *CRYAB* and numerous *DNAJ* co-chaperones. This upregulation of proteins related to quality-control machinery suggests that disease-associated oligodendrocytes are engaged in a chronic response to maintain proteostasis against cellular stress (Figure 11C).

Our next question was if the disease reshapes the cellular composition of oligodendroglia in the striatum. Using scCODA, we identified a clear region-specific remodeling. In Pu, we detected a specific increase of stress-associated states (PDAO-1: +5.6%; PDAO-2: +1.5%; PDAO-3: +3.0%; PDA-OPCs: +2.3%) occurring in parallel with a decrease of homeostatic populations (MOL-A: −9.1%; MOL-F: −3.7%) (Figure 11D).

While similar directional trends existed in CN, the statistical significance was only present in Pu. Importantly, when we stratified the analysis by sex, these compositional shifts remained consistent (Supplementary Figure 3). This indicates that the emergence of these stress states is a fundamental feature of the disease pathology, independent of biological sex.

Because the OPALIN-expressing mature oligodendrocytes appeared to be the most altered population with three distinct disease-altered subpopulations, we selected this group for a deeper regulatory analysis. We employed Hotspot co-expression modeling to identify the coordinated gene modules driving these cell states (Supplementary Figure 4). The results reported different biological properties:

- Immature States: Modules 4 (*KCNIP4, RBFOX1*) and 5 (*MDGA2, CNTN1*) marked the early, immature oligodendrocyte populations (immOL-A/B) (Supplementary Figure 4).
- Healthy Homeostasis: in contrast, the healthy MOL-A population was defined by Modules 10 and 14, which are enriched for mitochondrial genes and regulators of cellular morphology (*GRID2, ZFPM2*), reflecting a metabolically active, myelinating state (Supplementary Figure 4).
- Disease Divergence: the disease-associated clusters abandoned these homeostatic programs in favor of distinct pathological modules. PDAO-1 was characterized by Modules 1 and 2, a signature driven by heat shock responses and iron-handling machinery (*CRYAB, FTH1, FTL, HSPA1A*). Conversely, PDAO-2 displayed a radical functional shift towards immunomodulation; it was preferentially associated with Modules 6 and 13, enriched for cytokine signaling and antigen processing genes (*ETV5, QDPR, ARHGAP24, CTNNA2*) (Supplementary Figure 4).

This reveals that disease-associated oligodendrocytes are not a uniform entity, they separate into distinct functional phenotypes, one related to proteostasis/iron stress, and another to an immune role.

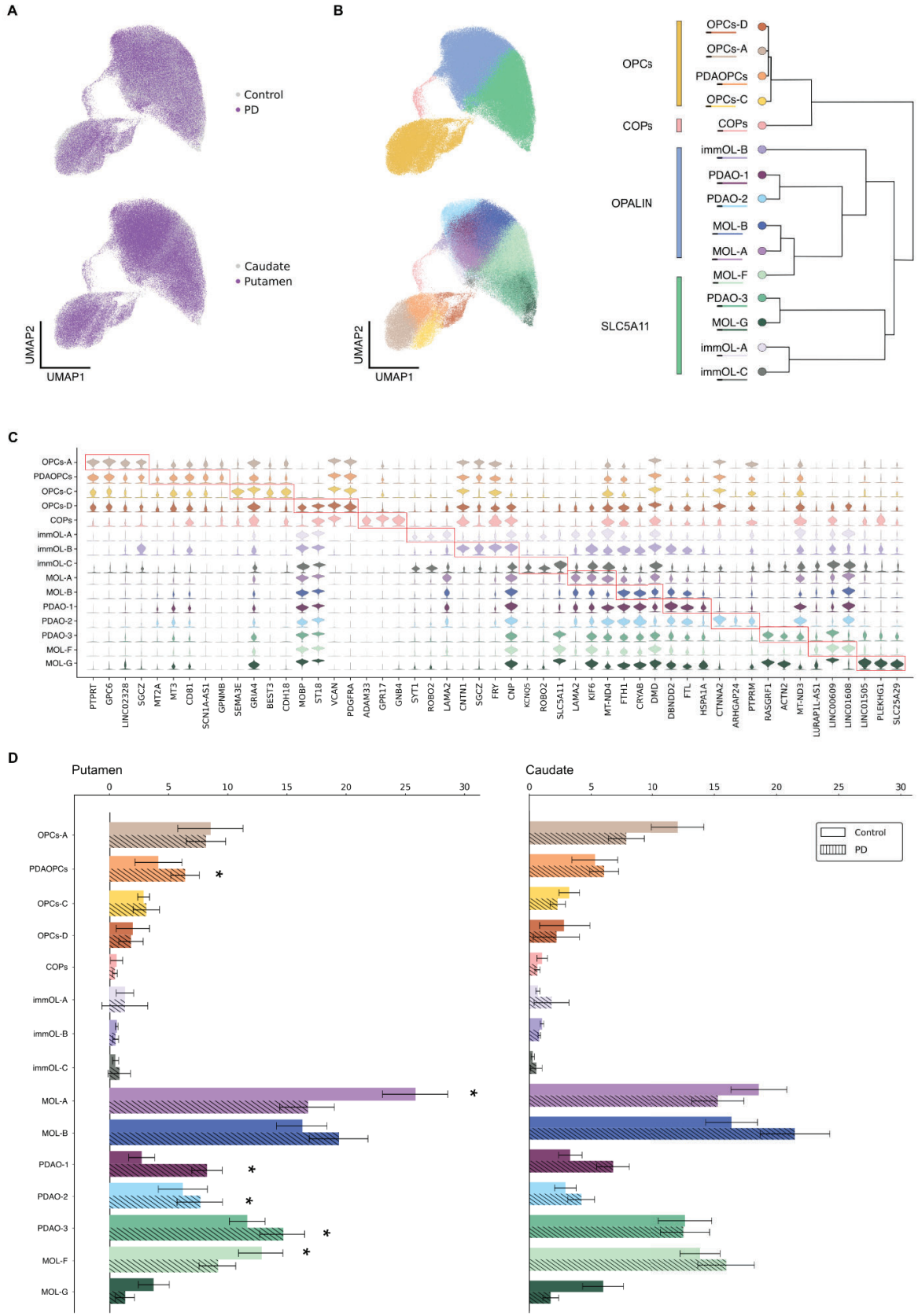
A
Control
PD
Caudate
Putamen
UMAP2
UMAP1
B
UMAP2
UMAP1
OPCs
COPs
OPALIN
SLC5A11
OPCs-D
OPCs-A
PDAOPCs
OPCs-C
COPs
immOL-B
PDAO-1
PDAO-2
MOL-B
MOL-A
MOL-F
PDAO-3
MOL-G
immOL-A
immOL-C
C
OPCs-A
PDAOPCs
OPCs-C
OPCs-D
COPs
immOL-A
immOL-B
immOL-C
MOL-A
MOL-B
PDAO-1
PDAO-2
PDAO-3
MOL-F
MOL-G
PTPRT
GPC6
LINC02328
SGCZ
MT2A
MT3
CD81
SCN1A-AS1
GPNMB
SEMA3E
GRIA4
BEST3
CDH18
MOBP
ST18
VCAN
PDGFRA
ADAM33
GPR17
GNB4
SYT1
ROBO2
LAMA2
CNTN1
SGCZ
FRY
CNP
KCNQ5
ROBO2
SLC5A11
LAMA2
KIF6
MT-ND4
FTH1
CRYAB
DMD
DBNDD2
FTL
HSPA1A
CTNNA2
ARHGAP24
PTPRM
RASGRF1
ACTN2
MT-ND3
LURAP1L-AS1
LINC00609
LINC01608
LINC01505
PLEKHG1
SLC25A29
D
Putamen
Caudate
0
5
10
15
20
25
30
Control
PD
OPCs-A
PDAOPCs
OPCs-C
OPCs-D
COPs
immOL-A
immOL-B
immOL-C
MOL-A
MOL-B
PDAO-1
PDAO-2
PDAO-3
MOL-F
MOL-G
*

Figure 11. Quantitative characterization of oligodendrocyte and OPCs subpopulations. A. UMAP projections illustrate a homogeneous distribution of cells from each anatomical region and clinical condition across the identified oligodendroglial populations, indicating that clustering was not driven by region- or condition-specific biases. **B.** Major oligodendrocyte lineage classes, including OPCs, committed oligodendrocyte precursors (COPs), and mature oligodendrocytes subdivided into OPALIN^{+} and SLC5A11^{+} subsets (top left). A higher-resolution UMAP (bottom left) highlights the finer substructure within oligodendrocytes and OPCs, with subpopulations arranged according to transcriptomic similarity. These relationships are further summarized in the accompanying dendrogram (right), which reflects hierarchical clustering based on gene expression correlations. **C.** Stacked violin plots display the expression patterns of representative marker genes across subpopulations, providing a visual overview of lineage-defining and state-specific transcriptional signatures. **D.** Relative abundances of each subpopulation are presented as barplots, calculated as the percentage of total nuclei per condition. Statistically significant compositional changes, as determined by scCODA (posterior probability of inclusion corresponding to a confidence threshold < 0.2), are indicated by asterisks (*).

8.1.3. Functional decoding: from transcriptome to phenotype

Once we established the existence of these stress-associated populations, we next wanted to understand their biological implications. We moved beyond simple gene lists to a comprehensive Gene Set Enrichment Analysis (GSEA), mapping the transcriptional alterations in PD against curated biological repositories (GO, KEGG, Reactome).

The analysis reveals a fundamental "reprogramming" of the oligodendrocyte machinery. In control-enriched populations (like MOL-A), the dominant pathways are constructive: they drive neurogenesis, synaptic organization, and the complex signaling required for lineage differentiation. In contrast, the PD-associated clusters have largely abandoned these supportive functions. Their cellular profile is almost entirely consumed by survival mechanisms, specifically, mitochondrial maintenance and protein homeostasis. We observed a massive upregulation of pathways governing ribosome assembly, translational control, and chaperone-mediated protein folding, often coupled with apoptotic and immune-activation signatures (Figure 12A, 12B).

It is important to understand that dysfunction does not look the same in every cell; we identified distinct states of pathology within the disease-associated clusters:

- **PDAO-1** (stress-related cells): this state is defined by a proteostatic persistence. It is characterized by intense activity in protein modification and cell cycle regulation pathways, suggesting a cell overwhelmed by misfolded proteins and struggling to maintain viability.
- **PDAO-2** (immune-related cells): here, the shift is immunological. These cells display a robust enrichment for innate immune mechanisms and apoptotic signaling, particularly pathways mediated by DAP12 and interferons. They appear to have effectively transitioned from a myelinating cell to a quasi-immune effector.

- **PDAO-3** (metabolic-compromised cells): this population exhibits a distinct metabolic profile, heavily engaged in lipid/steroid synthesis and organelle stress responses, diverting energy away from myelin maintenance.

Even the progenitor pool is affected. While healthy OPCs-A are wired for synaptic modulation and neural circuit integration, the **PDAOPCs** show signatures of adaptive immune engagement and antigen receptor signaling. This suggests that in the PD striatum, progenitors are being recruited into immune surveillance roles rather than repairing tissue (Figure 12A, 12B).

Finally, we asked if these transcriptomic alterations translate into physical tissue damage. We quantified Myelin Basic Protein (MBP) immunoreactivity in CN and Pu to serve as a sign of structural integrity (Figure 12C).

The data confirmed that in Pu, PD tissue exhibits a significant reduction in MBP signal compared to controls ($p = 0.047$) (Figure 12D). More importantly, this loss is not random. We found a direct, inverse correlation between myelin levels and the cellular composition of the tissue. As the ratio of stress-states (PDAO-1 and PDAO-2) rises and the proportion of healthy homeostatic cells (MOL-A) falls, myelin density collapses (Figure 12E, 12F). This provides a mechanistic bridge between the molecular data and the clinical reality: the emergence of these stress-responsive states is directly linked to the physical demyelination of the striatum.

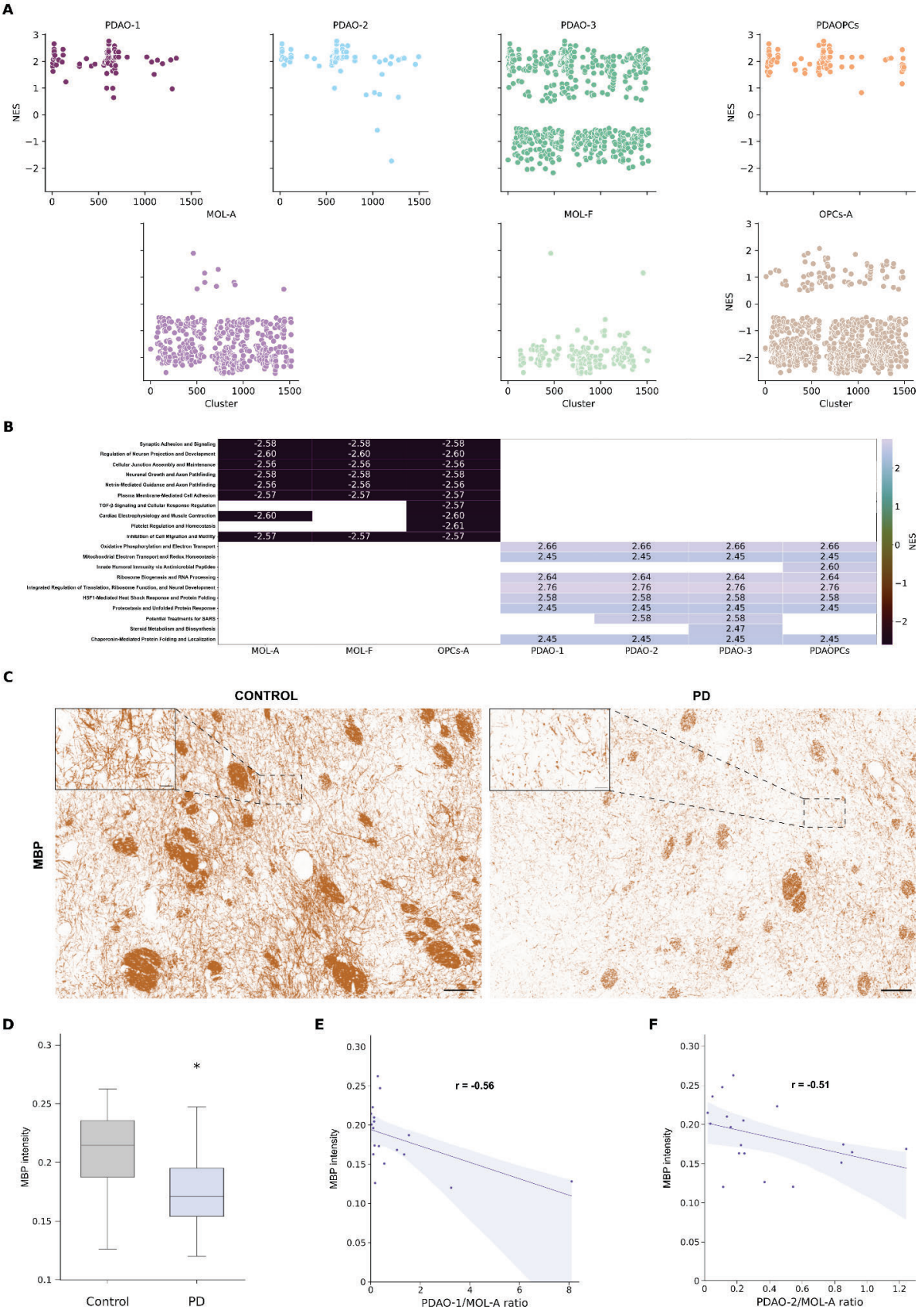

Figure 12. Gene set enrichment profiling and MBP expression in PD-associated oligodendroglial subpopulations. A. Gene Set Enrichment Analysis (GSEA) was performed to characterize pathway-level alterations in oligodendrocyte lineage

subpopulations associated with PD. For each comparison (PDAO-1 vs MOL-A, PDAO-2 vs MOL-A, PDAO-3 vs MOL-F, and PDAOPCs vs OPCs-A), normalized enrichment scores (NES) were calculated and organized according to the cell type in which pathways were upregulated. Dot plots display the NES values for significantly enriched superpathways within each comparison. Only pathways meeting stringent criteria (false discovery rate, FDR < 0.05; absolute NES > 0.5) were retained for visualization and interpretation. **B.** To provide a global overview of enrichment patterns across subpopulations, we generated a heatmap summarizing the top 20 GSEA-derived superpathways, including the 10 most positively and 10 most negatively enriched gene sets ranked by NES magnitude. In this representation, rows correspond to superpathways and columns to the oligodendroglial subpopulations under study. Each cell reflects the NES value for a given pathway-subpopulation pair, with the color scale indicating the direction and strength of enrichment. **C.** To evaluate whether these transcriptional changes were accompanied by alterations at the protein level, we performed immunohistochemical staining for myelin basic protein (MBP) in Pu from control and PD cases. Representative low-magnification images (scale bar: 100 μm) and higher-magnification insets (scale bar: 20 μm) are shown. **D.** Quantitative analysis revealed a modest but statistically significant reduction in MBP expression in PD compared to controls ($p = 0.047$, $t = 2.11$), as illustrated in the corresponding boxplots. **E, F.** Finally, we explored the relationship between disease-associated oligodendrocyte subpopulations and MBP levels. A negative correlation was observed between the PDAO-1/MOL-A ratio and MBP expression ($r = -0.56$, $p = 0.02$), as well as between the PDAO-2/MOL-A ratio and MBP expression ($r = -0.51$, $p = 0.02$).

8.1.4. Oligodendrocyte differentiation trajectory and PD-associated alterations

To understand how the disease alters cellular fate, we first had to establish the baseline in healthy populations. By computationally excluding the disease-specific clusters, we used trajectory inference algorithms (VIA and Slingshot) to map the standard developmental process of striatal oligodendrocytes.

This analysis defined the canonical trajectory as a linear progression: it initiates with the OPC-A progenitor, transitions through a committed intermediate (COP), and follows into the myelinating MOL-A and MOL-B states. These stages are molecularly defined by the upregulation of adhesion factors like *LAMA2*. The trajectory reaches its terminus at MOL-F, a highly specialized population dedicated to the cholesterol biosynthesis required for the maintenance of the mature myelin sheath (Figure 13A).

However, the data also unveiled a previously uncharacterized, alternative lineage branch (Supplementary Figure 5). In this parallel pathway, OPC-D progenitors appear to bypass the standard sequence, transitioning through an intermediate immOL-C state that connects directly to MOL-E. This suggests the existence of a secondary, perhaps accelerated, maturation route that operates alongside the primary lineage (Figure 13A)

When we integrated the PD-enriched populations into this model, the distortions in the landscape became evident. The pathology does not only arrest development, it actively deviates cells from their healthy trajectories into maladaptive states (Figure 13B, 13C).

- Mid-Stage Interruption: the stress-responsive PDAO-1 cluster appears to branch directly from MOL-A. This implies a critical failure point where cells meant to progress to full maturity (MOL-B/F) are instead driven into a dysfunctional, stress-response phenotype (Figure 13B, 13C).

- Terminal Instability: PDAO-3 traces its origins to MOL-F, suggesting that even fully mature, metabolically active oligodendrocytes are destabilized by the disease environment (Figure 13B, 13C).

- Early Compromise: most critically, the PDAOPC cluster maps back to the earliest OPC-A progenitors. This indicates that the pathological insult impacts the lineage at its very root, compromising the progenitor pool before differentiation even begins (Figure 13B, 13C).

To decipher the mechanics of this failure, we applied pseudotime-ordered factor analysis. In the healthy context, the maturation profile is driven by a tightly coordinated program of lipid metabolism and cell-cell adhesion genes, including *LAMA4*, *MOBP*, and *ERBB4* (Figure 13A).

In the PD-altered trajectories, this coordination collapses. The analysis reveals that the transition into disease-associated states (PDAOs) is driven by the specific dysregulation of these key genetic programs. Rather than sustaining the metabolic requirements of myelination, the transcriptional machinery is reoriented, providing a mechanistic explanation for why these cells fail to mature and instead accumulate in the vulnerable, non-functional states observed in the patient striatum (Figure 13C).

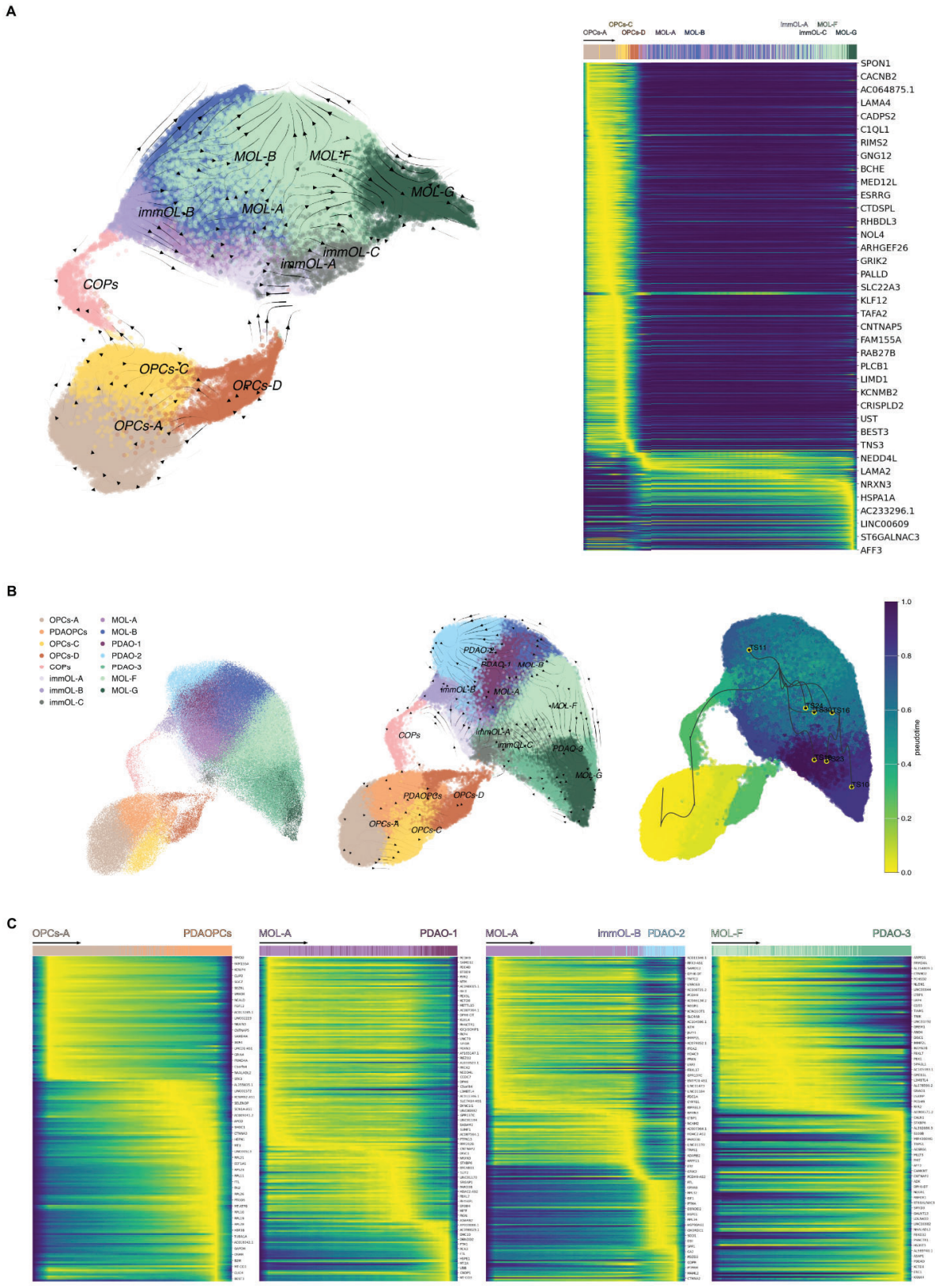

Figure 13. Pseudotemporal reconstruction of oligodendrocyte differentiation and divergent trajectories in Parkinson's disease. A. Pseudotime analysis was first performed on canonical oligodendrocyte lineage populations, excluding PD-enriched clusters to avoid bias in trajectory inference. The resulting UMAP representation delineates a

continuous differentiation trajectory from oligodendrocyte precursor cells (OPCs), through COPs/OPCs-D and immature oligodendrocytes (immOLs), and progressing toward mature states ranging from MOL-A to MOL-G (left). Directional arrows indicate the inferred progression along pseudotime. A corresponding heatmap (right) shows the expression dynamics of representative genes across pseudotime, highlighting stage-specific transcriptional programs associated with oligodendrocyte maturation. **B.** PD-associated subpopulations were subsequently incorporated to assess their alignment with the physiological trajectory. Pseudotime mapping indicates convergence at the MOL-A state, from which the trajectory diverges into two distinct branches corresponding to the PDAO-1 and PDAO-2 populations. **C.** A schematic summary integrates these findings, outlining the inferred differentiation hierarchy and the emergence of PD-associated oligodendroglial states, together with representative gene programs associated with each segment of the trajectory.

8.1.5. Collapse of the signaling infrastructure

To determine if the disease pathology disrupts the integration of oligodendrocytes within the striatal circuit, we employed CellChat to reconstruct the intercellular communication networks. This analysis infers directional signaling based on ligand-receptor expression profiles, allowing us to evaluate both the sending and reception capabilities of each cell state.

The data reveal a profound remodeling of these networks. The most striking feature is a collapse of the structural signaling in disease-associated populations. Specifically, the PDAO-1 cluster appears to become functionally isolated. When compared to the healthy MOL-A population, which serves as the primary anchor for extracellular matrix (ECM) and adhesion signaling, PDAO-1 cells exhibit a drastic downregulation of critical adhesion genes, including *NCAM*, *CADM*, laminins, and *CDH1* (Figure 14A, 14B). This is not a minor perturbation; markers like *NCAM* and *CDH1* were effectively undetectable in this group. Consequently, the outgoing signals required for myelination (particularly *LAMA2*-mediated laminin signaling) are affected in both PDAO-1 and PDAO-2. This implies an important adhesion deficit, suggesting these cells physically disconnect from the axonal unit and the surrounding matrix (Figure 14A, 14B).

While PDAO-1 disconnects, other populations adopt alternative signaling strategies. The PDAO-3 and MOL-G clusters (within the SLC5A11+ class) display an enriched capacity for cholesterol-related signaling. This aligns with the metabolic/biosynthetic profile we identified earlier, suggesting these cells are attempting to compensate for the crisis through altered lipid trafficking (*LAMA4*, *MOBP*, and *ERBB4*) (Figure 14A, 14B).

Conversely, the progenitor pool appears compromised from the start. PDAOPCs population displayed the lowest overall signaling capacity of any progenitor group, indicating that signaling deficits are not merely a late-stage consequence of degeneration but are imprinted early in the lineage (Figure 14A, 14B).

Finally, we examined how these cells are tuned for neuronal activity. We observed an enrichment of glutamatergic signaling components within the OPC compartment, a trend that was most exaggerated in the PDAOPCs (Figure 14C).

This prompted a focused analysis of neurotransmitter receptor expression across the lineage. While the major distinctions lay between progenitors and mature cells, we identified specific, dysregulated receptor profiles in the disease states. The PDAO-2 cluster, for instance, showed a strong, selective upregulation of *CHRNA10* and *GABRG1*, while both PDAO-1 and PDAO-2 exhibited significant overexpression of *GABRR2* (Figure 14C). This suggests that disease-associated oligodendrocytes do not just lose function; they acquire aberrant sensitivity to neurotransmitters. This dysregulated communication likely contributes to the disruption of the precise glia-neuron crosstalk required to maintain striatal neural circuitry.

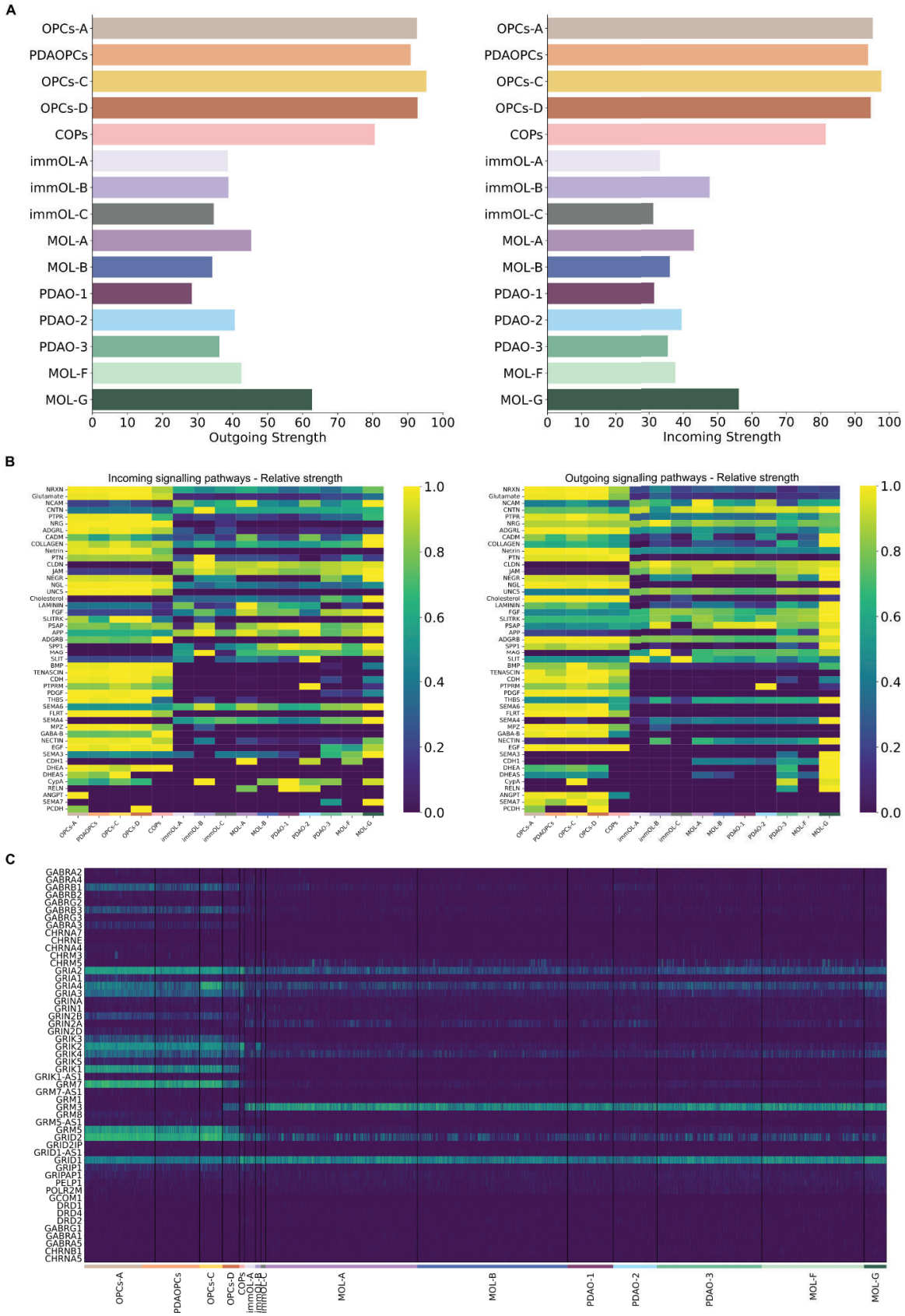

Figure 14. Altered intercellular signaling and neurotransmitter-related signatures in PD-associated oligodendrocytes. **A.** Barplots summarizing ligand-receptor interactions, quantifying both outgoing (ligand-driven) and incoming

(receptor-mediated) signaling strengths for each oligodendroglial subpopulation, representing a relative communication activity across populations. **B.** Representation of pathway-level signaling by estimating the relative strength of individual communication routes within each subpopulation. **C.** Expression of genes linked to neurotransmitter-related processes. A heatmap displays markers detected in at least 50 cells within any given population, enabling robust comparison across subtypes.

8.1.6. Spatial validation

To test the stress response in our single-nucleus taxonomy, we moved from dissociated nuclei to tissue. We applied spatial transcriptomics to map the anatomical distribution of over 435,000 oligodendroglial cells within the striatum. Using the cell2location framework, we projected our snRNA-seq annotations onto this spatial map (Figure 15A). The results confirmed the accuracy of our original classification: every single lineage subpopulation identified in the dissociated dataset was detected in the spatial data, preserving its distinct molecular identity across both CN and Pu (Figure 15A).

The spatial organization of these cells proved to be highly structured. Neighborhood enrichment analysis revealed that specific populations do not exist in isolation but form distinct cellular communities. We found that PDAO-1, PDAO-3, MOL-F, and MOL-G frequently co-occur in the same tissue niches (Figure 15B). Notably, these clusters showed a preferential localization to the white matter (WM) tracts crossing the striatum, suggesting that the pathology is also related to these structures (Figure 15C).

To understand the molecular base driving these spatial patterns, we used Hotspot co-expression analysis. This revealed a fundamental functional antagonism in the PD tissue (Figure 15D:

- **HSPR Module:** We defined a tight cluster of stress-response genes, including *HSPA1A*, *DNAJA1*, *HSP90AB1*, and *CRYAB*. In PD samples, this module is aggressively upregulated, tracking perfectly with the location of the disease-associated oligodendrocytes (PDAOs) (Figure 15D, 15E).

- **Myelination Module**: conversely, the gene program responsible for myelin stability (driven by *MAG*, *MOBP*, and *CNTN2*) is significantly suppressed (Figure 15D).

The most critical insight from this analysis is the inverse relationship between these two modules. In the PD striatum, we observe a reciprocal regulation: as the stress response (HSPR) increases, the myelination signal collapses (Figure 15D, 15E). This points to a severe functional trade-off. It appears that oligodendrocytes are forced to redirect their limited cellular resources toward managing acute proteotoxic stress, effectively sacrificing their primary function (myelin maintenance), to ensure

short-term survival. These alterations represent a potent mechanism driving the progressive myelin loss observed in PD.

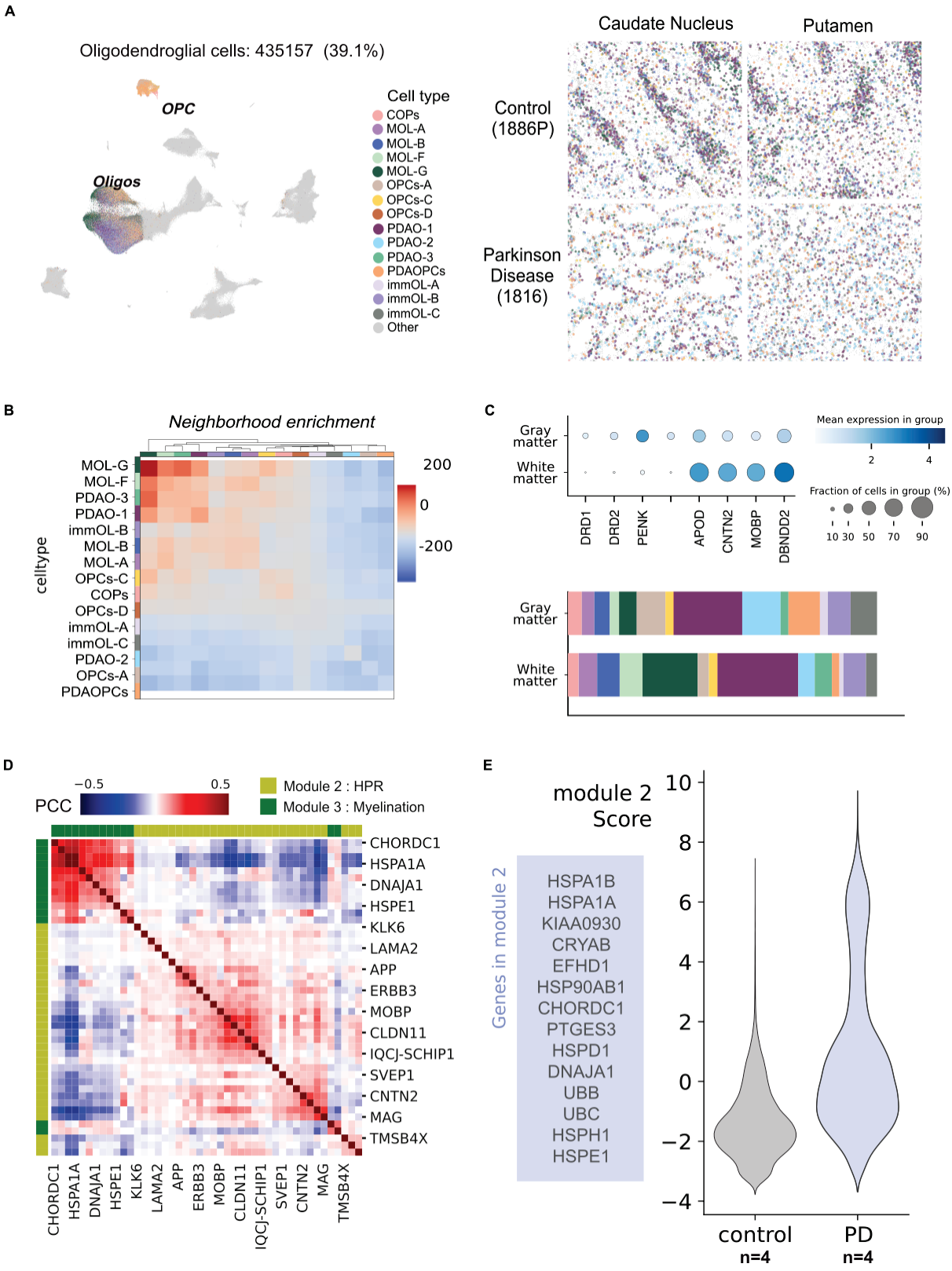

Figure 15. A. UMAP representation of oligodendrocyte populations profiled using spatial transcriptomics, aligned with the subpopulations previously defined by snRNA-seq analysis (left). Spatial maps display the anatomical distribution of these oligodendrocyte subtypes across CN and Pu (right). **B.** A heatmap illustrates neighborhood enrichment scores for all identified subpopulations, providing an overview of spatial proximity and co-localization patterns. **C.** Spatial localization of oligodendrocyte subtypes within gray matter (GM) and white matter (WM) regions is shown. GM and WM areas were defined according to regional marker expression (top). Bar plots summarize the proportional distribution of oligodendroglial subpopulations within GM and WM compartments (bottom). **D.** A heatmap depicts the spatial distribution of gene expression modules, including module 2 (heat shock protein response, HSPR) and module 3 (myelination), across the analyzed regions. **E.** Violin plots display the expression levels of the HSPR module in control and PD samples.

8.2. Astrocyte heterogeneity and disease-associated states in Parkinson's Disease

8.2.1. Cellular heterogeneity of astrocytes and SVZ-derived populations in the human dorsal striatum

Our next goal was to understand transcriptomic changes in Astrocytes in PD. Single cell analysis reported 47.464 cells related to Astrocytes after quality control. These cells were distributed in six different subpopulations (Figure 16A).

The largest group we identified was Astrocytes 0 (**A0**). This subpopulation, defined by markers such as *CABLES1*, *RERG* and *CACNA1A*, represents a homeostatic phenotype found mostly in gray matter (Figure 16A-C). This population showed strong expression of genes related to astrocyte identity and synaptic maintenance, including *SLC7A10*, *HES4*, *HES5*, and *WIF1*. In addition, A0 astrocytes were rich in glutamate transporters (*SLC1A2*) and perisynaptic adhesion molecules (*GPC5*, *NRXN1*), suggesting they are actively involved in neurotransmitter clearance and the stabilization of neuron-astrocyte interactions (Figure 16A, 16E).

Then, this homeostatic perspective changed in PD to two distinct reactive populations in the gray matter, named AR1 and AR2 in this study (Figure 16A). Although both populations are reactive, they follow very different molecular programs:

- **AR1**. Marked by the expression of *CRYAB*, *FTH1*, and *HSPA4L*, shows a high relationship with proteostasis and oxidative stress. We observed high expression of heat shock protein genes and unfolded protein response related genes (*HSPA1A*, *HSP90AA1*, *CRYAB*, *DDIT3*, *HSPD1*). Additionally, AR1 expressed genes like *ANGPT12*, *MMP24*, *SLC13A4*, *PROCR*, and *SELENOM*, suggesting a role in neurovascular remodeling, tissue restructuring and anti-regenerative WNT-related processes (Figure 16E).

- **AR2**. In contrast to AR1, AR2 is characterized by *CHI3L1*, *FN1* and *SOD2* expression, showing a metabolic shift toward hypoxia-associated pathways and reactive astrogliosis (*HILPDA*, *ANGPTL4, CEBPD, JUNB, CEBPB*). Their profile is associated with metal handling (*MTs* and *FTL*) and mitochondrial metabolism (*NDUF* and *COX* family genes). Moreover, these cells express inflammatory and tissue remodeling genes like *APOE, APOC1, IRF1, IRF7, CCND2, FN1*, and *IL13RA1* (Figure 16E).

Apart from these populations enriched in grey matter, we identified two populations increased in white matter regions:

- White Matter Astrocytes (**WMAs**): these cells (*RGS6*, *LGR5*, *LUZP2*) were enriched for biological roles involved in solute transport and metabolic regulation (*SLC14A1*, *FKBP5*, *PDK4*). Also, they express signaling and adhesion-related genes (*NTRK2*, *CDH20*, *CNTN1*), pointing to a role in supporting axonal integrity and maintaining white matter homeostasis.

- Astrocytes Restricted Precursors (**ARP**): this population (*CD44, RYR3, KAZN*) appeared as a hybrid, progenitor-like state. They combined standard astrocyte identity with inflammatory priming and early matrix remodeling. Interestingly, they expressed developmental regulators like *TCF7L1*, *GLIS3*, *DAAM2*, and *BMPR2*, while showing metabolic flexibility through increased glycolytic genes like *PFKFB3*.

Finally, we detected a specific population of Subventricular Zone Cells (**SVZCs**), with specific expression of *ADAMTSL3*, *CCDC85A*, and *FOS*, located in the lateral ventricle (only in CN). These cells expressed programs related to niche organization and neuroblast migration (*ROBO2*, *SEMA3D*, *SPARC*, *ELN*, *DSCAML1*). Their expression of neurogenic commitment genes like *SOX11*, *KIT*, *KITLG*, *SFRP2*, and *NR4A2* confirms their status as progenitor or early neurogenic cells.

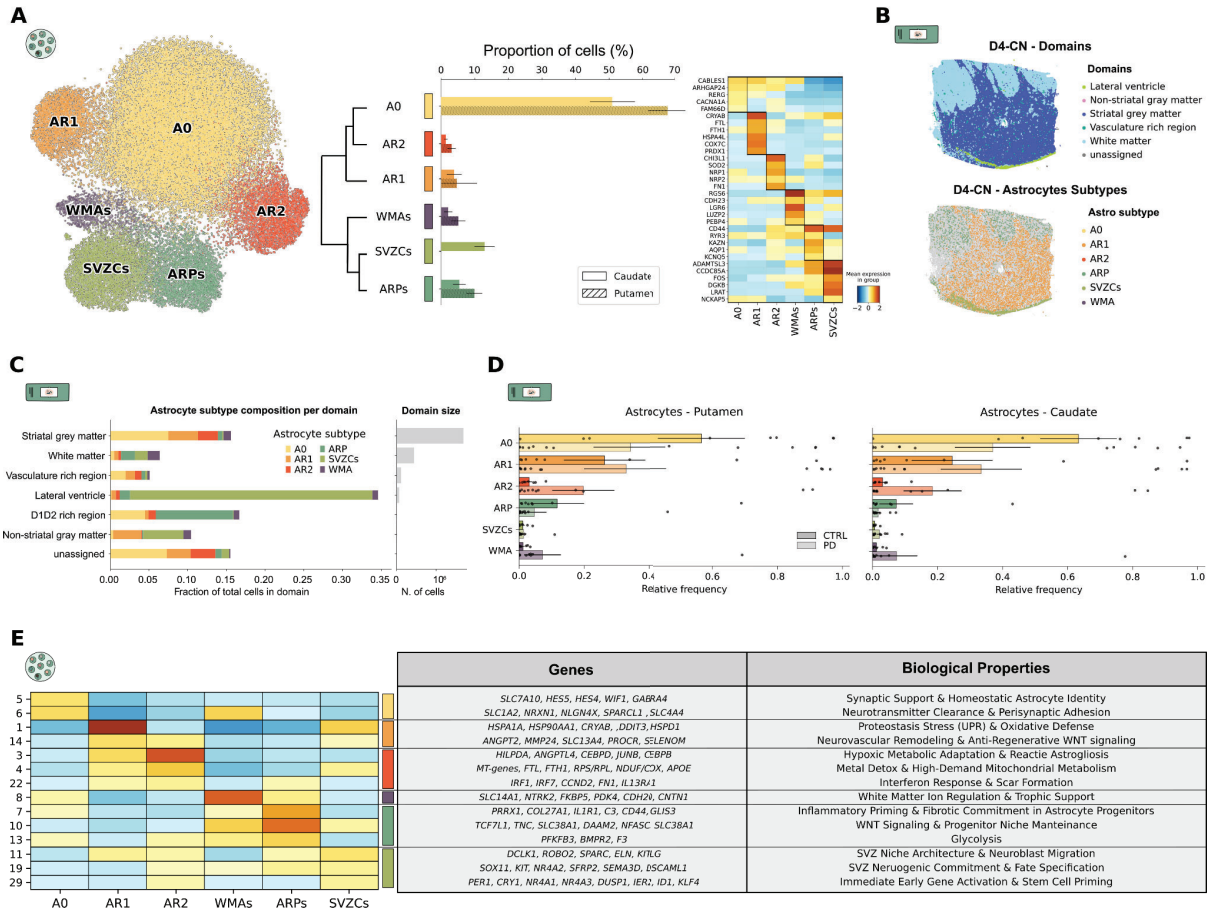

Figure 16. A. UMAP visualization of astrocyte subpopulations and subventricular zone cells (SVZCs) from single-nucleus RNA sequencing data (left). Bar plots summarize the distribution of each subpopulation across the two sequenced brain regions, indicating their relative representation. Distinct gene expression signatures characterize each population (right). **B.** Spatial distribution illustrated by two spatial images colored by domain and subpopulation. **C.** Distribution of frequencies of each astrocytic subpopulation and SVZCs among each domain. **D.** Frequencies of each subpopulation per Condition and Region in spatial transcriptomics data. **E.** Heatmap displaying the expression of selected gene modules across astrocyte and SVZC subpopulations. Rows correspond to individual modules, with representative genes indicated and accompanied by manual annotation of their associated biological functions.

8.2.2. Reactive astrocyte expansion and stress-driven transcriptional reprogramming in PD

We next explored how PD influences the distribution of astrocyte states within the striatum. To quantify shifts in astrocytic subpopulations' composition, we transformed the data with compositional log-ratio and applied MWU test in snRNA-seq data across CN and Pu. In these subpopulations, a consistent pattern emerged. Reactive populations AR1 and AR2 tended to be more abundant in PD samples in both regions (Figure 17D, 17F, 17G). However, only the increase of AR1 in Pu reached statistical significance. In parallel, the homeostatic A0 population showed a relative decline in PD in both CN and Pu, with a significant reduction observed in CN (Figure 17D, 17F, 17G).

To understand how PD reshapes astrocyte biology at the transcriptional level, we performed differential expression analysis comparing astrocytes from PD donors with those from control individuals. We then overlaid the resulting disease-associated gene signatures onto the marker profiles of each astrocyte subpopulation. This integrative approach revealed that PD-related transcriptional changes aligned most strongly with the reactive states AR1 and AR2 (Figure 17F, 17G).

In both CN and Pu, AR1-associated differentially expressed genes (DEGs) reflected a stress-adaptive and proteostatic program. Upregulated transcripts included heat shock proteins (*HSPA1A, DNAJB1*), antioxidant regulators (*PARK7*, *SOD1*), and core astrocytic homeostatic genes (*AQP4, GJA1*) (Figure 17H). This pattern is consistent with a protective, non-inflammatory response aimed at buffering cellular stress while preserving essential astrocytic functions. In contrast, AR2-associated DEGs defined a more overtly inflammatory and metabolically stressed phenotype. These cells exhibited increased expression of immune-related genes (*IFNGR2*, *IL7*), extracellular matrix components and remodeling factors (FN1), metabolic stress mediators (*NAMPT*, *ANGPTL4*, *HILPDA*), and mitochondrial oxidative stress markers such as SOD2 (Figure 17H). These signatures suggest that PD promotes a spectrum of reactive adaptations, ranging from compensatory stress responses to immune-engaged remodeling states.

To further contextualize these findings within established PD-related pathways, we calculated a module score based on genes included in the KEGG Parkinson's disease ontology. This analysis demonstrated a significant enrichment of the KEGG PD signature within the AR1 population in both CN and Pu (Figure 17F, 17G), reinforcing the close association between this stress-responsive astrocyte state and canonical PD molecular pathways.

Finally, using the Xenium spatial transcriptomics data, we assessed whether astrocytic gene expression patterns displayed spatial organization within gray matter. Spatial autocorrelation analysis using Moran's I yielded uniformly low values (<0.2) across genes, indicating limited spatial structuring of astrocyte transcriptional heterogeneity at this scale (Figure 17I). Moreover, no clear differences in spatial organization were observed between PD and control samples. These results suggest that, within the gray matter, astrocytic diversity in PD is driven more by transcriptional state changes than by strong spatial segregation.

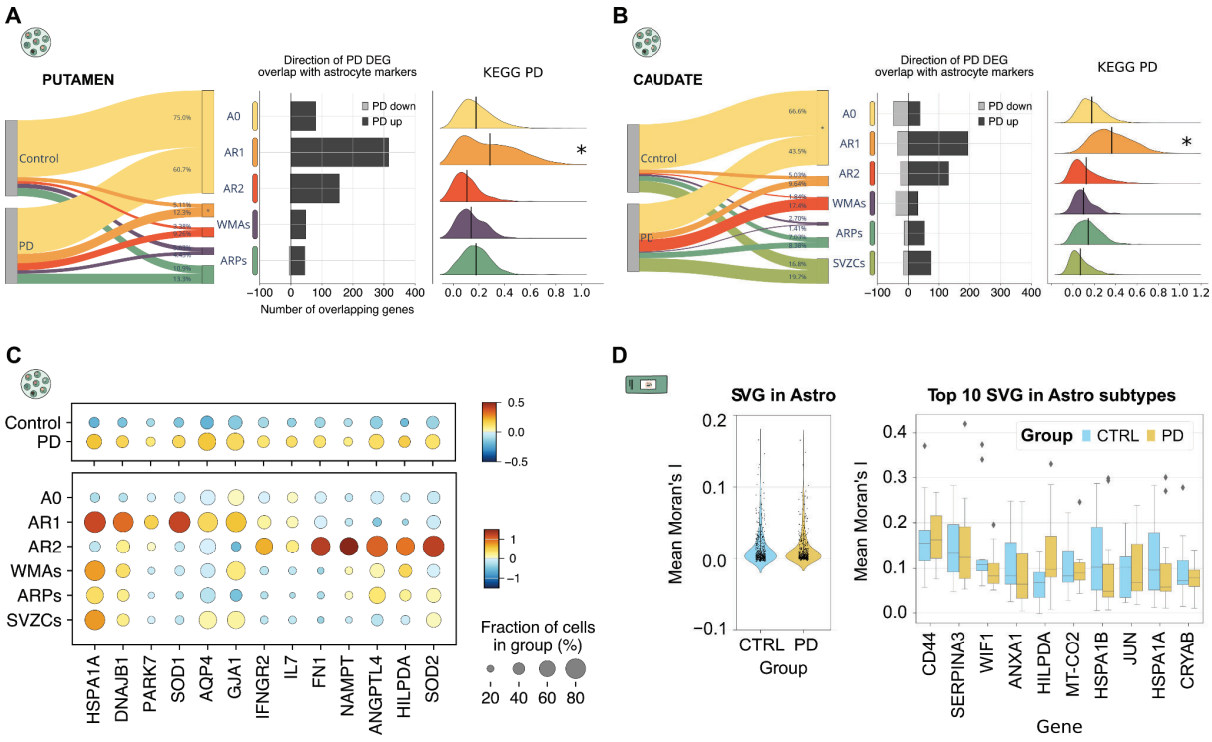

Figure 17. Distribution and transcriptional features of astrocyte subpopulations across conditions. A. Bar plots depicting the relative frequencies of each astrocyte subpopulation by condition in Pu (left). Overlap analysis illustrates the intersection between differentially expressed genes identified between conditions in Pu astrocytes and the marker genes defining each subpopulation (middle). Ridge plots display the expression of genes included in the KEGG Parkinson's disease pathway across astrocyte populations in Pu, with the mean expression for each distribution indicated by a black horizontal bar (right). B**.** Bar plots showing the relative frequencies of astrocyte subpopulations by condition in CN (left). Overlap analysis between condition-specific differentially expressed genes in CN astrocytes and subpopulation marker genes is presented (middle). Ridge plots represent the expression levels of KEGG Parkinson's disease pathway genes across astrocyte subtypes in CN, with mean expression values highlighted by a black horizontal bar (right). **C.** Representation of genes of interest from differential expression analysis and posterior overlap with subpopulations' markers. **D**. Violin plots showing the distribution of mean Moran's I scores across all profiled genes in striatal gray matter astrocytes, stratified by condition (left). Boxplots showing the distribution of mean Moran's I scores for the ten genes with the highest spatial variability, grouped by clinical status (right).

8.2.3. Disease-driven astrocyte state transitions from A0 to AR1 and AR2

Due to the proximity of A0 and AR1/AR2 populations at transcriptomic level, we decided to run a trajectory inference analysis to test if there could exist any progression from A0 to AR1 and/or AR2 because of PD.

Using Slingshot, A0 is demonstrated to have two branches, one to AR1 and one to AR2. Then, we wanted to determine what genes drive this divergence, A0 to AR1 seems to be a fast process in which many genes related to PD are involved. On the other hand, A0 AR2 is a more continuous process, with genes involved in neuroinflammation and stress response (Figure 9).

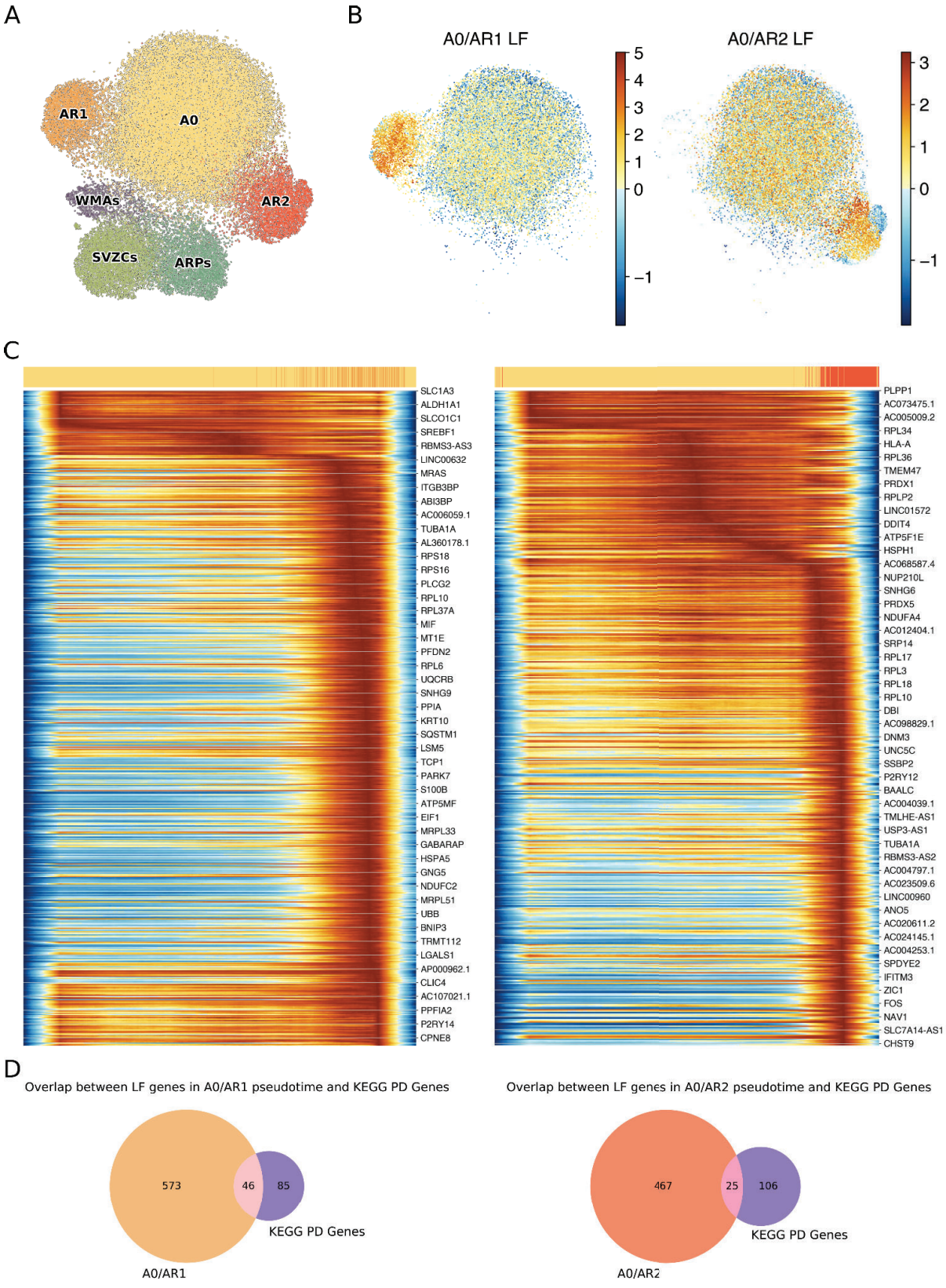

Figure 17. A. UMAP of subpopulations identified in astrocytic class and SVZCs. **B.** UMAPs restricted to A0 and AR1 (left) and A0 and AR2 (right). The colormap represents the divergence on pseudotime of these populations. **C.** Heatmap

representing latent factor genes involved in A0 to AR1 (left) and A0 to AR2 (right) divergences, ordered by pseudotime (top). D. Overlaps between genes from latent factor analysis and KEGG PD genes in A0-AR1 analysis (left) and A0-AR2 (right).

8.3. Microglial activation states and neuroimmune remodeling in the parkinsonian dorsal striatum

8.3.1. Single-nucleus transcriptomics reveals multiple microglial states in the human dorsal striatum

Out of the 270.000 nuclei, 27,601 cells were subsetted and classified as microglia. Clustering of dorsal striatal microglia revealed four transcriptionally distinct subpopulations. The predominant population corresponded to homeostatic microglia (**MH**; *CX3CR1*, *SYNDIG1*, *KCNIP1*), accounting for roughly 70-80% of all microglial cells detected by snRNA-seq (Figure 18A, 18C). These cells exhibited a transcriptional program consistent with continuous environmental surveillance and maintenance of tissue integrity. Canonical homeostatic receptors such as *P2RY12* and *CX3CR1* were robustly expressed, alongside genes involved in cytoskeletal remodeling and process motility (*NAV3*, *DOCK4*, SRGAP3), supporting their dynamic interaction with the surrounding parenchyma. Notably, MH cells also expressed genes associated with synaptic sensing and neuron-glia communication, including *GRIA1-3, GRM5, NRXN1, NLGN1, RYR2*, and *ANK3*. Together with markers of metabolic stability and microglial identity (*IGF1, TET1, MTERF1, COPG2*), this profile is consistent with a population specialized in long-term homeostatic support rather than overt immune activation (Figure 18A, 18E).

The second most abundant cluster corresponded to disease-associated microglia (**DAM**; *FTL, APOE, FTH1*). These cells displayed coordinated activation of stress-response and metabolic pathways, including increased expression of oxidative phosphorylation components (*COX7C, ATP5F1E, NDUFS5*) and proteostasis-related genes (*HSPA5, HSP90B1, DDIT3*), as well as ribosomal proteins (RPL and RPS families), suggestive of elevated biosynthetic demand (Figure 18A, 18E). DAM cells were further characterized by enrichment of phagolysosomal and lipid metabolism programs, with upregulation of lysosomal and debris-clearing genes (*CTSD, CTSL, GPNMB, MERTK, CD9*) and lipid-handling regulators (*APOE, PPARG, MGLL*). Complement components such as *C1QC* were also elevated (Figure 18A, 18E). The convergence of enhanced phagocytic capacity, lipid remodeling, and cellular stress responses (features widely associated with neurodegenerative conditions) supports the classification of this cluster as disease-associated microglia, previously described in the literature in the context of other diseases and brain regions.

A third subpopulation, termed Microglia-1 (**M1**; *TMEM163, SLC11A1, BCL6*), exhibited a distinctly pro-inflammatory transcriptional signature. These cells showed increased expression of cytokine-related genes, including *IL1B, SPP1*, and *OSM*, along with glycolysis-associated transporters such as *SLC2A3* and *SLC2A5*, indicating metabolic reprogramming toward an energetically demanding inflammatory state (Figure 18A, 18E). M1 microglia also expressed transcriptional regulators involved in immune activation and priming (*NFKBIZ, RUNX1, EGR1, IRF8, IKZF2*), as well as myeloid and endocytic markers (*CD14, FCGR3A, BIN1*). The enrichment of extracellular matrix and vascular-interacting genes (*ANGPT2, ECM2, COL6A6, CFTR*) further suggests that this subtype may actively engage with the local vasculature during inflammatory responses (Figure 18A, 18E).

Finally, we identified a microglial population characterized by strong activation of heat shock and proteostasis pathways, referred to here as **MH-HSP**. This state parallels the stress-responsive AR1 astrocyte phenotype. MH-HSP cells exhibited high expression of canonical heat shock and unfolded protein response genes (*HSPA1A, HSPA1B, HSP90AA1, DNAJB1, BAG3, HSPH1*), consistent with activation of HSF1-driven protein quality control mechanisms. In addition, these cells expressed glucocorticoid-responsive and metabolic regulators (*FKBP5, TSC22D3, PDK4, CPT1A*), along with genes involved in immune modulation and stress resolution (*PRDM1, PELI1, SERPINE1*) and autophagy-related pathways (*ULK1, BNIP3L*) (Figure 18A, 18E).

Across most anatomical domains, microglial composition reflected a mixture of these four states. An exception was the lateral ventricle region, which showed a marked enrichment of the MH-HSP subtype. Overall, these findings highlight a structured yet flexible microglial landscape in the striatum, spanning homeostatic surveillance, metabolic activation, inflammatory engagement, and stress adaptation.

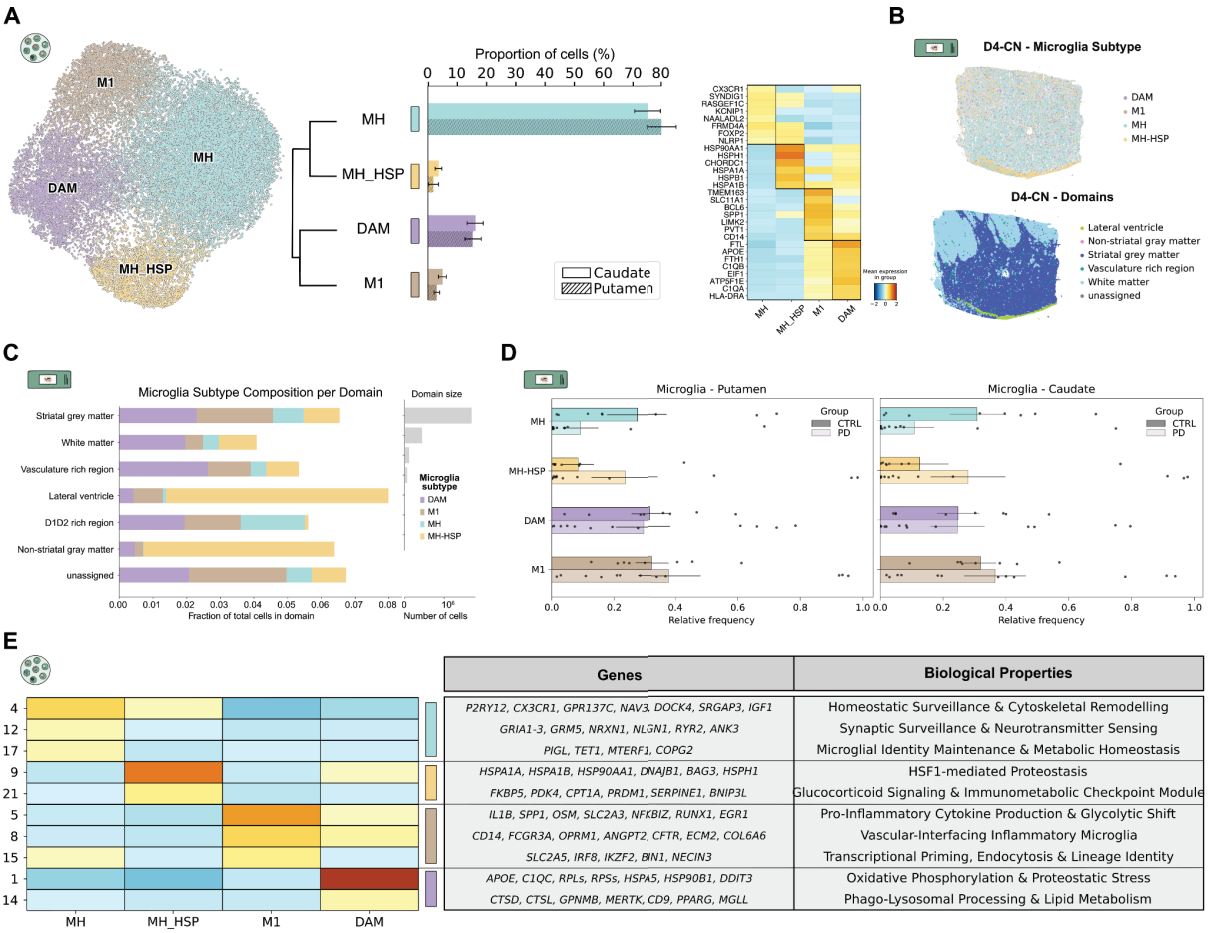

Figure 18. Transcriptomic and spatial characterization of microglia subpopulations. A. UMAP embedding of microglia subpopulations from single-nucleus RNA sequencing data (left). Bar graphs display the relative abundance of each subpopulation across the two analyzed brain regions. Markers for each subpopulation were identified (right). **B.** Spatial maps illustrate the anatomical distribution of these populations within the tissue, shown both by anatomical domain and by assigned subpopulation identity. **C.** For each domain, we represent the frequencies of each subpopulation. **D.** Comparisons between conditions per subpopulation and region. **E.** Heatmap representing the expression patterns of selected gene modules across microglia subtypes. Each row corresponds to a defined module, with representative genes indicated and accompanied by curated annotations describing their associated biological functions.

We next examined whether PD was associated with shifts in microglial composition. Using the snRNA-seq dataset, we compared the relative abundance of each microglial subtype between PD and control samples in both Pu and CN (Figure 19F, 19G). Across regions, PD samples showed a relative enrichment of reactive microglial states (including MH-HSP, M1, and DAM), accompanied by a reduction in the proportion of MH. Compositional proportions indicated that, although the reactive populations tended to increase in PD, these expansions did not reach statistical significance. In contrast, the decline in the MH population was statistically significant in PD in both striatal regions, suggesting a measurable shift away from baseline surveillance states (Figure 19F, 19G). These

tendencies were similar in spatial transcriptomics data, especially in the case of MH decrease and MH-HSP and M1 increase in PD (Figure 19D).

Beyond changes in relative abundance, we sought to determine how PD reshapes microglial gene expression programs. We therefore performed differential expression analysis comparing microglia from PD donors to those from control individuals (Figure 19F, 19G). The resulting PD-associated genes were then intersected with the marker signatures defining each microglial subpopulation, allowing us to assess whether disease-related transcriptional changes preferentially mapped to particular cellular states. This integrative analysis revealed that PD-linked expression patterns were most strongly aligned with the M1 and DAM populations in both Pu and CN (Figure 19F, 19G).

In both regions, PD differentially expressed genes overlapping with M1 population displayed a pronounced inflammatory signature, characterized by elevated *IL1B* and *NFKBIZ* expression (Figure 19F, 19G, 19H). This inflammatory program was accompanied by upregulation of amino acid transporters such as *SLC1A5* and tRNA synthetases including *GARS* and *WARS*, consistent with increased biosynthetic demand during active immune responses (Figure 19F, 19G, 19H). By contrast, the genes associated with PD and DAM were defined by a strong proteostatic and metabolic signature. These cells exhibited increased expression of Hsp70/Hsp90 co-chaperones (*HSPA8, DNAJB6, STIP1*), chaperonin complex components (*CCT3*), mitochondrial transcripts (*MT-ATP6, COX7C*), and vesicle trafficking genes (*CD63, SNAP23*), suggesting that DAM microglia in PD engage in sustained stress adaptation and metabolic remodeling (Figure 19F, 19G, 19H).

To further contextualize these findings within established PD-related pathways, we computed a module score based on genes included in the KEGG Parkinson's disease ontology. This analysis revealed a significant enrichment of the KEGG PD signature specifically within the DAM population in PD samples from both Pu and CN, reinforcing the close association between this microglial state and canonical PD molecular mechanisms (Figure 19F, 19G).

Finally, as observed for astrocytes, spatial autocorrelation analysis of the Xenium spatial transcriptomic data showed uniformly low Moran's I values (<0.2) across profiled genes (Figure 19I). These results indicate that, within the striatal gray matter, microglial transcriptional heterogeneity is not strongly structured by spatial proximity. Instead, disease-related differences appear to be driven primarily by shifts in cellular state rather than by pronounced spatial segregation.

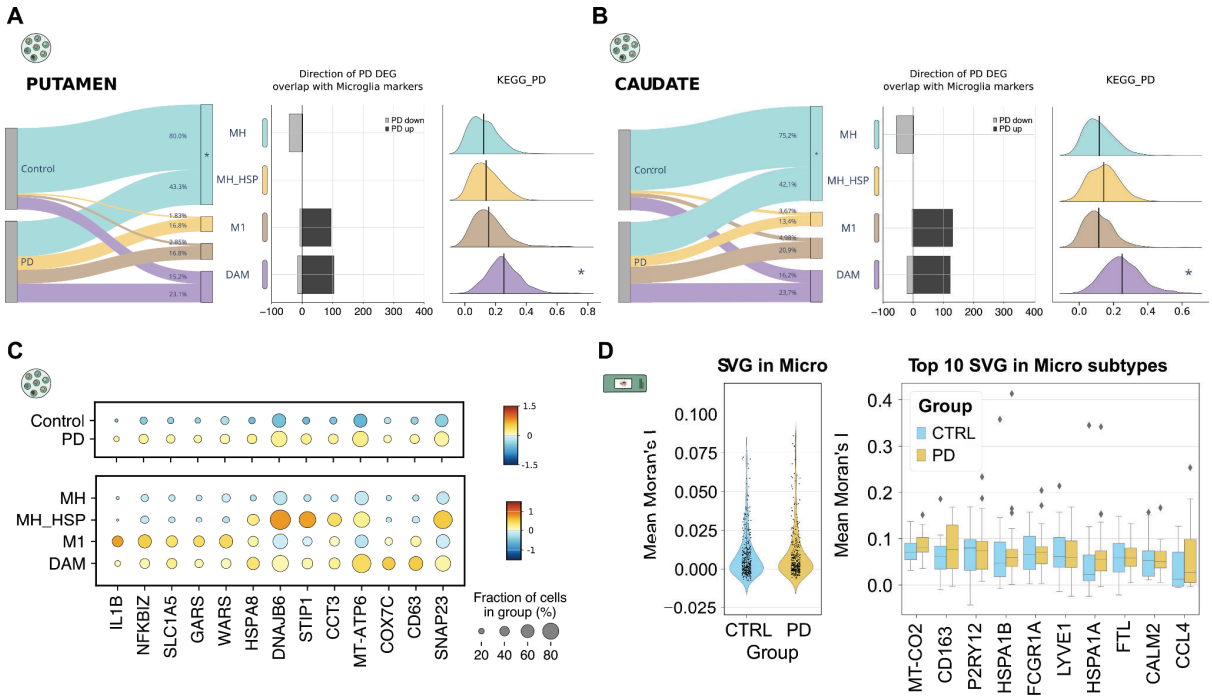

Figure 19. A. Sankey diagram showing the proportional representation of each astrocyte subpopulation stratified by condition in Pu (left). An overlap analysis depicts the intersection between genes differentially expressed across conditions in microglia in Pu and the marker genes that define individual subpopulations (middle). Ridge plots illustrate the expression profiles of genes included in the KEGG Parkinson's disease pathway across microglial populations in Pu; mean expression values for each distribution are indicated by a black vertical line (right). **B.** Bar charts summarizing the relative abundance of microglial subpopulations by condition in CN (left). An overlap diagram presents the shared genes between condition-associated differentially expressed genes in CN microglia and subpopulation-specific markers (middle). Ridge plots display the distribution of KEGG Parkinson's disease pathway gene expression across microglial subtypes in CN, with mean expression levels marked by a black horizontal line (right). **C.** Specific genes from DE analysis highlighted with a dotplot, subsetted both by subpopulation and condition. **D**. Violin plots display the mean Moran's I scores for all profiled genes, representing spatial gene expression variability in gray matter microglia, stratified by PD condition (left). This is complemented by a boxplot illustrating the distribution of scores for the top 10 genes with the highest mean Moran's I values, grouped by clinical status (right).

8.4. Braak Lewy Body stage-dependent remodeling and coordinated glial programs in Parkinson's Disease

To better understand how glial states relate to disease severity, we examined their distribution across neuropathological progression as defined by Braak LB staging. Importantly, rather than assuming that PD follows a single, uniform molecular trajectory, this analysis was designed to determine whether distinct glial programs dominate at different levels of pathological burden. This perspective allows the possibility that PD comprises alternative molecular response patterns that vary across individuals and stages (Figure 20A).

Stratification by Braak LB Stage revealed that subpopulations associated with homeostatic and supportive functions (A0, MH, MOL-A, and OPCs-A), were most abundant at Braak 0 and declined progressively with increasing pathology (Figure 20A). These populations are typically linked to synaptic maintenance, immune surveillance, and structural support, and their reduction with advancing stage is consistent with a gradual erosion of baseline glial functions. This decline appears to represent a general feature of disease progression, reflecting the diminishing stability of the homeostatic glial compartment.

Beyond this shared trend, however, the data pointed to the presence of two divergent and largely non-overlapping and non-progressive reactive programs. One program is characterized by inflammatory activation, marked by increased AR2 and M1, particularly at Braak 3 and Braak 5 (Figure 20A). The second program is defined by enrichment of unfolded protein response (UPR) and stress-adaptive signatures, including AR1 astrocytes, MH-HSP microglia, and oligodendroglial populations such as PDAO-1, PDAO-2, and PDAOPCs. Notably, these two programs did not appear to coexist within the same compositional context. At Braak 4, inflammatory populations (AR2 and M1) were proportionally reduced, while UPR-associated states were prominently expanded (Figure 20A). This pattern does not support a simple sequential transition from inflammation to proteostatic stress within the same biological trajectory. Rather, it suggests the existence of distinct molecular response programs in PD, with individual cases preferentially aligning with either a Reactive or a UPR profile. A natural question arising from this observation is whether the two programs simply track with the overall burden of Lewy body pathology. To address this, we examined their correlation with LB density using immunohistochemical measures available for a subset of donors (Supplementary Table 2). None of the PD-associated subpopulations showed a strong positive correlation with LB burden. Only PDAOPCs and AR1 displayed weak and non-significant associations in both Pu ($r = 0.50$, $p = 0.069$ and $r = 0.42$, $p = 0.134$, respectively) and CN ($r = 0.46$, $p = 0.131$ for PDAOPCs) (Supplementary Figure 6). This suggests that the emergence of these reactive programs is not simply a downstream response to local synuclein load, and that other disease-related factors contribute to determining which program a given individual engages.

From this perspective, the stage-specific fluctuations observed across Braak LB stages likely reflect shifts in the relative representation of these alternative response programs across individuals, rather than a uniform temporal progression from one state to another. The apparent decline of AR2 and M1 at Braak 4, for example, is best interpreted in compositional terms: the expansion of UPR-enriched populations reshapes the cellular landscape, making the inflammatory subsets proportionally less visible. Conversely, the reduction of UPR-associated populations at Braak 5 accentuates the relative contribution of inflammatory or residual homeostatic states. Thus, many of the observed “increases”

and “decreases” are related effects emerging from changes in the overall balance of the glial ecosystem.

These findings support a model in which PD is not defined by a single linear glial trajectory, but instead encompasses distinct molecular programs characterized by preferential engagement of either inflammatory (Reactive program) or proteostatic stress responses (UPR program). Braak LB staging, in this context, does not simply chart a chronological sequence of cellular states, but reveals how the relative dominance of these alternative programs varies across the spectrum of neuropathological severity. Although Reactive and UPR programs appear enriched at different Braak LB stages, we do not interpret this as evidence of a linear molecular transition. Braak LB staging captures anatomical progression of pathology, but does not necessarily explain the nature of the glial response. Our data suggest that distinct molecular response programs are preferentially represented in different individuals, and their apparent stage-specific enrichment likely reflects compositional differences across cases rather than a sequential biological switch.

To evaluate whether these molecular programs are associated with specific donor responses, we estimated the frequencies of each subpopulation in each subject analyzed in our snRNAseq study. Based on the presence of AR1 or AR2 we classified our donors in 3 different molecular responses: Reactive (enriched in AR2/M1), UPRhigh (enriched in AR1/MH-HSP), Homeostatic (absence of the previous AR1/AR2 subpopulations) (Figure 20B). As expected, subjects related to Reactive or UPRhigh responses are enriched in Braak 3 and 4 (Figure 20C).

Within the UPR response, UPR-associated subpopulations (AR1, MH-HSP, PDAOPCs, and PDAOs) covaried strongly across samples, suggesting that their activation is not a cell-autonomous event but part of a coordinated, multicellular response (Figure 20B). In fact, in UPR-high samples these subpopulations accounted for nearly all cells of a given type, indicating population-wide rather than scattered activation. When we dissected which of the three canonical UPR branches (IRE1α, ATF6, and PERK) support this response, no single pathway emerged as universally dominant. Instead, the data pointed to cell-type-specific preferences: elevated *MAPK8* in astrocytes, consistent with *IRE1α* engagement, and higher *ATF6* expression in microglia (Supplementary Figure 7), suggesting that different glial cell types may tune their unfolded protein response through partially distinct molecular paths even within the same coordinated program.

On the other hand, the Reactive donor group displayed an internal response. AR2 astrocytes and M1 microglia showed independent but functionally complementary regulatory architectures. M1 microglia were enriched for innate immune effector regulons, including NF-κB, IRF8, STAT2, and BACH1, alongside phagocytic remodeling programs driven by TFEC. AR2 astrocytes, by contrast, scored high

for regulons associated with stress-adapted cellular identity (HES1, RFX4), metabolic adaptation (SREBF1, EPAS1, FOXO1), and an IFN-γ-biased inflammatory response (STAT1, ARID5A) (Supplementary Figure 7). Despite these distinct profiles, both populations covaried strongly across samples (Figure 20B), pointing to a coordinated multicellular program. To explore the mechanism underlying this coordination, we performed cell-cell interaction analysis between AR2 and M1 (Supplementary Figure 7). This revealed prominent crosstalk through the complement-mediated C3-CD81 axis, damage-associated HMGB1-TLR4 signaling, lipid and lysosomal pathways (APOE-ABCA1, PSAP-LRP1/SORT1), and fate-modulating interactions such as SEMA4D-PLXNB1 and CNTN1-NOTCH1. Together, these interactions define a feed-forward astrocyte-microglia network that couples inflammation, metabolic strain, and impaired clearance in the PD striatum

Since many PD-associated DEGs were predominantly expressed in glial subpopulations that were subsequently related to individual donor programs, we asked whether these transcriptional changes reflect group-specific responses or a disease program shared across all PD cases. Thus, we performed cell-type-specific DEA comparing Reactive and UPR programs against homeostatic controls, and then we compared these results with the global PD-versus-control analysis to separate core disease hallmarks from group-specific signatures (Figure 20D).

For every cell type, the number of DEGs identified within each PD-associated donor group (Reactive or UPRhigh) substantially exceeded those found in the global comparison (Figure 20D). Microglia and astrocytes showed the highest transcriptomic alterations, as expected, but important shifts were also observed in oligodendroglia and perivascular macrophages, with many upregulated genes specifically in the UPR-high group. Ependymal cells in the UPR-high group similarly displayed widespread upregulation alongside a broad set of downregulated genes across both donor groups (Figure 20D).

Comparing PD-specific with reactive and UPRhigh DEGs revealed that the majority of PD-associated transcriptional changes are restricted to one donor group rather than shared across both (Figure 20E). In astrocytes, 79.1% (230+113/441) of PD-DE genes were differentially expressed in only one of the two PD-associated programs, with only a small fraction shared across all groups or restricted to PD alone (91 and 7 genes respectively). GSEA confirmed that each gene subset is enriched for distinct molecular functions.

The largest set of PD-DEGs overlapped with the UPR-high donor group. These genes were broadly shared across multiple glial cell types (Figure 20F) and were primarily enriched in cellular survival and transcriptomic repair programs, including UPR activation (Figure 20E). In microglia, this group included genes involved in histidine catabolism, a pathway that can generate antioxidants or histamine

to suppress pro-inflammatory TNF-α production under proteotoxic stress. In oligodendroglia, enrichment for Cajal body protein localization functions pointed toward increased spliceosome assembly, suggesting an attempt to repair transcripts damaged by PD-related stress (Figure 20E).

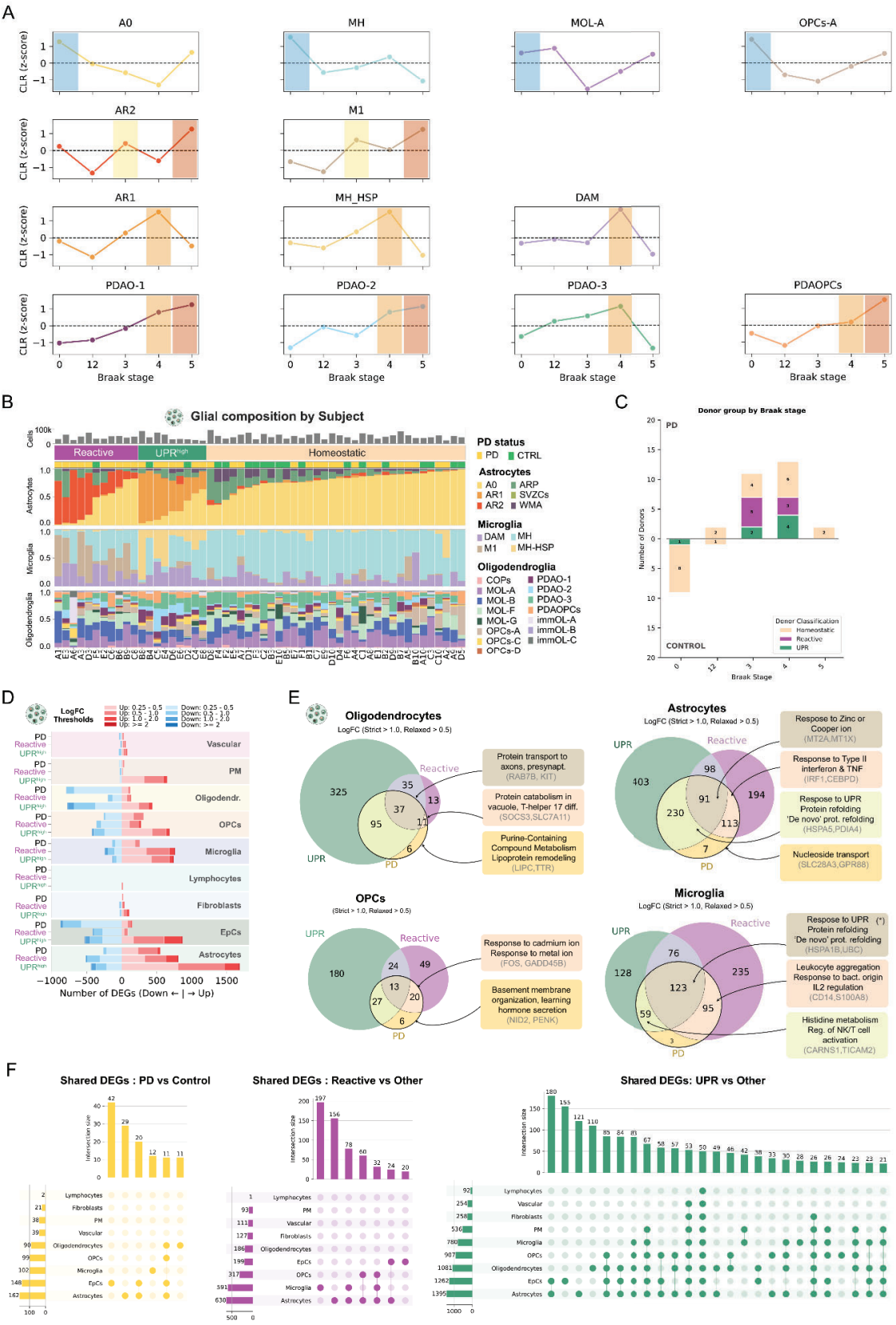
A
A0
MH
MOL-A
OPCs-A
AR2
M1
AR1
MH_HSP
DAM
PDAO-1
PDAO-2
PDAO-3
PDAOPCs
CLR (z-score)
Braak stage
B
Glial composition by Subject
Reactive
UPR^High
Homeostatic
PD status
PD
CTRL
Astrocytes
A0
AR1
AR2
ARP
SVZCs
WMA
Microglia
DAM
M1
MH
MH-HSP
Oligodendroglia
COPs
MOL-A
MOL-B
MOL-F
MOL-G
OPCs-A
OPCs-C
OPCs-D
PDAO-1
PDAO-2
PDAO-3
PDAOPCs
immOL-A
immOL-B
immOL-C
C
Donor group by Braak stage
PD
CONTROL
Number of Donors
Donor Classification
Homeostatic
Reactive
UPR
Braak Stage
D
LogFC Thresholds
Vascular
PM
Oligodendr.
OPCs
Microglia
Lymphocytes
Fibroblasts
EpCs
Astrocytes
Number of DEGs (Down ← | → Up)
E
Oligodendrocytes
LogFC (Strict > 1.0, Relaxed > 0.5)
Protein transport to axons, presynapt. (RAB7B, KIT)
Protein catabolism in vacuole, T-helper 17 diff. (SOCS3,SLC7A11)
Purine-Containing Compound Metabolism Lipoprotein remodeling (LIPC,TTR)
Astrocytes
LogFC (Strict > 1.0, Relaxed > 0.5)
Respose to Zinc or Cooper ion (MT2A,MT1X)
Response to Type II interferon & TNF (IRF1,CEBPD)
Respose to UPR Protein refolding 'De novo' prot. refolding (HSPA5,PDIA4)
Nucleoside transport (SLC28A3,GPR68)
OPCs
(Strict > 1.0, Relaxed > 0.5)
Response to cadmium ion Response to metal ion (FOS, GADD45B)
Basement membrane organization, learning hormone secretion (NID2, PENK)
Microglia
LogFC (Strict > 1.0, Relaxed > 0.5)
Respose to UPR (*) Protein refolding 'De novo' prot. refolding (HSPA1B,UBC)
Leukocyte aggregation Response to bact. origin IL2 regulation (CD14,S100A8)
Histidine metabolism Reg. of NK/T cell activation (CARNS1,TICAM2)
F
Shared DEGs : PD vs Control
Shared DEGs : Reactive vs Other
Shared DEGs: UPR vs Other
Intersection size

Figure 20. A. Lineplots representing the evolution of CLR transformed compositional data per Braak LB stage for each subpopulation, evaluating populations of interest due to relationships in other analyses between Control and PD. **B.** Stacked barplots per subject representing the frequencies of each subpopulation grouped depending on the program they are related to (reactive, UPR, homeostatic). **C.** Stacked histogram, divided in Control (bottom) and PD (top) showing the number of subjects and the response they are associated with in each Braak LB stage. **D.** Stacked bar plots showing the number of upregulated and downregulated differentially expressed genes per cell type across three comparisons: PD versus control, UPR-high versus homeostatic, and Reactive versus homeostatic. Genes were considered significant at adjusted $p < 0.05$ and $|\log_2 FC| > 0.25$, and bars are further stratified by fold-change magnitude. **E.** Venn diagrams illustrate the degree of overlap in differentially expressed genes (DEGs) among PD, UPR-high, and Reactive conditions across major glial populations: oligodendrocytes (top left), OPCs (bottom left), astrocytes (top right), and microglia (bottom right). Key intersections are annotated to indicate enriched pathways and representative genes that characterize these shared transcriptional responses. **F.** Overlap of differentially expressed genes across cell types. Upset plots were used to visualize how differentially expressed genes (both upregulated and downregulated) are shared between cell types under three comparisons: PD versus control (left), UPR-high versus homeostatic states (middle), and Reactive versus homeostatic states (right). To keep the focus on the most meaningful patterns, only gene intersections with more than 10 shared genes are shown.

8.5. Supplementary Information

8.5.1. Supplementary Figures

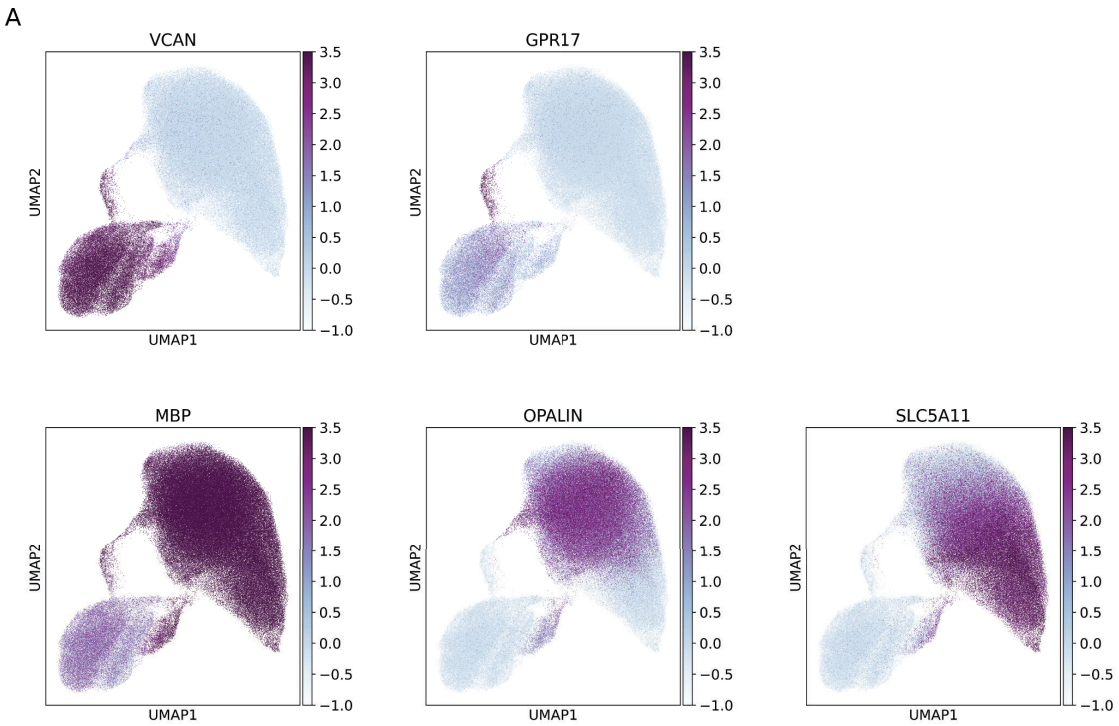

Supplementary Figure 1. Canonical marker genes used to distinguish cell classes within the oligodendroglial lineage. *VCAN* marks OPCs, *GPR17* marks COPs, and *MBP* marks mature oligodendrocytes, which are further subdivided based on the expression of *OPALIN* and *SLC5A11*.

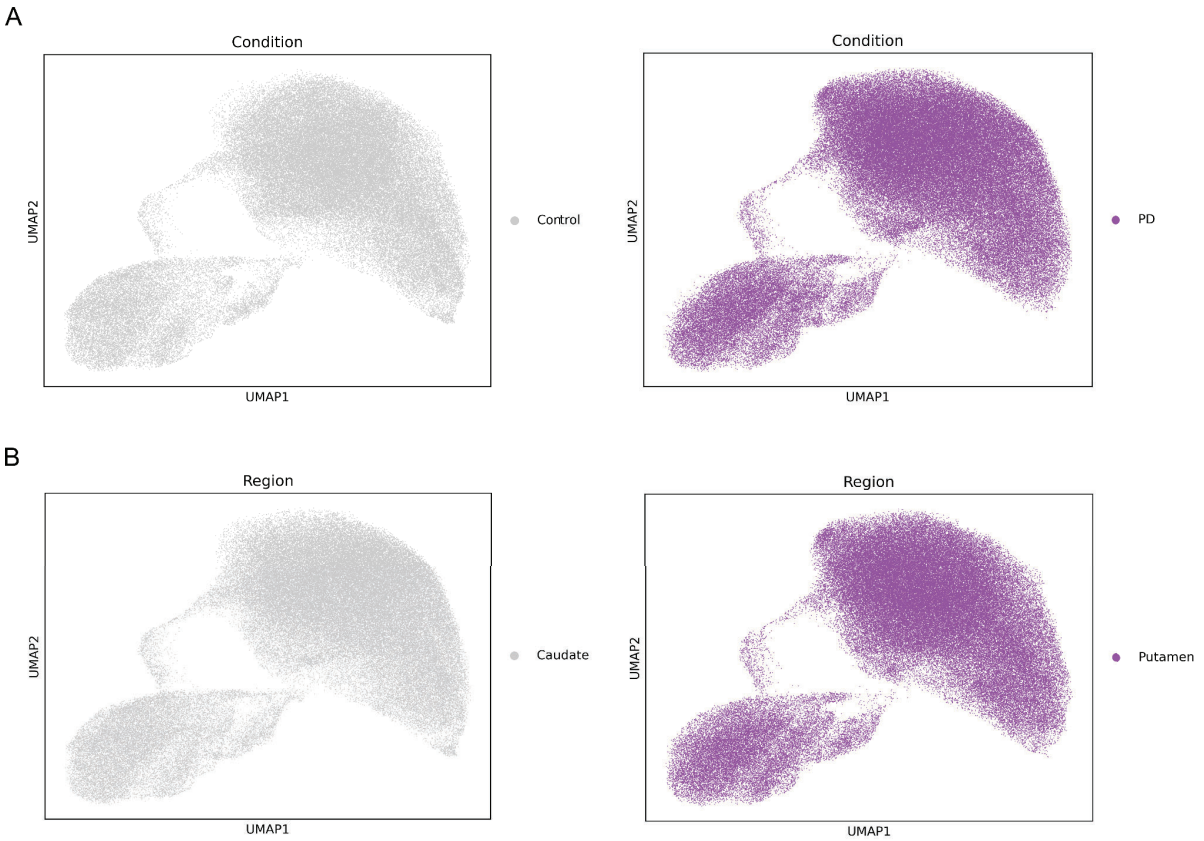

Supplementary Figure 2. UMAP projections illustrate a consistent and well-balanced distribution of cells across both conditions and striatal regions.

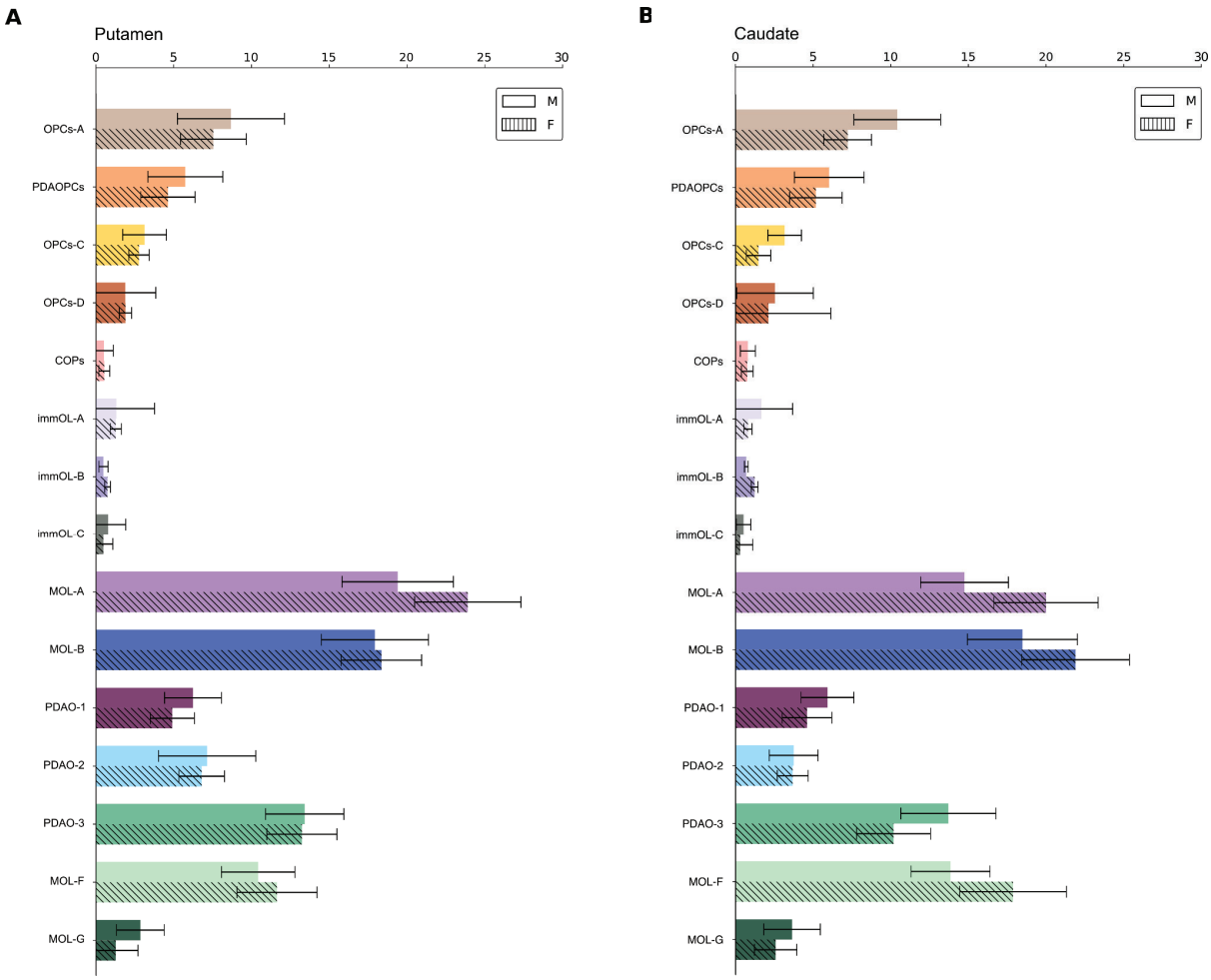

Supplementary Figure 3. Distribution of cell-type frequencies across dorsal striatal regions, stratified by sex.

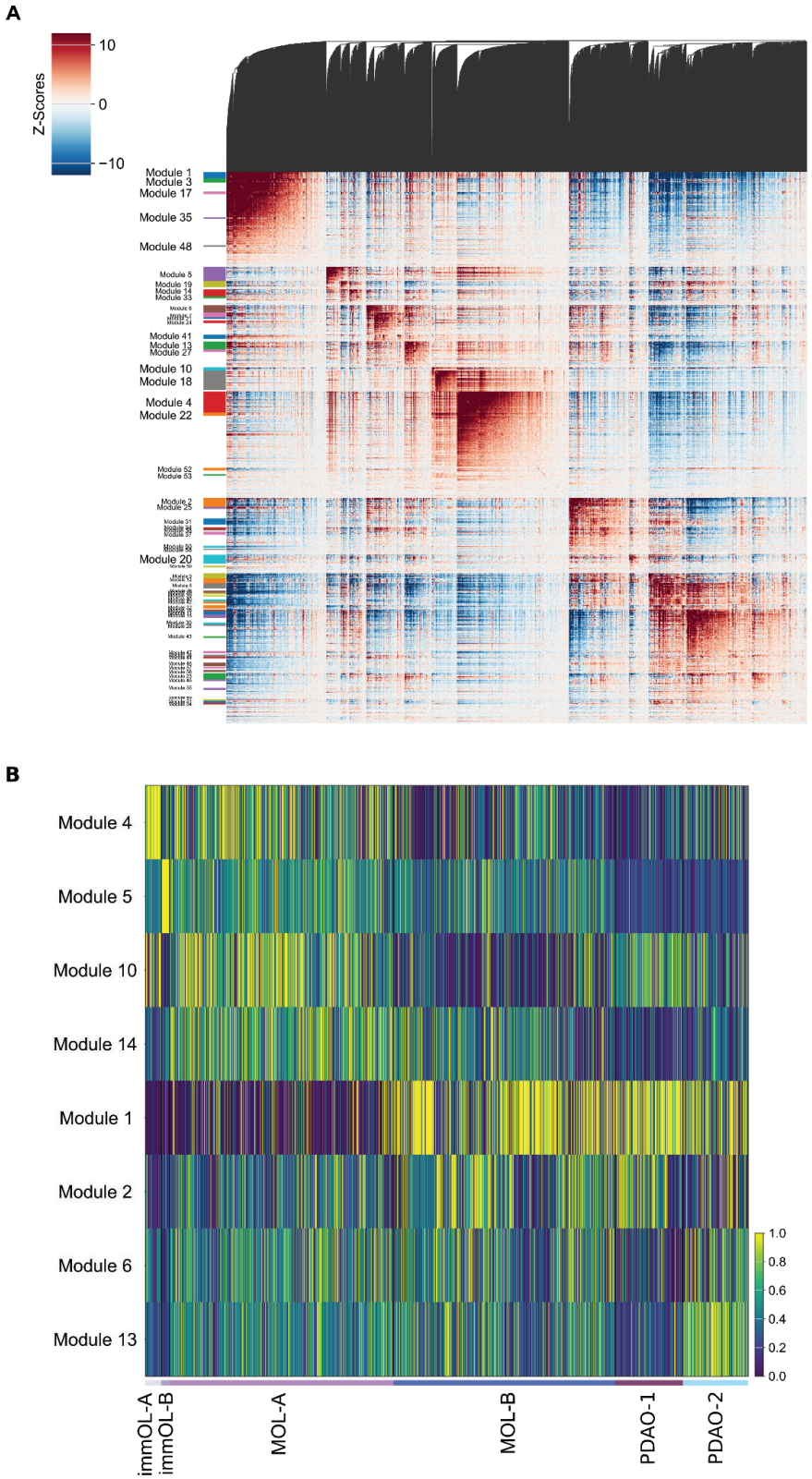

Supplementary Figure 4. A. Heatmap showing gene modules identified through Hotspot analysis, based on patterns of local gene–gene correlations within the dataset. **B.** Heatmap displaying the association between these modules and subpopulation-specific marker genes, highlighting the distinct transcriptional signatures that define each identified cell group.

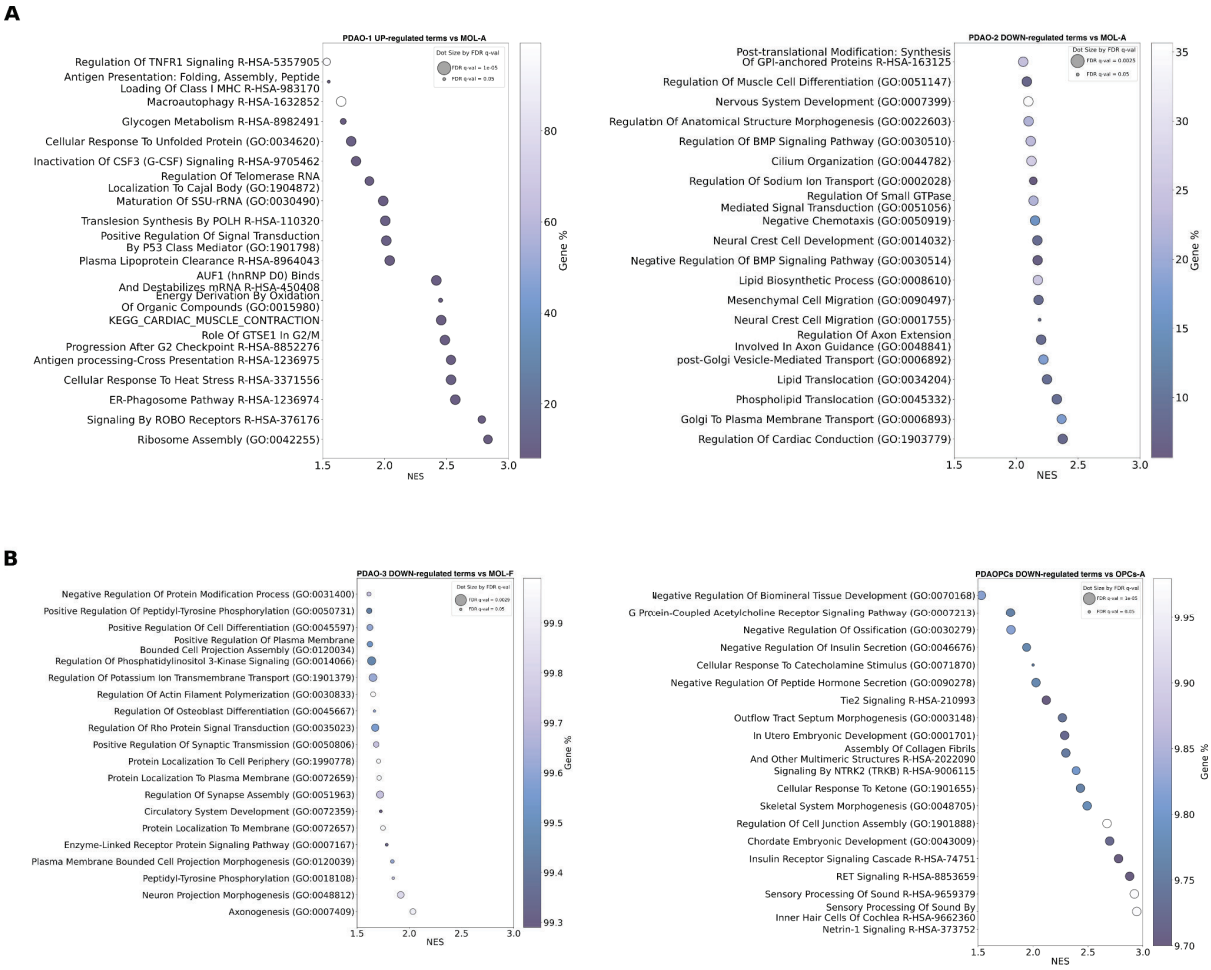

Supplementary Figure 5. A. (Left) GSEA results showing the top 20 enriched pathways (GO, KEGG, and Reactome) with increased expression in PDAO-1 compared to MOL-A, ranked by gene ratio. (Right) Top 20 pathways with reduced expression in PDAO-2 relative to MOL-A, also ordered by gene ratio. **B.** (Left) Top 20 pathways significantly downregulated in PDAO-3 compared to MOL-F, based on gene ratio. (Right) Top 20 downregulated pathways in PDAOPCs relative to OPCs-A, ranked in the same way.

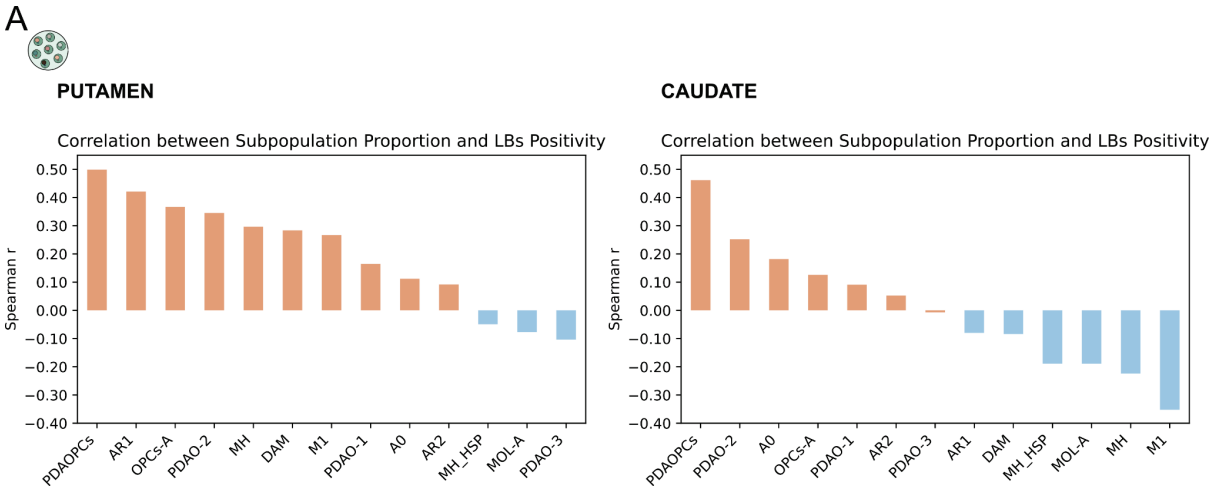

Supplementary Figure 6. Correlation analysis between subpopulations of interest in snRNA-seq data and LB load both in Pu (left) and CN (right).

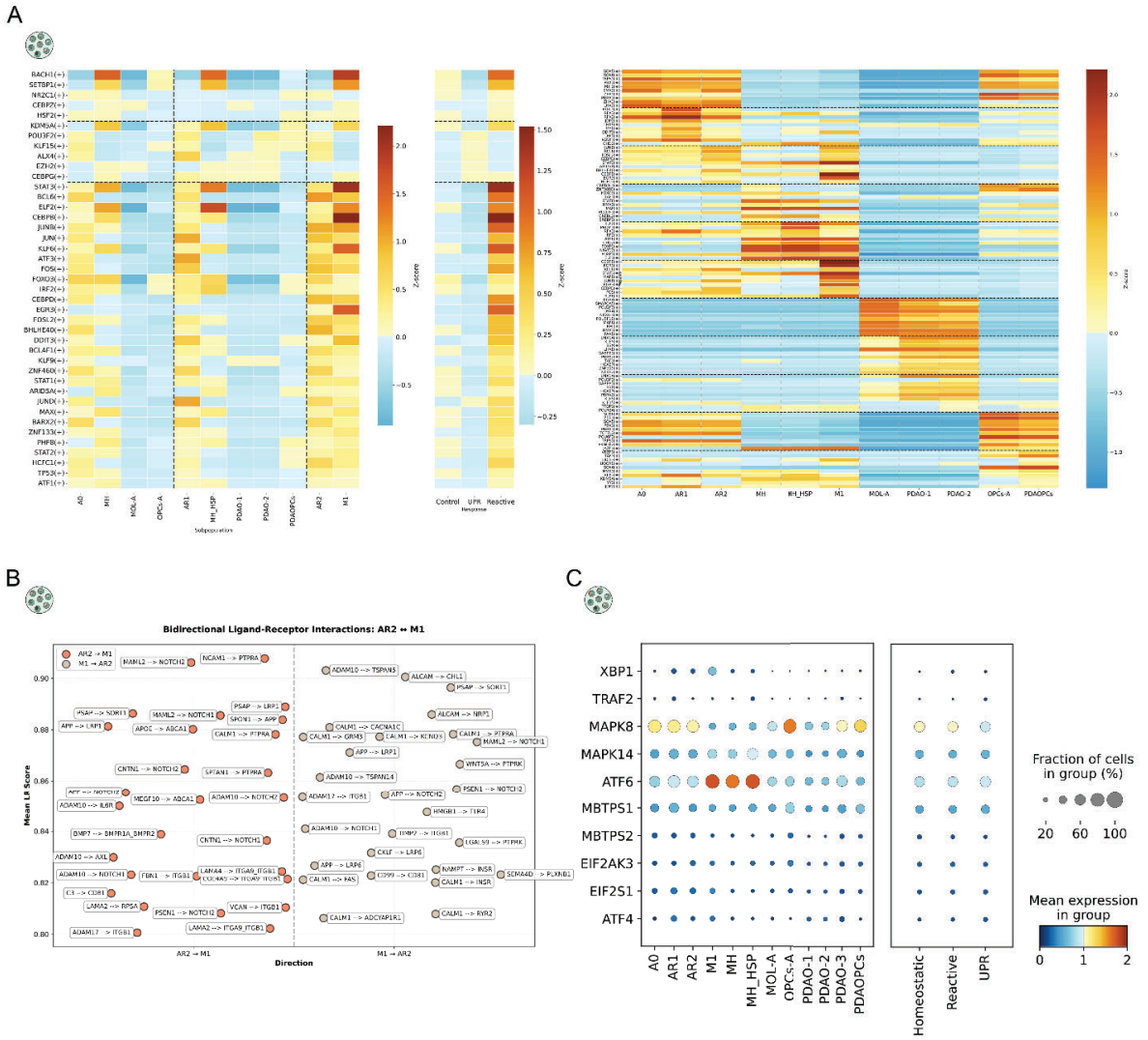

Supplementary Figure 7. A. Regulon activity across glial subpopulations was assessed using the SCENIC pipeline and summarized in two separate matrixplots. The first displays regulons whose activity was consistently elevated in subpopulations belonging to either the UPR or Reactive program compared to control-like subpopulations; only regulons showing coherent enrichment across subpopulations within the same response category were included. Rows correspond to individual regulons and columns to glial subpopulations, ordered by response category (Control-like, UPR, and Reactive) (left). The second matrixplot focuses on subpopulation-specific regulon activity, retaining only those regulons whose upregulation was restricted to a single subpopulation and not shared with others across the dataset (right). **B.** Ligand-receptor interactions between AR2 astrocytes and M1 microglia were inferred using LIANA. Interactions in which AR2 acts as the ligand-expressing population and M1 as the receptor-expressing population are highlighted in red; the reverse directionality is shown in brown. **C.** Expression of canonical UPR branch markers across glial subpopulations and molecular programs (Control-like, UPR, and Reactive) is displayed as a dotplot. Genes are grouped according to the UPR branch they belong to: IRE1α (*XBP1, TRAF2, MAPK8, MAPK14*), ATF6 (*ATF6, MBTPS1, MBTPS2*), and PERK (*EIF2AK3, EIF2S1, ATF4*). The size of each dot reflects the proportion of cells expressing the gene within a given subpopulation, while color intensity indicates the mean expression level among expressing cells.

8.5.2. Supplementary Tables

Brain Bank	Sex of Donor	Brain area	Number of samples	Age of Donor	Number of nuclei
MADRC	male	Caudate	21	63 – 88	57815
MADRC	male	Putamen	26	59 – 88	58247
MADRC	female	Caudate	7	58 – 81	16370
MADRC	female	Putamen	7	58 – 81	12729
NIH	male	Caudate	10	25 – 90	15620
NIH	male	Putamen	11	25 – 90	12175
NIH	female	Caudate	0	-	0
NIH	female	Putamen	0	-	0
PUKBB	male	Caudate	10	58 – 90	19098
PUKBB	male	Putamen	12	58 – 90	31100
PUKBB	female	Caudate	9	61 – 89	19152
PUKBB	female	Putamen	10	61 – 89	24463

Supplementary Table 1. Single-nuclei transcriptomics metadata for all donors included in this study grouped by Brain Bank, Sex and Brain area.

Subject	Condition	PU Area µm²	CN Area µm²	Total Area µm²	LBs Total	LBs PU	LBs CN	LBs/ Area	LBs/ Area (Pu)	LBs/ Area (CN)
N3	Control	27380394.7	16537493.7	43917888.4	57	31	26	1,30E+08	1,13E+08	1,57E+08
C2	Control	17226249.2	7783474.1	25009723.3	256	143	113	1,02E+09	8,30E+08	1,45E+09
N1	Control	3857379.6	5950636	9808015.6	35	14	21	3,57E+08	3,63E+08	3,53E+08
B3	Control	8049560	4585330.5	12634890.5	18	18	0	1,42E+08	2,24E+08	0
C1	Control	14541555.9	6622821.6	21164377.5	15	14	1	7,09E+07	9,63E+07	1,51E+07
A9	Control	12453170.4	10233385.6	22686556	93	48	45	4,10E+08	3,85E+08	4,40E+08
C9	Control	6153378.4	1864739.8	8018118.2	11	7	4	1,37E+08	1,14E+08	2,15E+08
C3	Control	7377811.3	12562294	19940105.3	3	1	2	1,50E+07	1,36E+07	1,59E+07
A7	PD	6937581.9	2174851.9	9112433.8	27	24	3	2,96E+08	3,46E+08	1,38E+07
C7	PD	16065934.9	11975097.4	28041032.3	314	213	101	1,12E+08	1,33E+08	8,43E+08
C10	PD	43186886.2	19744141.4	62931027.6	675	549	126	1,07E+09	1,27E+09	6,38E+08
B8	PD	12082007	3764396.2	15846403.2	44	34	10	2,78E+08	2,81E+08	2,66E+08
C4	PD	29270571.7	12226130	41496701.7	844	357	487	2,03E+08	1,22E+09	3,98E+09
B7	PD	7481026.6	7222681.6	14703708.2	73	47	26	4,96E+08	6,28E+08	3,60E+07
C6	PD	16604985.1	21655442.5	38260427.6	489	350	139	1,28E+09	2,11E+09	6,42E+08
A8	PD	21590342.8	7622376.3	29212719.1	282	219	63	9,65E+08	1,01E+09	8,27E+08

Supplementary Table 2. Metadata and α-synuclein immunohistochemical data for the subset of donors analyzed for Lewy body (LB) inclusions. For each subject, raw LB counts and area-normalized values (LBs/µm²) are provided per brain region.

9. Discussion

9.1. Overview and conceptual framework

This thesis presents one of the most comprehensive snRNA-seq and spatial transcriptomic characterizations of glial heterogeneity in the human dorsal striatum in PD to date. snRNA-seq data from 56 donors from three different brain banks was combined with image-based spatial transcriptomics in a subset of 24 subjects, allowing simultaneous molecular characterization of oligodendrocytes and their precursors, astrocytes, and microglia across the CN and Pu. These findings were integrated with clinical data, including Braak LB staging in a subset of samples (Braak et al., 2003). Cohort validation through TH and α-syn immunohistochemistry confirmed the pathological integrity of these samples. TH immunoreactivity was markedly reduced in Pu of PD cases, while α-syn aggregates were significantly increased, consistent with the established pattern of dopaminergic denervation and synucleinopathy in PD tissue (Kordower et al., 2013; Wakabayashi et al., 2000).

Applying snRNA-seq specifically to the dorsal striatum addresses a gap in the existing literature. Most single-cell transcriptomic studies in PD have focused on the SNpc, because it is the region of hallmark dopaminergic neurodegeneration (Kamath et al., 2022; Martirosyan et al., 2024; Smajić et al., 2022). The dorsal striatum has received less attention at this resolution, representing a gap this study aims to address. We profiled around 270,000 high-quality glial nuclei, enabling interrogation of cellular composition and molecular states across all major glial classes at a level of detail that was not possible in postmortem human tissue until recently (Ding et al., 2020).

9.2. Oligodendrocyte lineage dysfunction: stress and failed maturation

The oligodendrocyte lineage was the most numerically dominant glial population in our dataset and showed the most extensive molecular disruption in PD tissue. Oligodendrocytes accounted for over 56% of captured glial nuclei. Subclustering of approximately 200,000 OL-lineage cells reported 15 transcriptionally distinct subpopulations, four of which (PDAOPCs, PDAO-1, PDAO-2, and PDAO-3) were consistently and significantly enriched in PD tissue. Bae *et al*. (Bae et al., 2023) previously identified 2 OL subpopulations defined by protein folding stress and inflammatory reprogramming in the PD striatum. The present data extend those findings in sample size and resolution, and add spatial and trajectory-based dimensions not previously done.

All four disease-associated states shared a core transcriptional feature: coordinated upregulation of heat shock proteins (*HSPA1A, HSPA1B, HSP90AA1,* and *CRYAB*), together with multiple *DNAJ* co-chaperones. This proteostatic signature is difficult to fit with the myelination-oriented profile of healthy OL populations such as MOL-A, fitting more with a cellular response to α-syn-driven protein

misfolding stress. This interpretation is consistent with documented α-syn inclusions in oligodendrocytes in PD postmortem tissue (Wakabayashi et al., 2000) and with *HSP70* induction in murine synucleinopathy models (Bae et al., 2023). Beyond this shared stress response, the four states diverge functionally: PDAO-1 is characterized by upregulation of protein quality-control and cell cycle stress pathways; PDAO-2 shows an immunologically active profile enriched for *DAP12* and interferon-related genes; and PDAO-3 displays a metabolic bias toward lipid and steroid biosynthesis, suggesting a compensatory attempt to sustain myelin lipid production. This degree of intra-lineage phenotypic divergence has been described in MS oligodendroglia (Jäkel & Dimou, 2017), but has not previously been characterized in PD striatum.

Compositional shifts were strongly region-specific. Pu showed statistically significant increase of all four PD-associated states alongside depletion of healthy populations (MOL-A: -9.1%; MOL-F: -3.7%), while CN showed equivalent directional trends that did not reach significance, a pattern consistent with the well-established differential vulnerability of Pu to dopaminergic denervation (Kordower et al., 2013). These changes were sex-independent. Pseudotime trajectory analysis indicated that disease-associated states do not arise independently but branch from specific points along the canonical OPC → COP → MOL-A → MOL-F differentiation lineage: PDAO-1 diverges from MOL-A, PDAO-3 originates from terminally differentiated MOL-F, and PDAOPCs trace back to early OPC-A progenitors. This suggests that pathological alterations affect the lineage at multiple maturational stages simultaneously, impairing both differentiated myelinating cells and the progenitor pool that would replace them .

The functional consequences of this transcriptional reprogramming were confirmed at the protein level. MBP immunoreactivity was significantly reduced in PD Pu ($p = 0.047$), and this loss correlated inversely with cellular composition, specifically with the PDAO-1/MOL-A ratio ($r = -0.56$, $p = 0.02$) and the PDAO-2/MOL-A ratio ($r = -0.51$, $p = 0.02$). This provides a direct mechanistic link between single-cell molecular data and tissue-level myelin pathology that, to our knowledge, has not been previously demonstrated in human postmortem striatum.

Intercellular communication analysis using CellChat revealed widespread disruption of the adhesion signaling that maintains oligodendrocyte-axon contact. PDAO-1 cells showed a decrease of *NCAM*, *CADM*, laminin (*LAMA2*), and *CDH1* signaling molecules, which are required for the physical connection between myelinating processes and axonal membranes (Jin et al., 2021). This suggests that these cells get rid off from axons independently of cell death, which would compromise myelin integrity even when oligodendrocytes survive. Hotspot spatial co-expression analysis identified a reciprocal relationship between the stress response module (*HSPA1A, DNAJA1, HSP90AB1, CRYAB*) and the myelination module (*MAG, MOBP, CNTN2*): the two programs are inversely regulated across

PD tissue, with stress response genes having transcriptional dominance as myelination-related genes decrease.

These findings are consistent with a model in which oligodendrocytes redirect cellular resources away from myelin maintenance and toward proteostatic survival. This mechanism may be adaptive in the short term but represents a possible driver of the progressive white matter disruption observed in the PD striatum, one that has been underappreciated (Ettle et al., 2016; Nave, 2010).

9.3. Astrocyte reactivity in the parkinsonian striatum: between stress and inflammation

Astrocytes have been implicated in PD pathophysiology, but most of these works have focused on the substantia nigra (Escartin et al., 2021; Sofroniew & Vinters, 2010). In our study, the analysis of approximately 47,000 astrocyte nuclei from the striatum identified six transcriptionally distinct subpopulations: a homeostatic population (A0) enriched for synaptic glutamate transport and perisynaptic adhesion genes; two reactive gray matter states (AR1 and AR2); one white matter-associated population (WMA); a restricted precursor population (ARP); and a subventricular zone cell population (SVZC) located in the lateral ventricle of the CN. This degree of astrocyte heterogeneity within a single brain region is consistent with snRNA-seq surveys emphasizing functional diversity across human and mouse brain astrocytes (Bayraktar et al., 2020; Zeisel et al., 2018), but its characterization, specifically in PD striatum has not been previously reported.

AR1 and AR2 are the two reactive populations most relevant to PD. AR1 cells, marked by *CRYAB, FTH1*, and *HSPA4L*, show a transcriptional profile dominated by heat shock proteins, unfolded protein response components, and genes associated with neurovascular remodeling. This profile closely resembles the stress-adaptive signature we identified in PDAO-1 oligodendrocytes, which suggests that the proteostatic disruption in PD striatum is not restricted to a single cell type but reflects a broader tissue-level response. AR2 cells, defined by CHI3L1, FN1, and SOD2, are more inflammatory: they show cytokine receptor activation, immune effector gene expression including *CCL2*, and metabolic markers of hypoxia-like remodeling such as *HILPDA* and *ANGPTL4*. The distinction between a proteostatic (AR1) and inflammatory (AR2) reactive state has conceptual overlap with the A1/A2 astrocyte classification (Liddelow et al., 2017), though recent evidence argues against a strict binary in favor of a continuous reactive spectrum (Escartin et al., 2021), a view our data appear to support.

Compositional analysis showed a relative increase in AR1 cells in PD Pu, reaching statistical significance, while the homeostatic A0 population declined significantly in CN. These findings align with prior reports of reactive astrogliosis in PD (Sofroniew & Vinters, 2010), but add regional and

subtype-level resolution that was not previously available. The enrichment of KEGG Parkinson's disease pathway genes in AR1 cells in both regions supports the interpretation that this reactive state is not simply a generic gliosis response but is molecularly linked to canonical PD pathways. This finding overlaps with that from Smajić *et al.* (Smajić et al., 2022), who reported pan-glial activation in PD midbrain enriched for PD-related molecular signatures.

Differential expression analysis in AR2 cells was particularly informative. In both CN and Pu, AR2 cells in PD showed upregulation of metallothionein genes (*MT1X, MT2A*), indicators of oxidative stress and metal dysregulation; elevated *CCL2*, a chemokine associated with immune cell recruitment and neuroinflammation; and increased *HIF1A-AS3*, a marker of hypoxic or metabolic stress. Upregulation of *NDUFS6* in CN AR2 cells points toward compromised mitochondrial Complex I function, a deficit repeatedly linked to dopaminergic neuron degeneration in PD (Joshi et al., 2019; A. H. Schapira, 1993). That striatal astrocytes recapitulate these mitochondrial stress signatures transcriptionally suggests that oxidative pathology in PD is not confined to dopaminergic neurons but may propagate through glial-to-glial and glial-to-neuron interactions.

Slingshot trajectory inference showed that the homeostatic A0 population bifurcates toward either AR1 or AR2. The A0-to-AR1 transition appeared relatively abrupt and enriched for canonical PD genes, whereas the A0-to-AR2 transition was more gradual and associated with neuroinflammatory and general stress-response programs. This asymmetry between two reactive trajectories originating from the same precursor state is not easily explained by existing analyses. One interpretation is that the nature of the primary insult determines which reactive trajectory the cell follows, and that different patients or disease stages may preferentially engage one over the other.

The SVZC population detected in CN, expressing neurogenic commitment genes including *SOX11, KIT*, and *NR4A2* alongside progenitor and neuroblast migration markers such as *ROBO2, SEMA3D,* and *SPARC*, represents an unusual finding in this context. The extent of neurogenesis in the adult human brain remains discussed (Boldrini et al., 2018; Sorrells et al., 2018), and the precise nature of these cells is therefore difficult to define. At present, it is unclear whether they reflect a residual developmental population that persists into adulthood, a reactive progenitor-like state induced by the diseased environment, or a population with capacity to contribute to cellular replacement. Each of these possibilities carries different biological implications, particularly in the setting of neurodegeneration. Our data do not allow us to distinguish between these three possibilities, as transcriptomic profiles alone cannot establish lineage potential or functional output. This limitation highlights the need for targeted experimental approaches, such as lineage tracing, functional assays, or spatially resolved validation, to determine the origin and fate of these cells. Clarifying this point would be especially relevant in the context of PD, and whether these cells constitute a residual

developmental population, a reactive progenitor state, or a functionally meaningful source of cellular replacement is a doubt we cannot resolve with our data alone.

9.4. Microglial States in the PD Striatum: from Surveillance to Chronic Stress

Microglia represented around 10% of the total glial nuclei captured in our dataset, but showed a high heterogeneity despite their relatively low abundance. Clustering showed four transcriptionally distinct subpopulations: homeostatic microglia (MH), defined by surveillance markers *P2RY12, CX3CR1,* and *SRGAP3*; disease-associated microglia (DAM), defined by *APOE, FTL*, and *FTH1*; a pro-inflammatory M1 population enriched for *IL1B, SPP1,* and transcriptional immune activators; and MH-HSP cells, a heat-shock-protein-enriched state similar to the AR1 astrocyte and PDAO-1 oligodendrocyte phenotypes described above.

The presence of a DAM subpopulation in human PD striatum fits with several recent studies demonstrating disease-associated microglial states across neurodegenerative conditions (Alzheimer Disease and models of amyotrophic lateral sclerosis, multiple sclerosis, and Alzheimer's disease) (Keren-Shaul et al., 2017; Krasemann et al., 2017). First described in Alzheimer's disease models in the context of amyloid pathology, DAM are now understood as a conserved microglial response to multiple forms of neurodegeneration, driven in part through the TREM2-APOE signaling (Krasemann et al., 2017). In our data, DAM cells showed coordinated activation of phagocytosis-related genes (*CTSD, CTSL, GPNMB, MERTK, CD9*), lipid metabolism regulators (*APOE, PPARG, MGLL*), and complement components (*C1QC*), alongside increased ribosomal and chaperone gene expression. This profile is consistent with microglia trying to clear damaged material, for example α-syn aggregates and myelin debris, but doing it under chronic metabolic stress that reduces their effectiveness (Shokr, 2025).

The overlap between PD-associated differentially expressed genes and the DAM marker profile, together with significant KEGG PD pathway enrichment within the DAM population, establishes a direct molecular connection between this microglial state and canonical PD pathways. This is a novel finding in the striatal context and supports the interpretation that DAM-like microglia in PD are a protective profile. They appear to represent an incomplete adaptive response, capable of initiating debris clearance but unable to fully remove the proteostatic load maintained by chronic α-syn pathology (Prinz et al., 2021).

The M1 population, enriched for *IL1B, NFKBIZ,* and glycolytic transporters including *SLC2A3*, represents a distinct inflammatory trajectory. These cells show the classically activated pro-inflammatory microglia described in earlier neuroinflammation studies (Heneka et al., 2015;

Tansey & Goldberg, 2010), characterized by high cytokine output and metabolic reprogramming toward aerobic glycolysis. Differential expression analysis showed that markers of M1 overlapping with genes increased in PD were most pronounced across both CN and Pu, featuring elevated tRNA synthetases and amino acid transporters consistent with the translational demands of active cytokine production.

The MH-HSP population is perhaps the most conceptually interesting of the four. The transcriptional profile is dominated by HSF1-target genes (*HSPA1A, HSPA1B, DNAJB1, HSPH1*) alongside glucocorticoid-responsive metabolic regulators (*FKBP5, PDK4*), placing it in the same functional category as AR1 astrocytes and PDAO-1 oligodendrocytes. The recurrence of this HSP-driven stress signature across all three major glial cell types in the same tissue does not seem like a coincidence. It suggests a pan-glial proteostatic activation rather than a cell-type-specific stress response. Spatially, MH-HSP cells were notably concentrated near the lateral ventricle region, raising the possibility that this state is particularly prominent at the CSF-brain interface, where α-syn concentrations or inflammatory signals may be elevated compared to deeper parenchymal regions.

Compositionally, reactive microglial states (DAM, M1, MH-HSP) showed a consistent expansion trend in PD samples across both striatal regions, accompanied by a statistically significant reduction of homeostatic MH cells. The decrease in homeostatic compartment evidences similarities with observations in PD midbrain (Smajić et al., 2022) and is broadly consistent with the idea that disease progression involves a shift away from steady-state surveillance toward activation states that, while initially protective, may contribute to secondary neuronal injury through sustained cytokine release and oxidative stress (Boche et al., 2013; Tansey & Goldberg, 2010).

9.5. Braak Lewy Body Stage-Dependent Glial Dynamics and the Two Endophenotypes of PD

One of the more unexpected findings from this thesis concerns how glial state composition relates to neuropathological progression across Braak LB stages (Braak et al., 2003). The classical model of PD progression treats Braak LB staging as a linear progression of pathological mechanisms, with each stage representing a more advanced disease state. The data presented here do not support that view completely.

Across all three glial classes, homeostatic populations (A0, MH, MOL-A, and OPCs-A) were most abundant at Braak LB stage 0 and decreased with increasing pathological severity. The affection of glial support functions is expected and consistent with the known deterioration of synaptic integrity, neurovascular coupling, and immune surveillance as disease advances (Braak et al., 2003; X. Zhang et al., 2022). What was not expected was the behavior of reactive populations across stages. Rather than

a uniform escalation of all reactive states in parallel with Braak LB score, we found a pattern of mutual exclusivity between two distinct reactive programs.

The first, which we refer to as Reactive response (inflammatory), is characterized by expansion of AR2 astrocytes and M1 microglia, and was most prominent at Braak LB stages 3 and 5. The second, the UPR program, is defined by enrichment of AR1 astrocytes, MH-HSP microglia, and PD-associated oligodendroglial clusters (PDAO-1, PDAO-2, PDAOPCs), and was increased at Braak LB stage 4. These two programs did not co-occur within the same compositional context. When populations in the Reactive program were prominent, stress-adaptive populations were relatively suppressed, and vice versa. This mutual exclusivity was confirmed at the individual donor level: subjects showing clear AR2 and M1 predominance lacked UPR-associated subpopulations, and vice versa.

This suggests that PD is not a single-trajectory disease at the glial level. Instead, the data are consistent with at least two distinct molecular responses in relation to glial affection. Individual patients appear to align preferentially with either a Reactive program or a UPR one. Braak LB staging, under this interpretation, does not show a chronological sequence but reflects a shift of these two programs across a population of donors with varying pathological severities. This is broadly consistent with the growing recognition of clinical and molecular heterogeneity within PD (Deng et al., 2025; Fereshtehnejad et al., 2017).

These phenotypes are relevant to therapeutic targeting. Anti-inflammatory strategies aimed at M1 and AR2 states may be most appropriate for patients whose glial profile is reactive, while approaches targeting proteostasis enhancement or UPR attenuation may fit better to those with a predominantly stress-adaptive signature. Whether glial response correlates with clinical subtype, disease course, or genetic background is a question this dataset cannot fully explain, but that represents an interesting direction for future work.

A question that naturally follows from the discovery of these programs is whether these glial responses could be detected in living patients, rather than only in postmortem tissue. Eninger *et al*. (Eninger et al., 2022) showed that glial activation states defined by single-cell transcriptomics in α-synucleinopathy mouse models are largely mirrored by specific protein changes in the CSF, and that many of these proteins can be quantified in human samples. If the inflammatory and proteostatic programs we describe here produce comparably distinct proteomic signatures, which, given how molecularly different they are from each other, seems plausible, CSF or even blood-based profiling could potentially be used to assign patients to one program or the other without relying on postmortem data. That would mean that the glial heterogeneity we document here is not just biologically

interesting, but could translate into a way of identifying which patients are more likely to benefit from anti-inflammatory strategies versus those where targeting proteostatic stress might make more sense. Obviously, this requires validation and additional work, but the conceptual path from our transcriptomic atlas to that kind of application is not as improbable as it might initially seem.

10. Conclusions

This thesis presents what is, to our knowledge, the most comprehensive transcriptomic and spatial atlas of glial heterogeneity in the human parkinsonian dorsal striatum to date. Furthermore, our data reveal a consistent and coordinated remodeling across all three major glial lineages, with direct implications for our understanding of PD pathogenesis and future therapeutic strategies.

The following conclusions can be drawn:

1. The glial lineage in the human dorsal striatum turned out to be considerably more heterogeneous than expected, with oligodendrocytes, astrocytes, and microglia each resolving into molecularly distinct subpopulations that had not been previously described at this resolution.
2. Homeostatic glial populations, including MOL-A oligodendrocytes, A0 astrocytes, and MH microglia, decrease progressively in the PD striatum, reflecting a gradual loss of the supportive glial functions required for neuronal homeostasis.
3. The oligodendrocyte lineage undergoes profound transcriptional reprogramming in PD, giving rise to disease-associated states (PDAO-1, PDAO-2, PDAO-3, PDAOPCs) that shift from myelination toward proteostatic survival, a shift that is mechanistically linked to myelin alterations, disrupted axonal adhesion, and altered neurotransmitter receptor expression.
4. Astrocytes transition from homeostatic, synapse-supporting identities toward two divergent reactive phenotypes: a proteostatic state (AR1) and an inflammatory state (AR2), both of which are enriched for PD-associated molecular signatures.
5. Microglia shift away from homeostatic surveillance toward disease-associated states including phagocytically stressed DAM cells, pro-inflammatory M1 microglia, and an HSP-enriched phenotype (MH-HSP) that mirrors the proteostatic stress response observed across all three glial lineages.
6. PD does not follow a single, uniform glial trajectory. Individual donors preferentially show either a Reactive (inflammatory) or a UPR (proteostatic) program that we describe here, and these two responses alternate in dominance across Braak LB stages, suggesting the existence of distinct molecular responses within the disease.
7. These glial programs could serve as a basis for patient stratification and personalized therapeutic targeting, with anti-inflammatory strategies being more appropriate for Reactive-dominant patients and proteostasis-enhancing approaches for UPR-dominant ones.

11. References

Abbott, N. J., Rönnbäck, L., & Hansson, E. (2006). Astrocyte-endothelial interactions at the blood-brain barrier. *Nature Reviews. Neuroscience*, *7*(1), 41–53. https://doi.org/10.1038/nrn1824

Adams, L., Song, M. K., Yuen, S., Tanaka, Y., & Kim, Y.-S. (2024). A single-nuclei paired multiomic analysis of the human midbrain reveals age- and Parkinson's disease–associated glial changes. *Nature Aging*, *4*(3), 364–378. https://doi.org/10.1038/s43587-024-00583-6

Agarwal, D., Sandor, C., Volpato, V., Caffrey, T. M., Monzón-Sandoval, J., Bowden, R., Alegre-Abarrategui, J., Wade-Martins, R., & Webber, C. (2020). A single-cell atlas of the human substantia nigra reveals cell-specific pathways associated with neurological disorders. *Nature Communications*, *11*, 4183. https://doi.org/10.1038/s41467-020-17876-0

Akay, L. A., Effenberger, A. H., & Tsai, L.-H. (2021). Cell of all trades: Oligodendrocyte precursor cells in synaptic, vascular, and immune function. *Genes & Development*, *35*(3–4), 180–198. https://doi.org/10.1101/gad.344218.120

Albin, R. L., Young, A. B., & Penney, J. B. (1989). The functional anatomy of basal ganglia disorders. *Trends in Neurosciences*, *12*(10), 366–375. https://doi.org/10.1016/0166-2236(89)90074-x

Alexander, G. E., DeLong, M. R., & Strick, P. L. (1986). Parallel organization of functionally segregated circuits linking basal ganglia and cortex. *Annual Review of Neuroscience*, *9*, 357–381. https://doi.org/10.1146/annurev.ne.09.030186.002041

Alliot, F., Godin, I., & Pessac, B. (1999). Microglia derive from progenitors, originating from the yolk sac, and which proliferate in the brain. *Brain Research. Developmental Brain Research*, *117*(2), 145–152. https://doi.org/10.1016/s0165-3806(99)00113-3

Alvarez, J. I., Dodelet-Devillers, A., Kebir, H., Ifergan, I., Fabre, P. J., Terouz, S., Sabbagh, M., Wosik, K., Bourbonnière, L., Bernard, M., van Horssen, J., de Vries, H. E., Charron, F., & Prat, A. (2011). The Hedgehog pathway promotes blood-brain barrier integrity and CNS immune quiescence. *Science*, *334*(6063), 1727–1731. https://doi.org/10.1126/science.1206936

Araque, A., Parpura, V., Sanzgiri, R. P., & Haydon, P. G. (1999). Tripartite synapses: Glia, the unacknowledged partner. *Trends in Neurosciences*, *22*(5), 208–215. https://doi.org/10.1016/s0166-2236(98)01349-6

Arena, G., Sharma, K., Agyeah, G., Krüger, R., Grünewald, A., & Fitzgerald, J. C. (2022). Neurodegeneration and Neuroinflammation in Parkinson's Disease: A Self-Sustained Loop. *Current Neurology and Neuroscience Reports*, *22*(8), 427–440. https://doi.org/10.1007/s11910-022-01207-5

Ascherio, A., & Schwarzschild, M. A. (2016). The epidemiology of Parkinson's disease: Risk factors and prevention. *The Lancet. Neurology*, *15*(12), 1257–1272. https://doi.org/10.1016/S1474-4422(16)30230-7

Athauda, D., & Foltynie, T. (2015). The ongoing pursuit of neuroprotective therapies in Parkinson disease. *Nature Reviews. Neurology*, *11*(1), 25–40. https://doi.org/10.1038/nrneurol.2014.226

Azevedo, C., Teku, G., Pomeshchik, Y., Reyes, J. F., Chumarina, M., Russ, K., Savchenko, E., Hammarberg, A., Lamas, N. J., Collin, A., Gouras, G. K., Klementieva, O., Hallbeck, M., Taipa, R., Vihinen, M., & Roybon, L. (2022). Parkinson's disease and multiple system atrophy patient iPSC-derived oligodendrocytes exhibit alpha-synuclein–induced changes in maturation and immune reactive properties. *Proceedings of the National Academy of Sciences of the United States of America*, *119*(12), e2111405119. https://doi.org/10.1073/pnas.2111405119

Bae, E.-J., Pérez-Acuña, D., Rhee, K. H., & Lee, S.-J. (2023). Changes in oligodendroglial subpopulations in Parkinson's disease. *Molecular Brain*, *16*, 65. https://doi.org/10.1186/s13041-023-01055-5

Bailey, H. M., & Cookson, M. R. (2024). How Parkinson's Disease-Linked LRRK2 Mutations Affect Different CNS Cell Types. *Journal of Parkinson's Disease*, *14*(7), 1331–1352. https://doi.org/10.3233/JPD-230432

Barba-Reyes, J. M., Harder, L., Marco Salas, S., Jaisa-aad, M., Muñoz-Castro, C., Garma, L. D., Rafati, N., Nilsson, M., Hyman, B. T., Serrano-Pozo, A., & Muñoz-Manchado, A. B. (2025).

Oligodendroglia vulnerability in the human dorsal striatum in Parkinson's disease. *Acta Neuropathologica*, *149*(1), 46. https://doi.org/10.1007/s00401-025-02884-5

Barres, B. A. (2008). The mystery and magic of glia: A perspective on their roles in health and disease. *Neuron*, *60*(3), 430–440. https://doi.org/10.1016/j.neuron.2008.10.013

Bayraktar, O. A., Bartels, T., Holmqvist, S., Kleshchevnikov, V., Martirosyan, A., Polioudakis, D., Ben Haim, L., Young, A. M. H., Batiuk, M. Y., Prakash, K., Brown, A., Roberts, K., Paredes, M. F., Kawaguchi, R., Stockley, J. H., Sabeur, K., Chang, S. M., Huang, E., Hutchinson, P., … Rowitch, D. H. (2020). Astrocyte layers in the mammalian cerebral cortex revealed by a single-cell in situ transcriptomic map. *Nature Neuroscience*, *23*(4), 500–509. https://doi.org/10.1038/s41593-020-0602-1

Bélanger, M., Allaman, I., & Magistretti, P. J. (2011). Brain energy metabolism: Focus on astrocyte-neuron metabolic cooperation. *Cell Metabolism*, *14*(6), 724–738. https://doi.org/10.1016/j.cmet.2011.08.016

Ben-Shlomo, Y., Darweesh, S., Llibre-Guerra, J., Marras, C., San Luciano, M., & Tanner, C. (2024). The epidemiology of Parkinson's disease. *Lancet*, *403*(10423), 283–292. https://doi.org/10.1016/S0140-6736(23)01419-8

Berg, D., Postuma, R. B., Adler, C. H., Bloem, B. R., Chan, P., Dubois, B., Gasser, T., Goetz, C. G., Halliday, G., Joseph, L., Lang, A. E., Liepelt-Scarfone, I., Litvan, I., Marek, K., Obeso, J., Oertel, W., Olanow, C. W., Poewe, W., Stern, M., & Deuschl, G. (2015). MDS research criteria for prodromal Parkinson's disease. *Movement Disorders: Official Journal of the Movement Disorder Society*, *30*(12), 1600–1611. https://doi.org/10.1002/mds.26431

Bergman, H., Wichmann, T., & DeLong, M. R. (1990). Reversal of experimental parkinsonism by lesions of the subthalamic nucleus. *Science*, *249*(4975), 1436–1438. https://doi.org/10.1126/science.2402638

Bido, S., Muggeo, S., Massimino, L., Marzi, M. J., Giannelli, S. G., Melacini, E., Nannoni, M., Gambarè, D., Bellini, E., Ordazzo, G., Rossi, G., Maffezzini, C., Iannelli, A., Luoni, M., Bacigaluppi, M., Gregori, S., Nicassio, F., & Broccoli, V. (2021). Microglia-specific overexpression of α-synuclein leads to severe dopaminergic neurodegeneration by phagocytic

exhaustion and oxidative toxicity. *Nature Communications*, *12*(1), Article 1. https://doi.org/10.1038/s41467-021-26519-x

Birk, S., Bonafonte-Pardàs, I., Feriz, A. M., Boxall, A., Agirre, E., Memi, F., Maguza, A., Yadav, A., Armingol, E., Fan, R., Castelo-Branco, G., Theis, F. J., Bayraktar, O. A., Talavera-López, C., & Lotfollahi, M. (2025). Quantitative characterization of cell niches in spatially resolved omics data. *Nature Genetics*, *57*(4), 897–909. https://doi.org/10.1038/s41588-025-02120-6

Boche, D., Perry, V. H., & Nicoll, J. a. R. (2013). Review: Activation patterns of microglia and their identification in the human brain. *Neuropathology and Applied Neurobiology*, *39*(1), 3–18. https://doi.org/10.1111/nan.12011

Bogers, J. S., Bloem, B. R., & Den Heijer, J. M. (2023). The Etiology of Parkinson's Disease: New Perspectives from Gene-Environment Interactions. *Journal of Parkinson's Disease*, *13*(8), 1281–1288. https://doi.org/10.3233/JPD-230250

Boldrini, M., Fulmore, C. A., Tartt, A. N., Simeon, L. R., Pavlova, I., Poposka, V., Rosoklija, G. B., Stankov, A., Arango, V., Dwork, A. J., Hen, R., & Mann, J. J. (2018). Human Hippocampal Neurogenesis Persists throughout Aging. *Cell Stem Cell*, *22*(4), 589-599.e5. https://doi.org/10.1016/j.stem.2018.03.015

Booth, H. D. E., Hirst, W. D., & Wade-Martins, R. (2017). The Role of Astrocyte Dysfunction in Parkinson's Disease Pathogenesis. *Trends in Neurosciences*, *40*(6), 358–370. https://doi.org/10.1016/j.tins.2017.04.001

Braak, H., Del Tredici, K., Rüb, U., de Vos, R. A. I., Jansen Steur, E. N. H., & Braak, E. (2003). Staging of brain pathology related to sporadic Parkinson's disease. *Neurobiology of Aging*, *24*(2), 197–211. https://doi.org/10.1016/s0197-4580(02)00065-9

Braidy, N., Gai, W.-P., Xu, Y. H., Sachdev, P., Guillemin, G. J., Jiang, X.-M., Ballard, J. W. O., Horan, M. P., Fang, Z. M., Chong, B. H., & Chan, D. K. Y. (2013). Uptake and mitochondrial dysfunction of alpha-synuclein in human astrocytes, cortical neurons and fibroblasts. *Translational Neurodegeneration*, *2*(1), 20. https://doi.org/10.1186/2047-9158-2-20

Bryois, J., Skene, N. G., Hansen, T. F., Kogelman, L. J. A., Watson, H. J., Liu, Z., Eating Disorders Working Group of the Psychiatric Genomics Consortium, International Headache Genetics

Consortium, 23andMe Research Team, Brueggeman, L., Breen, G., Bulik, C. M., Arenas, E., Hjerling-Leffler, J., & Sullivan, P. F. (2020). Genetic identification of cell types underlying brain complex traits yields insights into the etiology of Parkinson's disease. *Nature Genetics*, *52*(5), 482–493. https://doi.org/10.1038/s41588-020-0610-9

Burda, J. E., & Sofroniew, M. V. (2014). Reactive gliosis and the multicellular response to CNS damage and disease. *Neuron*, *81*(2), 229–248. https://doi.org/10.1016/j.neuron.2013.12.034

Büttner, M., Ostner, J., Müller, C. L., Theis, F. J., & Schubert, B. (2021). scCODA is a Bayesian model for compositional single-cell data analysis. *Nature Communications*, *12*(1), 6876. https://doi.org/10.1038/s41467-021-27150-6

Calabresi, P., Picconi, B., Tozzi, A., Ghiglieri, V., & Di Filippo, M. (2014). Direct and indirect pathways of basal ganglia: A critical reappraisal. *Nature Neuroscience*, *17*(8), 1022–1030. https://doi.org/10.1038/nn.3743

Carlsson, A. (1993). Thirty years of dopamine research. *Advances in Neurology*, *60*, 1–10.

Chaudhuri, K. R., Healy, D. G., Schapira, A. H. V., & National Institute for Clinical Excellence. (2006). Non-motor symptoms of Parkinson's disease: Diagnosis and management. *The Lancet. Neurology*, *5*(3), 235–245. https://doi.org/10.1016/S1474-4422(06)70373-8

Chen, K. H., Boettiger, A. N., Moffitt, J. R., Wang, S., & Zhuang, X. (2015). Spatially resolved, highly multiplexed RNA profiling in single cells. *Science (New York, N.Y.)*, *348*(6233), aaa6090. https://doi.org/10.1126/science.aaa6090

Chen, K., Wang, H., Ilyas, I., Mahmood, A., & Hou, L. (2023). Microglia and Astrocytes Dysfunction and Key Neuroinflammation-Based Biomarkers in Parkinson's Disease. *Brain Sciences*, *13*(4), 634. https://doi.org/10.3390/brainsci13040634

Christodoulou, C. C., Onisiforou, A., Zanos, P., & Papanicolaou, E. Z. (2023). Unraveling the transcriptomic signatures of Parkinson's disease and major depression using single-cell and bulk data. *Frontiers in Aging Neuroscience*, *15*, 1273855. https://doi.org/10.3389/fnagi.2023.1273855

Codolo, G., Plotegher, N., Pozzobon, T., Brucale, M., Tessari, I., Bubacco, L., & de Bernard, M. (2013). Triggering of inflammasome by aggregated α-synuclein, an inflammatory response in synucleinopathies. *PloS One*, *8*(1), e55375. https://doi.org/10.1371/journal.pone.0055375

Cole, K. L. H., Early, J. J., & Lyons, D. A. (2017). Drug discovery for remyelination and treatment of MS. *Glia*, *65*(10), 1565–1589. https://doi.org/10.1002/glia.23166

Colonna, M., & Butovsky, O. (2017). Microglia Function in the Central Nervous System During Health and Neurodegeneration. *Annual Review of Immunology*, *35*, 441–468. https://doi.org/10.1146/annurev-immunol-051116-052358

Connolly, B. S., & Lang, A. E. (2014). Pharmacological treatment of Parkinson disease: A review. *JAMA*, *311*(16), 1670–1683. https://doi.org/10.1001/jama.2014.3654

Corces, M. R., Shcherbina, A., Kundu, S., Gloudemans, M. J., Frésard, L., Granja, J. M., Louie, B. H., Eulalio, T., Shams, S., Bagdatli, S. T., Mumbach, M. R., Liu, B., Montine, K. S., Greenleaf, W. J., Kundaje, A., Montgomery, S. B., Chang, H. Y., & Montine, T. J. (2020). Single-cell epigenomic analyses implicate candidate causal variants at inherited risk loci for Alzheimer's and Parkinson's diseases. *Nature Genetics*, *52*(11), 1158–1168. https://doi.org/10.1038/s41588-020-00721-x

Dadwal, S., & Heneka, M. T. (2024). Microglia heterogeneity in health and disease. *FEBS Open Bio*, *14*(2), 217–229. https://doi.org/10.1002/2211-5463.13735

Davalos, D., Grutzendler, J., Yang, G., Kim, J. V., Zuo, Y., Jung, S., Littman, D. R., Dustin, M. L., & Gan, W.-B. (2005). ATP mediates rapid microglial response to local brain injury in vivo. *Nature Neuroscience*, *8*(6), 752–758. https://doi.org/10.1038/nn1472

Degirmenci, Y., Angelopoulou, E., Georgakopoulou, V. E., & Bougea, A. (2023). Cognitive Impairment in Parkinson's Disease: An Updated Overview Focusing on Emerging Pharmaceutical Treatment Approaches. *Medicina*, *59*(10), 1756. https://doi.org/10.3390/medicina59101756

Dehestani, M., Kozareva, V., Blauwendraat, C., Fraenkel, E., Gasser, T., & Bansal, V. (2024). Transcriptomic changes in oligodendrocytes and precursor cells associate with clinical

outcomes of Parkinson's disease. *Molecular Brain*, *17*(1), 56. https://doi.org/10.1186/s13041-024-01128-z

DeLong, M. R. (1990). Primate models of movement disorders of basal ganglia origin. *Trends in Neurosciences*, *13*(7), 281–285. https://doi.org/10.1016/0166-2236(90)90110-v

Deng, X., Mehta, A., Xiao, B., Ray Chaudhuri, K., Tan, E.-K., & Tan, L. C. (2025). Parkinson's disease subtypes: Approaches and clinical implications. *Parkinsonism & Related Disorders*, *130*, 107208. https://doi.org/10.1016/j.parkreldis.2024.107208

DeTomaso, D., & Yosef, N. (2021). Hotspot identifies informative gene modules across modalities of single-cell genomics. *Cell Systems*, *12*(5), 446-456.e9. https://doi.org/10.1016/j.cels.2021.04.005

Dickson, D. W. (2012). Parkinson's disease and parkinsonism: Neuropathology. *Cold Spring Harbor Perspectives in Medicine*, *2*(8), a009258. https://doi.org/10.1101/cshperspect.a009258

Dimitrov, D., Schäfer, P. S. L., Farr, E., Rodriguez-Mier, P., Lobentanzer, S., Badia-i-Mompel, P., Dugourd, A., Tanevski, J., Ramirez Flores, R. O., & Saez-Rodriguez, J. (2024). LIANA+ provides an all-in-one framework for cell–cell communication inference. *Nature Cell Biology*, *26*(9), 1613–1622. https://doi.org/10.1038/s41556-024-01469-w

Ding, J., Adiconis, X., Simmons, S. K., Kowalczyk, M. S., Hession, C. C., Marjanovic, N. D., Hughes, T. K., Wadsworth, M. H., Burks, T., Nguyen, L. T., Kwon, J. Y. H., Barak, B., Ge, W., Kedaigle, A. J., Carroll, S., Li, S., Hacohen, N., Rozenblatt-Rosen, O., Shalek, A. K., … Levin, J. Z. (2020). Systematic comparison of single-cell and single-nucleus RNA-sequencing methods. *Nature Biotechnology*, *38*(6), 737–746. https://doi.org/10.1038/s41587-020-0465-8

Dorsey, E. R., Sherer, T., Okun, M. S., & Bloem, B. R. (2018). The Emerging Evidence of the Parkinson Pandemic. *Journal of Parkinson's Disease*, *8*(s1), S3–S8. https://doi.org/10.3233/JPD-181474

Emre, M., Aarsland, D., Brown, R., Burn, D. J., Duyckaerts, C., Mizuno, Y., Broe, G. A., Cummings, J., Dickson, D. W., Gauthier, S., Goldman, J., Goetz, C., Korczyn, A., Lees, A., Levy, R., Litvan, I., McKeith, I., Olanow, W., Poewe, W., … Dubois, B. (2007). Clinical diagnostic criteria for dementia associated with Parkinson's disease. *Movement Disorders: Official*

Journal of the Movement Disorder Society, *22*(12), 1689–1707; quiz 1837. https://doi.org/10.1002/mds.21507

Endo, F., Kasai, A., Soto, J. S., Yu, X., Qu, Z., Hashimoto, H., Gradinaru, V., Kawaguchi, R., & Khakh, B. S. (2022). Molecular basis of astrocyte diversity and morphology across the CNS in health and disease. *Science (New York, N.Y.)*, *378*(6619), eadc9020. https://doi.org/10.1126/science.adc9020

Eninger, T., Müller, S. A., Bacioglu, M., Schweighauser, M., Lambert, M., Maia, L. F., Neher, J. J., Hornfeck, S. M., Obermüller, U., Kleinberger, G., Haass, C., Kahle, P. J., Staufenbiel, M., Ping, L., Duong, D. M., Levey, A. I., Seyfried, N. T., Lichtenthaler, S. F., Jucker, M., & Kaeser, S. A. (2022). Signatures of glial activity can be detected in the CSF proteome. *Proceedings of the National Academy of Sciences*, *119*(24), e2119804119. https://doi.org/10.1073/pnas.2119804119

Eroglu, C., & Barres, B. A. (2010). Regulation of synaptic connectivity by glia. *Nature*, *468*(7321), 223–231. https://doi.org/10.1038/nature09612

Errea, O., & Rodriguez-Oroz, M. C. (2021). Oligodendrocytes, a New Player in the Etiology of Parkinson's Disease. *Movement Disorders: Official Journal of the Movement Disorder Society*, *36*(1), 83. https://doi.org/10.1002/mds.28393

Escartin, C., Galea, E., Lakatos, A., O'Callaghan, J. P., Petzold, G. C., Serrano-Pozo, A., Steinhäuser, C., Volterra, A., Carmignoto, G., Agarwal, A., Allen, N. J., Araque, A., Barbeito, L., Barzilai, A., Bergles, D. E., Bonvento, G., Butt, A. M., Chen, W.-T., Cohen-Salmon, M., … Verkhratsky, A. (2021). Reactive astrocyte nomenclature, definitions, and future directions. *Nature Neuroscience*, *24*(3), 312–325. https://doi.org/10.1038/s41593-020-00783-4

Ettle, B., Schlachetzki, J. C. M., & Winkler, J. (2016). Oligodendroglia and Myelin in Neurodegenerative Diseases: More Than Just Bystanders? *Molecular Neurobiology*, *53*(5), 3046–3062. https://doi.org/10.1007/s12035-015-9205-3

Fahn, S. (2008). The history of dopamine and levodopa in the treatment of Parkinson's disease. *Movement Disorders: Official Journal of the Movement Disorder Society*, *23 Suppl 3*, S497-508. https://doi.org/10.1002/mds.22028

Fancy, S. P. J., Harrington, E. P., Yuen, T. J., Silbereis, J. C., Zhao, C., Baranzini, S. E., Bruce, C. C., Otero, J. J., Huang, E. J., Nusse, R., Franklin, R. J. M., & Rowitch, D. H. (2011). Axin2 as regulatory and therapeutic target in newborn brain injury and remyelination. *Nature Neuroscience*, *14*(8), 1009–1016. https://doi.org/10.1038/nn.2855

Fereshtehnejad, S.-M., Zeighami, Y., Dagher, A., & Postuma, R. B. (2017). Clinical criteria for subtyping Parkinson's disease: Biomarkers and longitudinal progression. *Brain: A Journal of Neurology*, *140*(7), 1959–1976. https://doi.org/10.1093/brain/awx118

Fernandes, H. J. R., Patikas, N., Foskolou, S., Field, S. F., Park, J.-E., Byrne, M. L., Bassett, A. R., & Metzakopian, E. (2020). Single-Cell Transcriptomics of Parkinson's Disease Human In Vitro Models Reveals Dopamine Neuron-Specific Stress Responses. *Cell Reports*, *33*(2), 108263. https://doi.org/10.1016/j.celrep.2020.108263

Fields, R. D. (2015). A new mechanism of nervous system plasticity: Activity-dependent myelination. *Nature Reviews. Neuroscience*, *16*(12), 756–767. https://doi.org/10.1038/nrn4023

Franklin, R. J. M., & Ffrench-Constant, C. (2017). Regenerating CNS myelin—From mechanisms to experimental medicines. *Nature Reviews. Neuroscience*, *18*(12), 753–769. https://doi.org/10.1038/nrn.2017.136

Frost, B., & Diamond, M. I. (2010). Prion-like mechanisms in neurodegenerative diseases. *Nature Reviews. Neuroscience*, *11*(3), 155–159. https://doi.org/10.1038/nrn2786

Funfschilling, U., Supplie, L. M., Mahad, D., Boretius, S., Saab, A. S., Edgar, J., Brinkmann, B. G., Kassmann, C. M., Tzvetanova, I. D., Mobius, W., Diaz, F., Meijer, D., Suter, U., Hamprecht, B., Sereda, M. W., Moraes, C. T., Frahm, J., Goebbels, S., & Nave, K.-A. (2012). Glycolytic oligodendrocytes maintain myelin and long-term axonal integrity. *Nature*, *485*(7399), 517–521. https://doi.org/10.1038/nature11007

Gaertner, Z., Oram, C., Schneeweis, A., Schonfeld, E., Bolduc, C., Chen, C., Dombeck, D., Parisiadou, L., Poulin, J.-F., & Awatramani, R. (n.d.). Molecular and spatial transcriptomic classification of midbrain dopamine neurons and their alterations in a LRRK2G2019S model of Parkinson's disease. *eLife*, *13*, RP101035. https://doi.org/10.7554/eLife.101035

Gao, C., Jiang, J., Tan, Y., & Chen, S. (2023). Microglia in neurodegenerative diseases: Mechanism and potential therapeutic targets. *Signal Transduction and Targeted Therapy*, *8*(1), 359. https://doi.org/10.1038/s41392-023-01588-0

Garma, L. D., Harder, L., Barba-Reyes, J. M., Marco Salas, S., Díez-Salguero, M., Nilsson, M., Serrano-Pozo, A., Hyman, B. T., & Muñoz-Manchado, A. B. (2024). Interneuron diversity in the human dorsal striatum. *Nature Communications*, *15*(1), 6164. https://doi.org/10.1038/s41467-024-50414-w

GBD 2016 Parkinson's Disease Collaborators. (2018). Global, regional, and national burden of Parkinson's disease, 1990-2016: A systematic analysis for the Global Burden of Disease Study 2016. *The Lancet. Neurology*, *17*(11), 939–953. https://doi.org/10.1016/S1474-4422(18)30295-3

Ginhoux, F., Greter, M., Leboeuf, M., Nandi, S., See, P., Gokhan, S., Mehler, M. F., Conway, S. J., Ng, L. G., Stanley, E. R., Samokhvalov, I. M., & Merad, M. (2010). Fate mapping analysis reveals that adult microglia derive from primitive macrophages. *Science (New York, N.Y.)*, *330*(6005), 841–845. https://doi.org/10.1126/science.1194637

Glass, C. K., Saijo, K., Winner, B., Marchetto, M. C., & Gage, F. H. (2010). Mechanisms underlying inflammation in neurodegeneration. *Cell*, *140*(6), 918–934. https://doi.org/10.1016/j.cell.2010.02.016

Goetz, C. G., Tilley, B. C., Shaftman, S. R., Stebbins, G. T., Fahn, S., Martinez-Martin, P., Poewe, W., Sampaio, C., Stern, M. B., Dodel, R., Dubois, B., Holloway, R., Jankovic, J., Kulisevsky, J., Lang, A. E., Lees, A., Leurgans, S., LeWitt, P. A., Nyenhuis, D., … Movement Disorder Society UPDRS Revision Task Force. (2008). Movement Disorder Society-sponsored revision of the Unified Parkinson's Disease Rating Scale (MDS-UPDRS): Scale presentation and clinimetric testing results. *Movement Disorders: Official Journal of the Movement Disorder Society*, *23*(15), 2129–2170. https://doi.org/10.1002/mds.22340

Gordon, R., Albornoz, E. A., Christie, D. C., Langley, M. R., Kumar, V., Mantovani, S., Robertson, A. A. B., Butler, M. S., Rowe, D. B., O'Neill, L. A., Kanthasamy, A. G., Schroder, K., Cooper, M. A., & Woodruff, T. M. (2018). Inflammasome inhibition prevents α-synuclein pathology

and dopaminergic neurodegeneration in mice. *Science Translational Medicine*, *10*(465), eaah4066. https://doi.org/10.1126/scitranslmed.aah4066

Grindberg, R. V., Yee-Greenbaum, J. L., McConnell, M. J., Novotny, M., O'Shaughnessy, A. L., Lambert, G. M., Araúzo-Bravo, M. J., Lee, J., Fishman, M., Robbins, G. E., Lin, X., Venepally, P., Badger, J. H., Galbraith, D. W., Gage, F. H., & Lasken, R. S. (2013). RNA-sequencing from single nuclei. *Proceedings of the National Academy of Sciences of the United States of America*, *110*(49), 19802–19807. https://doi.org/10.1073/pnas.1319700110

Guo, S., Wang, H., & Yin, Y. (2022). Microglia Polarization From M1 to M2 in Neurodegenerative Diseases. *Frontiers in Aging Neuroscience*, *14*, 815347. https://doi.org/10.3389/fnagi.2022.815347

Habib, N., Avraham-Davidi, I., Basu, A., Burks, T., Shekhar, K., Hofree, M., Choudhury, S. R., Aguet, F., Gelfand, E., Ardlie, K., Weitz, D. A., Rozenblatt-Rosen, O., Zhang, F., & Regev, A. (2017). Massively parallel single-nucleus RNA-seq with DroNc-seq. *Nature Methods*, *14*(10), 955–958. https://doi.org/10.1038/nmeth.4407

Halliday, G. M., Holton, J. L., Revesz, T., & Dickson, D. W. (2011). Neuropathology underlying clinical variability in patients with synucleinopathies. *Acta Neuropathologica*, *122*(2), 187–204. https://doi.org/10.1007/s00401-011-0852-9

Hammond, C., Bergman, H., & Brown, P. (2007). Pathological synchronization in Parkinson's disease: Networks, models and treatments. *Trends in Neurosciences*, *30*(7), 357–364. https://doi.org/10.1016/j.tins.2007.05.004

Hammond, T. R., Dufort, C., Dissing-Olesen, L., Giera, S., Young, A., Wysoker, A., Walker, A. J., Gergits, F., Segel, M., Nemesh, J., Marsh, S. E., Saunders, A., Macosko, E., Ginhoux, F., Chen, J., Franklin, R. J. M., Piao, X., McCarroll, S. A., & Stevens, B. (2019). Single cell RNA sequencing of microglia throughout the mouse lifespan and in the injured brain reveals complex cell-state changes. *Immunity*, *50*(1), 253-271.e6. https://doi.org/10.1016/j.immuni.2018.11.004

Hartline, D. K., & Colman, D. R. (2007). Rapid conduction and the evolution of giant axons and myelinated fibers. *Current Biology: CB*, *17*(1), R29-35. https://doi.org/10.1016/j.cub.2006.11.042

Hasel, P., Aisenberg, W. H., Bennett, F. C., & Liddelow, S. A. (2023). Molecular and metabolic heterogeneity of astrocytes and microglia. *Cell Metabolism*, *35*(4), 555–570. https://doi.org/10.1016/j.cmet.2023.03.006

Hely, M. A., Reid, W. G. J., Adena, M. A., Halliday, G. M., & Morris, J. G. L. (2008). The Sydney multicenter study of Parkinson's disease: The inevitability of dementia at 20 years. *Movement Disorders: Official Journal of the Movement Disorder Society*, *23*(6), 837–844. https://doi.org/10.1002/mds.21956

Heneka, M. T., Carson, M. J., El Khoury, J., Landreth, G. E., Brosseron, F., Feinstein, D. L., Jacobs, A. H., Wyss-Coray, T., Vitorica, J., Ransohoff, R. M., Herrup, K., Frautschy, S. A., Finsen, B., Brown, G. C., Verkhratsky, A., Yamanaka, K., Koistinaho, J., Latz, E., Halle, A., … Kummer, M. P. (2015). Neuroinflammation in Alzheimer's disease. *The Lancet. Neurology*, *14*(4), 388–405. https://doi.org/10.1016/S1474-4422(15)70016-5

Hirsch, E. C., & Hunot, S. (2009). Neuroinflammation in Parkinson's disease: A target for neuroprotection? *The Lancet. Neurology*, *8*(4), 382–397. https://doi.org/10.1016/S1474-4422(09)70062-6

Hoehn, M. M., & Yahr, M. D. (1967). Parkinsonism: Onset, progression and mortality. *Neurology*, *17*(5), 427–442. https://doi.org/10.1212/wnl.17.5.427

Horan-Portelance, L., Iba, M., Acri, D. J., Gibbs, J. R., & Cookson, M. R. (2024). Imaging spatial transcriptomics reveals molecular patterns of vulnerability to pathology in a transgenic α-synucleinopathy model. *bioRxiv: The Preprint Server for Biology*, 2024.07.31.606032. https://doi.org/10.1101/2024.07.31.606032

Hrvatin, S., Hochbaum, D. R., Nagy, M. A., Cicconet, M., Robertson, K., Cheadle, L., Zilionis, R., Ratner, A., Borges-Monroy, R., Klein, A. M., Sabatini, B. L., & Greenberg, M. E. (2018). Single-cell analysis of experience-dependent transcriptomic states in the mouse visual cortex. *Nature Neuroscience*, *21*(1), 120–129. https://doi.org/10.1038/s41593-017-0029-5

Iovino, L., Tremblay, M. E., & Civiero, L. (2020). Glutamate-induced excitotoxicity in Parkinson's disease: The role of glial cells. *Journal of Pharmacological Sciences*, *144*(3), 151–164. https://doi.org/10.1016/j.jphs.2020.07.011

Islam, S., Zeisel, A., Joost, S., La Manno, G., Zajac, P., Kasper, M., Lönnerberg, P., & Linnarsson, S. (2014). Quantitative single-cell RNA-seq with unique molecular identifiers. *Nature Methods*, *11*(2), 163–166. https://doi.org/10.1038/nmeth.2772

Jäkel, S., & Dimou, L. (2017). Glial Cells and Their Function in the Adult Brain: A Journey through the History of Their Ablation. *Frontiers in Cellular Neuroscience*, *11*, 24. https://doi.org/10.3389/fncel.2017.00024

Jankovic, J. (2008). Parkinson's disease: Clinical features and diagnosis. *Journal of Neurology, Neurosurgery, and Psychiatry*, *79*(4), 368–376. https://doi.org/10.1136/jnnp.2007.131045

Jiang, H., Zhang, X., Feng, S., & Feng, W. (2025). Integrated Single-Cell and Spatial Transcriptomic Analysis Identifies ISR-Related Genes Driving Immune Regulation in Parkinson's Disease. *Journal of Inflammation Research*, *18*, 9321–9341. https://doi.org/10.2147/JIR.S521744

Jin, S., Guerrero-Juarez, C. F., Zhang, L., Chang, I., Ramos, R., Kuan, C.-H., Myung, P., Plikus, M. V., & Nie, Q. (2021). Inference and analysis of cell-cell communication using CellChat. *Nature Communications*, *12*(1), 1088. https://doi.org/10.1038/s41467-021-21246-9

Joshi, A. U., Minhas, P. S., Liddelow, S. A., Haileselassie, B., Andreasson, K. I., Dorn, G. W., & Mochly-Rosen, D. (2019). Fragmented mitochondria released from microglia trigger A1 astrocytic response and propagate inflammatory neurodegeneration. *Nature Neuroscience*, *22*(10), 1635–1648. https://doi.org/10.1038/s41593-019-0486-0

Kalia, L. V., & Lang, A. E. (2015). Parkinson's disease. *Lancet (London, England)*, *386*(9996), 896–912. https://doi.org/10.1016/S0140-6736(14)61393-3

Kamath, T., Abdulraouf, A., Burris, S. J., Langlieb, J., Gazestani, V., Nadaf, N. M., Balderrama, K., Vanderburg, C., & Macosko, E. Z. (2022). Single-cell genomic profiling of human dopamine neurons identifies a population that selectively degenerates in Parkinson's disease. *Nature Neuroscience*, *25*(5), Article 5. https://doi.org/10.1038/s41593-022-01061-1

Kambey, P. A., Liu, W.-Y., Wu, J., Bosco, B., Nadeem, I., Kanwore, K., & Gao, D.-S. (2023). Single-nuclei RNA sequencing uncovers heterogenous transcriptional signatures in Parkinson's disease associated with nuclear receptor-related factor 1 defect. *Neural Regeneration Research*, *18*(9), 2037–2046. https://doi.org/10.4103/1673-5374.366493

Kędzia, D., Galita, G., Majsterek, I., & Rozpędek-Kamińska, W. (2026). Microglia, Astrocytes, and Oligodendrocytes in Parkinson's Disease: Neuroinflammatory Crosstalk and Emerging Therapeutic Strategies. *Biomolecules*, *16*(1), 156. https://doi.org/10.3390/biom16010156

Keren-Shaul, H., Spinrad, A., Weiner, A., Matcovitch-Natan, O., Dvir-Szternfeld, R., Ulland, T. K., David, E., Baruch, K., Lara-Astaiso, D., Toth, B., Itzkovitz, S., Colonna, M., Schwartz, M., & Amit, I. (2017). A Unique Microglia Type Associated with Restricting Development of Alzheimer's Disease. *Cell*, *169*(7), 1276-1290.e17. https://doi.org/10.1016/j.cell.2017.05.018

Kim, S., Pajarillo, E., Nyarko-Danquah, I., Aschner, M., & Lee, E. (2023). Role of Astrocytes in Parkinson's Disease Associated with Genetic Mutations and Neurotoxicants. *Cells*, *12*(4), 622. https://doi.org/10.3390/cells12040622

Kim, Y. S., Choi, J., & Yoon, B.-E. (2020). Neuron-Glia Interactions in Neurodevelopmental Disorders. *Cells*, *9*(10), 2176. https://doi.org/10.3390/cells9102176

Klein, A. M., Mazutis, L., Akartuna, I., Tallapragada, N., Veres, A., Li, V., Peshkin, L., Weitz, D. A., & Kirschner, M. W. (2015). Droplet barcoding for single-cell transcriptomics applied to embryonic stem cells. *Cell*, *161*(5), 1187–1201. https://doi.org/10.1016/j.cell.2015.04.044

Kordower, J. H., Olanow, C. W., Dodiya, H. B., Chu, Y., Beach, T. G., Adler, C. H., Halliday, G. M., & Bartus, R. T. (2013). Disease duration and the integrity of the nigrostriatal system in Parkinson's disease. *Brain: A Journal of Neurology*, *136*(Pt 8), 2419–2431. https://doi.org/10.1093/brain/awt192

Krasemann, S., Madore, C., Cialic, R., Baufeld, C., Calcagno, N., El Fatimy, R., Beckers, L., O'Loughlin, E., Xu, Y., Fanek, Z., Greco, D. J., Smith, S. T., Tweet, G., Humulock, Z., Zrzavy, T., Conde-Sanroman, P., Gacias, M., Weng, Z., Chen, H., … Butovsky, O. (2017). The TREM2-APOE Pathway Drives the Transcriptional Phenotype of Dysfunctional

Microglia in Neurodegenerative Diseases. *Immunity*, *47*(3), 566-581.e9. https://doi.org/10.1016/j.immuni.2017.08.008

Kuhlmann, T., Miron, V., Cui, Q., Wegner, C., Antel, J., & Brück, W. (2008). Differentiation block of oligodendroglial progenitor cells as a cause for remyelination failure in chronic multiple sclerosis. *Brain: A Journal of Neurology*, *131*(Pt 7), 1749–1758. https://doi.org/10.1093/brain/awn096

Lago-Baldaia, I., Fernandes, V. M., & Ackerman, S. D. (2020). More Than Mortar: Glia as Architects of Nervous System Development and Disease. *Frontiers in Cell and Developmental Biology*, *8*. https://doi.org/10.3389/fcell.2020.611269

Lake, B. B., Chen, S., Hoshi, M., Plongthongkum, N., Salamon, D., Knoten, A., Vijayan, A., Venkatesh, R., Kim, E. H., Gao, D., Gaut, J., Zhang, K., & Jain, S. (2019). A single-nucleus RNA-sequencing pipeline to decipher the molecular anatomy and pathophysiology of human kidneys. *Nature Communications*, *10*(1), 2832. https://doi.org/10.1038/s41467-019-10861-2

Lee, A. J., Kim, C., Park, S., Joo, J., Choi, B., Yang, D., Jun, K., Eom, J., Lee, S.-J., Chung, S. J., Rissman, R. A., Chung, J., Masliah, E., & Jung, I. (2023). Characterization of altered molecular mechanisms in Parkinson's disease through cell type–resolved multiomics analyses. *Science Advances*, *9*(15), eabo2467. https://doi.org/10.1126/sciadv.abo2467

Lee, E.-K., Kim, Y., Wei, S., Ryu, D., Hwang, N., Fang, S., & Oh, C.-M. (2025). *Deciphering Regional Transcriptomic Alterations in a 6-OHDA Rat Model of Parkinson's Disease through Integrated Single Cell and Spatial Analyses*. Research Square. https://doi.org/10.21203/rs.3.rs-6849869/v1

Li, K., Li, J., Zheng, J., & Qin, S. (2019). Reactive Astrocytes in Neurodegenerative Diseases. *Aging and Disease*, *10*(3), 664–675. https://doi.org/10.14336/AD.2018.0720

Li, Y., Xia, Y., Yin, S., Wan, F., Hu, J., Kou, L., Sun, Y., Wu, J., Zhou, Q., Huang, J., Xiong, N., & Wang, T. (2021). Targeting Microglial α-Synuclein/TLRs/NF-kappaB/NLRP3 Inflammasome Axis in Parkinson's Disease. *Frontiers in Immunology*, *12*, 719807. https://doi.org/10.3389/fimmu.2021.719807

Liang, J.-Y., Yuan, X.-L., Jiang, J.-M., Zhang, P., & Tan, K. (2025). Targeting the NLRP3 inflammasome in Parkinson's disease: From molecular mechanism to therapeutic strategy. *Experimental Neurology*, *386*, 115167. https://doi.org/10.1016/j.expneurol.2025.115167

Liddelow, S. A., Guttenplan, K. A., Clarke, L. E., Bennett, F. C., Bohlen, C. J., Schirmer, L., Bennett, M. L., Münch, A. E., Chung, W.-S., Peterson, T. C., Wilton, D. K., Frouin, A., Napier, B. A., Panicker, N., Kumar, M., Buckwalter, M. S., Rowitch, D. H., Dawson, V. L., Dawson, T. M., … Barres, B. A. (2017). Neurotoxic reactive astrocytes are induced by activated microglia. *Nature*, *541*(7638), 481–487. https://doi.org/10.1038/nature21029

Lindström, V., Gustafsson, G., Sanders, L. H., Howlett, E. H., Sigvardson, J., Kasrayan, A., Ingelsson, M., Bergström, J., & Erlandsson, A. (2017). Extensive uptake of α-synuclein oligomers in astrocytes results in sustained intracellular deposits and mitochondrial damage. *Molecular and Cellular Neurosciences*, *82*, 143–156. https://doi.org/10.1016/j.mcn.2017.04.009

Little, S., & Brown, P. (2014). The functional role of beta oscillations in Parkinson's disease. *Parkinsonism & Related Disorders*, *20 Suppl 1*, S44-48. https://doi.org/10.1016/S1353-8020(13)70013-0

Liu, S.-Y., Qiao, H.-W., Song, T.-B., Liu, X.-L., Yao, Y.-X., Zhao, C.-S., Barret, O., Xu, S.-L., Cai, Y.-N., Tamagnan, G. D., Sossi, V., Lu, J., & Chan, P. (2022). Brain microglia activation and peripheral adaptive immunity in Parkinson's disease: A multimodal PET study. *Journal of Neuroinflammation*, *19*(1), 209. https://doi.org/10.1186/s12974-022-02574-z

Lozzi, B., Huang, T.-W., Sardar, D., Huang, A. Y.-S., & Deneen, B. (2020). Regionally Distinct Astrocytes Display Unique Transcription Factor Profiles in the Adult Brain. *Frontiers in Neuroscience*, *14*, 61. https://doi.org/10.3389/fnins.2020.00061

Luk, K. C., Kehm, V., Carroll, J., Zhang, B., O'Brien, P., Trojanowski, J. Q., & Lee, V. M.-Y. (2012). Pathological α-Synuclein Transmission Initiates Parkinson-like Neurodegeneration in Non-transgenic Mice. *Science (New York, N.Y.)*, *338*(6109), 949–953. https://doi.org/10.1126/science.1227157

Ma, X., Chen, P., Wei, J., Zhang, J., Chen, C., Zhao, H., Ferguson, D., McGee, A. W., Dai, Z., & Qiu, S. (2024). Protocol for Xenium spatial transcriptomics studies using fixed frozen mouse brain sections. *STAR Protocols*, *5*(4), 103420. https://doi.org/10.1016/j.xpro.2024.103420

Macosko, E. Z., Basu, A., Satija, R., Nemesh, J., Shekhar, K., Goldman, M., Tirosh, I., Bialas, A. R., Kamitaki, N., Martersteck, E. M., Trombetta, J. J., Weitz, D. A., Sanes, J. R., Shalek, A. K., Regev, A., & McCarroll, S. A. (2015). Highly Parallel Genome-wide Expression Profiling of Individual Cells Using Nanoliter Droplets. *Cell*, *161*(5), 1202–1214. https://doi.org/10.1016/j.cell.2015.05.002

Mahmoud, S., Gharagozloo, M., Simard, C., & Gris, D. (2019). Astrocytes Maintain Glutamate Homeostasis in the CNS by Controlling the Balance between Glutamate Uptake and Release. *Cells*, *8*(2), 184. https://doi.org/10.3390/cells8020184

Marco Salas, S., Kuemmerle, L. B., Mattsson-Langseth, C., Tismeyer, S., Avenel, C., Hu, T., Rehman, H., Grillo, M., Czarnewski, P., Helgadottir, S., Tiklova, K., Andersson, A., Rafati, N., Chatzinikolaou, M., Theis, F. J., Luecken, M. D., Wählby, C., Ishaque, N., & Nilsson, M. (2025). Optimizing Xenium In Situ data utility by quality assessment and best-practice analysis workflows. *Nature Methods*, *22*(4), 813–823. https://doi.org/10.1038/s41592-025-02617-2

Marras, C., Hincapié, C. A., Kristman, V. L., Cancelliere, C., Soklaridis, S., Li, A., Borg, J., af Geijerstam, J.-L., & Cassidy, J. D. (2014). Systematic review of the risk of Parkinson's disease after mild traumatic brain injury: Results of the International Collaboration on Mild Traumatic Brain Injury Prognosis. *Archives of Physical Medicine and Rehabilitation*, *95*(3 Suppl), S238-244. https://doi.org/10.1016/j.apmr.2013.08.298

Martins-Ferreira, R., Calafell-Segura, J., Leal, B., Rodríguez-Ubreva, J., Martínez-Saez, E., Mereu, E., Pinho E Costa, P., Laguna, A., & Ballestar, E. (2025). The Human Microglia Atlas (HuMicA) unravels changes in disease-associated microglia subsets across neurodegenerative conditions. *Nature Communications*, *16*(1), 739. https://doi.org/10.1038/s41467-025-56124-1

Martirosyan, A., Ansari, R., Pestana, F., Hebestreit, K., Gasparyan, H., Aleksanyan, R., Hnatova, S., Poovathingal, S., Marneffe, C., Thal, D. R., Kottick, A., Hanson-Smith, V. J., Guelfi, S.,

Plumbly, W., Belgard, T. G., Metzakopian, E., & Holt, M. G. (2024). Correction: Unravelling cell type-specific responses to Parkinson's Disease at single cell resolution. *Molecular Neurodegeneration*, *19*(1), 28. https://doi.org/10.1186/s13024-024-00717-9

Masuda, T., Sankowski, R., Staszewski, O., & Prinz, M. (2020). Microglia Heterogeneity in the Single-Cell Era. *Cell Reports*, *30*(5), 1271–1281. https://doi.org/10.1016/j.celrep.2020.01.010

Mathys, H., Davila-Velderrain, J., Peng, Z., Gao, F., Mohammadi, S., Young, J. Z., Menon, M., He, L., Abdurrob, F., Jiang, X., Martorell, A. J., Ransohoff, R. M., Hafler, B. P., Bennett, D. A., Kellis, M., & Tsai, L.-H. (2019a). Single-cell transcriptomic analysis of Alzheimer's disease. *Nature*, *570*(7761), 332–337. https://doi.org/10.1038/s41586-019-1195-2

Mathys, H., Davila-Velderrain, J., Peng, Z., Gao, F., Mohammadi, S., Young, J. Z., Menon, M., He, L., Abdurrob, F., Jiang, X., Martorell, A. J., Ransohoff, R. M., Hafler, B. P., Bennett, D. A., Kellis, M., & Tsai, L.-H. (2019b). Single-cell transcriptomic analysis of Alzheimer's disease. *Nature*, *570*(7761), 332–337. https://doi.org/10.1038/s41586-019-1195-2

May, V. E. L., Ettle, B., Poehler, A.-M., Nuber, S., Ubhi, K., Rockenstein, E., Winner, B., Wegner, M., Masliah, E., & Winkler, J. (2014). α-Synuclein impairs oligodendrocyte progenitor maturation in multiple system atrophy. *Neurobiology of Aging*, *35*(10), 2357–2368. https://doi.org/10.1016/j.neurobiolaging.2014.02.028

Mazzulli, J. R., Xu, Y.-H., Sun, Y., Knight, A. L., McLean, P. J., Caldwell, G. A., Sidransky, E., Grabowski, G. A., & Krainc, D. (2011). Gaucher disease glucocerebrosidase and α-synuclein form a bidirectional pathogenic loop in synucleinopathies. *Cell*, *146*(1), 37–52. https://doi.org/10.1016/j.cell.2011.06.001

Mei, F., Fancy, S. P. J., Shen, Y.-A. A., Niu, J., Zhao, C., Presley, B., Miao, E., Lee, S., Mayoral, S. R., Redmond, S. A., Etxeberria, A., Xiao, L., Franklin, R. J. M., Green, A., Hauser, S. L., & Chan, J. R. (2014). Micropillar arrays as a high-throughput screening platform for therapeutics in multiple sclerosis. *Nature Medicine*, *20*(8), 954–960. https://doi.org/10.1038/nm.3618

Menu, P., & Vince, J. E. (2011). The NLRP3 inflammasome in health and disease: The good, the bad and the ugly. *Clinical and Experimental Immunology*, *166*(1), 1–15. https://doi.org/10.1111/j.1365-2249.2011.04440.x

Nalls, M. A., Blauwendraat, C., Vallerga, C. L., Heilbron, K., Bandres-Ciga, S., Chang, D., Tan, M., Kia, D. A., Noyce, A. J., Xue, A., Bras, J., Young, E., von Coelln, R., Simón-Sánchez, J., Schulte, C., Sharma, M., Krohn, L., Pihlstrom, L., Siitonen, A., … Singleton, A. B. (2019). Identification of novel risk loci, causal insights, and heritable risk for Parkinson's disease: A meta-genome wide association study. *The Lancet. Neurology*, *18*(12), 1091–1102. https://doi.org/10.1016/S1474-4422(19)30320-5

Nave, K.-A. (2010). Myelination and the trophic support of long axons. *Nature Reviews. Neuroscience*, *11*(4), 275–283. https://doi.org/10.1038/nrn2797

Nave, K.-A., & Werner, H. B. (2014). Myelination of the nervous system: Mechanisms and functions. *Annual Review of Cell and Developmental Biology*, *30*, 503–533. https://doi.org/10.1146/annurev-cellbio-100913-013101

Nimmerjahn, A., Kirchhoff, F., & Helmchen, F. (2005). Resting microglial cells are highly dynamic surveillants of brain parenchyma in vivo. *Science*, *308*(5726), 1314–1318. https://doi.org/10.1126/science.1110647

Nishiyama, A., Komitova, M., Suzuki, R., & Zhu, X. (2009). Polydendrocytes (NG2 cells): Multifunctional cells with lineage plasticity. *Nature Reviews. Neuroscience*, *10*(1), 9–22. https://doi.org/10.1038/nrn2495

Olah, M., Menon, V., Habib, N., Taga, M. F., Ma, Y., Yung, C. J., Cimpean, M., Khairallah, A., Coronas-Samano, G., Sankowski, R., Grün, D., Kroshilina, A. A., Dionne, D., Sarkis, R. A., Cosgrove, G. R., Helgager, J., Golden, J. A., Pennell, P. B., Prinz, M., … De Jager, P. L. (2020). Single cell RNA sequencing of human microglia uncovers a subset associated with Alzheimer's disease. *Nature Communications*, *11*(1), 6129. https://doi.org/10.1038/s41467-020-19737-2

Olanow, C. W., Stern, M. B., & Sethi, K. (2009). The scientific and clinical basis for the treatment of Parkinson disease (2009). *Neurology*, *72*(21 Suppl 4), S1-136. https://doi.org/10.1212/WNL.0b013e3181a1d44c

Ouchi, Y., Yoshikawa, E., Sekine, Y., Futatsubashi, M., Kanno, T., Ogusu, T., & Torizuka, T. (2005). Microglial activation and dopamine terminal loss in early Parkinson's disease. *Annals of Neurology*, *57*(2), 168–175. https://doi.org/10.1002/ana.20338

Overview of Xenium Algorithms | Official 10x Genomics Support. (n.d.). 10x Genomics. Retrieved April 27, 2026, from https://www.10xgenomics.com/support/software/xenium-onboard-analysis/2.0/algorithms-overview/xoa-algorithms

Palla, G., Spitzer, H., Klein, M., Fischer, D., Schaar, A. C., Kuemmerle, L. B., Rybakov, S., Ibarra, I. L., Holmberg, O., Virshup, I., Lotfollahi, M., Richter, S., & Theis, F. J. (2022). Squidpy: A scalable framework for spatial omics analysis. *Nature Methods*, *19*(2), Article 2. https://doi.org/10.1038/s41592-021-01358-2

Paolicelli, R. C., Bolasco, G., Pagani, F., Maggi, L., Scianni, M., Panzanelli, P., Giustetto, M., Ferreira, T. A., Guiducci, E., Dumas, L., Ragozzino, D., & Gross, C. T. (2011). Synaptic pruning by microglia is necessary for normal brain development. *Science*, *333*(6048), 1456–1458. https://doi.org/10.1126/science.1202529

Paolicelli, R. C., Sierra, A., Stevens, B., Tremblay, M.-E., Aguzzi, A., Ajami, B., Amit, I., Audinat, E., Bechmann, I., Bennett, M., Bennett, F., Bessis, A., Biber, K., Bilbo, S., Blurton-Jones, M., Boddeke, E., Brites, D., Brône, B., Brown, G. C., … Wyss-Coray, T. (2022). Microglia states and nomenclature: A field at its crossroads. *Neuron*, *110*(21), 3458–3483. https://doi.org/10.1016/j.neuron.2022.10.020

Parkinson, J. (2002). An essay on the shaking palsy. 1817. *The Journal of Neuropsychiatry and Clinical Neurosciences*, *14*(2), 223–236; discussion 222. https://doi.org/10.1176/jnp.14.2.223

Pellerin, L., & Magistretti, P. J. (1994). Glutamate uptake into astrocytes stimulates aerobic glycolysis: A mechanism coupling neuronal activity to glucose utilization. *Proceedings of the*

National Academy of Sciences of the United States of America, *91*(22), 10625–10629. https://doi.org/10.1073/pnas.91.22.10625

Philips, T., & Rothstein, J. D. (2017). Oligodendroglia: Metabolic supporters of neurons. *The Journal of Clinical Investigation*, *127*(9), 3271–3280. https://doi.org/10.1172/JCI90610

Pike, A. F., Varanita, T., Herrebout, M. A. C., Plug, B. C., Kole, J., Musters, R. J. P., Teunissen, C. E., Hoozemans, J. J. M., Bubacco, L., & Veerhuis, R. (2021). α-Synuclein evokes NLRP3 inflammasome-mediated IL-1β secretion from primary human microglia. *Glia*, *69*(6), 1413–1428. https://doi.org/10.1002/glia.23970

Poewe, W., Seppi, K., Tanner, C. M., Halliday, G. M., Brundin, P., Volkmann, J., Schrag, A.-E., & Lang, A. E. (2017). Parkinson disease. *Nature Reviews. Disease Primers*, *3*, 17013. https://doi.org/10.1038/nrdp.2017.13

Postuma, R. B., Berg, D., Stern, M., Poewe, W., Olanow, C. W., Oertel, W., Obeso, J., Marek, K., Litvan, I., Lang, A. E., Halliday, G., Goetz, C. G., Gasser, T., Dubois, B., Chan, P., Bloem, B. R., Adler, C. H., & Deuschl, G. (2015). MDS clinical diagnostic criteria for Parkinson's disease. *Movement Disorders: Official Journal of the Movement Disorder Society*, *30*(12), 1591–1601. https://doi.org/10.1002/mds.26424

Poulin, J.-F., Zou, J., Drouin-Ouellet, J., Kim, K.-Y. A., Cicchetti, F., & Awatramani, R. B. (2014). Defining midbrain dopaminergic neuron diversity by single-cell gene expression profiling. *Cell Reports*, *9*(3), 930–943. https://doi.org/10.1016/j.celrep.2014.10.008

Prinz, M., Masuda, T., Wheeler, M. A., & Quintana, F. J. (2021). Microglia and Central Nervous System–Associated Macrophages—From Origin to Disease Modulation. *Annual Review of Immunology*, *39*(Volume 39, 2021), 251–277. https://doi.org/10.1146/annurev-immunol-093019-110159

Ransohoff, R. M. (2016). A polarizing question: Do M1 and M2 microglia exist? *Nature Neuroscience*, *19*(8), 987–991. https://doi.org/10.1038/nn.4338

Rasband, M. N., & Peles, E. (2015). The Nodes of Ranvier: Molecular Assembly and Maintenance. *Cold Spring Harbor Perspectives in Biology*, *8*(3), a020495. https://doi.org/10.1101/cshperspect.a020495

Reynolds, R. H., Botía, J., Nalls, M. A., Hardy, J., Gagliano Taliun, S. A., & Ryten, M. (2019). Moving beyond neurons: The role of cell type-specific gene regulation in Parkinson's disease heritability. *Npj Parkinson's Disease*, *5*(1), 6. https://doi.org/10.1038/s41531-019-0076-6

Richardson, W. D., Young, K. M., Tripathi, R. B., & McKenzie, I. (2011). NG2-glia as multipotent neural stem cells: Fact or fantasy? *Neuron*, *70*(4), 661–673. https://doi.org/10.1016/j.neuron.2011.05.013

Richter-Landsberg, C., & Leyk, J. (2013). Inclusion body formation, macroautophagy, and the role of HDAC6 in neurodegeneration. *Acta Neuropathologica*, *126*(6), 793–807. https://doi.org/10.1007/s00401-013-1158-x

Rodriques, S. G., Stickels, R. R., Goeva, A., Martin, C. A., Murray, E., Vanderburg, C. R., Welch, J., Chen, L. M., Chen, F., & Macosko, E. Z. (2019). Slide-seq: A scalable technology for measuring genome-wide expression at high spatial resolution. *Science*, *363*(6434), 1463–1467. https://doi.org/10.1126/science.aaw1219

Rohan, Z., Milenkovic, I., Lutz, M. I., Matej, R., & Kovacs, G. G. (2016). Shared and Distinct Patterns of Oligodendroglial Response in α-Synucleinopathies and Tauopathies. *Journal of Neuropathology and Experimental Neurology*, *75*(12), 1100–1109. https://doi.org/10.1093/jnen/nlw087

Sadick, J. S., O'Dea, M. R., Hasel, P., Dykstra, T., Faustin, A., & Liddelow, S. A. (2022). Astrocytes and oligodendrocytes undergo subtype-specific transcriptional changes in Alzheimer's disease. *Neuron*, *110*(11), 1788-1805.e10. https://doi.org/10.1016/j.neuron.2022.03.008

Salazar Campos, J. M., Burbulla, L. F., & Jäkel, S. (2025). Are oligodendrocytes bystanders or drivers of Parkinson's disease pathology? *PLOS Biology*, *23*(1), e3002977. https://doi.org/10.1371/journal.pbio.3002977

Sanchez-Guajardo, V., Barnum, C. J., Tansey, M. G., & Romero-Ramos, M. (2013). Neuroimmunological processes in Parkinson's disease and their relation to α-synuclein: Microglia as the referee between neuronal processes and peripheral immunity. *ASN NEURO*, *5*(2), e00112. https://doi.org/10.1042/AN20120066

Sankowski, R., Süß, P., Benkendorff, A., Böttcher, C., Fernandez-Zapata, C., Chhatbar, C., Cahueau, J., Monaco, G., Gasull, A. D., Khavaran, A., Grauvogel, J., Scheiwe, C., Shah, M. J., Heiland, D. H., Schnell, O., Markfeld-Erol, F., Kunze, M., Zeiser, R., Priller, J., & Prinz, M. (2024). Multiomic spatial landscape of innate immune cells at human central nervous system borders. *Nature Medicine*, *30*(1), 186–198. https://doi.org/10.1038/s41591-023-02673-1

Scelsi, C. L., Rahim, T. A., Morris, J. A., Kramer, G. J., Gilbert, B. C., & Forseen, S. E. (2020). The Lateral Ventricles: A Detailed Review of Anatomy, Development, and Anatomic Variations. *AJNR. American Journal of Neuroradiology*, *41*(4), 566–572. https://doi.org/10.3174/ajnr.A6456

Schafer, D. P., Lehrman, E. K., Kautzman, A. G., Koyama, R., Mardinly, A. R., Yamasaki, R., Ransohoff, R. M., Greenberg, M. E., Barres, B. A., & Stevens, B. (2012). Microglia Sculpt Postnatal Neural Circuits in an Activity and Complement-Dependent Manner. *Neuron*, *74*(4), 691–705. https://doi.org/10.1016/j.neuron.2012.03.026

Schapira, A. H. (1993). Mitochondrial complex I deficiency in Parkinson's disease. *Advances in Neurology*, *60*, 288–291.

Schapira, A. H. V. (2015). Glucocerebrosidase and Parkinson disease: Recent advances. *Molecular and Cellular Neurosciences*, *66*(Pt A), 37–42. https://doi.org/10.1016/j.mcn.2015.03.013

Schenck, C. H., Boeve, B. F., & Mahowald, M. W. (2013). Delayed emergence of a parkinsonian disorder or dementia in 81% of older men initially diagnosed with idiopathic rapid eye movement sleep behavior disorder: A 16-year update on a previously reported series. *Sleep Medicine*, *14*(8), 744–748. https://doi.org/10.1016/j.sleep.2012.10.009

Serrano-Pozo, A., Li, H., Li, Z., Muñoz-Castro, C., Jaisa-aad, M., Healey, M. A., Welikovitch, L. A., Jayakumar, R., Bryant, A. G., Noori, A., Connors, T. R., Hu, M., Zhao, K., Liao, F., Lin, G., Pastika, T., Tamm, J., Abdourahman, A., Kwon, T., … Das, S. (2024). Astrocyte transcriptomic changes along the spatiotemporal progression of Alzheimer's disease. *Nature Neuroscience*, *27*(12), 2384–2400. https://doi.org/10.1038/s41593-024-01791-4

Shah, S., Lubeck, E., Zhou, W., & Cai, L. (2016). In Situ Transcription Profiling of Single Cells Reveals Spatial Organization of Cells in the Mouse Hippocampus. *Neuron*, *92*(2), 342–357. https://doi.org/10.1016/j.neuron.2016.10.001

Shin, J. H., Ruhno, K. E., Shin, C., Kim, H. J., Nam, S. J., Chung, S. J., Moon, J. H., & Kim, H.-J. (2025). Distinct spatial transcriptomic patterns of substantia Nigra in Parkinson disease and Parkinsonian subtype of multiple system atrophy. *Acta Neuropathologica Communications*, *13*(1), 193. https://doi.org/10.1186/s40478-025-02107-8

Shokr, M. M. (2025). "Rewiring brain immunity: Targeting microglial metabolism for neuroprotection in neurodegenerative disorders." *Metabolic Brain Disease*, *40*(8), 326. https://doi.org/10.1007/s11011-025-01739-y

Sierra, A., Beccari, S., Diaz-Aparicio, I., Encinas, J. M., Comeau, S., & Tremblay, M.-È. (2014). Surveillance, Phagocytosis, and Inflammation: How Never-Resting Microglia Influence Adult Hippocampal Neurogenesis. *Neural Plasticity*, *2014*, 610343. https://doi.org/10.1155/2014/610343

Silver, J., & Miller, J. H. (2004). Regeneration beyond the glial scar. *Nature Reviews. Neuroscience*, *5*(2), 146–156. https://doi.org/10.1038/nrn1326

Smajić, S., Prada-Medina, C. A., Landoulsi, Z., Ghelfi, J., Delcambre, S., Dietrich, C., Jarazo, J., Henck, J., Balachandran, S., Pachchek, S., Morris, C. M., Antony, P., Timmermann, B., Sauer, S., Pereira, S. L., Schwamborn, J. C., May, P., Grünewald, A., & Spielmann, M. (2022). Single-cell sequencing of human midbrain reveals glial activation and a Parkinson-specific neuronal state. *Brain*, *145*(3), 964–978. https://doi.org/10.1093/brain/awab446

Sofroniew, M. V., & Vinters, H. V. (2010). Astrocytes: Biology and pathology. *Acta Neuropathologica*, *119*(1), 7–35. https://doi.org/10.1007/s00401-009-0619-8

Sonninen, T.-M., Hämäläinen, R. H., Koskuvi, M., Oksanen, M., Shakirzyanova, A., Wojciechowski, S., Puttonen, K., Naumenko, N., Goldsteins, G., Laham-Karam, N., Lehtonen, M., Tavi, P., Koistinaho, J., & Lehtonen, Š. (2020). Metabolic alterations in Parkinson's disease astrocytes. *Scientific Reports*, *10*(1), 14474. https://doi.org/10.1038/s41598-020-71329-8

Sorrells, S. F., Paredes, M. F., Cebrian-Silla, A., Sandoval, K., Qi, D., Kelley, K. W., James, D., Mayer, S., Chang, J., Auguste, K. I., Chang, E. F., Gutierrez, A. J., Kriegstein, A. R., Mathern, G. W., Oldham, M. C., Huang, E. J., Garcia-Verdugo, J. M., Yang, Z., & Alvarez-Buylla, A. (2018). Human hippocampal neurogenesis drops sharply in children to undetectable levels in adults. *Nature*, *555*(7696), 377–381. https://doi.org/10.1038/nature25975

Spillantini, M. G., Schmidt, M. L., Lee, V. M., Trojanowski, J. Q., Jakes, R., & Goedert, M. (1997). Alpha-synuclein in Lewy bodies. *Nature*, *388*(6645), 839–840. https://doi.org/10.1038/42166

Stackhouse, T. L., & Mishra, A. (2021). Neurovascular Coupling in Development and Disease: Focus on Astrocytes. *Frontiers in Cell and Developmental Biology*, *9*, 702832. https://doi.org/10.3389/fcell.2021.702832

Ståhl, P. L., Salmén, F., Vickovic, S., Lundmark, A., Navarro, J. F., Magnusson, J., Giacomello, S., Asp, M., Westholm, J. O., Huss, M., Mollbrink, A., Linnarsson, S., Codeluppi, S., Borg, Å., Pontén, F., Costea, P. I., Sahlén, P., Mulder, J., Bergmann, O., … Frisén, J. (2016). Visualization and analysis of gene expression in tissue sections by spatial transcriptomics. *Science*, *353*(6294), 78–82. https://doi.org/10.1126/science.aaf2403

Stassen, S. V., Kobashi, M., Lam, E. Y., Huang, Y., Ho, J. W. K., & Tsia, K. K. (2024). StaVia: Spatially and temporally aware cartography with higher-order random walks for cell atlases. *Genome Biology*, *25*(1), 224. https://doi.org/10.1186/s13059-024-03347-y

Street, K., Risso, D., Fletcher, R. B., Das, D., Ngai, J., Yosef, N., Purdom, E., & Dudoit, S. (2018). Slingshot: Cell lineage and pseudotime inference for single-cell transcriptomics. *BMC Genomics*, *19*(1), 477. https://doi.org/10.1186/s12864-018-4772-0

Su, D., Cui, Y., He, C., Yin, P., Bai, R., Zhu, J., Lam, J. S. T., Zhang, J., Yan, R., Zheng, X., Wu, J., Zhao, D., Wang, A., Zhou, M., & Feng, T. (2025). Projections for prevalence of Parkinson's disease and its driving factors in 195 countries and territories to 2050: Modelling study of Global Burden of Disease Study 2021. *BMJ*, *388*, e080952. https://doi.org/10.1136/bmj-2024-080952

Subramanian, A., Tamayo, P., Mootha, V. K., Mukherjee, S., Ebert, B. L., Gillette, M. A., Paulovich, A., Pomeroy, S. L., Golub, T. R., Lander, E. S., & Mesirov, J. P. (2005). Gene set enrichment analysis: A knowledge-based approach for interpreting genome-wide expression profiles. *Proceedings of the National Academy of Sciences of the United States of America*, *102*(43), 15545–15550. https://doi.org/10.1073/pnas.0506580102

Sun, R., & Jiang, H. (2024). Border-associated macrophages in the central nervous system. *Journal of Neuroinflammation*, *21*(1), 67. https://doi.org/10.1186/s12974-024-03059-x

Tang, F., Barbacioru, C., Wang, Y., Nordman, E., Lee, C., Xu, N., Wang, X., Bodeau, J., Tuch, B. B., Siddiqui, A., Lao, K., & Surani, M. A. (2009). mRNA-Seq whole-transcriptome analysis of a single cell. *Nature Methods*, *6*(5), 377–382. https://doi.org/10.1038/nmeth.1315

Tanner, C. M., Kamel, F., Ross, G. W., Hoppin, J. A., Goldman, S. M., Korell, M., Marras, C., Bhudhikanok, G. S., Kasten, M., Chade, A. R., Comyns, K., Richards, M. B., Meng, C., Priestley, B., Fernandez, H. H., Cambi, F., Umbach, D. M., Blair, A., Sandler, D. P., & Langston, J. W. (2011). Rotenone, paraquat, and Parkinson's disease. *Environmental Health Perspectives*, *119*(6), 866–872. https://doi.org/10.1289/ehp.1002839

Tansey, M. G., & Goldberg, M. S. (2010). Neuroinflammation in Parkinson's disease: Its role in neuronal death and implications for therapeutic intervention. *Neurobiology of Disease*, *37*(3), 510–518. https://doi.org/10.1016/j.nbd.2009.11.004

Tansey, M. G., Wallings, R. L., Houser, M. C., Herrick, M. K., Keating, C. E., & Joers, V. (2022). Inflammation and immune dysfunction in Parkinson disease. *Nature Reviews Immunology*, *22*(11), 657–673. https://doi.org/10.1038/s41577-022-00684-6

Tiklová, K., Nolbrant, S., Fiorenzano, A., Björklund, Å. K., Sharma, Y., Heuer, A., Gillberg, L., Hoban, D. B., Cardoso, T., Adler, A. F., Birtele, M., Lundén-Miguel, H., Volakakis, N., Kirkeby, A., Perlmann, T., & Parmar, M. (2020). Single cell transcriptomics identifies stem cell-derived graft composition in a model of Parkinson's disease. *Nature Communications*, *11*(1), 2434. https://doi.org/10.1038/s41467-020-16225-5

Trainor, A. R., MacDonald, D. S., & Penney, J. (2024). Microglia: Roles and genetic risk in Parkinson's disease. *Frontiers in Neuroscience*, *18*, 1506358. https://doi.org/10.3389/fnins.2024.1506358

Trapnell, C. (2015). Defining cell types and states with single-cell genomics. *Genome Research*, *25*(10), 1491–1498. https://doi.org/10.1101/gr.190595.115

Tremblay, M.-E., Cookson, M. R., & Civiero, L. (2019). Glial phagocytic clearance in Parkinson's disease. *Molecular Neurodegeneration*, *14*(1), 16. https://doi.org/10.1186/s13024-019-0314-8

Tsunemi, T., Ishiguro, Y., Yoroisaka, A., Valdez, C., Miyamoto, K., Ishikawa, K., Saiki, S., Akamatsu, W., Hattori, N., & Krainc, D. (2020). Astrocytes Protect Human Dopaminergic Neurons from α-Synuclein Accumulation and Propagation. *The Journal of Neuroscience: The Official Journal of the Society for Neuroscience*, *40*(45), 8618–8628. https://doi.org/10.1523/JNEUROSCI.0954-20.2020

Van de Sande, B., Flerin, C., Davie, K., De Waegeneer, M., Hulselmans, G., Aibar, S., Seurinck, R., Saelens, W., Cannoodt, R., Rouchon, Q., Verbeiren, T., De Maeyer, D., Reumers, J., Saeys, Y., & Aerts, S. (2020). A scalable SCENIC workflow for single-cell gene regulatory network analysis. *Nature Protocols*, *15*(7), Article 7. https://doi.org/10.1038/s41596-020-0336-2

Vecchiarelli, H. A., & Tremblay, M.-È. (2023). Microglial Transcriptional Signatures in the Central Nervous System: Toward A Future of Unraveling Their Function in Health and Disease. *Annual Review of Genetics*, *57*, 65–86. https://doi.org/10.1146/annurev-genet-022223-093643

Verkhratsky, A., & Nedergaard, M. (2018). Physiology of Astroglia. *Physiological Reviews*, *98*(1), 239–389. https://doi.org/10.1152/physrev.00042.2016

Viganò, F., & Dimou, L. (2016). The heterogeneous nature of NG2-glia. *Brain Research*, *1638*(Pt B), 129–137. https://doi.org/10.1016/j.brainres.2015.09.012

Vishnumukkala, T., Che Mohd Nassir, C. M. N., Hein, Z. M., Kalerammana Gopalakrishna, P., Karikalan, B., Alkatiri, A., Jagadeesan, S., Naik, V. R., Thomas, W., Mohd Moklas, M. A., & Kamaruzzaman, M. A. (2025). Glial Cells as Emerging Therapeutic Targets in Neurodegenerative Diseases: Mechanistic Insights and Translational Perspectives. *Cells*, *14*(19), 1497. https://doi.org/10.3390/cells14191497

Wakabayashi, K., Hayashi, S., Yoshimoto, M., Kudo, H., & Takahashi, H. (2000). NACP/α-synuclein-positive filamentous inclusions in astrocytes and oligodendrocytes of Parkinson's disease brains. *Acta Neuropathologica*, *99*(1), 14–20. https://doi.org/10.1007/PL00007400

Wang, J., Wang, F., Mai, D., & Qu, S. (2020). Molecular Mechanisms of Glutamate Toxicity in Parkinson's Disease. *Frontiers in Neuroscience*, *14*, 585584. https://doi.org/10.3389/fnins.2020.585584

Wang, Q., Wang, M., Choi, I., Sarrafha, L., Liang, M., Ho, L., Farrell, K., Beaumont, K. G., Sebra, R., De Sanctis, C., Crary, J. F., Ahfeldt, T., Blanchard, J., Neavin, D., Powell, J., Davis, D. A., Sun, X., Zhang, B., & Yue, Z. (2024). Molecular profiling of human substantia nigra identifies diverse neuron types associated with vulnerability in Parkinson's disease. *Science Advances*, *10*(2), eadi8287. https://doi.org/10.1126/sciadv.adi8287

Wolf, F. A., Angerer, P., & Theis, F. J. (2018). SCANPY: Large-scale single-cell gene expression data analysis. *Genome Biology*, *19*(1), 15. https://doi.org/10.1186/s13059-017-1382-0

Wolock, S. L., Lopez, R., & Klein, A. M. (2019). Scrublet: Computational Identification of Cell Doublets in Single-Cell Transcriptomic Data. *Cell Systems*, *8*(4), 281-291.e9. https://doi.org/10.1016/j.cels.2018.11.005

Xu, J., Farsad, H. L., Hou, Y., Barclay, K., Lopez, B. A., Yamada, S., Saliu, I. O., Shi, Y., Knight, W. C., Bateman, R. J., Benzinger, T. L. S., Yi, J. J., Li, Q., Wang, T., Perlmutter, J. S., Morris, J. C., & Zhao, G. (2023). Human striatal glia differentially contribute to AD- and PD-specific neurodegeneration. *Nature Aging*, *3*(3), Article 3. https://doi.org/10.1038/s43587-023-00363-8

Yaqubi, M., Groh, A. M. R., Dorion, M.-F., Afanasiev, E., Luo, J. X. X., Hashemi, H., Sinha, S., Kieran, N. W., Blain, M., Cui, Q.-L., Biernaskie, J., Srour, M., Dudley, R., Hall, J. A., Sonnen, J. A., Arbour, N., Prat, A., Stratton, J. A., Antel, J., & Healy, L. M. (2023). Analysis of the microglia transcriptome across the human lifespan using single cell RNA sequencing. *Journal of Neuroinflammation*, *20*(1), 132. https://doi.org/10.1186/s12974-023-02809-7

Youle, R. J., & Narendra, D. P. (2011). Mechanisms of mitophagy. *Nature Reviews Molecular Cell Biology*, *12*(1), 9–14. https://doi.org/10.1038/nrm3028

Yun, S. P., Kam, T.-I., Panicker, N., Kim, S., Oh, Y., Park, J.-S., Kwon, S.-H., Park, Y. J., Karuppagounder, S. S., Park, H., Kim, S., Oh, N., Kim, N. A., Lee, S., Brahmachari, S., Mao, X., Lee, J. H., Kumar, M., An, D., … Ko, H. S. (2018). Block of A1 astrocyte conversion by microglia is neuroprotective in models of Parkinson's disease. *Nature Medicine*, *24*(7), 931–938. https://doi.org/10.1038/s41591-018-0051-5

Zeisel, A., Hochgerner, H., Lönnerberg, P., Johnsson, A., Memic, F., van der Zwan, J., Häring, M., Braun, E., Borm, L. E., La Manno, G., Codeluppi, S., Furlan, A., Lee, K., Skene, N., Harris, K. D., Hjerling-Leffler, J., Arenas, E., Ernfors, P., Marklund, U., & Linnarsson, S. (2018). Molecular Architecture of the Mouse Nervous System. *Cell*, *174*(4), 999-1014.e22. https://doi.org/10.1016/j.cell.2018.06.021

Zhang, H., Li, X., Liao, D., Luo, P., & Jiang, X. (2021). Alpha/Beta-Hydrolase Domain-Containing 6: Signaling and Function in the Central Nervous System. *Frontiers in Pharmacology*, *12*, 784202. https://doi.org/10.3389/fphar.2021.784202

Zhang, S., Yan, M., Jiang, X., Liu, Y., Ma, W., Ding, L., Lu, Z., Luo, Y., Tian, X., & Wang, Q. (2025). Oligodendrocyte-astrocyte crosstalk in Parkinson's disease mediates neuronal ferroptosis via the FGF signaling pathway. *Npj Parkinson's Disease*, *11*(1), 136. https://doi.org/10.1038/s41531-025-00995-0

Zhang, X., Zhang, R., Nisa Awan, M. U., & Bai, J. (2022). The Mechanism and Function of Glia in Parkinson's Disease. *Frontiers in Cellular Neuroscience*, *16*. https://doi.org/10.3389/fncel.2022.903469

Zheng, G. X. Y., Terry, J. M., Belgrader, P., Ryvkin, P., Bent, Z. W., Wilson, R., Ziraldo, S. B., Wheeler, T. D., McDermott, G. P., Zhu, J., Gregory, M. T., Shuga, J., Montesclaros, L., Underwood, J. G., Masquelier, D. A., Nishimura, S. Y., Schnall-Levin, M., Wyatt, P. W., Hindson, C. M., … Bielas, J. H. (2017). Massively parallel digital transcriptional profiling of single cells. *Nature Communications*, *8*, 14049. https://doi.org/10.1038/ncomms14049

Zhou, B., Zuo, Y.-X., & Jiang, R.-T. (2019). Astrocyte morphology: Diversity, plasticity, and role in neurological diseases. *CNS Neuroscience & Therapeutics*, *25*(6), 665–673. https://doi.org/10.1111/cns.13123

Zhu, B., Park, J.-M., Coffey, S. R., Russo, A., Hsu, I.-U., Wang, J., Su, C., Chang, R., Lam, T. T., Gopal, P. P., Ginsberg, S. D., Zhao, H., Hafler, D. A., Chandra, S. S., & Zhang, L. (2024). Single-cell transcriptomic and proteomic analysis of Parkinson's disease brains. *Science Translational Medicine*, *16*(771), eabo1997. https://doi.org/10.1126/scitranslmed.abo1997

Zhu, J., Cui, Y., Zhang, J., Yan, R., Su, D., Zhao, D., Wang, A., & Feng, T. (2024). Temporal trends in the prevalence of Parkinson's disease from 1980 to 2023: A systematic review and meta-analysis. *The Lancet. Healthy Longevity*, *5*(7), e464–e479. https://doi.org/10.1016/S2666-7568(24)00094-1

12. Acknowledgements

Esta tesis no habría sido posible sin el apoyo de ciertas personas. En primer lugar, quiero agradecer a mi tutora Ana Muñoz, por haberme guiado y ayudado durante todo este trabajo. También por haberme dado siempre libertad en cuanto a proponer ideas y hacer que mi opinión cuente. Creo que hemos sacado adelante proyectos muy interesantes y aunque con mis más y mis menos, me ha gustado formar parte de esto y me llevo un gran aprendizaje.

También me gustaría agradecer a mi familia y pareja, por su paciencia y apoyo durante este tiempo. Alba, ya cerramos la época de que expliques de qué va mi tesis a los demás. Gracias sobre todo por darme siempre otra forma de ver las cosas y estar siempre ahí. Gracias a mi madre y mi hermana por su cariño. Papá, ya puedes decirme doctor unas 30 veces al día. Os quiero.

Gracias también a todos los compañeros que han aportado un mínimo granito de arena durante estos años. En especial me gustaría acordarme de Mónica, ya que hemos estado juntos en esto desde el día uno. También de Inés e Isa que hicieron el camino un poquito más ameno.

Muchas gracias a todos.

13. Appendix

13.1. Publications

Acta Neuropathologica (2025) 149:46
https://doi.org/10.1007/s00401-025-02884-5

ORIGINAL PAPER

Oligodendroglia vulnerability in the human dorsal striatum in Parkinson's disease

Juan M. Barba-Reyes[1] · Lisbeth Harder[2] · Sergio Marco Salas[3,4] · Methasit Jaisa-aad[5,6] · Clara Muñoz-Castro[5,6] · Leonardo D. Garma[2] · Nima Rafati[7] · Mats Nilsson[3] · Bradley T. Hyman[5,6] · Alberto Serrano-Pozo[5,6] · Ana B. Muñoz-Manchado[1,2,8]

Received: 13 February 2025 / Revised: 15 April 2025 / Accepted: 23 April 2025
© The Author(s) 2025

Abstract

Oligodendroglia are the responsible cells for myelination in the central nervous system and their involvement in Parkinson's disease (PD) is poorly understood. We performed sn-RNA-seq and image-based spatial transcriptomics of human caudate nucleus and putamen (dorsal striatum) from PD and control brain donors to elucidate the diversity of oligodendroglia and how they are affected by the disease. We profiled a total of ~ 200.000 oligodendroglial nuclei, defining 15 subclasses, from precursor to mature cells, 4 of which are disease-associated. These PD-specific populations are characterized by the overexpression of heat shock proteins, as well as distinct expression signatures related to immune responses, myelination alterations, and disrupted cell signaling pathways. We have also identified impairments in cell communication and oligodendrocyte development, evidenced by changes in neurotransmitter receptors expression and cell adhesion molecules. In addition, we observed significant disruptions in oligodendrocyte development, with aberrant differentiation trajectories and shifts in cell proportions, particularly in the transition from mature oligodendrocytes to disease-associated states. Quantitative immunohistochemical analysis revealed decreased myelin levels in the PD striatum, which correlated with transcriptomic alterations. Furthermore, spatial transcriptomics mapping revealed the distinct localization of disease-associated populations within the striatum, with evidence of impaired myelin integrity. Thus, we uncover oligodendroglia as a critical cell type in PD and a potential new therapeutic target for myelin-based interventions.

Keywords Neurodegeneration · Sc-RNA-seq · Spatial transcriptomics · Striatum · Oligodendrocyte · Myelin

Abbreviations

PD	Parkinson's disease
SNpc	Substantia nigra pars compacta
LBs	Lewy bodies
LNs	Lewy neurites
OLs	Oligodendrocytes
AD	Alzheimer's disease
sc/sn-RNA-seq	Single-cell/single-nucleus RNA sequencing
OPCs	Oligodendrocyte progenitor cells
MS	Multiple sclerosis
GWAS	Genome Wide Association Studies
Pu	Putamen
CN	Caudate nucleus
PDA-OLs	PD-associated oligodendrocytes

✉ Ana B. Muñoz-Manchado
ana.munoz@uca.es

1 Unit of Cell Biology, Department of Neuroscience, Institute for Biomedical Research and Innovation of Cádiz (INiBICA), University of Cádiz, Cádiz, Spain

2 Laboratory of Molecular Neurobiology, Department of Medical Biochemistry and Biophysics, Karolinska Institutet, Stockholm, Sweden

3 Science for Life Laboratory, Department of Biochemistry and Biophysics, Stockholm University, Stockholm, Sweden

4 Institute of Computational Biology, Computational Health Center, Helmholtz, Munich, Germany

5 Department of Neurology, Massachusetts General Hospital, Boston, MA, USA

6 Harvard Medical School, Boston, MA, USA

7 National Bioinformatics Infrastructure Sweden, Science for Life Laboratory, Department of Medical Biochemistry and Microbiology, Uppsala University, Uppsala, Sweden

8 Ciber of Mental Health (CIBERSAM), ISCIII, 28029 Madrid, Spain

Published online: 05 May 2025

FACS	Fluorescent-activated cell sorting
RT	Reverse transcription
UMIs	Unique molecular identifiers
PCA	Principal component analysis
PCs	Principal components
scCODA	Single-cell compositional data analysis
GSEA	Gene Set Enrichment Analysis
NES	Normalized Enrichment Score
FDR	False discovery rate
GO	Gene ontology
KEGG	Kyoto Encyclopedia of Genes and Genomes
MBP	Myelin basic protein
TH	Tyrosine hydroxylase
ROIs	Regions of interest
α-syn	α-Synuclein
kNN	K-nearest neighbors
GCN	Graph convolutional network
WM	White matter
GM	Gray matter
SEM	Standard error mean
COPs	Committed OPCs
MOL	Mature oligodendrocytes
HSP	Heat shock proteins
immOL	Immature OLs
TCA	Citric acid
LAMA2	Laminin-2
ECM	Extracellular matrix
CAMs	Cell adhesion molecules
HSPR	Heat shock protein response
MSA	Multiple system atrophy

Introduction

Parkinson's disease (PD) has a significant impact on society due to its widespread implications both in patients' health and caretakers, with a rapid increase in incidence over the past 2 decades [55, 57]. PD is a heterogeneous condition, with mutations in multiple genes presenting with a similar parkinsonian syndrome and a single causative mutation resulting in a range of clinical presentations [9, 36]. This heterogeneity suggests different underlying mechanisms at a biological level that are not yet fully understood. While the loss of dopaminergic neurons in the *substantia nigra pars compacta* (SNpc) and the accumulation of intracellular α-synuclein aggregates in Lewy bodies (LBs) and Lewy neurites (LNs) have long been associated with the development of PD [21, 31], recent studies have demonstrated the involvement of glial cells, in particular oligodendrocytes (OLs), in neurodegenerative disorders such as PD and Alzheimer's disease (AD) [16, 23, 29, 47, 48, 52, 62, 64, 85].

While they have traditionally been considered homogeneous populations [4, 15, 34], recent advancements including single-cell/single-nucleus RNA sequencing (sc/sn-RNA-seq) have revealed that OLs are heterogeneous, comprising numerous subpopulations and states that participate in distinct biological processes [35, 46], redefining the maturation process as a continuum. Indeed, OLs are known to progress through distinct developmental states, starting as oligodendrocyte progenitor cells (OPCs), which proliferate and differentiate into pre-myelinating OLs, that eventually mature into fully myelinating oligodendrocytes [5, 12]. These different states correspond to distinct transcriptomic and morphologic profiles that can also vary along brain regions [6, 7, 40, 65, 75, 77].

Recent works suggest that alterations in myelin integrity and OL survival can play a crucial role in the progression of neurodegenerative diseases and MS [30, 35, 46–48, 62]. Interestingly a few studies have also demonstrated a connection between OLs and PD [2, 3, 13, 51, 79]. Bryois et al. [13] found a genetic association between PD GWAS variants and OLs, while Wakabayashi et al. [79] and Arai et al. [2] observed α-synuclein inclusions in OLs of PD brains. These findings suggest that OLs may play a critical role in the development of PD. However, few studies have investigated the role of the OL lineage in PD, particularly in the dorsal striatum [3, 72], a brain region that includes the putamen (Pu) and caudate nucleus (CN) and is central to PD pathophysiology [41] and therapeutic development, as it receives the nigrostriatal axons from the dopaminergic neurons of the SNpc [71].

In this study, we elucidated the transcriptomic changes induced by PD across OLs lineage populations using sn-RNA-seq in the dorsal striatum from 63 donors and image-based spatial transcriptomics in a subset of them. Our results reveal distinct transcriptomic states of PD-associated oligodendrocytes (PDA-OLs), delineating diverse altered functional pathways, the spatial organization of OLs, and the potential biological consequences of OL dysfunction for the extent of both dopaminergic neuron loss and LB/LN formation.

Materials and methods

Human tissue

Human brain samples for this study were obtained from donors with a clinical and neuropathological diagnosis of PD and controls not meeting clinical or neuropathological diagnostic criteria for any neurodegenerative disease. Specifically, the CN and Pu were dissected from coronal slabs at the level of the *nucleus accumbens*. The control group comprised 27 individuals (Pu = 27, CN = 24)

ranging in age from 25 to over 90 years. The PD group included 36 individuals (Pu = 35, C*N* = 34) aged between 60 and over 90 years. Samples were collected from three sources: the Human Brain and Spinal Fluid Resource Center (Los Angeles, CA, USA), the Parkinson's UK Brain Bank at Imperial College London (London, UK), and the Massachusetts Alzheimer's Disease Research Center (Charlestown, MA, USA). Donors or their next-of-kin provided written informed consent for brain autopsy, and the study was approved by the review board of each brain bank. Detailed information regarding the samples is provided in Supplementary Table 1. Since PD is more common in men, the control and PD groups were not matched by sex (i.e., there were 19 females and 44 males in the full cohort, control: 18/9 and PD: 26/10 male/female). Consequently, the study lacks sufficient power to robustly analyze sex-specific effects, such as differences in cell class proportions or the influence of sex on gene expression regulation.

Tissue dissociation

Nuclei isolation from fresh frozen tissue was conducted following the protocol outlined by the Allen Institute for Brain Science (https://www.protocols.io/view/isolation-of-nuclei-from-adult-human-brain-tissue-eq2lyd1nqlx9/v2), with specific guidelines. All procedures were performed at 4 °C to maintain sample integrity. Tissue samples (100–150 mg) were thawed on ice and homogenized in 2 mL of chilled, nuclease-free homogenization buffer. The buffer composition included 10 mM Tris (pH 8), 250 mM sucrose, 25 mM KCl, 5 mM $MgCl_2$, 0.1 mM DTT, protease inhibitor cocktail (1×, 50×stock in 100% ethanol, G6521, Promega), 0.2 U/µL RNasin Plus (N2615, Promega), and 0.1% Triton X-100. Homogenization was carried out using a dounce tissue grinder with loose and tight pestles (20 strokes each; 357,538, Wheaton). The nuclei solution was filtered sequentially through 70 µm and 30 µm strainers. Tubes and strainers were rinsed with an additional homogenization buffer to achieve a final volume of 6 mL. The filtered solution was centrifuged at 900 rcf for 10 min, after which the supernatant was discarded, leaving 50 µL of buffer above the pellet. The pellet was resuspended in 200 µL homogenization buffer, yielding a final volume of 250 µL. Next, the suspension was mixed 1:1 with 50% iodixanol (OptiPrep Density Gradient Medium, D1556, Sigma) prepared in 60 mM Tris (pH 8), 250 mM sucrose, 150 mM KCl, and 30 mM $MgCl_2$. This mixture was carefully layered over 500 µL of 29% iodixanol in a 1.5 mL tube and centrifuged at 13,500 rcf for 20 min. Following centrifugation, the supernatant was gently removed to avoid disrupting the pellet. The pellet was resuspended in 50 µL of chilled, nuclease-free blocking buffer containing 1×PBS, 1% BSA, and 0.2 U/µL RNasin Plus. This suspension was transferred to a fresh tube, brought to a total volume of 500 µL with blocking buffer, and prepared for fluorescent activated cell sorting (FACS). For neuronal enrichment, 1 µL of NeuN antibody (1:500, Millimark mouse anti-NeuN PE conjugated, FCMAB317PE, Merck) was added to the samples, which were incubated on ice in the dark for 30 min. After centrifugation at 400 rcf for 5 min, the supernatant was discarded, leaving approximately 50 µL of buffer above the pellet. The pellet was resuspended in 500 µL of blocking buffer, passed through a 20 µm filter into FACS tubes, and stained with 1 µL of DAPI (0.1 mg/mL, D3571, Invitrogen) prior to sorting.

Fluorescent-activated nuclei sorting

The nuclei suspension was maintained in darkness throughout the sorting process, which was developed using a flow cytometer (either BD FACSAria Fusion or BD FACSAria III) at 4 ℃. Gating was performed based on DAPI and phycoerythrin signals, separating the nuclei into two distinct populations: $NeuN^+$ and $NeuN^-$. Each sorted population was collected into separate tubes containing 50 µL of blocking buffer, with sorting continued until approximately 200,000 nuclei per population were obtained. Following sorting, the nuclei populations were centrifuged at 400 rcf for 4 min. The supernatant was carefully removed, leaving approximately 30 µL of buffer to resuspend the pellet. The samples were kept on ice to preserve their integrity for subsequent analysis.

Library preparation

Library preparation from the sorted nuclei suspensions was carried out using the Chromium Next GEM Single Cell 3' Reagent Kit v3.1 (PN-1000268, 10×Genomics). Nuclei populations were manually counted, and their concentrations were adjusted to a range of 200–1700 nuclei/µL. Following the manufacturer's protocol (CG000204 Rev D, 10×Genomics), reverse transcription (RT) mix was added to the nuclei suspensions. For library preparation, samples were either loaded into separate lanes on the Chromium Next GEM Chip G (PN-1000120, 10×Genomics) for each population (targeting a recovery of 5000 nuclei per population) or mixed prior to loading, with proportions of 70% NeuN + and 30% NeuN − nuclei (targeting a recovery of 5000 or 7000 nuclei). Subsequent cDNA synthesis and library preparation were conducted in accordance with the manufacturer's instructions, utilizing the Single Index Kit T Set A (PN-1000213, 10×Genomics). Quality control and quantification steps within the protocol were performed using the Agilent High Sensitivity DNA Kit (5067–4626, Agilent Technologies) and the KAPA Library Quantification

Kit (2700098952, Roche) to ensure the accuracy and reliability of the prepared libraries.

Illumina sequencing

Pooled libraries were prepared by combining up to 19 samples for a target nucleus recovery of 5000 or up to 16 samples for a target recovery of 7000 nuclei. Sequencing was conducted on a NovaSeq S6000 platform using an S4–200 (v1.5) flow cell with eight lanes, employing a 28–8–0–91 read configuration. The sequencing was carried out at the National Genomics Infrastructure in Stockholm, Sweden.

sn-RNA-seq data analysis

Pre-processing

Raw single-nuclei RNA sequencing (sn-RNA-seq) data were processed into count matrices using CellRanger (v3.0.0, 10 × Genomics). The sequencing reads were aligned to the hg38 genome (GRCh38.p5; NCBI:GCA_000001405.20), incorporating both intronic and exonic sequences during the alignment process.

Quality control

To identify potential doublets, we used Scrublet [84] for each sample individually, conducting 100 iterations with automated threshold detection, default parameters, and a fixed random seed. Nuclei identified as doublets in more than 10% of the Scrublet runs were excluded. Quality control based on the distribution of unique molecular identifiers (UMIs) and unique genes detected per nucleus was then performed. Nuclei with fewer than 500 UMIs or 1200 genes were removed, as were those with more than 250,000 UMIs, over 15,000 genes, or exceeding 10% mitochondrial content. For the remaining nuclei, we modeled the logarithmic relationship between the number of unique genes and UMIs as a second-degree polynomial function. Nuclei exhibiting significant deviations from the polynomial fit—defined as a difference greater than 2000 between log-transformed gene counts and the predicted value based on UMI counts—were classified as outliers and excluded. In addition, nuclei expressing high levels of marker genes corresponding to multiple cell types were removed. To assess this, a cell type score was calculated for each subtype (Oligodendrocytes, Microglia, OPCs, Neurons, Astrocytes, Vascular cells) for each nucleus, based on the mean expression of canonical marker genes. The score distributions were evaluated across the dataset, revealing bimodal patterns in all cases. These distributions were modeled as Gaussian mixtures, and a threshold was set at the mean of the lower Gaussian distribution plus four standard deviations. Nuclei exceeding the threshold for multiple cell types were classified as doublets and excluded. To further reduce contamination from neighboring regions, such as the claustrum or amygdala, nuclei expressing regional marker genes (*NEUROD2, TMEM155, CARTPT, SLC17A7*) were removed, with markers derived from the Allen Brain Atlas [32]. The number of nuclei excluded at each stage of this filtering process is summarized in Supplementary Fig. 1.

Oligodendrocytes detection

Count matrices were analyzed using Scanpy [82] to facilitate clustering and cell type annotation, with a focus on identifying oligodendroglia. Principal component analysis (PCA) was performed, and a neighborhood graph was computed using the first 30 principal components (PCs). Clustering was conducted using the Louvain algorithm at a resolution of 0.2. The resulting clusters were annotated as either glial cells or neurons based on the expression profiles of canonical marker genes:

Astrocytes —*AQP4*, *ADGRV1*
Microglia—*CSF1R*, *FYB1*
Oligodendrocytes—*MBP*, *MOG*, *MAG*
OPCs—*PTPRZ1*, *PDGFRA*, *VCAN*
Vascular cells—*EBF1*, *ABCB1*, *ABCA9*
Neurons—*MEG3*

Oligodendrocytes and OPCs were selected, and genes were filtered based on their expression per cell. Genes detected in less than three cells were removed (1389 genes).

Oligodendroglia lineage classification

Oligodendroglia nuclei were projected onto the first 15 PCs calculated on their 10% of most variable genes and re-clustered using the Louvain algorithm. Harmony [43] algorithm was used to remove the batch effect and integrate the data. The function scanpy.tl.rank_genes_groups from Scanpy [82] was used to perform a differential expression analysis between the clusters through a Wilcoxon rank-sum test. Marker genes were selected manually from the top ranked genes (log fold change > 0.5 and p value < 0.05) to characterize and name each of the oligodendroglia clusters as a different oligodendroglia subclass. Markers for each subpopulation are represented in Supplementary Table 2.

Hierarchical analysis

Hierarchical clustering of the identified subpopulations was performed using the scanpy.tl.dendrogram function from the Scanpy [82] package. The clustering was based on the Pearson correlation method to measure similarity between subpopulations, and the complete linkage method was applied to define the cluster structure. This approach allowed

for the visualization of relationships between subpopulations based on their transcriptomic profiles.

Compositional analysis

The differences in cellular proportion composition between conditions and brain regions were analyzed using the single-cell compositional data analysis (scCODA), a Bayesian model specifically designed to analyze changes in compositional data, particularly from single-nuclei RNA sequencing experiments. This method accounts for the inherent dependencies in compositional data, providing more accurate insights compared to both compositional and non-compositional alternatives. scCODA has been demonstrated to outperform other approaches in this domain, as described by Büttner et al. [14].

Module analysis

To identify specific gene modules associated with oligodendroglia subpopulations, particularly those linked to *OPALIN* expression, we applied Hotspot [20] to our subsetted dataset. Hotspot detects gene modules by leveraging co-expression patterns and analyzing single-nuclei transcriptomic data, enabling the identification of functionally related gene clusters. We used default parameters but restricted our analysis to the top 10,000 highly variable genes to focus on the most relevant features of the dataset.

Gene set enrichment analysis

Gene set enrichment analysis (GSEA) was performed using the Python package GSEApy (version 1.0.4). Pathways were considered significantly enriched if they exhibited a Normalized Enrichment Score (NES) greater than 0.5 and a false discovery rate (FDR) q-value below 0.05, to account for multiple hypothesis testing. The analysis was conducted using Gene Ontology (GO), Kyoto Encyclopedia of Genes and Genomes (KEGG), and Reactome databases as reference sets for pathway annotation and functional enrichment.

GSEA superpathways

GSEA results from all comparisons were processed in Python to generate superpathways and summarize enrichment patterns. Redundant pathways across contrasts were merged, with summary metrics including mean NES, average FDR, and gene coverage calculated for each. To evaluate pathway similarity, we adapted the code from https://github.com/ayushnoori/brainstorm/blob/master/R/pathway-clustering-functions.R in Python, calculating Jaccard indices based on gene set overlaps, and hierarchical clustering (average linkage, threshold = 0.8) was applied to group similar pathways. Each cluster (except for the top 10 with the highest and lowest NES, which were annotated manually) was annotated with mean values for statistics columns and gene and pathways content. To generate informative labels, we applied KeyBERT (initialized with allenai-specter) for unsupervised keyword extraction. Pathway names were used as input, and the top two ranked n-gram phrases (1–3 words) were selected as superpathway descriptors.

Correlation analysis (PDAO-1/PDAO-2/MOLA ratio vs MBP)

To estimate correlations between subpopulations altered in PD (PDAO-1/PDAO-2/MOLA) and MBP values, we subsetted the data for samples showing values for all the variables (number of cells related to each subpopulation and MBP intensity). To be more precise, we calculated the percentage of cells in each sample related to PDAO-1/PDAO-2/MOL-A subpopulations and we only retained samples with more than five cells associated with a subpopulation. Finally, we used spearman correlation test with the following rationale: (PDAO-1 or PDAO-2 percentages per sample)/MOL-A and MBP intensity.

Trajectory analysis

Trajectory analysis was conducted using two complementary methods. First, StaVia [68] was applied to integrate spatial and temporal data for mapping oligodendroglia differentiation. This method utilizes higher order random walks to trace lineage pathways and identify intermediate states. We executed the function run_VIA with default settings, modifying only the knn parameter to 15 for consistency across analyses. The second method, Slingshot [69], aligns single-cell data by identifying developmental lineages and connecting clusters to predict differentiation trajectories, effectively modeling the continuous maturation of oligodendroglia. Slingshot was also run with default parameters.

Factor analysis

To investigate the genes associated with the differentiation process, we employed factor analysis using the scikit-learn Python package. Factor analysis is a statistical method that models observed variables as linear combinations of potential underlying latent variables, known as factors. This technique aims to identify latent structures that explain the observed variability in the dataset while minimizing noise.

In this study, factor analysis was applied to pseudotime-marked gene expression data to uncover the primary latent factors driving gene expression changes during

differentiation. The input data were normalized and scaled prior to analysis to ensure consistency and comparability across genes. By leveraging factor analysis, we identified key gene sets that contribute to distinct phases of the differentiation trajectory.

Communication analysis

With the aim of understanding the kind of communications and the quantity of them in oligodendroglia subpopulations, we used CellChat [37]. This method identifies ligand–receptor interactions across different subpopulations, constructing communication networks that reveal key signaling pathways involved in oligodendrocytes development. This analysis was developed in R, and we subsetted some populations, limiting the number of cells to 10,000 (comprising 5000 Control and 5000 PD randomly selected) in the case the number of cells of the subpopulation exceeded this number.

Immunohistochemistry with peroxidase-DAB method

Eight-µm-thick formalin-fixed paraffin-embedded sections from the striatum (contralateral to samples used for sn-RNA-seq and spatial transcriptomics) at the level of the nucleus accumbens were immunostained in a Leica BOND RX fully automated research stainer using the BOND kit (Leica Biosystems, DS9800). Primary antibodies and concentrations were as follows: mouse anti-α-syn clone LB509 (Thermo Fisher Scientific Cat# 18–0215, RRID:AB_2925241, 1:200), mouse anti-myelin basic protein (MBP) amino acids 129–138 clone 1 (Millipore Cat# MAB382, RRID:AB_94971, 1:250), and rabbit anti-tyrosine hydroxylase (TH) polyclonal (Cell Signaling Technology Cat# 2792, RRID:AB_2303165, 1:100). The immunohistochemistry protocol included bake and dewax steps, a 20-min-long heat-induced epitope retrieval (with ER2 solution for α-syn and with ER1 solution for MBP and TH), and hematoxylin counterstaining. Sections were coverslipped with Permount mounting media and whole-slide images were obtained under the 40 × objective (numerical aperture 0.95, resolution 0.17 µm/pixel) of an Olympus VS120 virtual slide scanner (Olympus, Tokyo, Japan).

Immunohistochemistry images analysis and quantification

All slide images were processed and analyzed using QuPath (version 0.4.3). Quantitative analysis focused on detecting intensity features related to MBP, as well as identifying the density of TH-positive projections from the SNpc to the dorsal striatum and α-synuclein aggregations (Lewy bodies/neurites, LBs/LNs). For each image, random regions of interest (ROIs) were selected within the putamen and caudate nucleus. TH-positive projections and α-synuclein aggregation detection was performed independently using QuPath's pixel classifier tool. Five representative samples were chosen, and within each sample, the classifier was trained using 25 TH-positive and α-syn-positive annotations and 25 TH-negative or α-syn-negative annotations, resulting in a total of 125 TH-positive and 125 TH-negative annotations, and 125 α-syn-positive and 125 α-syn-negative annotations for classification.

The data obtained from MBP intensity measurements, TH projections quantification, and α-syn aggregate quantifications were further analyzed using the SciPy [78] Python library. A two-sample *t* test was applied to determine the T and *p* values for each brain region and condition. For MBP analysis, the mean of diaminobenzidine (DAB) intensity per pixel within the selected ROIs was used as the metric for quantification. TH differences were assessed by comparing the percentage of positive TH annotations, calculated as the area of TH-positive measurements, divided by the total area analyzed (μm^2). Similarly, α-syn differences were quantified based on the proportion of α-syn-positive regions relative to the total area (mm^2) examined in Pu or CN, respectively. In addition, Spearman's rank correlation analysis was performed to explore relationships between various feature pairs across different regions and experimental conditions.

Spatial transcriptomics (Xenium)

Spatial transcriptomics platform

Spatial transcriptomic analyses were conducted using the Xenium high-plex in situ platform (10 × Genomics), which facilitates subcellular-resolution characterization of RNA within tissue sections, similarly as previously done in Garma et al. [28].

Gene panel design

The Xenium technology employs oligonucleotide probes designed to quantify the expression of genes in a predefined panel. For this study, a gene panel comprising 266 genes from the Xenium Human Brain Gene Expression Panel was utilized. An additional 100 genes were selected based on our sn-RNA-seq dataset, generating a custom gene panel (Xenium Custom Gene Expression Panel 51–100 (Z3DREH), PN-1000561, 10× Genomics).

Experimental workflow

Tissue blocks from human subjects ($N = 4$; including Pu and CN) were retrieved from − 80 ℃ storage and transferred on dry ice to a cryostat (CryoStar NX70, Thermo Scientific). Samples were mounted on the specimen holder using Tissue Tek O.C.T. Compound (4583, Sakura) and allowed to acclimate to − 20 ℃ within the cryostat chamber for 5 min. Tissue sections of 10 µm thickness were obtained and placed directly within the imaging region of precooled Xenium slides (12 × 24 mm, PN-3000941, 10× Genomics). Adherence of the sections to the slides was facilitated by briefly warming the reverse side of the slides with gentle pressure, followed by immediate refreezing on the cryobar. Tissue-mounted slides were retained in the cryostat during the sectioning process and subsequently stored at − 80 ℃. Downstream processing, including probe hybridization, ligation, and rolling circle amplification, was conducted at the in situ Sequencing Infrastructure Unit (Science for Life Laboratory, Stockholm), following the manufacturer's protocol (CG000582 Rev E, 10× Genomics). Background fluorescence was minimized via chemical quenching. Tissue sections were imaged using the Xenium Analyser instrument (10× Genomics), which also facilitated signal decoding and data acquisition.

Oligodendroglia identification

Xenium experiments provide spatial positions of all decoded reads. Therefore, the first step in processing these datasets is to segment individual cells and identify its composition. In this study, cells from Xenium experiments were defined based on default nuclear Xenium segmentation. This conservative approach minimizes the possibilities of missegmentation, as illustrated by Marco Salas et al. [45]. Segmented cells were then preprocessed using Scanpy to identify oligodendroglia. Essentially, pre-processing of the spatial dataset involved filtering out low-quality cells. Cells with fewer than 40 total counts or fewer than 10 detected genes were excluded. The data were then normalized, log-transformed, and subjected to neighbor graph construction using Scanpy's pre-processing pipeline. A UMAP embedding was generated to visualize clusters, and Leiden clustering was applied with a resolution of 0.8 to identify distinct cell populations.

Oligodendroglia clusters (clusters 0, 3, and 9) were identified based on the expression of known oligodendroglia marker gene expression (*MBP, OLIG1, OLIG2, PDGFRA*, among others). The selected clusters were subsetted into a new AnnData object for further analysis. Marker gene expression was visualized spatially using matplotlib and scanpy to confirm the presence and distribution of oligodendrocytes.

Oligodendroglia cell type assignment

Cell type deconvolution was performed using the cell2location [42] package, which infers the spatial distribution of cell types by integrating sc-RNA-seq data as a reference. First, the single-cell reference dataset, generated in this study, was preprocessed to define a knowledge base of oligodendroglia cell type-specific gene expression profiles. Genes were filtered to retain those expressed in at least five cells, representing at least 3% of the total dataset, and exceeding a mean expression cutoff of 1.12. The spatial dataset, including only predefined oligodendroglia cells, was filtered to retain genes that overlapped with the single-cell reference. Cell2location's setup function was used to prepare the spatial AnnData object for model training, specifying the sample batch as a key parameter. A regression model was trained on the reference data to estimate cell-type-specific mean expression levels. The spatial data were then analyzed using the cell2location model, which was trained for 3000 epochs with a detection alpha parameter of 200 and batch size of 10,000. Posterior distributions of cell abundances were exported to generate quantitative summaries of cell type probabilities for each spatial location. The q50 quantile (median) cell type abundances were visualized and further analyzed to identify the dominant cell types in each spatial coordinate. For oligodendrocytes, additional analysis of spatial localization and confidence intervals was performed using the posterior distributions.

Neighborhood enrichment analysis

To assess the neighborhood enrichment of oligodendrocytes, spatial interaction networks were constructed for each sample in the dataset. The AnnData object containing oligodendroglia profiled with Xenium was first subsetted by sample, and spatial neighbors were computed using Squidpy's [53] spatial_neighbors function with a radius of 124 um. This process was repeated for all samples, and the resulting AnnData objects were concatenated into a unified dataset.

Neighborhood enrichment was calculated using Squidpy's nhood_enrichment function, with the cell type annotation, defined using cell2location, as the cluster key. This analysis computes z-scores representing the degree of enrichment or depletion of specific cell types in the neighborhoods of other cell types. Visualization of neighborhood enrichment was performed using a heatmap with a diverging colormap (coolwarm), highlighting significant positive and negative interactions. Parameters such as color scale limits (vmax = 200, vmi$N$ = -200) and figure size were adjusted to optimize clarity and interpretability. Overall, this method provides insights into the spatial interactions and organization of oligodendrocytes in their local tissue environment,

enabling a deeper understanding of their roles in tissue architecture and function.

Module identification using hotspot

We used Hotspot [20] to identify gene expression modules in oligodendroglia profiles derived from Xenium spatial transcriptomics data. Hotspot identifies informative genes and gene modules based on how gene variation aligns with cell similarity metrics. Informative genes show expression patterns concordant with local cell similarity. In summary, we initialized Hotspot with the following parameters:

- Layer key: 'raw' for raw expression values.
- Model: Negative binomial (danb).
- Latent obsm key: 'X_pca'.
- UMI counts key: Total UMI counts per cell.

A k-nearest neighbors (kNN) graph (20 neighbors, unweighted) was created to compute gene autocorrelations. Genes with FDR < 0.05 were selected as significant. Local correlations for these genes were computed using parallel processing. Gene modules were defined using a minimum threshold of five genes, with core genes meeting an FDR threshold of 0.05. Module scores for each cell were calculated and stored. Differences in module scores between PD and control groups were analyzed using the Wilcoxon rank-sum test. Violin plots visualized score distributions, with test statistics and *p* values annotated.

Niche identification using NicheCompass

NicheCompass [8] was used to identify cellular domains by integrating spatial transcriptomics data across all samples. A latent graph embedding was computed using a graph convolutional network (GCN) model with categorical covariates such as replicates. NicheCompass was run for 400 epochs with regularization to optimize ligand-receptor-based niche identification. Clustering was performed on the latent embeddings using the Leiden algorithm with a resolution of 0.2. After clustering, niches with fewer than 200 cells were filtered out, leaving three robust niches, that could be annotated as white matter (WM), gray matter (GM), and vascular niches based on their expression and cellular composition. These niches were characterized by their communication program activity, spatial localization, and enriched gene targets.

Statistical analysis

Statistical analyses were conducted using Python-based computational tools. Differential expression analysis was performed using the Wilcoxon rank-sum test, with marker genes selected based on a log fold change > 0.5 and *p* value < 0.05. Hierarchical clustering of subpopulations was conducted to assess similarity based on Pearson correlation. Cellular compositional differences between conditions and brain regions were analyzed using a Bayesian model designed for sn-RNA-seq data. GSEA statistical significance was assessed using permutation-based methods (a Kolmogorov–Smirnov-like statistic), which compares the observed enrichment of genes in a gene set against a random distribution. Spearman's rank correlation was used to examine relationships between specific features, such as the percentages of PDAO-1 or PDAO-2 and MOL-A/MBP intensity. Two-sample *t* tests were used to compare MBP intensity, TH-positive dots, and α-syn-positive areas across conditions and brain regions, generating T and *p* values.

Sample sizes were determined based on prior studies and experimental feasibility. Detailed statistical results and methodologies are presented in the figures and legends.

Results

The human dorsal striatum shows great diversity of oligodendroglia and specific associated subclasses for PD

To elucidate the genetic networks and underlying molecular changes in OLs lineage cells within the context of PD in the dorsal striatum, we isolated and sequenced individual nuclei from freshly preserved human brain tissue samples obtained from CN and Pu of $N = 27$ controls and $N = 36$ PD donors. By employing sn-RNA-seq through a well-established workflow (Fig. 1a), we obtained 200,000 individual nuclei associated with OLs lineage cells (Fig. 1c). Notably, this dataset represents the most extensive compilation of human OLs lineage cell transcriptomic information from the dorsal striatum available to date. Control and PD groups were matched by age but not by sex due to the higher prevalence of PD in men (Fig. 1c). The average number of cells per donor and striatum (including CN and Pu) was approximately 3000 (Fig. 1c). To characterize and confirm the loss of dopaminergic neuron projections and the presence of LBs/LNs in PD samples, we performed immunohistochemical analysis for tyrosine hydroxylase (TH) and α-synuclein (α-syn) in the contralateral CN and Pu of MADRC control ($N = 10$ (α-syn), $N = 8$ (TH)) and PD ($N = 8$ (α-syn and TH)) donors, (Fig. 1b, Supplementary Fig. 2), for whom formalin-fixed paraffin-embedded sections were available. The analysis of immunoreactivity revealed a significant reduction in TH immunoreactivity (Control = 1.66 ± 0.58 (SEM) versus PD = 0.21 ± 0.05 (SEM), $p = 0.027$, $t = 2.47$) and a marked increase in α-syn immunoreactivity (Control = 0.004 ± 0.0017 versus PD = 0.01 ± 0.002, $p = 0.035$,

$t = 2.31$) specifically in the Pu of PD patients (Fig. 1b, Supplementary Fig. 2), reflecting the expected loss of TH-positive dopaminergic neuron projections and the aggregation of α-syn in LB/LNs in PD, respectively.

PD-associated clusters show specific transcriptomic signatures including stress-reactive and immunological responses

After implementing a robust quality control process (Supplementary Fig. 1), we conducted an initial clustering to identify four main classes: oligodendrocyte progenitor cells (OPCs) expressed *VCAN* as marker gene; committed OPCs (COPs) expressed *GPR17* as marker gene; and mature oligodendrocytes (MOL) were identified by the expression of *MBP*, and further subdivided based on the expression levels of *OPALIN* or *SLC5A11* marker genes (Fig. 2b). These classes were represented in both control and PD as well as in CN and Pu (Fig. 2a, b, Supplementary Fig. 3). Subsequently, cell classes were sub-clustered identifying 15 distinct subpopulations. Due to their clear enrichment in PD, we annotated some of these as PD-associated (PDA) (Fig. 2b, d). OPCs displayed four subclasses: OPCs-A (expressing the gene markers *VCAN/GPC6/SGCZ*), PDAOPCs (*VCAN/MT3/CD81*), OPCs-C (*VCAN/SEMA3E/GRIA4*), and OPCs-D (*VCAN/ST18*). MOLs expressing *OPALIN* comprised five subpopulations: MOL-A (*LAMA2/KIF6*), MOL-B (*FTH1/CRYAB/DMD*), PDAO-1 (*DBNDD2/FTL/HSPA1A*), PDAO-2 (*CTNNA2/ARHGAP24*), and MOL-F (*LURAP1L-AS1, LINC00609, LINC01608*). Within the *SLC5A11*$^+$ population, distinctions were made between PDAO-3 (*ACTN2/MT-ND3*) and MOL-G (*LINC01505, PLEKHG1, SLC25A29*) (Fig. 2b, c). The identified subpopulations represent a continuum; therefore, they do not correspond to distinct OL subtypes, but rather reflect different states within a specific subpopulation, exemplified by either different stages of differentiation or activity specialization. This is particularly evident in MOLs, where most subpopulations share common markers, with their key distinction lying in their gene expression levels rather than in the presence or absence of specific markers. These findings suggest that transcriptomic variability within MOLs is mainly driven by different functional states rather than by the emergence of discrete cell types.

After identifying distinct subpopulations within the OLs lineage, we characterized each by differential gene expression analysis (Fig. 2c, Supplementary Table 2). Of note, the disease-specific clusters (PDAOPCs, PDAO-1, PDAO-2, and PDAO-3) exhibited upregulated expression of heat shock proteins (HSP) families 70 and 90, including *HSPA1A, HSPB1, HSP90AB1, HSPA1B, HSPA8, HSP90AA1*, and *HSPA5*, as well as *CRYAB* and *DNAJ* family members. Thus, the elevated levels of these chaperone genes in PDAO-1 and PDAO-2 subpopulations underscore an enhanced cellular response to stress and their involvement in protein folding and proteostasis processes within the OLs lineage (Fig. 2c).

To assess the potential disease and region specificity of these subclasses, we conducted a compositional proportion analysis using scCODA. In Pu, PD samples exhibited modest increases in PDAO-1 (+5.6%), PDAO-2 (+1.5%), PDAO-3 (+3.0%), and PDAOPCs (+2.3%), alongside a reduction in MOL-A (−9.1%) and MOL-F (−3.7%) (Fig. 2d). Notably, these PD-induced alterations were only significant in Pu, although the same tendency was observed in CN (Fig. 2d). Thus, in the striatum, particularly in the Pu, a subset of OLs exhibit a prominent stress response in PD (Fig. 2d). Furthermore, to control for potential sex-related effects, we performed a similar compositional proportion analysis stratified by sex and found no significant differences between males and females in any of the identified subpopulations, suggesting that the observed changes are independent of sex (Supplementary Fig. 4).

We next focused on *OPALIN*$^+$ MOLs as they showed to be the most affected class with three altered populations in PD (Fig. 2b, d). To confirm the gene markers associated with the *OPALIN*$^+$ subpopulations, including PDAO-1 and PDAO-2, and identify gene co-expression patterns and cellular programs associated with those gene markers, we performed Hotspot analysis. This analysis revealed several gene modules, of which Modules 4 (genes *KCNIP4*, *RBFOX1*) and 5 (*MDGA2*, *CNTN1*, *LUZP2*, *FRY*, *GRIK2*) were associated with immature OLs-A (immOL-A) and immature OLs-B (immOL-B), respectively. Interestingly, Modules 10 and 14, increased in MOL-A, included mitochondrial genes and genes regulating projection development (*GRID2*, *ZFPM2*), respectively. PDAO-1 showed increased expression of Modules 1 and 2, which were associated with HSP genes (*CRYAB*, *FTH1*, *FTL*, *HSPA1A*, *HSPA1B*, *HSPH1*), while PDAO-2 was linked to Modules 6 and 13, which are enriched in response to cytokines and antigen processing and presentation (*ETV5*, *QDPR*, *ARHGAP24*, *CTNNA2*) (Supplementary Fig. 5).

Disrupted myelination and key pathways in parkinson's disease-associated oligodendrocyte subpopulations

In light of the significant changes observed within the mature OLs associated with PD (included in the OPALIN + and SLC5A11 + subclasses), we conducted a GSEA on the most affected subpopulations, employing established databases such as GO, KEGG, and Reactome, to better understand the functional pathways implicated in PD. Our analysis focused on four key comparisons based on the compositional and

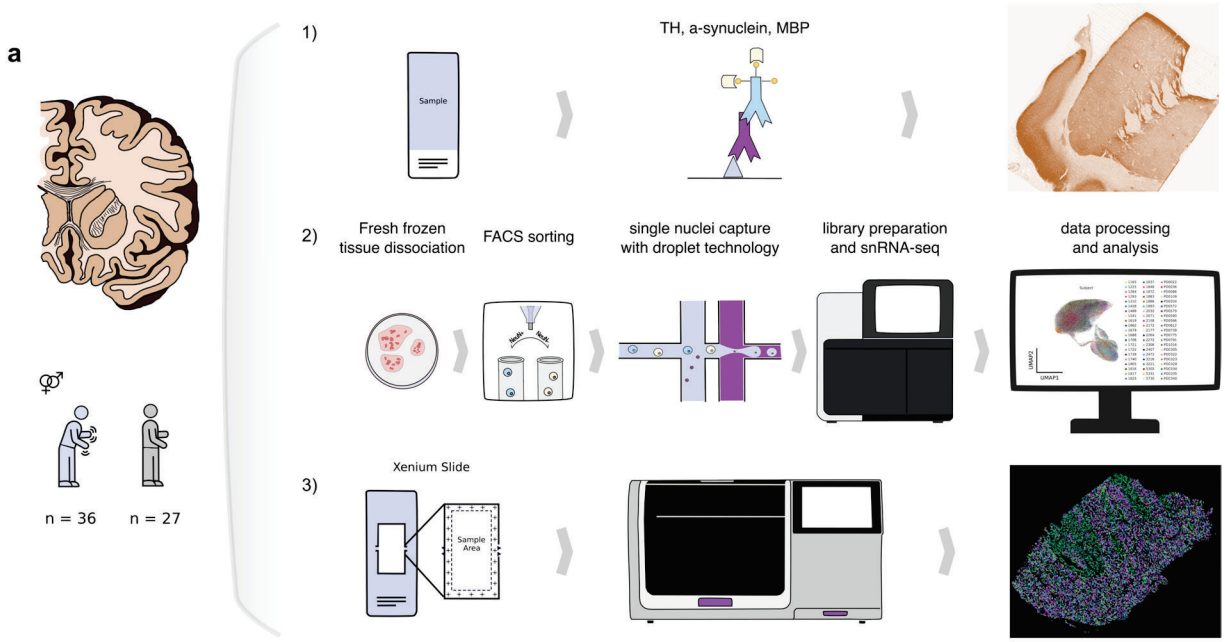
a
1)
Sample
TH, a-synuclein, MBP
2)
Fresh frozen tissue dissociation
FACS sorting
single nuclei capture with droplet technology
library preparation and snRNA-seq
data processing and analysis
n = 36
n = 27
3)
Xenium Slide
Sample Area

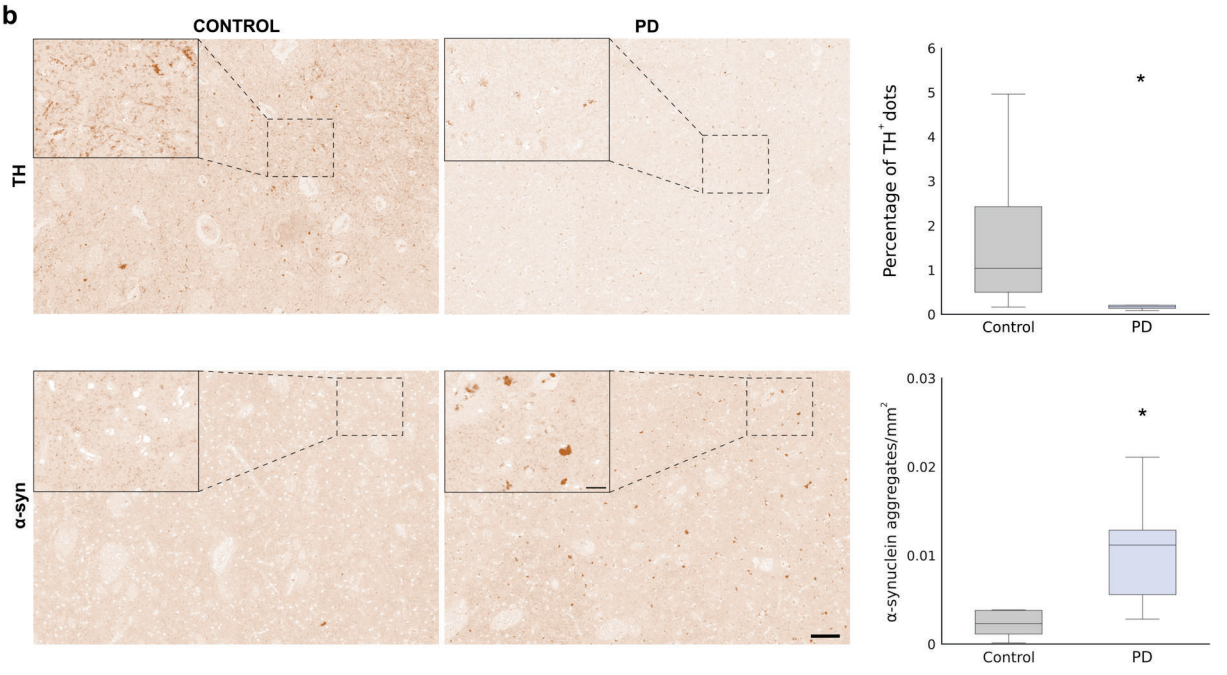
b
CONTROL
PD
TH
α-syn
Percentage of TH+ dots
α-synuclein aggregates/mm2
Control
PD
*

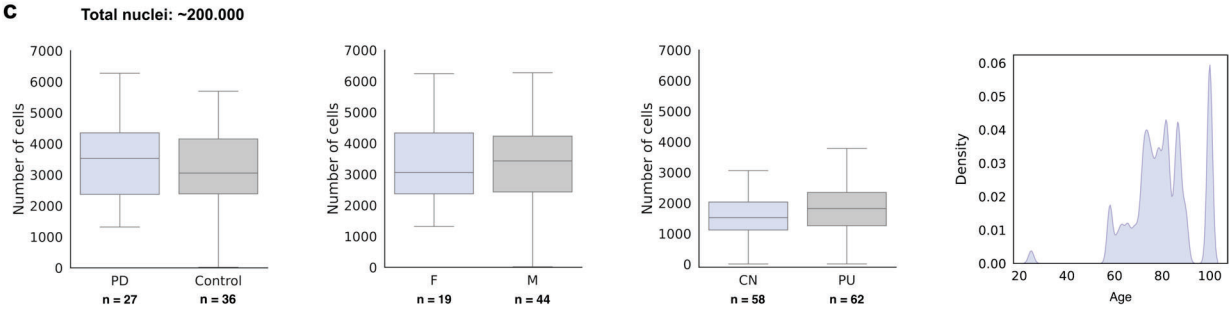
c
Total nuclei: ~200.000
Number of cells
PD
Control
n = 27
n = 36
F
M
n = 19
n = 44
CN
PU
n = 58
n = 62
Density
Age

◂**Fig. 1** Experimental design and quantitative analysis of TH and α-synuclein in the Putamen. Schematic overview of the experimental design (**a**). Immunohistochemical analysis of tyrosine hydroxylase (TH) and α-synuclein (α-syn) in the putamen. Box plots illustrate the distribution of marker expression in control and Parkinson's disease (PD) conditions. Statistical significance was determined using two-sided *t* tests, with significance indicated with an asterisk (TH analysis: $p = 0.027$, $t = 2.47$; α-syn analysis: $p = 0.03$, $t = 2.39$). Scales are set at 100 µm for low power images and at 20 µm for insets (**b**). Quantitative analysis of sequenced nuclei for OLs and OPCs, categorized by condition, sex, and region, along with the age distribution frequencies of the subjects (**c**)

dendrogram analyses: MOL-A vs PDAO-1 and 2, PDAO-3 vs MOL-F, and PDAOPCs vs OPCs-A, based on OPALIN, SLC5A11, and PDGFRA expression levels. To integrate the pathway information across conditions, identified pathways were grouped into superpathways based on their gene composition similarity (Fig. 3a, b). This approach enabled a broader understanding of the biological processes that define each cellular state or subpopulation.

Overall, PDA subpopulations were primarily associated with mitochondrial activity and proteostasis, encompassing functions such as translation, ribosome biogenesis, protein folding, stress responses, and metabolic regulation (Fig. 3b, Supplementary Table 3). These were accompanied by signatures of apoptosis and immune-related pathways. In contrast, enriched control subpopulations were associated with superpathways involved in neural development, including regulation of neurogenesis, synapse assembly, dendritic morphogenesis, and signaling mechanisms related to ion transport, cell adhesion, and cellular differentiation within the nervous system (Fig. 3b).

Within this general framework, distinct functional specializations emerged across specific comparisons. For instance, PDAO-1 exhibited an upregulation of cellular stress and immune responses, particularly those involving protein modification, cell cycle control, and pro-inflammatory signaling (Supplementary Table 3). PDAO-2, by contrast, was marked by enhanced innate immune signaling and apoptotic pathways mediated by DAP12 and interferon responses (Supplementary Table 3). Meanwhile, MOL-A demonstrated a unique molecular profile involving glycosphingolipid metabolism, TRP channel signaling, transcriptional regulation, and specialized functions like myelination and ciliary transport (Supplementary Table 3).

PDAO-3 revealed a metabolic profile, including pathways for steroid and lipid biosynthesis, intracellular and organelle-specific processes, signaling networks, and stress-related transcriptional regulation (Supplementary Table 3). In parallel, MOL-F was characterized by upregulation in nucleotide metabolism, cholesterol biosynthesis, calcium signaling, and gene expression pathways linked to MET–PTK2 and TAZ signaling axes (Supplementary Table 3).

Lastly, the dysregulated PDAOPCs presented an enrichment in adaptive immune signaling, antigen receptor regulation, and DNA repair mechanisms, pointing to roles in host defense, autoimmunity, and immune tolerance (Supplementary Table 3). In contrast, the healthy OPC-A subpopulation showed increased activity in signaling regulation, transcriptional control, vesicle transport, ion homeostasis, synaptic function, and structural remodeling within the neuronal system (Supplementary Table 3).

Furthermore, to assess the impact of PD on myelin quantity, we conducted a quantitative immunohistochemistry analysis using the MBP marker, which is indicative of myelination levels (Fig. 3c). The results revealed a decrease in MBP immunoreactivity within the Pu in PD vs control donors (control = 0.21 ± 0.01, PD = 0.17 ± 0.009, p value = 0.047, $t = 2.11$) (Fig. 3d). In addition, to further elucidate the relationship between MBP immunoreactivity in the Pu and the relative abundance of OLs subpopulations, we conducted a correlation analysis between MBP immunoreactive signal and the ratios of PDAO-1 and PDAO-2 to MOL-A, reflecting the aforementioned shifts in cell population proportions in PD. We observed a significant negative correlation, indicating that as the ratio of PDAO-1/MOL-A ($r = -0.56$, p value = 0.02) and/or PDAO-2/MOL-A ($r = -0.51$, p value = 0.02) increases (suggesting a shift of MOL-A to PDAO-1 and/or PDAO-2), MBP levels decrease (Fig. 3e, f).

Trajectory inference reveals disrupted oligodendrocyte differentiation pathways in Parkinson's disease

To understand the normal differentiation process and identify deviations from normality associated with PDAOs clusters in PD, we conducted trajectory inference analyses using the VIA and Slingshot algorithms. To infer the normal differentiation pathway, we considered all OL clusters except PDAOs, with samples from both conditions and regions. The differentiation process we identified is as follows: precursor cells, specifically OPCs-A, represent the original state and undergo differentiation into OPCs-C. These then further mature into COPs and immOL-B. Subsequent differentiation toward MOLs progresses through MOL-A and MOL-B populations, which are implicated in the initiation of myelination, as evidenced by the expression of Laminin-2 (*LAMA2*) and other cell adhesion molecules (CAMs). As differentiation advances, the MOL-F population emerges, characterized by the expression of genes associated with cholesterol metabolism, a process critical for the myelin sheath wrapping characteristic of mature oligodendrocytes (Fig. 4a). Intriguingly, we identified a previously unreported branch in the differentiation trajectory (Supplementary

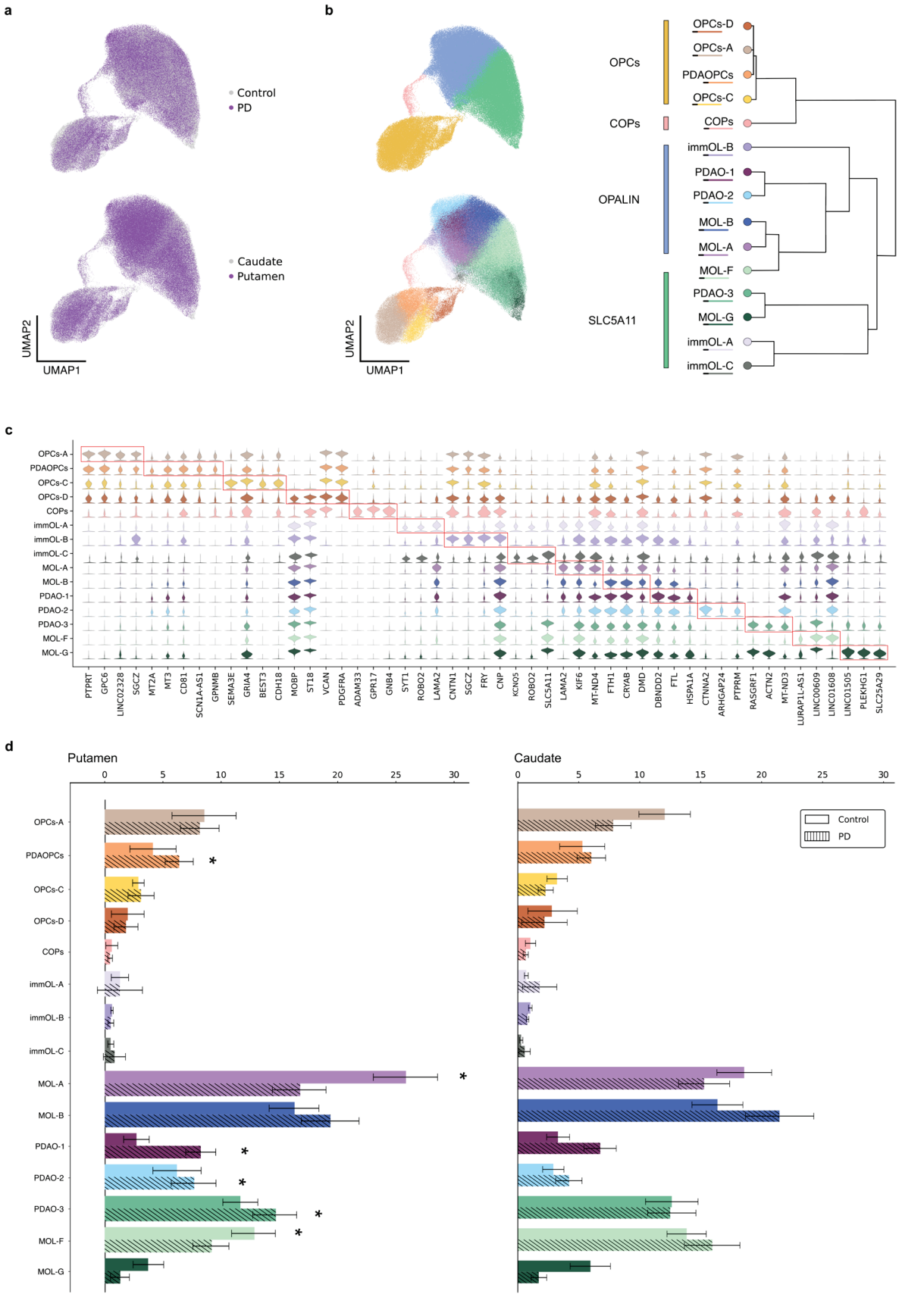
a
Control
PD
Caudate
Putamen
UMAP2
UMAP1
b
OPCs
COPs
OPALIN
SLC5A11
OPCs-D
OPCs-A
PDAOPCs
OPCs-C
COPs
immOL-B
PDAO-1
PDAO-2
MOL-B
MOL-A
MOL-F
PDAO-3
MOL-G
immOL-A
immOL-C
c
d
Putamen
Caudate
Control
PD

◂**Fig. 2** Quantitative analysis of oligodendrocytes and OPCs subpopulations. UMAPs display the uniform distribution of cells from each region and condition across all subpopulations (**a**). UMAP representing principal oligodendrocyte (OL) and oligodendrocyte progenitor cells (OPC) classes: OPCs, COPs, MOLs-*OPALIN*+, MOLs-*SLC5A11*+(**b**, Top Left). UMAP visualization depicting OLs and OPCs subpopulations, with distribution within subclasses based on transcriptomic similarity (**b**, Bottom Left), as illustrated in the dendrogram (**b**, Right). Stacked violin plots representing marker expression profiles for each subpopulation (**c**). Bar plots showing the percentages of each subpopulation, calculated based on the total number of nuclei in each condition (**d**). Asterisks (*) indicate significantly altered populations based on scCODA *p* value of confidence (< 0.2)

Fig. 6): OPC-D transitions through immOL-C to immOL-A, ultimately converging toward MOL-A/MOL-F. Moreover, immOL-C is also linked to MOL-E, suggesting a potential alternative pathway facilitating direct differentiation and maturation processes (Fig. 4a).

When analyzing all the clusters, including those PDAOs, and samples from both conditions and regions, we observed deviations in this normal differentiation trajectory. PDA clusters appeared to originate from specific healthy populations, exhibiting altered differentiation pathways in the diseased striatum. Specifically, PDAO-1 likely emerged directly from MOL-A in PD striatum, reflecting a disruption in the normal differentiation pathway of MOL-A to MOL-B and MOL-F. PDAO-2 showed a more ambiguous origin, potentially involving disruptions at the MOL-A and/or immOL-B differentiation stages, indicative of a complex pathological process (Fig. 4c). In the case of PDAO-3, it appeared to arise from perturbations in MOL-F, suggesting PD-associated alterations in this late-stage differentiation population. Finally, the same applied to PDAOPCs, which originated from OPCs-A, highlighting disruptions in the earliest stages of OL lineage differentiation.

To further investigate the molecular mechanisms underlying these differentiation pathways, we applied factor analysis to pseudotime-ordered gene expression data, which enabled us to identify distinct genetic signatures underpinning the differentiation trajectories (Fig. 4c, Supplementary Table 4), highlighting potential molecular mechanisms involved in disease-associated alterations. Factor analysis revealed specific genetic signatures involved in the transitions observed in normal differentiation, including genes critical for myelination, cholesterol metabolism, and cell adhesion (*LAMA4, LAMA2, MOBP, ERBB4*). When applied to pathological trajectories, factor analysis highlighted specific gene dysregulations associated with PDA clusters, providing insights into molecular mechanisms disrupted by disease (Fig. 4c). These findings underscore the role of aberrant gene regulation in driving pathological deviations from normal OL differentiation.

Altered intercellular interactions and neurotransmitter signatures in Parkinson's disease-associated oligodendrocyte subclasses

We further aimed to examine potential intercellular communication among the identified subpopulations and to determine whether communication patterns differ between control and PD striatum. With CellChat, we evaluated outgoing and incoming signaling dynamics based on the expression of known ligand–receptor pairs across subpopulations. Our results revealed significant disruptions in communication patterns within PD-associated clusters. Specifically, the analysis demonstrated a marked reduction in the expression of extracellular matrix (ECM) and adhesion molecules genes, such as *NCAM, CADM*, Laminin, and *CDH1*, in PDAO-1 compared to MOL-A, the latter exhibiting the highest expression levels of these molecules within the *OPALIN*$^{+}$ class (Fig. 5a, b). These findings suggest a weakening of adhesion and ECM-mediated signaling in PDAOs subpopulations. Indeed, there was a sharp decline in outgoing signals linked to myelination, particularly those associated with Laminin (*LAMA2*), in both PDAO-1 and PDAO-2. Furthermore, critical cell adhesion molecules (e.g., *NCAM, CADM,* and *CDH1*) were nearly absent in PDAO-1, highlighting substantial deficits in the ability of this cluster to engage in adhesion-based communication, likely contributing to the broader dysregulation of cellular networks in PD (Fig. 5b).

In contrast, cholesterol-related molecules, particularly within the *SLC5A11*$^{+}$ class, were elevated in these subpopulations (PDAO-3, MOL-G), aligning with the distinct biological profile of these populations demonstrated with hierarchical clustering, annotation, and GSEA analyses. Notably, the PDAOPCs subpopulation exhibited the lowest levels of general communication molecules among precursor cells, further suggesting disrupted intercellular interactions in early-stage OL precursors in PD (Fig. 5b).

Another striking finding from the CellChat analysis was the distinct upregulation of glutamate-related signaling molecules in OPC subpopulations, particularly in PDAOPCs. This observation prompted a deeper investigation into neurotransmitter signaling profiles across OL subpopulations (Fig. 5c). While the most pronounced differences were observed between OPCs and MOLs, key neurotransmitter-associated genes were also found to be differentially expressed in PD-specific clusters. For instance, *CHRNA10* and *GABRG1* were highly expressed in PDAO-2, while *GABRR2* was significantly upregulated in both PDAO-1 and PDAO-2. These findings point to a distinct alteration in neurotransmitter signaling in PD-associated OLs, likely contributing to their functional deficits.

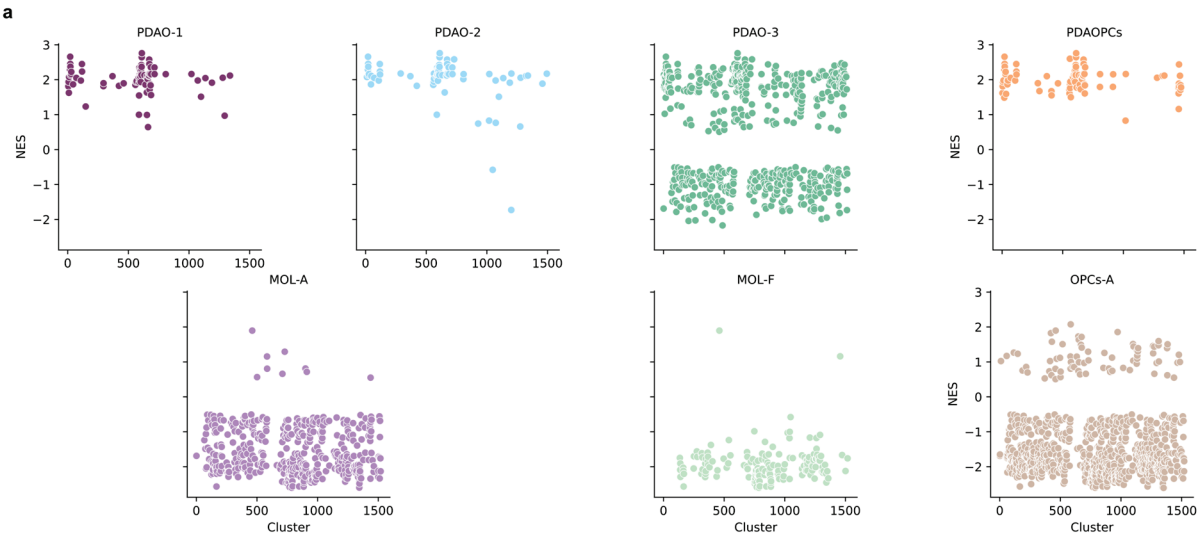
a
PDAO-1
PDAO-2
PDAO-3
PDAOPCs
MOL-A
MOL-F
OPCs-A
NES
Cluster

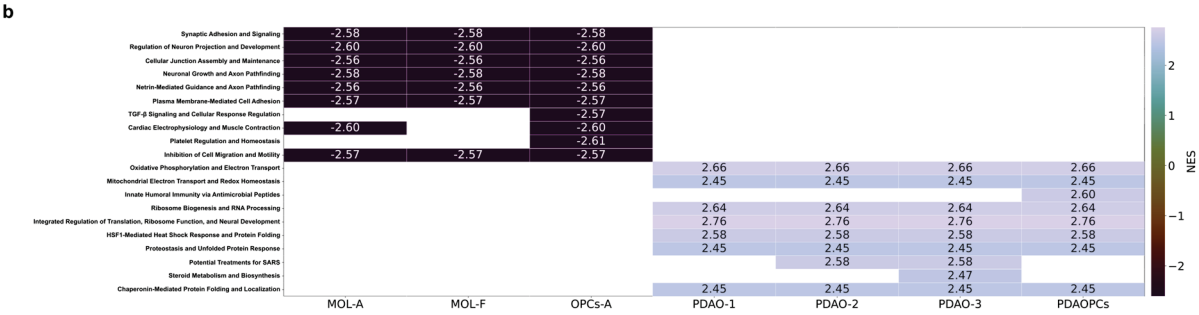
b
Synaptic Adhesion and Signaling
Regulation of Neuron Projection and Development
Cellular Junction Assembly and Maintenance
Neuronal Growth and Axon Pathfinding
Netrin-Mediated Guidance and Axon Pathfinding
Plasma Membrane-Mediated Cell Adhesion
TGF-β Signaling and Cellular Response Regulation
Cardiac Electrophysiology and Muscle Contraction
Platelet Regulation and Homeostasis
Inhibition of Cell Migration and Motility
Oxidative Phosphorylation and Electron Transport
Mitochondrial Electron Transport and Redox Homeostasis
Innate Humoral Immunity via Antimicrobial Peptides
Ribosome Biogenesis and RNA Processing
Integrated Regulation of Translation, Ribosome Function, and Neural Development
HSF1-Mediated Heat Shock Response and Protein Folding
Proteostasis and Unfolded Protein Response
Potential Treatments for SARS
Steroid Metabolism and Biosynthesis
Chaperonin-Mediated Protein Folding and Localization
MOL-A
MOL-F
OPCs-A
PDAO-1
PDAO-2
PDAO-3
PDAOPCs
NES

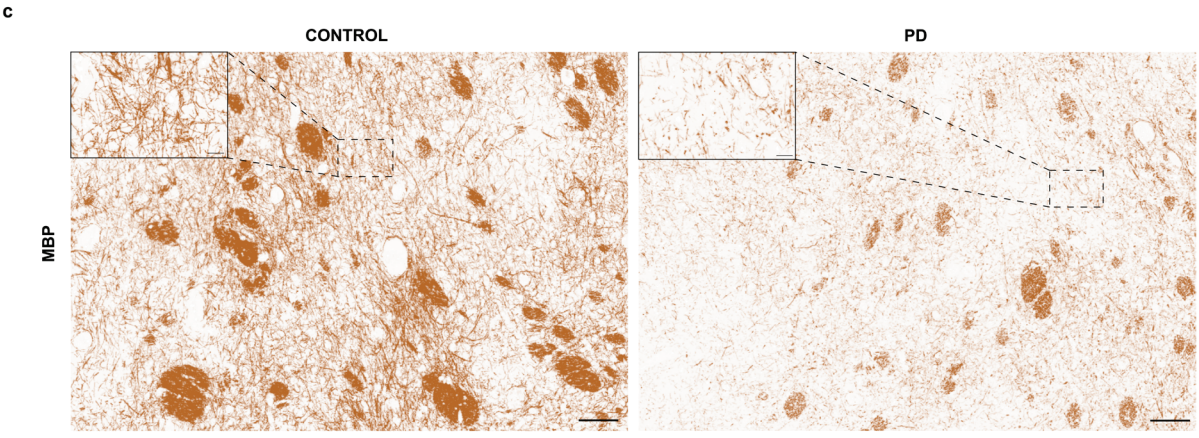
c
CONTROL
PD
MBP

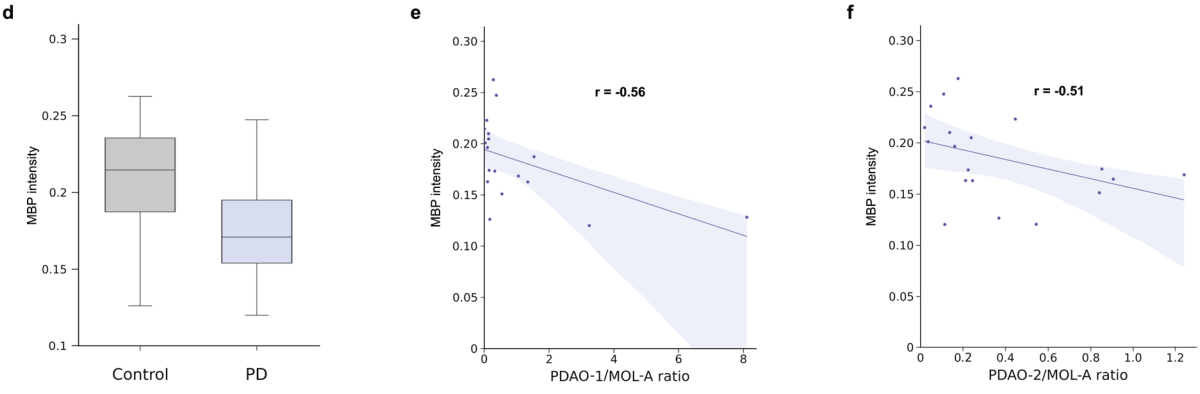
d
MBP intensity
Control
PD
e
r = -0.56
PDAO-1/MOL-A ratio
f
r = -0.51
PDAO-2/MOL-A ratio

◂**Fig. 3** Gene Set Enrichment Analysis and MBP expression in PD-associated oligodendrocytes subpopulations. Each panel displays Normalized Enrichment Scores (NES) for clusters/superpathways derived from GSEA results, grouped by the cell type in which they are upregulated and based on the comparison they are related to (PDAO-1 vs MOL-A, PDAO-2 vs MOL-A, PDAO-3 vs MOL-F, PDAOPCs vs OPCs-A)**.** Dot plots within each facet represent NES values per cluster for that specific cell type. Superpathways were filtered based on an FDR < 0.05 and an absolute NES value > 0.5 (**a**). Heatmap illustrates the distribution of NES values obtained from GSEA superpathways across the studied subpopulations for the top 20 clusters, including the 10 most positively and 10 most negatively enriched clusters based on NES magnitude. Rows represent GSEA-derived superpathways, while columns correspond to subpopulations of interest. Each cell reflects the NES for a given superpathway-cell type combination, with the color gradient indicating the level of enrichment (**b**). Immunohistochemical analysis of MBP in the Pu region under control and PD conditions. Scales are set at 100 µm for the low power images and at 20 µm for their insets (**c**). Boxplots illustrating the distribution of MBP expression in control and PD conditions. p value = 0.047, t = 2.11 (**d**). Scatter plot depicting the correlation between the ratio of PDAO-1 to MOL-A cells and MBP expression. $r = -0.56$, p value = 0.02 (**e**). Scatter plot showing the correlation between the ratio of PDAO-2 to MOL-A cells and MBP expression. $r = -0.51$, p value = 0.02 (**f**)

Spatial mapping reveals oligodendrocyte subpopulations and myelin-related alterations in Parkinson's disease

To validate the cell populations identified through sn-RNA-seq and further analyze other tissue-related variables, we employed spatial transcriptomics. This technique preserves the spatial organization of gene expression within the tissue, enabling the direct mapping of sn-RNA-seq-defined cell populations to their native anatomical contexts. By integrating these high-dimensional data modalities, we evaluated the robustness and biological relevance of sn-RNA-seq-derived clusters, ensuring that the identified populations are spatially resolved and assessing whether they localize to distinct striatal regions or whether they correspond to distinct functional domains within the same region.

Through spatial transcriptomics, we profiled 435,157 oligodendroglia cells. Using the cell2location model, we transferred sn-RNA-seq annotations to cells identified as OLs or OPCs in the spatial dataset (Fig. 6a). Analysis of the 366 profiled genes enabled the identification of all sn-RNA-seq-derived subpopulations within the OL lineage across both CN and Pu in the spatial transcriptomic dataset (Fig. 6a).

A noteworthy observation was the spatial distribution of these subpopulations within the tissue. Neighborhood enrichment analysis identified four main co-localizing subpopulations: PDAO-1, PDAO-3, MOL-F, and MOL-G (Fig. 6b). PDAO-3, MOL-F, and MOL-G were characterized by their maintenance of a myelin-related profile and appeared to be predominantly located within the WM tracts that cross through the striatum (Fig. 6c).

To better understand the molecular changes specific to PD, we conducted a Hotspot analysis to identify distinct gene expression modules that show significant variance between control and PD donors. This analysis highlighted two key modules with notable differences: heat shock protein response (HSPR) and myelination. Specifically, we observed a significant upregulation of the HSPR module in PD, accompanied by a marked downregulation of the myelination module, pointing to opposing trends in these two pathways (Fig. 6d, e).

The HSPR module, associated with cellular stress responses, exhibited strong correlations among genes encoding heat shock proteins, including *HSPA1A, DNAJA1, HSP90AB1*, and *CRYAB*. This module showed elevated activity in PD, suggesting an amplified cellular stress response in affected cells. Importantly, the activity of the HSPR module in PD was strongly correlated with the transcriptional signatures of PDAOs, further reinforcing the robustness of this finding (Fig. 6d, e).

In contrast, the myelination module, which encompasses genes critical for myelin formation and maintenance, such as *MAG, MOBP,* and *CNTN2*, was significantly downregulated in PD, suggesting an impairment of myelination processes. The reduced co-expression among genes in this module further underscore the disruption of myelin-related pathways in PD (Fig. 6d, e).

Interestingly, the activity of the HSPR and myelination modules appeared to be inversely related. In PD samples, the increased activity of the HSPR module coincided with a decrease in the myelination module, suggesting a potential trade-off between cellular stress response mechanisms and the maintenance of myelin. This interplay likely reflects a previously unrecognized critical aspect of PD pathophysiology, where OL energy and/or machinery resources are likely diverted to manage stress, compromising other vital processes like myelination (Fig. 6d).

Discussion

PD is a complex neurodegenerative disorder with no cure and unknown trigger in the vast majority of sporadic cases. Understanding the different key alterations with cell type specificity is crucial to develop treatments that can halt the progression of the disease. Traditionally, PD has been associated with dopaminergic neuron degeneration and Lewy bodies. Recently, oligodendroglia has emerged as a potential critical cell type in this disease [1, 13, 18, 64], but its involvement has not been investigated in depth. Characterizing the diversity of OLs and their precursors, as well as how they are affected in one of the most impacted

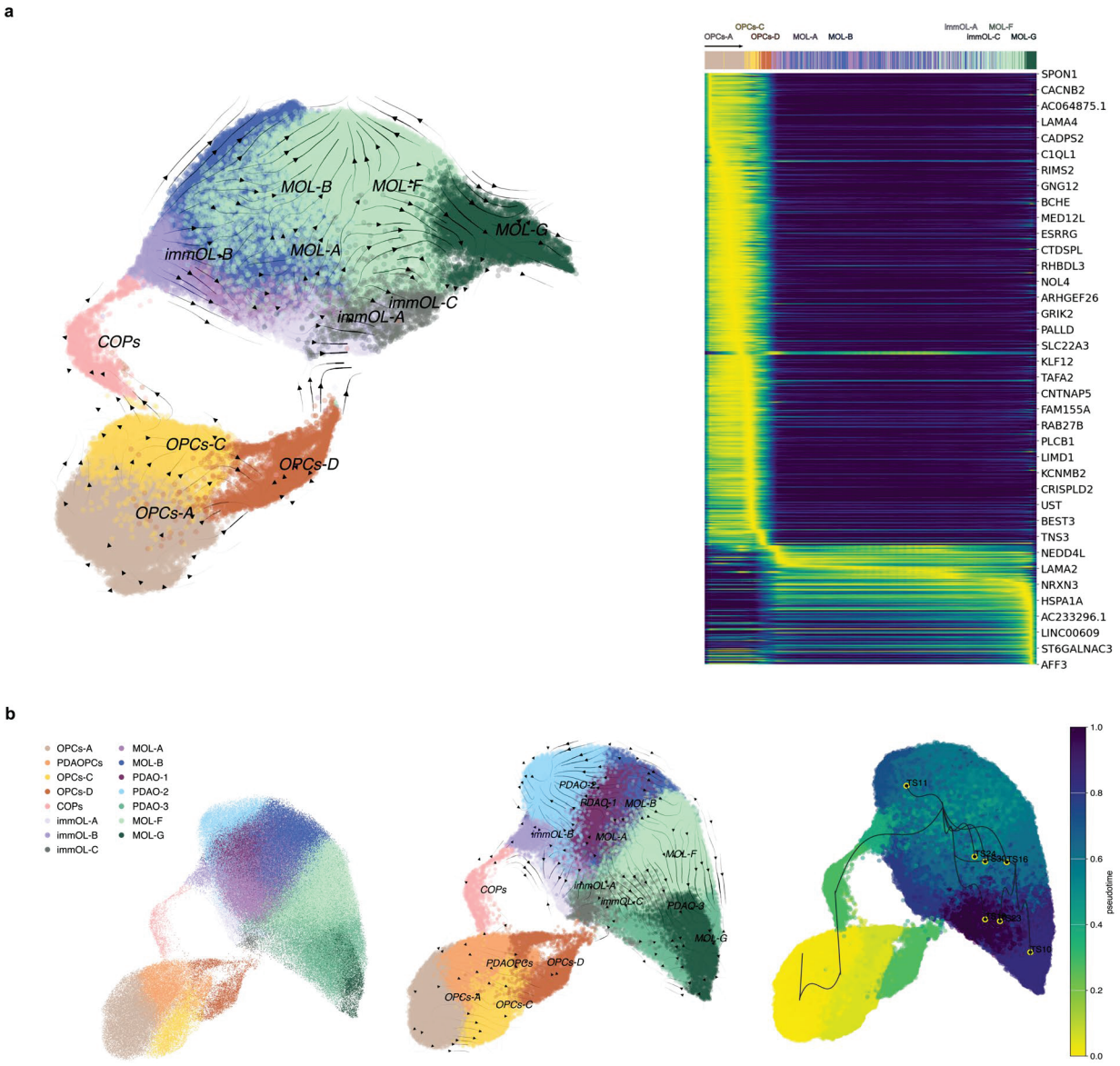
a
OPCs-A
OPCs-C
OPCs-D
MOL-A
MOL-B
immOL-A
immOL-C
MOL-F
MOL-G
immOL-B
COPs
SPON1
CACNB2
AC064875.1
LAMA4
CADPS2
C1QL1
RIMS2
GNG12
BCHE
MED12L
ESRRG
CTDSPL
RHBDL3
NOL4
ARHGEF26
GRIK2
PALLD
SLC22A3
KLF12
TAFA2
CNTNAP5
FAM155A
RAB27B
PLCB1
LIMD1
KCNMB2
CRISPLD2
UST
BEST3
TNS3
NEDD4L
LAMA2
NRXN3
HSPA1A
AC233296.1
LINC00609
ST6GALNAC3
AFF3
b
PDAOPCs
PDAO-1
PDAO-2
PDAO-3
TS11
TS16
TS23
TS10
pseudotime
1.0
0.8
0.6
0.4
0.2
0.0
c
PDAOPCs
PDAO-1
PDAO-2
PDAO-3

◂**Fig. 4** Pseudotime analysis of oligodendrocyte differentiation and divergent trajectories in PD. Pseudotime UMAP generated via StaVia analysis, excluding the expanded populations associated with PD. Arrows depict the progression of the differentiation trajectory, which proceeds from oligodendrocyte progenitor cells (OPCs) through COPs/OPCs-D, followed by immature oligodendrocytes (immOLs), and culminating in the transition from MOL-A to MOL-G (**a**, Left). Heatmap illustrating the expression of key genes involved in this differentiation process (**a**, Right). UMAP visualizations of differentiation trajectories in PD-associated clusters. Pseudotime analysis highlights a convergence point at MOL-A, from which the differentiation diverges into PDAO-1 and PDAO-2 clusters (**b**). Schematic representation of genes associated with differentiation pathways, tracing potential origins and pathways leading to the development of PD-associated clusters (**c**)

brain regions in PD (the dorsal striatum), is essential for uncovering the mechanisms underlying oligodendroglia dysfunction and its contribution to neurodegeneration.

In this work, we have built the largest dataset, to our knowledge, of sn-RNA-seq from CN and Pu samples from PD and control donors, and applied one of the most recent and sensitive spatial transcriptomics approaches to delineate the main transcriptomic changes of oligodendroglia with their neuroanatomical correlation in this neurodegenerative disorder.

The complexity of OLs and OPCs has only recently been elucidated in specific brain regions [3, 35, 46, 74, 88]. In our study, we analyzed more than 200 K nuclei from CN and Pu of 63 donors, identifying 4 main classes and 15 distinct subclasses. The main classes (OPCs, COPs, *OPALIN*$^{+}$ MOLs and *SCL5A11*$^{+}$) were previously described [3, 46, 54, 62, 64, 74, 88].

Among our subclasses, MOL-A and G (Int0 and Int3 in Sadick et al. [62]), and immOL-B (Int4 in Sadick et al. [62] and FRY population in Smajic et al. [64]) have been previously identified. Importantly, our large study enabled the identification of novel subclasses, including OPCs-C, OPCs-D, MOL-F, and immOL-A and C, as well as those associated with the disease, such as PDAOPCs and PDAO-1, PDAO-2, and PDAO-3. While MOL-B and PDAO-2 showed similarities with previous described populations, they have a distinct transcriptomic profile (Supplementary Table 5): PDAO-2 share similarities with the disease-associated OLs (DAOs) identified in MS by Falcão et al. [24], including pathways involved in antigen processing and presentation via major histocompatibility complex class I and II (MHC-I and -II), and immune OLs (imOLs) from Jäkel et al. [35] (related to OPC1 in Falcão et al. [24]) sharing *ARHGAP24* and *CTNNA2* among others. Thus, although DAOs have been observed in neurodegenerative diseases like MS (Falcão et al. [24]) and AD (Jäkel et al. [35]), the transcriptomic profile of PDAO-2 demonstrates unique characteristics (Supplementary Table 5), suggesting a disease-specific role in PD.

Alterations in HSPs have been associated with microglia in the midbrain in PD [64] and with specific signatures of OLs in PD [25, 64], but their role with OLs population specificity has not been previously described. The elevated expression of HSP-related genes, including *HSPA1A*, *HSPB1*, and *HSP90AB1*, along with increased chaperone-associated transcripts, highlights a potential role in stress adaptation and prevention of protein aggregation [76]. Intriguingly, α-syn aggregation in OLs is the neuropathological hallmark of multiple system atrophy (MSA) but is not a feature of PD. Trajectory inference analysis indicates that PDAO-1 likely derives from the MOL-A lineage and it exhibits significant impairments in myelination-related processes compared to MOL-A, demonstrating a maladaptive response in OLs during PD progression. This includes down-regulation of genes involved in myelin assembly—such as actin cytoskeleton components and adhesion molecules like laminins and cadherins as demonstrated with CellChat—and reduced neuronal communication, potentially contributing to the striatal WM alterations observed in PD. Although demyelination or remyelination failure are not established PD hallmarks, few works have pointed in that direction [10, 87] and support our findings.

PDAO-2, a distinct OL subpopulation, displays an immunological profile, including increased expression of neurotransmitter receptors (*GABRG1*, *GABRR2*) and immune-related genes (*HLA-C*, *HLA-A*). This aligns with findings that OLs can acquire immune-like functions in neurodegeneration, including antigen presentation and cytokine release [24, 35]. In PD, OL may influence microglia and astrocyte activity, contributing to the chronic neuroinflammatory environment [22, 49, 50]. Furthermore, reduced expression of myelination-associated communication molecules like Laminin [39] and Opalin [26] in PDAO-2 may indicate a shift from a supportive role in myelination toward an immunomodulatory function, as reported in other disorders like MS and AD [38, 86]. Thus, PDAO-2 may represent a dysfunctional OLs state that contributes to myelin loss and neuroinflammation in PD progression.

The negative correlation between MBP expression and the proportion of PDAO-1 and PDAO-2 underscores the critical role of OLs dysfunction in demyelination and neurodegeneration across neurological disorders, including PD [10, 17, 19, 27, 51, 87]. The increase of these subpopulations, alongside decreased MBP levels, suggests a shift in OL function away from myelination toward stress and immune responses, impairing their capacity to maintain and repair myelin and exacerbating neurodegeneration.

Two additional PD-associated subclasses, PDAO-3 and PDAOPCs, were identified. PDAO-3, a mature OL population, exhibits transcriptomic alterations indicative of

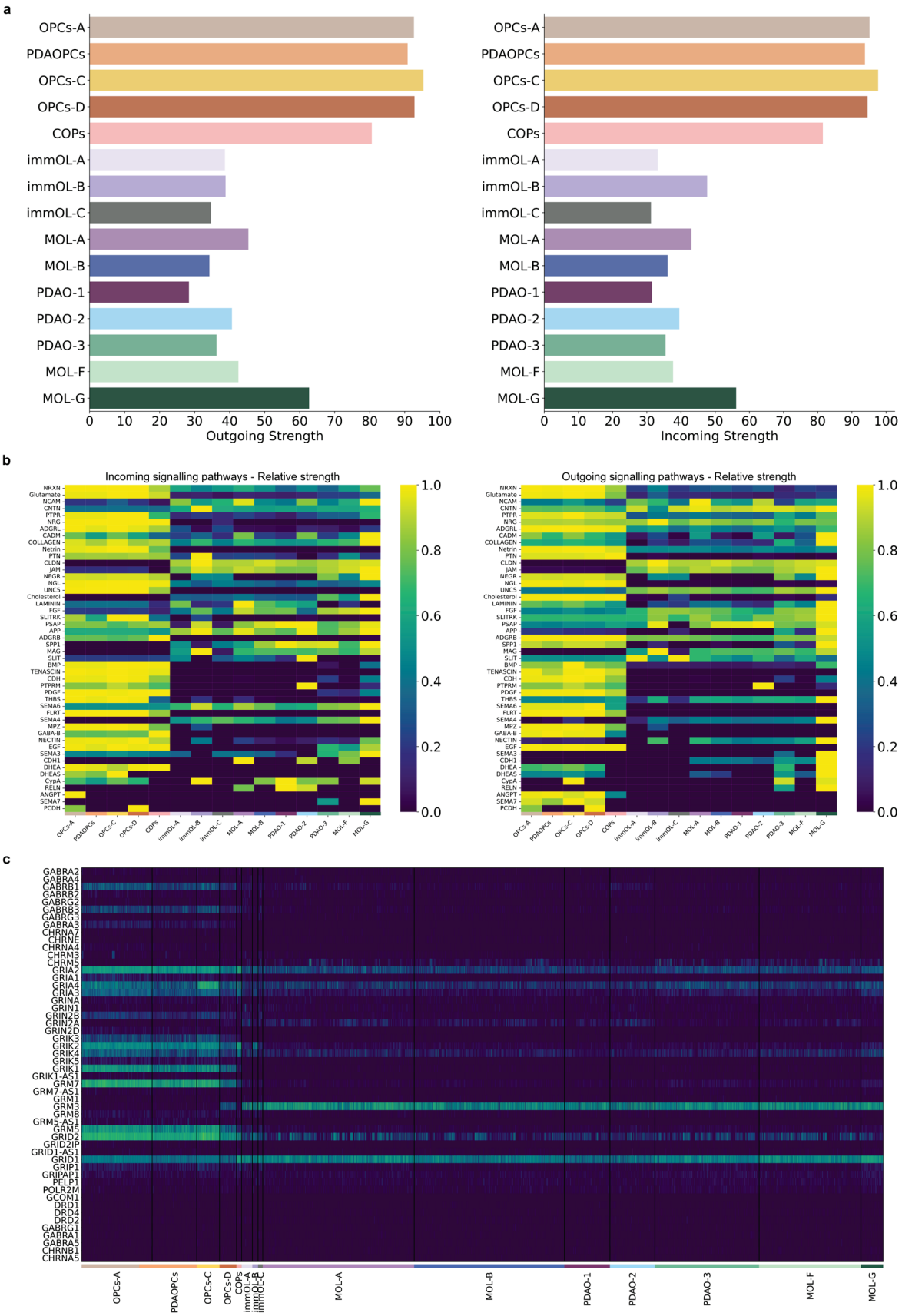
a
OPCs-A
PDAOPCs
OPCs-C
OPCs-D
COPs
immOL-A
immOL-B
immOL-C
MOL-A
MOL-B
PDAO-1
PDAO-2
PDAO-3
MOL-F
MOL-G
0 10 20 30 40 50 60 70 80 90 100
Outgoing Strength
Incoming Strength
b
Incoming signalling pathways - Relative strength
Outgoing signalling pathways - Relative strength
1.0
0.8
0.6
0.4
0.2
0.0
c
GABRA2
GABRA4
GABRB1
GABRB2
GABRG2
GABRB3
GABRG3
GABRA3
CHRNA7
CHRNE
CHRNA4
CHRM3
CHRM5
GRIA2
GRIA1
GRIA4
GRIA3
GRINA
GRIN1
GRIN2B
GRIN2A
GRIN2D
GRIK3
GRIK2
GRIK4
GRIK5
GRIK1
GRIK1-AS1
GRM7
GRM7-AS1
GRM1
GRM3
GRM8
GRM5-AS1
GRM5
GRID2
GRID2IP
GRID1-AS1
GRID1
GRIP1
GRIPAP1
PELP1
POLR2M
GCOM1
DRD1
DRD4
DRD2
GABRG1
GABRA1
GABRA5
CHRNB1
CHRNA5
OPCs-A
PDAOPCs
OPCs-C
OPCs-D
COPs
immOL-A
immOL-B
immOL-C
MOL-A
MOL-B
PDAO-1
PDAO-2
PDAO-3
MOL-F
MOL-G

◂**Fig. 5** Disrupted intercellular communication and neurotransmitter signatures in PD-associated oligodendrocytes. Bar plots illustrating the outgoing and incoming communication strengths for each subpopulation, as determined by ligand-receptor interaction analysis (**a**). Relative signaling pathway strengths are depicted for each subpopulation, highlighting distinct communication profiles (**b**). Heatmap displaying the expression levels of neurotransmitter-associated markers identified in at least 50 cells within any given population, showcasing distinct molecular signatures across subpopulations (**c**)

dual roles in stress adaptation and impaired myelination. GSEA indicates upregulation of autophagy, sphingolipid metabolism, and cytokine signaling, concurrent with downregulation of processes like cell projection organization and integrin signaling. Spatial transcriptomics further demonstrates the enrichment of PDAO-3 in striatal WM tracts, underscoring its potential role in the myelin deficits observed in PD [33, 56], and supporting the increased expression of cholesterol-related molecules identified in this subpopulation through CellChat analysis.

PDAOPCs, a subset of OPCs, exhibit heightened activity in pathways related to mitochondrial function and mitophagy, coupled with enhanced antigen presentation capabilities, indicating an adaptive response to cellular stress and metabolic demands in the PD microenvironment. However, the reduced expression of intercellular communication molecules suggests a compromise in PDAOPCs ability to mature into myelinating OLs, likely contributing to the myelin alterations observed within Pu of PD patients. In addition, PDAOPCs exhibit a distinct glutamate-related signaling profile, implicating them in altered neurotransmitter dynamics and interactions with neuronal circuits in PD. Together, these features point to PDAOPCs as an early, vulnerable oligodendroglia population whose dysfunction propagates broader myelin and connectivity deficits in PD.

Overall, the transcriptomic changes were more prominent in Pu than CN, as illustrated by changes in OL composition, which is consistent with the more severe reduction in TH and MBP immunoreactivity in Pu versus CN, as well as increased α-synuclein aggregations. These findings align with the spatio-temporal progression of the nigrostriatal pathway degeneration in PD [11, 60]. Pu is critically involved in motor control and well-established to be affected in PD [10, 17, 66], further supporting our findings and reinforcing Pu involvement in disease pathology and its critical role in motor control. However, it remains unclear whether the observed changes in OLs represent a primary pathogenic process in PD or arise secondarily due to the degeneration of dopaminergic projections. Given the selective vulnerability of dopamine terminals in Pu and the accumulation of α-synuclein, it is plausible that the myelinated fibers within this region undergo secondary degeneration, triggering the transcriptional reprogramming observed in OL subpopulations, with changes in GABA receptor expression serving as an example of how alterations in neurotransmitter levels might influence these processes. Conversely, experimental evidence demonstrates that α-synuclein can transfer from neurons to OLs [59], and α-synuclein inclusions were detected in OLs of PD patients [2, 79], indicating a potential primary role for oligodendroglial in PD pathology and reinforcing the presence of enriched pathways related to protein misfolding and proteostasis. The interplay between OL alterations, dopaminergic neuronal loss, and α-synuclein dynamics remains unresolved; however, our data point to WM dysfunction as a potentially underrecognized component of PD-related pathology in the basal ganglia.

Importantly, determining whether the affected fibers belong to the striatopallidal (indirect pathway) or striatonigral (direct pathway) projections is crucial, as each pathway plays a distinct and opposing role in motor regulation. Further experiments and approaches are needed to determine this. Such information could clarify which component of the basal ganglia circuitry is primarily disrupted in PD in Pu, as recent studies have identified the striatopallidal route as a critical component of the basal ganglia circuitry for motor control [44], suggesting that OL-associated dysfunction within this pathway could exacerbate motor deficits. Moreover, aberrant GABAergic signaling from MSNs along these fibers may impact OL function by altering their maturation, impairing myelination, or inducing immune-like phenotypes (as in the case of PDAO-2), particularly in regions where OL–GABA interactions are spatially enriched.

Our results add to a growing body of evidence underscoring the critical interplay between glial and neuronal dysfunction in PD and suggest that oligodendroglial pathology may be a promising target for therapeutic intervention aimed at slowing or halting disease progression. Our transcriptomic analysis emerged two candidate therapeutic targets: RHO GTPase signaling and oxidative stress pathways, both of which are dysregulated in PDA OL subpopulations. Among agents modulating the RHO pathway, Fasudil, a ROCK inhibitor, is being tested in clinical trials for PD (NCT05931575) [83] and has exhibited both neuroprotective and remyelinating properties in MS [81, 83]. Moreover, Catalpol has shown neuroprotective efficacy in MPTP-induced PD models [80] attributed to its capacity to reduce oxidative stress and promote OL regeneration and remyelination [70, 80]. Furthermore, Fingolimod, an FDA-approved therapy against MS [63], has been shown to exert both neuroprotective and remyelinating effects by enhancing OL survival and function in PD-related models such as those induced by rotenone and 6-OHDA [58, 89]. Lastly, since PD is twice as common in men

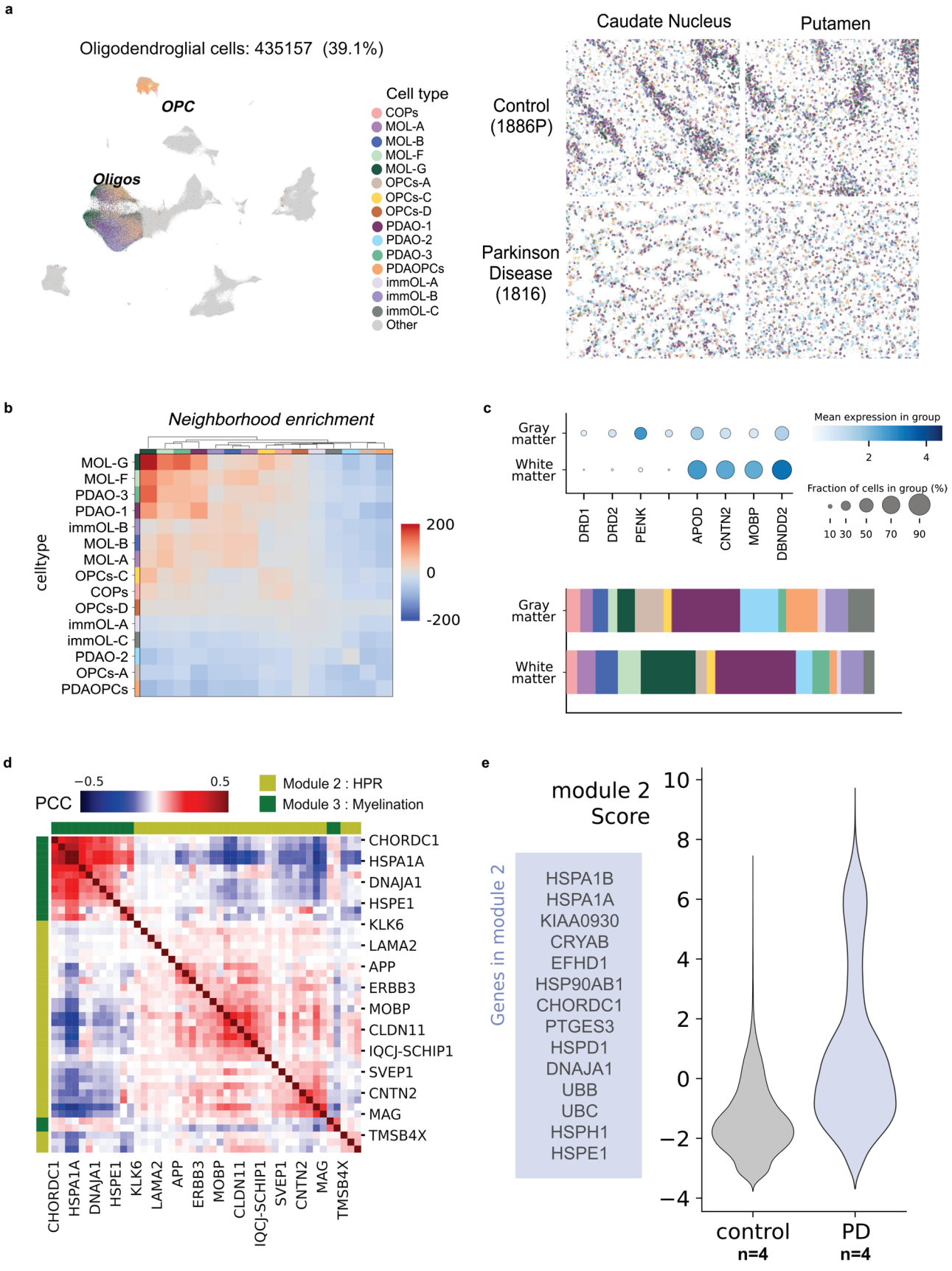
a
Oligodendroglial cells: 435157 (39.1%)
OPC
Oligos
Cell type
COPs
MOL-A
MOL-B
MOL-F
MOL-G
OPCs-A
OPCs-C
OPCs-D
PDAO-1
PDAO-2
PDAO-3
PDAOPCs
immOL-A
immOL-B
immOL-C
Other
Caudate Nucleus
Putamen
Control (1886P)
Parkinson Disease (1816)
b
Neighborhood enrichment
celltype
MOL-G
MOL-F
PDAO-3
PDAO-1
immOL-B
MOL-B
MOL-A
OPCs-C
COPs
OPCs-D
immOL-A
immOL-C
PDAO-2
OPCs-A
PDAOPCs
200
0
-200
c
Gray matter
White matter
DRD1
DRD2
PENK
APOD
CNTN2
MOBP
DBNDD2
Mean expression in group
2
4
Fraction of cells in group (%)
10 30 50 70 90
Gray matter
White matter
d
PCC
−0.5
0.5
Module 2 : HPR
Module 3 : Myelination
CHORDC1
HSPA1A
DNAJA1
HSPE1
KLK6
LAMA2
APP
ERBB3
MOBP
CLDN11
IQCJ-SCHIP1
SVEP1
CNTN2
MAG
TMSB4X
e
module 2 Score
Genes in module 2
HSPA1B
HSPA1A
KIAA0930
CRYAB
EFHD1
HSP90AB1
CHORDC1
PTGES3
HSPD1
DNAJA1
UBB
UBC
HSPH1
HSPE1
10
8
6
4
2
0
−2
−4
control
n=4
PD
n=4

◂**Fig. 6** Spatial transcriptomics reveals region-specific oligodendrocyte distribution and molecular signatures in PD. UMAP illustrating oligodendrocyte populations profiled through spatial transcriptomics, corresponding to the populations identified via sn-RNA-seq (**a**, Left). Spatial distribution of oligodendrocyte subpopulations across CN and Pu (**a**, Right). Heatmap depicting neighborhood enrichment patterns for all identified subpopulations, highlighting spatial co-localization (**b**). Spatial localization of oligodendrocyte subpopulations within the gray matter (GM) and white matter (WM) areas (**c**). These regions were categorized based on marker expression (**c,** Top). Bar plots illustrate the distribution of oligodendroglia subpopulations across both GM and WM (**c**, Bottom). Heatmap represents the distribution of module 2 (heat shock protein response, HSPR) and module 3 (myelination), demonstrating a negative correlation between these modules (**d**). Violin plots showing an increased expression of HSPR module in PD (**e**)

than in women, estrogen-based therapies have been investigated and, although the underlying mechanisms remain incompletely understood, they have shown neuroprotective effects in PD models [61, 67]. Notably, in a cuprizone-induced demyelination model, treatment with 17 β-estradiol was found to prevent both demyelination and OL loss [73], supporting its potential to mitigate OL dysfunction in PD as well.

Collectively, these findings highlight the need to unravel the mechanisms underlying OLs dysfunction in PD, as such insights are crucial for guiding the development of therapies that protect myelin and promote neuronal health. Moreover, the role of PDA populations in exacerbating neurodegeneration through the disruption of essential glial–neuronal interactions underscores their critical contribution to the dysfunction of the basal ganglia circuit that characterizes PD.

Conclusion

Our study provides a comprehensive characterization of oligodendroglia heterogeneity in the dorsal striatum of Parkinson's disease, highlighting distinct disease-associated subtypes with impaired myelination and immune-like properties. The emergence of these dysfunctional states suggests that OLs are not merely bystanders but active contributors to PD pathology. We hypothesize that a maladaptive oligodendroglia response—characterized by disrupted maturation, immune activation, and myelin instability—exacerbates neurodegeneration and impairs basal ganglia function. Targeting these pathogenic OLs states may offer novel therapeutic strategies to protect myelin integrity and slow disease progression.

Supplementary Information The online version contains supplementary material available at https://doi.org/10.1007/s00401-025-02884-5.

Acknowledgements The authors acknowledge the Massachusetts Alzheimer's Disease Research Center (especially Patrick Dooley and Tessa Connors), the Parkinson's UK Brain Bank at Imperial funded by Parkinson's UK (a charity registered in England and Wales, 258197, and in Scotland, SC037554), and the NIH NeuroBioBank (NIH Ref-1851, Requestor: Professor Ernest Arenas, R.I.P.), for the supply of tissue samples and associated clinical and neuropathological data. The authors also want to thank the National Genomics Infrastructure in Stockholm funded by Science for Life Laboratory and SNIC/Uppsala Multidisciplinary Center for Advanced Computational Science for assistance with massively parallel sequencing and access to the UPPMAX computational infrastructure. Further thanks go to Katarina Tiklova and Chika Yokota from the In Situ Sequencing Infrastructure Unit at the Science for Life Laboratory, Stockholm. The authors also thank Ayush Noori for making available his pathway clustering code which served as the foundation for our GSEA Superpathway analysis, and the *Centro de Investigación Biomédica en Red de Salud Mental*-CIBERSAM (CB/07/09/0033). Finally, we are extremely grateful to the brain donors and their families who have made this study possible.

Author contributions Concept and design: JMBR, ABMM Tissue acquisition and processing: LH, MJ, CMC, ASP, ABMM Sequencing: LH, ABMM Data analysis: JMBR, SMS, LDG, NR Interpretation of the data: JMBR, ABMM Supervision:ABMM Resources: MN, BTH, ASP, ABMM Writing—original draft: JMBR, ABMM Writing—review & editing: JMBR, LH, SMS, MN, BTH, ASP, ABMM.

Funding Funding for open access publishing: Universidad de Cádiz/CBUA. The authors acknowledge support from grants PID2019-109046GA-I00 and PID2022-136526OB-I00 by MCIN/AEI/https://doi.org/10.13039/501100011033and ERDF/EU (to A.B.M.-M. and 2019-FPI to J.M.B.-R.), RyC program RYC-2017–22594 (to A.B.M.-M.), the Swedish Foundation for Strategic Research FFL 18–0314 (A.B.M.-M.), the Swedish Research Council 2017–03349 (to A.B.M.-M.), the Prince Mahidol Award Youth Program (to M.J.), the Martin L. and Sylvia Seevak-Hoffman Fellowship for Alzheimer's Research (to M.J.), the Real Colegio Complutense at Harvard University (to C.M.-C.), and the US National Institute on Aging P30AG062421 (to B.T.H. and A.S.-P.).

Availability of data and material Single-nuclei RNA-seq and spatial transcriptomics data have been deposited at Figshare (10.6084/m9.figshare.28202405) and Zenodo (10.5281/zenodo.15304115) respectively and are publicly available as of the date of publication. Any additional information required to reanalyze the data reported in this paper is available from the lead contact upon request (Ana B. Muñoz-Manchado (ana.munoz@uca.es).

Declarations

Conflict of interest Dr. Hyman owns stock in Novartis; he serves on the SAB of Dewpoint and has an option for stock. He serves on a scientific advisory board or is a consultant for AbbVie,Alexion, Ambagon, Aprinoia Therapeutics, Arvinas, Avrobio, AstraZenica, Biogen, Bioinsights, BMS, Cure Alz Fund, Cell Signaling, Dewpoint, Latus, Merck, Novartis, Pfizer, Sanofi, Sofinnova, Takeda, TD Cowen, Vigil, Violet, Voyager, WaveBreak. His laboratory is supported by research grants from the National Institutes of Health, Cure Alzheimer's Fund, Tau Consortium, and the JPB Foundation—and a sponsored research agreement from Abbvie and Sanofi. He has a collaborative project with Biogen. Dr. Marco Salas is co-founder of spatialist AB, a spatial omics consulting company.

Ethical approval and consent to participate The study does not include living human subjects. Samples were collected from autopsies and

have been de-identified. Donors or their next-of-kin provided written informed consent for brain autopsy, and the study was approved by the review board of each brain bank.

Open Access This article is licensed under a Creative Commons Attribution 4.0 International License, which permits use, sharing, adaptation, distribution and reproduction in any medium or format, as long as you give appropriate credit to the original author(s) and the source, provide a link to the Creative Commons licence, and indicate if changes were made. The images or other third party material in this article are included in the article's Creative Commons licence, unless indicated otherwise in a credit line to the material. If material is not included in the article's Creative Commons licence and your intended use is not permitted by statutory regulation or exceeds the permitted use, you will need to obtain permission directly from the copyright holder. To view a copy of this licence, visit http://creativecommons.org/licenses/by/4.0/.

References

1. Agarwal D, Sandor C, Volpato V, Caffrey TM, Monzón-Sandoval J, Bowden R et al (2020) A single-cell atlas of the human substantia nigra reveals cell-specific pathways associated with neurological disorders. Nat Commun 11:4183. https://doi.org/10.1038/s41467-020-17876-0
2. Arai T, Uéda K, Ikeda K, Akiyama H, Haga C, Kondo H et al (1999) Argyrophilic glial inclusions in the midbrain of patients with Parkinson's disease and diffuse Lewy body disease are immunopositive for NACP/α-synuclein. Neurosci Lett 259:83–86. https://doi.org/10.1016/S0304-3940(98)00890-8
3. Bae E-J, Pérez-Acuña D, Rhee KH, Lee S-J (2023) Changes in oligodendroglial subpopulations in Parkinson's disease. Mol Brain 16:65. https://doi.org/10.1186/s13041-023-01055-5
4. Bakiri Y, Káradóttir R, Cossell L, Attwell D (2011) Morphological and electrical properties of oligodendrocytes in the white matter of the corpus callosum and cerebellum. J Physiol 589:559–573. https://doi.org/10.1113/jphysiol.2010.201376
5. Baumann N, Pham-Dinh D (2001) Biology of oligodendrocyte and myelin in the mammalian central nervous system. Physiol Rev 81:871–927. https://doi.org/10.1152/physrev.2001.81.2.871
6. Bechler ME, Byrne L, ffrench-Constant C (2015) CNS myelin sheath lengths are an intrinsic property of oligodendrocytes. Curr Biol 25:2411–2416. https://doi.org/10.1016/j.cub.2015.07.056
7. Binamé F, Sakry D, Dimou L, Jolivel V, Trotter J (2013) NG2 regulates directional migration of oligodendrocyte precursor cells via Rho GTPases and polarity complex proteins. J Neurosci 33:10858–10874. https://doi.org/10.1523/JNEUROSCI.5010-12.2013
8. Birk S, Bonafonte-Pardàs I, Feriz AM, Boxall A, Agirre E, Memi F et al (2025) Quantitative characterization of cell niches in spatially resolved omics data. Nat Genet. https://doi.org/10.1038/s41588-025-02120-6
9. Blauwendraat C, Nalls MA, Singleton AB (2020) The genetic architecture of Parkinson's disease. Lancet Neurol 19:170–178. https://doi.org/10.1016/S1474-4422(19)30287-X
10. Boshkovski T, Cohen-Adad J, Misic B, Arnulf I, Corvol J-C, Vidailhet M et al (2022) The Myelin-weighted connectome in Parkinson's disease. Mov Disord 37:724–733. https://doi.org/10.1002/mds.28891
11. Braak H, Tredici KD, Rüb U, de Vos RAI, Jansen Steur ENH, Braak E (2003) Staging of brain pathology related to sporadic Parkinson's disease. Neurobiol Aging 24:197–211. https://doi.org/10.1016/S0197-4580(02)00065-9
12. Bradl M, Lassmann H (2010) Oligodendrocytes: biology and pathology. Acta Neuropathol 119:37–53. https://doi.org/10.1007/s00401-009-0601-5
13. Bryois J, Skene NG, Hansen TF, Kogelman LJA, Watson HJ, Liu Z et al (2020) Genetic identification of cell types underlying brain complex traits yields insights into the etiology of Parkinson's disease. Nat Genet 52:482–493. https://doi.org/10.1038/s41588-020-0610-9
14. Büttner M, Ostner J, Müller CL, Theis FJ, Schubert B (2021) scCODA is a Bayesian model for compositional single-cell data analysis. Nat Commun 12:6876. https://doi.org/10.1038/s41467-021-27150-6
15. Chong SYC, Rosenberg SS, Fancy SPJ, Zhao C, Shen Y-AA, Hahn AT et al (2012) Neurite outgrowth inhibitor Nogo-A establishes spatial segregation and extent of oligodendrocyte myelination. Proc Natl Acad Sci U S A 109:1299–1304. https://doi.org/10.1073/pnas.1113540109
16. Corces MR, Shcherbina A, Kundu S, Gloudemans MJ, Frésard L, Granja JM et al (2020) Single-cell epigenomic analyses implicate candidate causal variants at inherited risk loci for Alzheimer's and Parkinson's diseases. Nat Genet 52:1158–1168. https://doi.org/10.1038/s41588-020-00721-x
17. Dean DC, Hurley SA, Kecskemeti SR, O'Grady JP, Canda C, Davenport-Sis NJ et al (2017) Association of amyloid pathology with myelin alteration in preclinical Alzheimer disease. JAMA Neurol 74:41–49. https://doi.org/10.1001/jamaneurol.2016.3232
18. Dehestani M, Kozareva V, Blauwendraat C, Fraenkel E, Gasser T, Bansal V (2024) Transcriptomic changes in oligodendrocytes and precursor cells associate with clinical outcomes of Parkinson's disease. Mol Brain 17:56. https://doi.org/10.1186/s13041-024-01128-z
19. Depp C, Sun T, Sasmita AO, Spieth L, Berghoff SA, Nazarenko T et al (2023) Myelin dysfunction drives amyloid-β deposition in models of Alzheimer's disease. Nature 618:349–357. https://doi.org/10.1038/s41586-023-06120-6
20. DeTomaso D, Yosef N (2021) Hotspot identifies informative gene modules across modalities of single-cell genomics. Cell Syst 12:446-456.e9. https://doi.org/10.1016/j.cels.2021.04.005
21. Dickson DW, Braak H, Duda JE, Duyckaerts C, Gasser T, Halliday GM et al (2009) Neuropathological assessment of Parkinson's disease: refining the diagnostic criteria. Lancet Neurol 8:1150–1157. https://doi.org/10.1016/S1474-4422(09)70238-8
22. Domingues HS, Portugal CC, Socodato R, Relvas JB (2016) Oligodendrocyte, astrocyte, and microglia crosstalk in myelin development, damage, and repair. Front Cell Dev Biol 4:71. https://doi.org/10.3389/fcell.2016.00071
23. Errea O, Rodriguez-Oroz MC (2021) Oligodendrocytes, a new player in the etiology of Parkinson's disease. Mov Disord 36:83. https://doi.org/10.1002/mds.28393
24. Falcão AM, van Bruggen D, Marques S, Meijer M, Jäkel S, Agirre E et al (2018) Disease-specific oligodendrocyte lineage cells arise in multiple sclerosis. Nat Med 24:1837–1844. https://doi.org/10.1038/s41591-018-0236-y
25. Fan L-Y, Yang J, Liu R-Y, Kong Y, Guo G-Y, Xu Y-M (2023) Integrating single-nucleus sequence profiling to reveal the transcriptional dynamics of Alzheimer's disease, Parkinson's disease, and multiple sclerosis. J Transl Med 21:649. https://doi.org/10.1186/s12967-023-04516-6
26. de Faria O, Dhaunchak AS, Kamen Y, Roth AD, Kuhlmann T, Colman DR et al (2019) TMEM10 promotes oligodendrocyte differentiation and is expressed by oligodendrocytes in human remyelinating multiple sclerosis plaques. Sci Rep 9:3606. https://doi.org/10.1038/s41598-019-40342-x
27. Franklin RJM (2002) Why does remyelination fail in multiple sclerosis? Nat Rev Neurosci 3:705–714. https://doi.org/10.1038/nrn917

28. Garma LD, Harder L, Barba-Reyes JM, Marco Salas S, Díez-Salguero M, Nilsson M et al (2024) Interneuron diversity in the human dorsal striatum. Nat Commun 15:6164. https://doi.org/10.1038/s41467-024-50414-w
29. Glass CK, Saijo K, Winner B, Marchetto MC, Gage FH (2010) Mechanisms underlying inflammation in neurodegeneration. Cell 140:918–934. https://doi.org/10.1016/j.cell.2010.02.016
30. Goldenberg MM (2012) Multiple sclerosis review. PT 37:175–184
31. Halliday GM, Holton JL, Revesz T, Dickson DW (2011) Neuropathology underlying clinical variability in patients with synucleinopathies. Acta Neuropathol 122:187–204. https://doi.org/10.1007/s00401-011-0852-9
32. Hawrylycz MJ, Lein ES, Guillozet-Bongaarts AL, Shen EH, Ng L, Miller JA et al (2012) An anatomically comprehensive atlas of the adult human brain transcriptome. Nature 489:391–399. https://doi.org/10.1038/nature11405
33. Herz DM, Eickhoff SB, Løkkegaard A, Siebner HR (2014) Functional neuroimaging of motor control in Parkinson's disease: a meta-analysis. Hum Brain Mapp 35:3227–3237. https://doi.org/10.1002/hbm.22397
34. del Hortega PR (1928) Tercera aportación al conocimiento morfológico e interpretación funcional de la oligodendroglía [Third contribution to the morphological knowledge and functional interpretation of oligodendroglia]. Memorias de la Real Soc Española de Historia Nat 14:5–122
35. Jäkel S, Agirre E, Falcão AM, van Bruggen D, Lee KW, Knuesel I et al (2019) Altered human oligodendrocyte heterogeneity in multiple sclerosis. Nature 566:543–547. https://doi.org/10.1038/s41586-019-0903-2
36. Jia F, Fellner A, Kumar KR (2022) Monogenic Parkinson's disease: genotype, phenotype, pathophysiology, and genetic testing. Genes (Basel) 13:471. https://doi.org/10.3390/genes13030471
37. Jin S, Guerrero-Juarez CF, Zhang L, Chang I, Ramos R, Kuan C-H et al (2021) Inference and analysis of cell-cell communication using Cell Chat. Nat Commun 12:1088. https://doi.org/10.1038/s41467-021-21246-9
38. Kalafatakis I, Karagogeos D (2021) Oligodendrocytes and microglia: key players in myelin development. Damage Repair Biomol 11:1058. https://doi.org/10.3390/biom11071058
39. Kang M, Yao Y (2022) Laminin regulates oligodendrocyte development and myelination. Glia 70:414–429. https://doi.org/10.1002/glia.24117
40. Kirby BB, Takada N, Latimer AJ, Shin J, Carney TJ, Kelsh RN et al (2006) In vivo time-lapse imaging shows dynamic oligodendrocyte progenitor behavior during zebrafish development. Nat Neurosci 9:1506–1511. https://doi.org/10.1038/nn1803
41. Kish SJ, Shannak K, Hornykiewicz O (1988) Uneven pattern of dopamine loss in the striatum of patients with idiopathic Parkinson's disease. N Engl J Med 318:876–880. https://doi.org/10.1056/NEJM198804073181402
42. Kleshchevnikov V, Shmatko A, Dann E, Aivazidis A, King HW, Li T et al (2022) Cell 2location maps fine-grained cell types in spatial transcriptomics. Nat Biotechnol 40:661–671. https://doi.org/10.1038/s41587-021-01139-4
43. Korsunsky I, Millard N, Fan J, Slowikowski K, Zhang F, Wei K et al (2019) Fast, sensitive and accurate integration of single-cell data with harmony. Nat Methods 16:1289–1296. https://doi.org/10.1038/s41592-019-0619-0
44. Labouesse MA, Torres-Herraez A, Chohan MO, Villarin JM, Greenwald J, Sun X et al (2023) A non-canonical striatopallidal Go pathway that supports motor control. Nat Commun 14:6712. https://doi.org/10.1038/s41467-023-42288-1
45. Marco Salas S, Kuemmerle LB, Mattsson-Langseth C, Tismeyer S, Avenel C, Hu T et al (2025) Optimizing Xenium in situ data utility by quality assessment and best-practice analysis workflows. Nat Methods 22:813–823. https://doi.org/10.1038/s41592-025-02617-2
46. Marques S, Zeisel A, Codeluppi S, van Bruggen D, Mendanha Falcão A, Xiao L et al (2016) Oligodendrocyte heterogeneity in the mouse juvenile and adult central nervous system. Science 352:1326–1329. https://doi.org/10.1126/science.aaf6463
47. Mathys H, Davila-Velderrain J, Peng Z, Gao F, Mohammadi S, Young JZ et al (2019) Single-cell transcriptomic analysis of Alzheimer's disease. Nature 570:332–337. https://doi.org/10.1038/s41586-019-1195-2
48. Mathys H, Peng Z, Boix CA, Victor MB, Leary N, Babu S et al (2023) Single-cell atlas reveals correlates of high cognitive function, dementia, and resilience to Alzheimer's disease pathology. Cell 186:4365-4385.e27. https://doi.org/10.1016/j.cell.2023.08.039
49. Miguel-Hidalgo JJ (2022) Astroglia in the vulnerability to and maintenance of stress-mediated neuropathology and depression. Front Cell Neurosci. https://doi.org/10.3389/fncel.2022.869779
50. Miguel-Hidalgo JJ (2023) Neuroprotective astroglial response to neural damage and its relevance to affective disorders. Explor Neuroprotective Ther. 3:328–345. https://doi.org/10.37349/ent.2023.00054
51. Nasrabady SE, Rizvi B, Goldman JE, Brickman AM (2018) White matter changes in Alzheimer's disease: a focus on myelin and oligodendrocytes. Acta Neuropathol Commun 6:22. https://doi.org/10.1186/s40478-018-0515-3
52. Ouchi Y, Yoshikawa E, Sekine Y, Futatsubashi M, Kanno T, Ogusu T et al (2005) Microglial activation and dopamine terminal loss in early Parkinson's disease. Ann Neurol 57:168–175. https://doi.org/10.1002/ana.20338
53. Palla G, Spitzer H, Klein M, Fischer D, Schaar AC, Kuemmerle LB et al (2022) Squidpy: a scalable framework for spatial omics analysis. Nat Methods 19:171–178. https://doi.org/10.1038/s41592-021-01358-2
54. Pandey S, Shen K, Lee S-H, Shen Y-AA, Wang Y, Otero-García M et al (2022) Disease-associated oligodendrocyte responses across neurodegenerative diseases. Cell Rep 40:111189. https://doi.org/10.1016/j.celrep.2022.111189
55. Poewe W, Seppi K, Tanner CM, Halliday GM, Brundin P, Volkmann J et al (2017) Parkinson disease. Nat Rev Dis Primers 3:17013. https://doi.org/10.1038/nrdp.2017.13
56. Politis M (2014) Neuroimaging in Parkinson disease: from research setting to clinical practice. Nat Rev Neurol 10:708–722. https://doi.org/10.1038/nrneurol.2014.205
57. Pringsheim T, Jette N, Frolkis A, Steeves TDL (2014) The prevalence of Parkinson's disease: a systematic review and meta-analysis. Mov Disord 29:1583–1590. https://doi.org/10.1002/mds.25945
58. Rajan S, Sood A, Jain R, Kamatham PT, Khatri DK (2024) Fingolimod exerts neuroprotection by regulating S1PR1 mediated BNIP3-PINK1-Parkin dependent mitophagy in rotenone induced mouse model of Parkinson's disease. Neurosci Lett 820:137596. https://doi.org/10.1016/j.neulet.2023.137596
59. Reyes JF, Rey NL, Bousset L, Melki R, Brundin P, Angot E (2014) Alpha-synuclein transfers from neurons to oligodendrocytes. Glia 62:387–398. https://doi.org/10.1002/glia.22611
60. Ruppert MC, Greuel A, Tahmasian M, Schwartz F, Stürmer S, Maier F et al (2020) Network degeneration in Parkinson's disease: multimodal imaging of nigro-striato-cortical dysfunction. Brain 143:944–959. https://doi.org/10.1093/brain/awaa019
61. Rymbai E, Sugumar D, Chakkittukandiyil A, Kothandan R, Selvaraj D (2024) Molecular insights into the potential effects of selective estrogen receptor β agonists in Alzheimer's and Parkinson's diseases. Cell Biochem Funct 42:e4014. https://doi.org/10.1002/cbf.4014

62. Sadick JS, O'Dea MR, Hasel P, Dykstra T, Faustin A, Liddelow SA (2022) Astrocytes and oligodendrocytes undergo subtype-specific transcriptional changes in Alzheimer's disease. Neuron 110:1788-1805.e10. https://doi.org/10.1016/j.neuron.2022.03.008
63. Sharma S, Mathur AG, Pradhan S, Singh DB, Gupta S (2011) Fingolimod (FTY720): first approved oral therapy for multiple sclerosis. J Pharmacol Pharmacother 2:49–51. https://doi.org/10.4103/0976-500X.77118
64. Smajić S, Prada-Medina CA, Landoulsi Z, Ghelfi J, Delcambre S, Dietrich C et al (2022) Single-cell sequencing of human midbrain reveals glial activation and a Parkinson-specific neuronal state. Brain 145:964–978. https://doi.org/10.1093/brain/awab446
65. Snaidero N, Möbius W, Czopka T, Hekking LHP, Mathisen C, Verkleij D et al (2014) Myelin membrane wrapping of CNS axons by PI(3,4,5)P3-dependent polarized growth at the inner tongue. Cell 156:277–290. https://doi.org/10.1016/j.cell.2013.11.044
66. Son S-J, Kim M, Park H (2016) Imaging analysis of Parkinson's disease patients using SPECT and tractography. Sci Rep 6:38070. https://doi.org/10.1038/srep38070
67. Song Y, Li S, Li X, Chen X, Wei Z, Liu Q et al (2020) The effect of estrogen replacement therapy on Alzheimer's disease and Parkinson's disease in postmenopausal women: a meta-analysis. Front Neurosci. https://doi.org/10.3389/fnins.2020.00157
68. Stassen SV, Kobashi M, Lam EY, Huang Y, Ho JWK, Tsia KK (2024) StaVia: spatially and temporally aware cartography with higher-order random walks for cell atlases. Genome Biol 25:224. https://doi.org/10.1186/s13059-024-03347-y
69. Street K, Risso D, Fletcher RB, Das D, Ngai J, Yosef N et al (2018) Slingshot: cell lineage and pseudotime inference for single-cell transcriptomics. BMC Genomics 19:477. https://doi.org/10.1186/s12864-018-4772-0
70. Sun Y, Ji J, Zha Z, Zhao H, Xue B, Jin L et al (2021) Effect and mechanism of catalpol on remyelination via regulation of the NOTCH1 signaling pathway. Front Pharmacol 12:628209. https://doi.org/10.3389/fphar.2021.628209
71. Surmeier DJ, Graves SM, Shen W (2014) Dopaminergic modulation of striatal networks in health and Parkinson's disease. Curr Opin Neurobiol 29:109–117. https://doi.org/10.1016/j.conb.2014.07.008
72. Takagi S, Hayakawa N, Kimoto H, Kato H, Araki T (2007) Damage to oligodendrocytes in the striatum after MPTP neurotoxicity in mice. J Neural Transm (Vienna) 114:1553–1557. https://doi.org/10.1007/s00702-007-0790-9
73. Taylor LC, Puranam K, Gilmore W, Ting JP-Y, Matsushima GK (2010) 17 β-estradiol protects male mice from cuprizone-induced demyelination and oligodendrocyte loss. Neurobiol Dis 39:127–137. https://doi.org/10.1016/j.nbd.2010.03.016
74. Teeple E, Joshi P, Pande R, Huang Y, Karambe A, Latta-Mahieu M et al (2021) Single nuclei sequencing of human putamen oligodendrocytes reveals altered heterogeneity and disease-associated changes in Parkinson's disease and multiple system atrophy. BioRxiv. https://doi.org/10.1101/2021.05.06.442967
75. Thomason EJ, Escalante M, Osterhout DJ, Fuss B (2020) The oligodendrocyte growth cone and its actin cytoskeleton: a fundamental element for progenitor cell migration and CNS myelination. Glia 68:1329–1346. https://doi.org/10.1002/glia.23735
76. Törner R, Kupreichyk T, Hoyer W, Boisbouvier J (2022) The role of heat shock proteins in preventing amyloid toxicity. Front Mol Biosci. https://doi.org/10.3389/fmolb.2022.1045616
77. Tsai H-H, Niu J, Munji R, Davalos D, Chang J, Zhang H et al (2016) Oligodendrocyte precursors migrate along vasculature in the developing nervous system. Science 351:379–384. https://doi.org/10.1126/science.aad3839
78. Virtanen P, Gommers R, Oliphant TE, Haberland M, Reddy T, Cournapeau D et al (2020) SciPy 1.0: fundamental algorithms for scientific computing in Python. Nat Methods 17:261–272. https://doi.org/10.1038/s41592-019-0686-2
79. Wakabayashi K, Hayashi S, Yoshimoto M, Kudo H, Takahashi H (2000) NACP/α-synuclein-positive filamentous inclusions in astrocytes and oligodendrocytes of Parkinson's disease brains. Acta Neuropathol 99:14–20. https://doi.org/10.1007/PL00007400
80. Wang L-Y, Yu X, Li X-X, Zhao Y-N, Wang C-Y, Wang Z-Y et al (2019) Catalpol exerts a neuroprotective effect in the MPTP mouse model of Parkinson's disease. Front Aging Neurosci 11:316. https://doi.org/10.3389/fnagi.2019.00316
81. Wang Q, Song L-J, Ding Z-B, Chai Z, Yu J-Z, Xiao B-G et al (2022) Advantages of Rho-associated kinases and their inhibitor fasudil for the treatment of neurodegenerative diseases. Neural Regen Res 17:2623–2631. https://doi.org/10.4103/1673-5374.335827
82. Wolf FA, Angerer P, Theis FJ (2018) SCANPY: large-scale single-cell gene expression data analysis. Genome Biol 19:15. https://doi.org/10.1186/s13059-017-1382-0
83. Wolff AW, Bidner H, Remane Y, Zimmer J, Aarsland D, Rascol O et al (2024) Protocol for a randomized, placebo-controlled, double-blind phase IIa study of the safety, tolerability, and symptomatic efficacy of the ROCK-inhibitor Fasudil in patients with Parkinson's disease (ROCK-PD). Front Aging Neurosci. https://doi.org/10.3389/fnagi.2024.1308577
84. Wolock SL, Lopez R, Klein AM (2019) Scrublet: computational identification of cell doublets in single-cell transcriptomic data. Cell Syst 8:281-291.e9. https://doi.org/10.1016/j.cels.2018.11.005
85. Xu J, Farsad HL, Hou Y, Barclay K, Lopez BA, Yamada S et al (2023) Human striatal glia differentially contribute to AD- and PD-specific neurodegeneration. Nat Aging 3:346–365. https://doi.org/10.1038/s43587-023-00363-8
86. Xu X, Han Y, Zhang B, Ren Q, Ma J, Liu S (2024) Understanding immune microenvironment alterations in the brain to improve the diagnosis and treatment of diverse brain diseases. Cell Commun Signal 22:132. https://doi.org/10.1186/s12964-024-01509-w
87. Yang K, Wu Z, Long J, Li W, Wang X, Hu N et al (2023) White matter changes in Parkinson's disease. npj Parkinsons Dis. 9:1–10. https://doi.org/10.1038/s41531-023-00592-z
88. Zeisel A, Muñoz-Manchado AB, Codeluppi S, Lönnerberg P, La Manno G, Juréus A et al (2015) Cell types in the mouse cortex and hippocampus revealed by single-cell RNA-seq. Science 347:1138–1142. https://doi.org/10.1126/science.aaa1934
89. Zhao P, Yang X, Yang L, Li M, Wood K, Liu Q et al (2017) Neuroprotective effects of fingolimod in mouse models of Parkinson's disease. FASEB J 31:172–179. https://doi.org/10.1096/fj.201600751R

Publisher's Note Springer Nature remains neutral with regard to jurisdictional claims in published maps and institutional affiliations.

Research Square

Preprints are preliminary reports that have not undergone peer review.
They should not be considered conclusive, used to inform clinical practice,
or referenced by the media as validated information.

Glial multicellular programs reveal distinct patient stratification in Parkinson's disease

Ana Munoz-Manchado

ana.munoz@uca.es

University of Cadiz https://orcid.org/0000-0002-1121-6072

Juan M. Barba Reyes

University of Cadiz

Sergio Marco Salas

Science for Life Laboratory, Department of Biochemistry and Biophysics, Stockholm University

Gabriel González Ulloa

University of Cadiz

Lisbeth Harder

Karolinska Institutet

Nima Rafati

National Bioinformatics Infrastructure Sweden, Uppsala University, SciLifeLab

Maria Chatzinikolaou

Science for Life Laboratory, Department of Biochemistry and Biophysics, Stockholm University

Fabian J. Theis

Institute of Computational Biology, Helmholtz Center

Bradley Hyman

Massachusetts General Hospital, Harvard Medical School https://orcid.org/0000-0002-7959-9401

Alberto Serrano-Pozo

https://orcid.org/0000-0003-0899-7530

Mats Nilsson

Stockholm University https://orcid.org/0000-0001-9985-0387

Article

Keywords:

Posted Date: April 30th, 2026

DOI: https://doi.org/10.21203/rs.3.rs-9520754/v1

License: This work is licensed under a Creative Commons Attribution 4.0 International License.
Read Full License

Additional Declarations: Yes there is potential Competing Interest. B.T.H owns stock in Novartis; he serves on the SAB of Dewpoint and has an option for stock. He serves on a scientific advisory board or is a consultant for AbbVie,Alexion, Ambagon, Aprinoia Therapeutics, Arvinas, Avrobio, AstraZenica, Biogen, Bioinsights, BMS, Cure Alz Fund, Cell Signaling, Dewpoint, Latus, Merck, Novartis, Pfizer, Sanofi, Sofinnova, Takeda, TD Cowen, Vigil, Violet, Voyager, WaveBreak. His laboratory is supported by research grants from the National Institutes of Health, Cure Alzheimer's Fund, Tau Consortium, and the JPB Foundation – and a sponsored research agreement from Abbvie and Sanofi. He has a collaborative project with Biogen. A.S.-P. is supported by research grants from the National Institutes of Health and the Alzheimer's Association, has received research funds from Abbvie, inc., and has a Material Transfer Agreement with Ionis Pharmaceuticals, Inc. S.M.S. is a co-founder of Spatialist AB, a consulting company focused on spatial transcriptomics data analysis. F.J.T. consults for Immunai, CytoReason, BioTuring, Genbio and Valinor Industries, and has ownership interest in RN.AI Therapeutics, Dermagnostix, and Cellarity. R.K.R. advised iuvando GmbH and consults for RN.AI Therapeutics. The rest of the authors declare no competing interests.

Title

Glial multicellular programs reveal distinct patient stratification in Parkinson's disease

Authors

Juan Manuel Barba-Reyes[1 #], Sergio Marco Salas[2,3,4 #], Gabriel Gonzalez-Ulloa[1], Lisbeth Harder[5], Nima Rafati[6], Maria Chatzinikolaou[3], Fabian J.Theis[2,7], Bradley T. Hyman[8,9], Alberto Serrano-Pozo[8,9], Mats Nilsson[3], Ana B. Muñoz-Manchado[1,5,10 *]

Affiliations

[1]Unit of Cell Biology, Department of Neuroscience, Institute for Biomedical Research and Innovation of Cádiz (INiBICA), University of Cádiz, Cádiz, Spain

[2]Institute of Computational Biology, Helmholtz Center, Munich, Germany.

[3]Science for Life Laboratory, Department of Biochemistry and Biophysics, Stockholm University, Stockholm, Sweden

[4]Department of Information Technology, Uppsala University, Uppsala, Sweden

[5]Laboratory of Molecular Neurobiology, Department of Medical Biochemistry and Biophysics, Karolinska Institutet, Stockholm, Sweden

[6]National Bioinformatics Infrastructure Sweden, Uppsala University, SciLifeLab, Department of Medical Biochemistry and Microbiology, Uppsala, Sweden

[7]TUM, School of Computation, Information and Technology, Technical University of Munich, Germany. TUM School of Life Sciences, Technical University of Munich, Germany

[8] Department of Neurology, Massachusetts General Hospital, Boston Massachusetts, USA

[9]Harvard Medical School, Boston Massachusetts, USA

[10]Ciber de Salud Mental (CIBERSAM), ISCIII, Madrid, 28029 Madrid, Spain.

#These authors contribute equally to this work.

*corresponding author

Abstract

Parkinson's disease (PD) is a neurodegenerative disorder characterized by nigrostriatal degeneration. While the role of glial cells in PD is increasingly recognized, the coordinated multicellular responses driving PD within the dorsal striatum remain poorly understood. By integrating single-nucleus RNA sequencing of 56 donors with targeted spatial transcriptomics, we disentangle regional from PD-related molecular programs across astrocytes, microglia and oligodendroglia. We identify PD-associated glial subpopulations organized into two distinct multicellular programs: one inflammatory and one UPR-associated, where each patient is dominated by one of these programs. Notably, these programs partition the molecular changes typically associated with PD into two specific, non-overlapping signatures. Multi-region analysis revealed these signatures are globally enriched across the sampled areas and Lewy body disease stages, from brainstem-predominant to neocortical, demonstrating that PD is characterized by mutually exclusive, brain-wide glial multicellular states. Our findings redefine glial alterations in PD as systemic and multicellular, providing a framework for patient stratification and the development of targeted, state-specific therapeutic interventions.

Introduction

Parkinson's disease (PD) is one of the most prevalent neurodegenerative disorders, affecting over 6 million people worldwide and being the fastest growing neurological disorder globally[1]. Clinically, PD manifests as a combination of motor symptoms such as bradykinesia, rigidity, and tremor, as well as non-motor deficits including cognitive impairment and mood disorders[2]. At the molecular level, PD is characterized by the aggregation of α-synuclein and other proteins into Lewy bodies (LB)[3] and the subsequent progressive loss of dopaminergic neurons (DANs) in the substantia nigra pars compacta (SNpc), leading to striatal dopamine depletion and the above hallmark motor symptoms. Current therapies primarily aim to replace dopamine or reduce its catabolism to mitigate motor symptoms[1], yet they do not halt disease progression, highlighting the urgent need to understand the mechanisms underlying cellular vulnerability.

Despite the central role of the SNpc in motor symptoms, PD involves diverse brain regions, with pathology typically spreading from the lower brainstem and olfactory bulb[4], affected even decades before the onset of motor symptoms, to the midbrain, limbic structures, and neocortex, as described by the Braak LB staging[5]. While some studies report alterations across brain regions[6], a substantial proportion of the studies focus on the midbrain, overlooking other relevant regions such as the dorsal striatum. In humans, the dorsal striatum comprising caudate nucleus (CN) and putamen (Pu), represents a hub for the integration of dopaminergic, glutamatergic, and cholinergic signaling and is the primary target of the nigrostriatal projections that degenerate in PD[7]. These properties make the dorsal striatum more than a passive receiver of dopaminergic input: it is where the functional consequences of nigral degeneration are expressed most directly, and where the motor and cognitive deficits that define PD ultimately originate[8,9].

Significant progress has been made in characterizing the PD-associated molecular programs across cell types[6,10–15]. In this context, glial cells are increasingly recognized as central players[10], as supported by transcriptomic studies reporting molecular dysregulations in glia[6,11,12,16,17], coupled with the discovery that many PD-associated risk genes are predominantly expressed in non-neuronal cells[18]. Among the glia, astrocytes have shown PD alterations related to disrupted α-syn handling, impaired proteostasis and mitochondrial function, metabolic and calcium dysregulation, and pro-inflammatory reprogramming[13], leading to toxic protein buildup and indirect neuronal damage. In the same line, microglia are thought to be one of the first cell types affected by the disease[19]. Diverse molecular pathways have been found activated in PD microglia, including unfolded protein response (UPR)[6,12,16], as well as proinflammatory programs[6,12,20]. Oligodendroglia in PD share several pathological features with other glial cells[12,21], such as inflammatory activation and stress responses. However, oligodendrocytes also exhibit unique alterations related to myelination and cell differentiation. Oligodendrocyte precursor cells (OPCs) additionally show impaired differentiation capacity potentially limiting their ability to replenish damaged myelin[14]. Beyond glia, other non-neuronal populations are increasingly implicated in the disease. For instance, emerging data indicates a breakdown of the neurovascular unit, where altered endothelial and pericyte activity compromises blood-brain barrier integrity[22]. While collectively these findings provide a comprehensive catalog of PD-associated molecular programs, the disease's inherent heterogeneity, prolonged clinical course, and diverse symptomatology, combined with the complex architecture of the dorsal striatum, leave significant knowledge gaps. It remains unclear how these alterations are coordinated across various cell populations or whether they function as primary drivers, secondary modulators, or

compensatory responses. Furthermore, the extent to which these cellular programs are universal across all patients or restricted to specific clinical subsets remains to be determined.

In this study, we analyze glial transcriptomic changes in the dorsal striatum. To map these changes, we combined single-nucleus RNA sequencing and Xenium spatial transcriptomics, from 56 donors (54 CN and 56 Pu). We identify, not only the glia diversity but also, for the first time, distinct multicellular programs that drive patient stratification linked to specific pathological features. Furthermore, we demonstrate that this stratification applies beyond the dorsal striatum, defining a brain-wide, rather than regional, patient profile.

Results

1. Transcriptomic single-nucleus analysis reveals distinct glial subpopulations in the dorsal striatum.

To reconstruct the cellular landscape of the human dorsal striatum in the context of PD, we profiled a large postmortem cohort of 56 individuals (20 neurotypical controls and 36 confirmed PD donors) (Fig. 1A, Extended Data Fig. 1, Extended Data Table 1) using single-nucleus RNA sequencing (snRNA-seq). We additionally performed image-based spatial transcriptomics (iST) using Xenium[23] in a subset of 24 subjects (12 controls, 12 PD donors). For each donor, both CN and Pu sections were profiled using a 366-gene panel (Methods).

Following stringent quality control (see Methods section), our snRNA-seq dataset included ~600.000 high-quality nuclei, with ~270.000 identified as glial and non-neuronal cells, forming the basis of a detailed human striatal atlas (Fig. 1B-D). The cellular composition of this dataset reflected the compositional reality of glial cells in the striatum, largely dominated by oligodendrocytes, followed by astrocytes, oligodendrocyte precursor cells (OPCs), and microglia. We also captured critical low-abundance populations, including ependymal cells, vascular-associated cells, Fibroblasts, perivascular macrophages, and lymphocytes, ensuring a complete view of the neurovascular niche (Fig. 1B-D, Extended Data Table 2). This cellular diversity was also confirmed in the iST datasets, where we obtained the expression profile of ~2.337.000 cells, classified in 12 major cell classes (Fig. 1E, Extended Data Fig. 2A-C). We identified consistent subpopulations within each major cell class across

both datasets (Fig. 1D, Extended Data Fig. 2D-G), with marked cellular heterogeneity within all glial and other non-neuronal populations. Importantly, these cell classes displayed comparable relative distributions across both regions and Braak LB stages (Fig. 1D). We further used module analysis[24] to break down these complex expression profiles into distinct gene programs, uncovering both unique and shared cellular functions (Extended Data Figure 3).

Because the dorsal striatum is a heterogeneous structure, we next employed NicheCompass[25] to identify tissue domains (Fig. 1F-G, see Methods). We identified two dominant domains: striatal gray matter (GM; 72.1% of cells), characterized by the presence of medium spiny neurons (MSN) (Fig. 1G), and white matter (WM; 19.0%), enriched in glial cells, particularly oligodendrocytes (Fig. 1G). In addition to these major domains, we detected regions corresponding to vasculature (5.1%), the lateral ventricle (2.8%) (Fig. 1F-G) and other rare sample-specific structures (<0.5%), including non-striatal grey matter (nsGM) and D1D2-rich regions. Domains exhibited a well-defined spatial organization, with WM regions located both surrounding and interspersed within the GM in the form of bundles (Fig. 1F). In addition to these bundles, the striatal GM was also embedded by vascular structures, enriched in immune and vascular cells. Finally, the lateral ventricle, marked by ependymal cells, was observed at the edge of the GM in a subset of samples, specifically adjacent to the CN (Fig. 1F-G), consistent with known neuroanatomical landmarks[26].

2. Striatal astrocytes adopt distinct UPR-associated and reactive phenotypes in Parkinson's disease

We next focused on resolving astrocyte heterogeneity in PD and control striatum. We identified approximately 50,000 cells grouped into six transcriptionally distinct clusters (Fig. 2A, Extended Data Table 3). The largest subpopulation, Astrocytes 0 (A0; *CABLES1*, *RERG*, *CACNA1A*), represents homeostatic astrocytes and was predominantly enriched in controls, especially in GM domains (Fig. 2A-G). A0 showed high expression of synaptic support and astrocyte identity genes (*SLC7A10*, *HES4*, *HES5*, *WIF1)* (Fig. 2E, Extended Data Table 4). In addition, the elevated levels of neurotransmitter transporters and perisynaptic adhesion molecules (*SLC1A2*, *GPC5*, *NRXN1*, *NLGN4X*, *SPARCL1*) suggests a specialized role in glutamate clearance and stabilization of neuron-astrocyte contacts, in agreement with astrocyte's role in synaptic homeostasis (Fig. 2E, Extended Data Table 4).

In contrast to A0, we identified two astrocytic reactive (AR) states, namely AR1 and AR2. Both AR subpopulations showed increased abundance in PD, although AR1 reached statistical significance only in Pu ($p < 0.05$) (Fig. 2A-B, 2D, 2F-G). While both AR states were enriched in GM, they presented distinct functional specializations (Fig. 2B, 2C). AR1[12] (*CRYAB*, *FTH1*, *HSPA4L*) was characterized by robust proteostasis and oxidative stress responses pathways, marked by the upregulation of unfolded protein response (UPR) and heat shock-related genes (*HSPA1A*, *HSP90AA1*, *CRYAB*, *DDIT3*, *HSPD1*) (Fig. 2E, Extended Data Table 4). AR1 also exhibited transcriptional signatures of neurovascular remodeling and anti-regenerative WNT-related processes, with elevated expression of *ANGPT2*, *MMP24*, *SLC13A4*, *PROCR* and *SELENOM* (Fig. 2E, Extended Data Table 4).

AR2 (*CHI3L1*, *FN1*, *SOD2*) represented a more immunologically active and metabolically adapted reactive state. This subpopulation was defined by a signature of reactive astrogliosis, overexpressing hypoxia-associated genes (*HILPDA, ANGPTL4*) and key regulatory transcription factors (*CEBPD, JUNB, CEBPB*) (Fig. 2E, Extended Data Table 4). To counter iron-mediated toxicity and energetic failure, AR2 upregulated iron-storage ferritins (*FTL*, *FTH1*) and key components of the mitochondrial respiratory chain (NDUF and COX families) (Fig. 2E, Extended Data Table 4). Inflammatory and tissue-remodeling signatures were also evident, characterized by the upregulation of lipid-transport apolipoproteins (*APOE*, *APOC1*) and interferon-regulatory factors (*IRF1*, *IRF7*). This profile, coupled with increased levels of the cell-cycle regulator *CCND2*, the matrix protein *FN1*, and the signaling receptor *IL13RA1*, indicates a shift toward interferon-mediated responses and the structural deposition required for glial scar formation (Fig. 2E, Extended Data Table 4).

AR1 and AR2 were also identified as the primary astrocytic drivers of transcriptomic reprogramming in PD, showing the strongest overlap in expression with astrocyte-specific DEGs in PD. (Fig. 2F-G, Methods). In both Pu and CN, AR1-associated DEGs reflected a proteostatic and antioxidant response described by elevated *HSPA1A, DNAJB1, PARK7,* and *SOD1* (Fig. 2H). Conversely, AR2-associated DEGs presented a pro-inflammatory profile, marked by immune-related genes (*IFNGR2, IL7*), extracellular matrix remodeling factors (*FN1*), and metabolic stress regulators (*NAMPT, ANGPTL4, HILPDA*), together with elevated mitochondrial stress signaling through *SOD2*[27] (Fig. 2H). In addition, pathway enrichment scores associated with KEGG PD ontology[28] revealed significant enrichment within AR1 cells in both regions (Pu: LFC = 0.77, p-value = 5.84×10^{-55}; CN: LFC = 1.39, p-value = 0) (Fig. 2F, 2G, Extended Data Table 5), linking this stress-responsive state to established PD-related molecular hallmarks.

Beyond the GM-associated subpopulations, two astrocytic subpopulations were enriched in WM. White Matter Astrocytes[29] (WMA; *RGS6*, *LGR5*, *LUZP2*) expressed genes associated with solute transport and metabolic adaptation (*SLC14A1*, *FKBP5*, *PDK4*) alongside axonal support and adhesion molecules (*NTRK2*, *CDH20*, *CNTN1)*, consistent with a role in WM integrity (Fig. 2A, 2E, Extended Data Table 4). Astrocyte Restricted Precursors[30] (ARP; *CD44*, *RYR3*, *KAZN*) represented a progenitor-like state combining astrocytic identity with inflammatory priming and early fibrotic commitment, marked by extracellular matrix and injury-associated genes (*PRRX1, COL27A1, TNC, GFAP, VIM*), inflammatory mediators (*IL1R1, C3, F3*), and developmental regulators (*TCF7L1, GLIS3, DAAM2, BMPR2*). Neither subpopulation was strictly confined to WM (Fig. 2A, 2E, Extended Data Table 4).

Finally, we identified a subpopulation corresponding to subventricular zone cells (SVZCs; *ADAMTSL3*, *CCDC85A*, *FOS*), restricted to the lateral ventricle domain and therefore exclusively observed in CN samples (Fig. 2A, 2C). SVZCs showed a transcriptional program consistent with SVZ niche organization and neuroblast migration[31], with enrichment for extracellular matrix and guidance genes (*SPARC, ELN, ROBO2, SEMA3D, DSCAML1*), neurogenic commitment markers (*KIT, KITLG, SOX11, SFRP2, NR4A2*), and an immediate early gene signature (*NR4A1, NR4A3, DUSP1, IER2, ID1, KLF4*) (Fig. 2E, Extended Data Table 4).

Spatial autocorrelation analysis (Moran's I) of the iST dataset showed consistently low scores across all profiled genes ($I < 0.2$) in both conditions, indicating that spatial organization is not a primary driver of striatal astrocytic heterogeneity in health or PD (Fig. 2I)

3. Striatal microglia exhibit distinct pro-inflammatory and UPR-associated phenotypes in Parkinson’s disease

Microglia also showed high molecular diversity, with transcriptional states tightly coupled to PD progression[11,12,32]. To characterize these shifts, we analyzed the approximately 30,000 cells in our single-nuclei dataset, divided into four subpopulations. Homeostatic microglia (MH) (*CX3CR1, SYNDIG1, KCNIP1*) represented 70-80% of all microglia in both Pu and CN (Fig. 3A, Extended Data Table 6). Their transcriptional profile reflected active environmental surveillance (*P2RY12, CX3CR1*), cytoskeletal dynamics (*NAV3, DOCK4, SRGAP3*), synaptic monitoring (*GRIA1-3, GRM5, NRXN1, NLGN1, RYR2, ANK3*), and metabolic stability (*IGF1, TET1*), consistent with long-term homeostatic maintenance rather than immune activation

(Fig. 3E, Extended Data Table 7). MH cells were significantly decreased in PD in both Pu and CN ($p = 0.013$ and $p = 0.042$, respectively) (Fig. 3D, 3F, 3G).

Mirroring our astrocyte findings, two microglial subpopulations were overrepresented in PD: pro-inflammatory Microglia (M1) and Heat Shock Protein-responsive Microglia (MH-HSP) (Fig. 3A, 3B, 3D-G). M1 cells (*TMEM163, SLC11A1, BCL6*) showed elevated inflammatory mediators (*IL1B, SPP1, OSM*), glycolytic transporters (*SLC2A3, SLC2A5*), immune activation markers (*NFKBIZ, RUNX1, EGR1, IRF8, IKZF2*), myeloid identity genes (CD14, FCGR3A, BIN1), and vascular-interfacing factors (*ANGPT2, ECM2, COL6A6*), consistent with a shift toward high-demand inflammatory metabolism and vascular interaction (Fig. 3E, Extended Data Table 7). In PD, M1 cells showed further upregulation of *IL1B, NFKBIZ*, amino acid transporters (*SLC1A5*), and tRNA synthetases (*GARS*, *WARS*), reflecting the elevated biosynthetic demands of active neuroinflammation (Fig. 3H).

The second PD-enriched subpopulation, MH-HSP, mirrored the AR1 astrocyte profile, with activation of proteostasis and stress-adaptation programs (Fig. 3A, 3B, 3D, 3F, 3G). MH-HSP cells showed elevated expression of HSF1-target heat shock genes (*HSPA1A, HSPA1B, HSP90AA1, DNAJB1, BAG3, HSPH1*), glucocorticoid-responsive metabolic regulators (*FKBP*5, TSC22D3, PDK4, CPT1A), immune modulators (*PRDM1, PELI1, SERPINE1*), and autophagy-related genes (*ULK1, BNIP3L*) (Fig. 3E, Extended Data Table 7). Although MH-HSP was more abundant in PD, this trend did not reach statistical significance (Fig. 3D, 3F, 3G).

Disease-associated microglia (DAM; *FTL, APOE, FTH1*) were the second most abundant microglial population (Fig. 3A). Their profile combined oxidative phosphorylation and proteostasis genes (*COX7C, ATP5F1E, NDUFS5, HSPA5, HSP90B1, DDIT3*), elevated ribosomal components (*RPLs, RPSs*), phago-lysosomal and lipid metabolism markers (*CTSD, CTSL, GPNMB, MERTK, CD9, APOE, PPARG, MGLL*), and complement genes (*C1QC*), consistent with established DAM signatures[33] reflecting active debris clearance under metabolic stress (Fig. 3E, Extended Data Table 7). Despite a non-significant compositional increase in PD, KEGG PD ontology scoring revealed significant enrichment in DAM in both regions (Pu: LFC = 0.96, $p_{adj} = 0$; CN: LFC = 0.97, $p_{adj} = 0$) (Extended Data Table 8), directly linking this state to PD-related molecular pathways (Fig. 3F, 3G). In PD, DAM showed a pronounced proteostatic signature driven by *HSP70/HSP90* co-chaperones (*HSPA8, DNAJB6, STIP1*), chaperonins (*CCT3*), mitochondrial transcripts (*MT-ATP6, COX7C*), and vesicle trafficking genes (*CD63, SNAP23*) (Fig. 3H).

Microglial composition was largely consistent across domains, with the exception of the lateral ventricle, which showed strong MH-HSP enrichment (Fig. 3C), likely reflecting the inherently stress-prone nature of this niche, where proteostatic programs are active even under homeostatic conditions. As observed for astrocytes, spatial autocorrelation analysis of Xenium data showed consistently low Moran's I scores (<0.2) across all profiled genes in GM, indicating that spatial organization is not a primary driver of striatal microglial heterogeneity in either health or PD (Fig. 3I).

4. Vascular and immune alterations during PD in the striatum

To complete the characterization of striatal glial diversity, we integrated the oligodendroglial lineage (oligodendrocytes and OPCs) profiled in detail in another study[14], which resolved 15 subpopulations including developmental states and PD-associated (PDA) clusters in both oligodendrocytes (PDAOs) and OPCs (PDAOPCs). These PD-enriched subpopulations shared molecular programs with the stress-responsive states identified in astrocytes (AR1) and microglia (MH-HSP). Their classifications were incorporated into the present study to enable the multicellular analyses described below.

Beyond glial cells, we also identified cellular diversity within other non-neuronal populations. For instance, vascular cells could be divided into five subpopulations, including endothelial cells (*CLDN5, PTPRB*), fibroblasts (*FLRT2, ABCA9, ATP1A2*), vascular leptomeningeal cells (VLMCs; *SAT1, THBS1, PTPRG, CYP1B1*), pericytes (*PDE8B, RGS5, PDGFRB*), and vascular smooth muscle cells (VSMCs; *MYH11, MCAM, PDE3A*). Among these, we only identified VSMCs to be significantly enriched in control subjects in CN, suggesting a disease-associated decrease of this population in PD (Extended Data Fig. 4).

Finally, lymphocytes represented the least abundant population in our dataset. These cells were categorized into five distinct subpopulations: CD4+ memory T cells (CD4_TM; *LEF1, PRKCA*), CD8+ tissue-resident memory effector cells (CD8_TRME; *MVB12B, IL7R, GNLY, PLEK*), CD8+ tissue-resident memory T cells (CD8_TRMM; *PARP8, PATJ, BCL2*), B cells (*ARHGAP24, MEF2C, CDK14*), and NK cells (*KLRF1, PDGFD, CD247, NKG7*) (Extended Data Fig. 4). Despite their low abundance, the presence of these subpopulations within the striatal GM aligns with recent evidence of peripheral immune cell infiltration in PD[34].

5. Glial stratification of PD donors reveals two mutually exclusive multicellular programs

While previous studies[6,11,12,14,15] and our results link PD to widespread transcriptomic shifts in non-neuronal populations, small cohort sizes have largely limited these findings to identifying associations between individual molecular programs and a diagnosis of PD. However, PD is a substantially heterogeneous disorder[35,36], characterized by a complex interplay of clinical trajectories, pathological burdens and multifaceted molecular landscapes.

We next focused on exploring donor heterogeneity. Importantly, due to striatum's architecture, we anticipated that inconsistent sampling of WM or ventricular space alongside GM would act as a primary driver of molecular variance, potentially masking true pathological signals. To mitigate this cofounder, we first assessed donor variability using iST datasets, where we can consider only cells located in the GM. Using Gloscope[37,38], we identified four distinct groups of donors. Although all groups included both controls and PD samples, Homeostatic 1 and 2 groups were strongly enriched in healthy donors, while UPR-high and Reactive groups were enriched in PD donors (Fig. 4A, 4B, 4C). Consistently, the two PD-enriched groups showed a higher abundance of glial subpopulations overrepresented in PD (Fig. 4D, 4E, Extended Data Fig. 5A-C). Cellular compositions of these groups were non-overlapping (Fig. 4D, 4E), suggesting a glial stratification of PD patients into distinct mutually exclusive multicellular programs. To confirm these findings, we extended the stratification analysis to snRNA-seq data by classifying donors into Homeostatic, Reactive, or UPR-high groups based on their cellular composition (see Methods). Despite the lack of spatial architecture in this dataset, the snRNA-seq donor groups exhibited cellular compositions highly consistent with the spatial results (Fig. 4F, Extended Data Fig. 5D-G).

The UPR-high donor group was found only in male donors (Fig. 4B) and was characterized by a high abundance of UPR-related subpopulations (AR1, MH-HSP, PDAOPCs, PDAOs) which covaried strongly across samples, suggesting coordinated multicellular regulation (Fig. 4D, 4E). In UPR-high related samples, these subpopulations accounted for nearly all cells of a given type, indicating population-wide activation. Analysis of the three canonical UPR branches (IRE1α, ATF6, and PERK[39]) did not point to a single dominant pathway, but suggested cell-type preferences: elevated MAPK8 in astrocytes, consistent with IRE1α signaling, and higher ATF6 expression in microglia (Extended Data Fig. 7).

In contrast, the Reactive donor group was defined by a high abundance of AR2 astrocytes and M1 microglia, which showed independent but complementary regulatory programs (Extended Data Fig. 4). M1 microglia were enriched for innate immune effector regulons (NF-κB, IRF8, STAT2, BACH1) and phagocytic remodeling (TFEC), while AR2 scored high for regulons associated with stress-adapted cellular identity (HES1, RFX4), metabolic adaptation (SREBF1, EPAS1, FOXO1), and an IFN-γ-biased inflammation (STAT1, ARID5A) (Extended Data Fig. 4). Despite these distinct profiles, both subpopulations covaried strongly across samples (Fig. 4C, Extended Data Fig. 5E), pointing to a coordinated multicellular program. Given that astrocytes and microglia are known to collaboratively participate in brain homeostasis and drive pathological[13,40,41], we next performed cell-cell interaction analysis between AR2 and M1 (Extended Data Fig. 7)[42,43]. Our analysis revealed prominent crosstalk through the complement-mediated C3-CD81 axis, damage-associated HMGB1-TLR4 signaling, lipid and lysosomal pathways (APOE-ABCA1, PSAP-LRP1/SORT1), and fate-modulating interactions (SEMA4D-PLXNB1, CNTN1-NOTCH1) (Extended Data Fig. 7). These interactions define a feed-forward astrocyte-microglia network coupling inflammation, metabolic strain, and impaired clearance in the PD striatum.

Since many PD-DEGs were predominantly expressed in subpopulations specific to individual donor groups, we asked whether PD-DEGs reflect group-specific responses or a shared disease program. Cell-type-specific differential expression analysis comparing each donor group against homeostatic controls, contrasted with the global PD-versus-control analysis, allowing us to separate core disease hallmarks from group-specific signatures (Fig. 4G, Extended Data Fig. 6). In every cell type, the number of DEGs within each donor group substantially exceeded those from the global comparison. Microglia and astrocytes showed the highest transcriptomic burden, but notable shifts were also observed in oligodendroglia, perivascular macrophages (with many upregulated genes in the UPRhigh group), and ependymal cells, which showed widespread upregulation in the UPR-high group alongside broad downregulation across both groups (Fig. 4G).

Next, we compared the PD-specific with the donor group-specific DEGs (Fig. 4H), identifying a high proportion of the PD-DEGs found to be differentially expressed in only one of the donor groups. In astrocytes, for instance, 79.1% (343/441) of PD-DEGs were DEGs in only one of the two PD-associated donor groups, with only a small fraction found of the genes identified as DEGs in all donor groups, or restricted to PD. Subsequently GSEA confirmed that each of these distinct gene subsets were enriched for specific molecular functions.

DEGs shared between PD and the UPR-high group were broadly distributed across glial cell types (Fig. 4I) and enriched for cellular survival and UPR repair programs (Fig. 4H, Extended Data Fig. 6). Microglia-specific genes in this group were involved in histidine catabolism (producing antioxidants or histamine to suppress TNF-α under proteotoxic stress), while oligodendroglial genes were enriched for Cajal body functions, suggesting increased spliceosome assembly to repair stress-damaged transcripts (Fig. 4H).

In contrast, DEGs shared between PD and the Reactive group captured the neurotoxic and immune-interactive components of disease, concentrated in microglia and astrocytes with some extension to OPCs (Fig. 4I). Astrocytes were defined by Type II interferon, *TNF*, and *p38 MAPK* pathway activation, while microglia showed enrichment for leukocyte aggregation genes (*ICAM-1, VCAM-1*), consistent with physical engagement of infiltrating T cells (Fig. 4H).

Importantly, a core set of DEGs shared across both PD-associated groups likely reflects general disease features. Astrocytes were enriched for metal response genes (zinc, copper, iron), consistent with their role as CNS metal gatekeepers and suggesting ferroptosis prevention as a shared baseline response. Oligodendrocytes showed enrichment for protein transport to protrusions. Notably, microglia showed proteostatic stress and chaperone-dependent folding genes across all three groups, consistent with their constitutive burden of extracellular α-syn clearance regardless of activation state (Fig. 4H).

Finally, a small subset of genes differentially expressed in PD but not in either donor group, potentially reflecting features of homeostatic PD donors, included nucleoside transport in astrocytes (consistent with a ρ0-like metabolic shift[44]), purine metabolism and lipoprotein remodeling in oligodendrocytes, basement membrane organization in OPCs, and fibroblast organization regulation in ependymal cells (Fig. 4H).

Altogether, our findings indicate that the striatal PD signature is a composite of distinct glial pathological states, where a shared core of cellular stress is layered with specialized transcriptomic programs that define the transition from a homeostatic baseline to either a shared or cell-type-specific diseased environment.

6. Systemic activation of divergent glial multicellular programs in PD

Next, we assessed whether these multicellular programs align with disease progression, using Braak LB stages as a proxy (Fig. 5A). As expected, homeostatic subpopulations (A0, MH, MOL-A, OPCs-A), were most abundant at BS 0 and declined as neuropathological burden increased, reflecting a progressive loss of basal glial support. In contrast, subpopulations related with the two PD-associated programs exhibited an alternating dominance rather than a sequential progression. Importantly, both PD-associated donor groups were represented across Braak LB stages (Fig. 5A-B). Subpopulations related to the reactive donor group (AR2, M1) peaked at BS 3 and 5, whereas the UPR-associated subpopulations (AR1, MH-HSP, PDAO/PDAOPCs) became most prominent at BS 4. This pattern across stages argues against a linear transition from one program to the other, suggesting instead that the two programs operate as distinct responses across individuals rather than a fixed temporal sequence. To determine if these two PD-associated multicellular programs map onto established pathological axes, we evaluated their correlation with LB burden using previously quantified immunohistochemical measures in a subset of donors (Extended Data Fig. 5B[14]). Remarkably, no strong positive correlation was found between any PD-associated subpopulation and LB density, with only PDAOPCs and AR1, presenting weak correlations in both Pu ($r = 0.5$, $p = 0.069$ and $r = 0.42$, $p = 0.134$, respectively) and CN ($r = 0.46$, $p = 0.131$ for PDAOPCs).

Since other brain regions have previously reported similar glial responses in PD [12,17,18,45], we hypothesized that our findings might apply beyond the dorsal striatum, potentially representing brain-wide molecular programs rather than a region-specific phenomenon. To explore this, we applied module scoring for our UPR-high and Reactive/M1 signatures (Fig. 2E, 3E) to a multi-region PD-atlas generated using snRNA-seq dataset[46], comparing areas along the pathological continuum: from early-affected (DMNX; dorsal motor nucleus of the Xth nerve; GPi: globus pallidus interna) to late-affected (PMC: primary motor cortex; DLPFC: dorsolateral prefrontal cortex) and relatively spared (PVC: primary visual cortex) tissues (Fig. 5C). Across nearly all regions, PD cells scored significantly higher than control cells for the analyzed modules (Fig. 5D-F), with the exception of the reactive astrocyte signature (Module 3), which exhibited enrichment in PD cells only within the PVC (Fig. 5F). Remarkably, as we observed in the striatum, the UPR and Reactive signatures remained negatively correlated across donors (Fig. 5E). In addition, UPR-high signatures for both microglia and astrocytes co-varied across donors, as well as between M1 microglia and reactive astrocytes,

suggesting that the multicellular programs described in the striatum are, to a large extent, conserved across brain regions (Fig. 5E).

To distinguish between transient stages and stable patient stratification, we examined cross-regional patterns within individual donors. If these signatures represented progressive waves, we would expect a sequential shift from early-affected regions (DMNX, GPi) toward the neocortex. Instead, signatures remained remarkably consistent across all regions within each donor (Fig. 5E, 5F). Leveraging the transcriptomic homogeneity of microglia, we classified donors as Reactive (>10% M1), UPR-high (>10% UPR), Homeostatic (both <10%), or Mixed (both >10%) (Fig. 5E, 5G). Notably, only two of 100 donors exhibited a mixed phenotype, reinforcing the existence of distinct, mutually exclusive molecular states. Comparison of these molecular groups against Braak LB stage revealed that while UPR-high donors tended toward later stages, both subtypes spanned the entire pathological spectrum. Notably, UPR-high cells occupied regions typically devoid of LBs in intermediate-stage (BS III-IV) donors (Fig. 5G). This suggests the UPR response is independent of local protein aggregation, potentially driven by soluble α-synuclein or a brain-wide, non-cell autonomous mechanism. As observed in the striatum, the UPR-high phenotype remained significantly overrepresented in male donors (Fig. 5G).

Discussion

In this study, we integrated snRNA-seq (~270,000 nuclei) with high-resolution spatial transcriptomics (iST) to generate a comprehensive cellular atlas of the human striatum and dissect PD-associated molecular programs. The intermingled architecture of the dorsal striatum makes spatial context a biological necessity rather than a technical refinement. By delineating discrete vascular, ventricular, and gray/white matter niches, we avoided the signal homogenization and sampling bias inherent to bulk or dissociated single-cell studies. This precise spatial control allowed us to ensure that the transcriptomic profiles reflect authentic cellular reprogramming of specific tissue domains rather than sampling differences, unmasking glial responses that would otherwise be lost to the noise of striatal heterogeneity.

A central part of the study was the characterization of astrocytes and microglia, which revealed functionally distinct subpopulations. Critically, the reactive states identified in each population were not redundant. In astrocytes, AR1 and AR2 captured proteostatic and inflammatory responses respectively, while in microglia, KEGG scoring identified DAM rather

than M1 as most strongly aligned with canonical PD pathways, suggesting that proteostatic load is an important defining feature.

When analyzing subpopulation co-occurrence across samples, we identified two independent multicellular programs that stratify PD donors into UPR-high, Reactive, or Homeostatic groups. While cell type-specific signatures within these programs have been linked to PD before[6,11,47], even specifically in the dorsal striatum[48], our data reveals for the first time that they form coordinated, mutually exclusive molecular signatures. The Reactive program represents a synchronized neuroinflammatory axis between microglia and astrocytes, a partnership increasingly recognized in neurodegeneration[33,41,49]. In contrast, the UPR-high program defines a distinct pathological state. Consistent with previous reports in the Pu[16] and prefrontal cortex[50], this UPR signature is characterized by widespread proteostatic stress markers and, notably, a lower burden of LBs, a finding that aligns our striatal data with broader cortical observations[50]. Many DEGs within these donor groups are lost in standard PD-vs-Control comparisons, as these signatures are restricted to specific subsets and their signals are diluted during aggregated analysis. In contrast, other programs appear to be present across PD-donors. For instance, metal detoxification in astrocytes, which have also been reported to happen in prefrontal cortex[50].

By extending our analysis to a multi-region atlas[46], we found that the UPR and Reactive profiles are not localized alterations but global activation patterns, showing high intra-donor consistency across the brain. This is particularly significant for the UPR-high signature: while the UPR is traditionally viewed as a local reaction to protein aggregation, we observed it in regions entirely lacking LB pathology, even in low Braak LB-stage donors. Our data suggests that PD-associated UPR activation is a brain-wide, potentially non-cell-autonomous phenomenon across glial networks. While such coordinated activation is a hallmark of viral brain infections[51], evidence for a similar mechanism in neurodegeneration remains limited[52]. Further research is now required to uncover the specific molecular drivers of this brain-wide glial synchrony.

Both multicellular programs were found across donors from all Braak LB stages. However, we identified subtle differences, with UPR-high donors presenting overall a higher Braak LB stage. In addition, while the Reactive phenotype showed no sex bias, the UPR-high signature was significantly enriched in men. This sex-specific divergence in the glial response is an intriguing finding that warrants further investigation, given that PD is twice as frequent in men than in women[53,54].

Despite these advances, several limitations should be noted. First, our snRNA-seq dataset and high-resolution spatial transcriptomics data is restricted to the dorsal striatum, meaning the cellular niches and glial subpopulations defined here, including the AR1/AR2 astrocyte states and DAM microglia, were characterized within a single brain region. Whether equivalent spatial organization and reactive subpopulations exist in other areas remains to be directly tested. Second, while cross-referencing with a multi-region transcriptomic atlas suggests that the UPR-high and Reactive programs extend beyond the striatum, this extrapolation relies on an external dataset and therefore represents a convergent observation rather than direct validation. Third, while we observed a significant enrichment of the UPR-high program in male donors, consistent with the higher epidemiological prevalence of PD in men, the biological mechanism underlying this sex-specific glial response remains unexplored in this study. Whether it reflects hormonal influences, sex-chromosome-linked gene regulation, or epigenetic differences in glial cells is an open question that future work should address. Together, these constraints underscore the need to investigate how brain-wide glial synchrony is organized spatially and whether regional microenvironments dictate how these programs are expressed.

In summary, our results offer a detailed atlas of glial cell types in the dorsal striatum and establish a model of PD characterized by distinct, non-overlapping multicellular programs. These differences are likely to contribute to variability in clinical presentation and disease progression. Critically, the brain-wide intra-donor consistency of these signatures opens a concrete avenue toward biomarker development that may be accessible through CSF or peripheral immune profiling. Transcription factors like *HSF1* to detect the UPR response and *STAT1/2* for the reactive signature could offer a route to patient stratification without requiring post-mortem tissue. Furthermore, the independence of the UPR-high program from local Lewy body burden observed even in regions devoid of pathology at intermediate Braak stages suggests that this glial state precedes or operates in parallel to canonical neuropathological progression. Integrating these molecular signatures with clinical and genetic data will be key to defining a biologically grounded classification of PD, guiding more precise diagnostic and therapeutic strategies tailored to the underlying glial state of each patient.

Methods

Human Tissue

This study is anchored in the analysis of high-quality postmortem human brain tissue. We selected donors based on a strict alignment of clinical history and postmortem neuropathological confirmation. The study consists of autopsy-confirmed Parkinson's disease cases and control donors free from clinical or pathological signs of neurodegeneration. To build this cohort, we coordinated with three major biobanks: the Human Brain and Spinal Fluid Resource Center (Los Angeles, CA, USA), the Parkinson's UK Brain Bank (London, UK), and the Massachusetts Alzheimer's Disease Research Center (Charlestown, MA, USA). For anatomical consistency, we performed targeted dissections of the Caudate nucleus and Putamen, specifically harvesting tissue from coronal slabs aligned at the level of the nucleus accumbens. The control group includes 20 individuals (Pu: n=20; CN: n = 18) aged 25 to over 90 years. The PD group is larger, comprising 36 donors (Pu: n = 35; CN: n = 34), all aged between 60 and 90+ years. All tissue was procured under strict ethical guidelines; written informed consent was obtained from donors or their next of kin, and the study protocols were approved by the respective Institutional Review Boards. (For clinical details, see Extended Data Table 1). We must address a specific demographic constraint. Parkinson's disease is sexually dimorphic, exhibiting a higher prevalence in men. Consequently, we were unable to construct a perfectly sex-matched cohort. Our final study

population includes 16 females and 40 males (Control: 6 females/14 males; PD: 10 females/26 males). We acknowledge that his imbalance limits our statistical power to rigorously evaluate the effect of sex as a biological variable, preventing a deep analysis of sex-specific gene expression patterns.

Tissue Dissociation

We isolated nuclei from fresh-frozen human brain tissue by adapting the Allen Institute for Brain Science protocol (https://www.protocols.io/view/isolation-of-nuclei-from-adult-human-brain-tissue-eq2lyd1nqlx9/v2) to fit our specific sample needs. To protect the RNA and prevent degradation, we performed every step at 4°C. The first step was thawing 100-150mg of tissue on ice. We then moved the tissue into 2 mL of ice-cold, nuclease-free homogenization buffer. This buffer was composed of: 10 mM Tris (pH 8), 250 mM sucrose, 25 mM KCl, 5 mM $MgCl_2$, 0.1 mM DTT, Protease inhibitor cocktail (1×, 50× stock in 100% ethanol, G6521, Promega), 0.2 U/µL RNasin Plus (N2615, Promega), and 0.1% Triton X-100. To homogenize the tissue without damaging the nuclei, we used a glass dounce homogenizer. We applied 20 strokes with a loose pestle, followed by 20 strokes with a tight pestle (357538, Wheaton) to ensure the dissociation was through but controlled. The resulting homogenate was passed through a 70 µm strainer and then a 30 µm strainer to clear out debris. We rinsed the strainers with extra buffer to bring the total volume to 6 mL. After centrifuging the liquid at 900 rcf for 10 minutes, we aspirated the supernatant, leaving roughly 50 µL of buffer over the pellet. We then gently resuspended the nuclei in 200 µL of buffer. To purify the sample, we mixed the suspension 1:1 with 50% iodixanol (OptiPrep Density Gradient Medium, D1556, Sigma) prepared in 60 mM Tris (pH 8), 250 mM sucrose, 150 mM KCl, and 30 mM $MgCl_2$. We layered this mixture over 500 µL of 29% iodixanol in a 1.5 mL tube and centrifuged it at 13,500 rcf for 20 minutes. We carefully removed the supernatant and resuspended the pellet in 50 µL of cold blocking buffer (1× PBS, 1% BSA, and 0.2 U/µL RNasin Plus). The final volume was adjusted to 500 µL to prepare for sorting. To target neurons specifically, we incubated the samples with 1 µL of PE-conjugated anti-NeuN antibody (1:500, Millimark mouse anti-NeuN PE conjugated, FCMAB317PE, Merck) for 30 minutes on ice, kept in the dark. We then pelleted the nuclei at 400 rcf for 5 minutes, removed the supernatant, and resuspended them in 500 µL of blocking buffer. Right before fluorescence-activated nuclei sorting (FANS), we filtered the suspension through a 20 µm mesh and added 1 µL of DAPI (0.1 mg/mL, D3571, Invitrogen) for staining.

Fluorescent-activated nuclei sorting (FANS)

We conducted the FANS at 4°C, using either a BD FACSAria Fusion or a BD FACSAria III flow cytometer. Throughout the sorting process, the nuclei suspension was shielded from light to prevent any loss of fluorescence. By gating the nuclei based on their DAPI and phycoerythrin signals, we were able to distinguish and separate two specific groups:

- NeuN-positive ($NeuN^+$): Neuronal nuclei.
- NeuN-negative ($NeuN^-$): Non-neuronal nuclei.

We collected each fraction into tubes already prepared with 50 µL of blocking buffer. The sorting continued until we reached a target of approximately 200,000 nuclei for each population. Once collection was finished, we concentrated the nuclei by centrifuging them at 400 rcf for 4 minutes. We then aspirated the supernatant, being careful to leave about 30 µL of buffer behind so we could safely resuspend the pellet. Throughout the remainder of the process, we kept the sorted nuclei on ice to maintain their stability for subsequent analysis.

Library Preparation

We used the Chromium Next GEM Single Cell 3′ Reagent Kit v3.1 from 10X Genomics (PN-1000268) to build our cDNA libraries from the sorted nuclei. Before starting the main protocol, we manually counted the nuclei and adjusted their concentration to stay within a range of 200 to 1700 nuclei/µL. This step was vital for maximizing capture efficiency. We then introduced the reverse transcription reagents, following the specific 10X Genomics guidelines (CG000204 Rev D, 10X Genomics). We approached the partitioning in two ways using the Chromium Next GEM Chip G (PN-1000120, 10X Genomics). In some instances, we loaded the nuclei fractions into separate lanes, aiming to recover about 5,000 nuclei for each. In other cases, we combined the populations before loading. For these mixed samples, we used a ratio of 70:30 ($NeuN^+$:$NeuN^-$) and targeted a recovery of 5,000 to 7,000 nuclei. We completed the remaining steps (cDNA amplification and final library construction) using the Single Index Kit T Set A (PN-1000213, 10x Genomics) as instructed by the manufacturer. To make sure the libraries would perform well during sequencing, we conducted several quality control checks:

- Size Distribution: We used the Agilent High Sensitivity DNA Kit (5067-4626, Agilent Technologies) to check the fragment sizes.

- Quantification: We determined the final concentration of the libraries using the KAPA Library Quantification Kit (2700098952, Roche).

These steps allowed us to confirm that the libraries were properly prepared and accurately measured before we proceeded to the sequencing stage.

Illumina Sequencing

Indexed libraries were multiplexed prior to sequencing, with pools comprising up to 19 samples when targeting a recovery of 5,000 nuclei per sample, or up to 16 samples when aiming for 7,000 nuclei. The pooled libraries were sequenced on an Illumina NovaSeq 6000 system using an S4-200 (v1.5) flow cell across eight lanes. A 28-8-0-91 base pair read configuration was applied, consistent with the requirements of the 10X Genomics 3′ gene expression workflow. Sequencing services were provided by the National Genomics Infrastructure (NGI) in Stockholm, Sweden.

snRNA-seq Data Analysis

Pre-Processing

Raw sequencing output from the single-nucleus RNA-seq experiments was converted into gene-by-cell count matrices using the Cell Ranger pipeline (v3.0.0, 10x Genomics). Reads were mapped to the human reference genome hg38 (GRCh38.p5; NCBI accession GCA_000001405.20). Given the nuclear origin of the RNA, the alignment strategy accounted for both exonic and intronic reads, thereby capturing the full spectrum of nuclear transcripts and improving quantification accuracy.

Quality-Control

The first step in our sequencing data was to identify potential doublets using Scrublet[55]. To ensure our results were consistent and reproducible, we ran the tool independently on each sample for 100 iterations, using a fixed random seed and automated thresholds. We then removed any nuclei that were flagged as doublets in more than 10% of those runs. Next, we set specific quality filters based on the distribution of unique molecular identifiers (UMIs) and gene counts. We excluded nuclei that fell below 500 UMIs or 1,200 genes, as these often represent poor-quality samples. On the high end, we removed those with more than 250,000

UMIs or 15,000 genes to avoid suspected multiplets. We also discarded any nuclei where mitochondrial transcripts made up more than 10% of the total content.

To further refine the data, we used a second-degree polynomial regression to model the relationship between log-transformed UMI counts and gene counts. If a nucleus deviated from this predicted curve by more than 2,000 counts, we classified it as an outlier and removed it. To catch more subtle doublets (specifically those involving different cell types), we checked the expression of marker genes for major brain classes, including neurons, astrocytes, and microglia.

- We calculated a cell-type score for every nucleus based on the average expression of these markers.
- Because these scores showed a bimodal distribution, we modeled them using Gaussian mixture distributions.
- We set a strict threshold at the mean of the lower component plus four standard deviations.

Any nucleus that scored above this threshold for more than one cell class was considered a doublet and was excluded. Finally, we wanted to ensure our data reflected the intended brain region. We looked for regional marker genes identified in the Allen Brain Atlas, such as *NEUROD2* and *SLC17A7*. We removed nuclei expressing markers associated with neighboring areas like the claustrum or amygdala to prevent contamination.

Glia and non-neuronal detection

Given that the primary focus of this work is on glial and other non-neuronal cell populations, our first analytical step was to clearly distinguish these cells from neuronal subtypes within the dataset. After normalization, we selected 2,500 highly variable genes (HVGs), which were used for downstream dimensionality reduction and clustering analyses.

Principal component analysis (PCA) was performed, and the top 15 principal components were selected to capture the most informative sources of transcriptional variation. To account for potential batch effects arising from differences in sample processing, we applied Harmony for data integration and correction. Using the corrected embeddings, we constructed a neighborhood graph in Scanpy[56] with 15 nearest neighbors and generated an initial UMAP projection to visualize the global organization of cells in low-dimensional space.

Cell clustering was performed using the Louvain algorithm, enabling the identification of transcriptionally distinct populations. Clusters were subsequently annotated based on the expression of well-established marker genes: OPCs (*PDGFRA*, *VCAN*), Oligodendrocytes (*MBP*, *PLP1*), Astrocytes (*GFAP, ALDH1L1, S100B*), Ependymal Cells (*FOXJ1*, *CCDC153*), Microglia (*CSF1R, CX3CR1, P2RY12*), Perivascular Macrophages (*CD163, MRC1*), Vascular Cells (*CLDN5, PECAM1*), Fibroblasts (*ABCA9, BICC1, COL12A1*), Lymphocytes (*PTPRC, CD3D, CD3G, CD3E*), Medium Spiny Neurons (*NGEF, PDE1B*), and Interneurons (*LHX6*). Following this classification, we subsetted the dataset to retain only glial and non-neuronal populations. This curated dataset formed the basis for all subsequent analyses.

Subclustering of glial and non-neuronal populations

We used a consistent analytical approach to subcluster all glial and non-neuronal lineages, ensuring that our results were comparable across different populations. Once we had our major cell classes (including astrocytes, microglia, vascular cells and lymphocytes), we focused on the 2,000 top variable genes (HVGs) in each group. We then ran PCA and kept the first 15 principal components, as these provided the most relevant information regarding the transcriptional differences within each lineage.

To account for technical differences between sequencing batches, we used the Harmony algorithm on each cell population. Using the corrected data, we built neighborhood graphs and identified clusters with the Louvain algorithm. We started with a base resolution of 0.2 but adjusted this for each lineage to capture the most meaningful biological details. In cases where a single cluster clearly contained distinct biological groups, we performed additional subclustering to separate them.

To figure out what each subcluster represented, we looked for genes that were expressed differently between subclusters. We used the scanpy.tl.rank_genes_groups function with a Wilcoxon rank-sum test. We specifically looked for candidate markers that met two criteria: a log fold change greater than 0.5, and an adjusted p-value of less than 0.05. We then manually reviewed these top genes to assign a biological identity to each subcluster. The full list of these marker genes and the resulting subpopulation names can be found in supplementary tables.

Hierarchical Analysis

To better understand how the different subpopulations relate to one another transcriptomically, we used the scanpy.tl.dendrogram function within the Scanpy framework. We measured the similarity between clusters by calculating Pearson correlation coefficients based on their gene expression profiles. For the hierarchy itself, we chose the complete linkage criterion. This method determines the structure by looking at the maximum distance between elements in different clusters when building higher-order groups.

Compositional Analysis

When comparing how subpopulation sizes changed between conditions, we had to address the fact that single-cell data is compositional. Since the cell-type percentages in any given sample must always add up to 100%, looking at raw percentages alone can be misleading results or render false associations. To solve this, we applied a centered log-ratio (CLR) transformation to our subpopulation proportions before running any statistical tests. Instead of looking at raw numbers, this method calculates the abundance of each subpopulation relative to the geometric mean of all populations in that same sample. This step is crucial because it removes the "constant-sum" constraint, making our comparisons statistically sound. Once the data was transformed, we used the Mann-Whitney U test to compare the values between different conditions.

Module Analysis

To uncover coordinated gene programs within glial subpopulations, we applied the Hotspot algorithm to the astrocyte and microglial datasets. This approach identifies modules of co-expressed genes by leveraging structured patterns within single-nucleus transcriptomic data, thereby highlighting groups of genes that are likely to participate in shared biological processes.

Analyses were conducted using default parameters, while restricting the input to the 10,000 top HVG in each lineage. This filtering step allowed us to concentrate on the most informative transcriptional features and reduce background noise. Through this strategy, we aimed to delineate gene modules that define functional heterogeneity within astrocytes and microglia and to better understand the molecular programs shaping their behavior in the context of disease.

Differential Expression Analysis

To identify transcriptional alterations associated with PD, we performed differential expression analysis comparing PD and Control samples for astrocytes and microglia separately. We considered all cells within each population rather than stratifying by subpopulation at this stage. This approach allowed us to capture global disease-associated transcriptional shifts at the level of the entire cell class.

Differential gene expression was computed using the sc.tl.rank_genes_groups function implemented in Scanpy, applying the Wilcoxon rank-sum test to compare nuclei labeled as “PD” against those labeled as “Control”, and using Benjamini-Hochberg’s correction for multiple hypotheses testing. Genes were classified as upregulated or downregulated in PD based on statistical significance and effect size criteria. To further interpret the biological relevance of these changes, we intersected the lists of differentially expressed genes with previously defined marker genes for astrocyte and microglial subpopulations. This overlap analysis enabled us to assess whether PD-associated transcriptional alterations preferentially corresponded to specific cellular states or subtypes within each lineage. By integrating global differential expression with subpopulation-specific signatures, we aimed to determine whether disease-related changes reflect broad shifts across the entire lineage or are driven by particular reactive or functionally distinct subpopulations.

KEGG PD Analysis

The aim of this analysis was to determine if genes linked to PD were more active in specific astrocyte or microglial subpopulations. To keep our findings relevant to the disease itself, we focused this enrichment analysis strictly on nuclei derived from PD samples. This allowed us to map out how disease-related molecular programs are distributed across different glial states within a pathological environment.

We started by gathering a list of PD-related genes from the KEGG database[28]. Using the sc.tl.score_genes function in Scanpy, we calculated a module score for every cell. This score represents the combined expression level of the KEGG PD gene set, resulting in a quantitative look at how strongly each cell is running the PD-associated transcriptional program.

To determine if specific subpopulations were significantly enriched with this PD signature, we compared the scores of cells in one cluster against all other cells using a one-versus-rest

approach. We then measured differences using Wilcoxon rank-sum test to evaluate these differences, determined the mean scores for each group and calculated the logfoldchanges, and controlled for errors by adjusting our p-values using the Benjamini-Hochberg's false discovery rate (FDR) procedure. This process helped us identify which glial populations were most involved in the PD-related gene activity.

Transcription Factors Analysis

Gene regulatory network activity was inferred using the SCENIC workflow[57]. Briefly, regulons (transcription factors and their predicted target genes) were identified and regulon activity per cell was quantified using the AUCell algorithm, generating an AUC matrix stored in the AnnData object. Downstream analyses were performed on regulon activity scores rather than gene expression levels.

To investigate regulatory programs associated with biological responses (Control-like, UPR, and Reactive), cells were grouped according to annotated glial subpopulations. For each subpopulation, regulon activity was compared against relevant reference subpopulations using pairwise statistical testing. Regulons significantly upregulated in one subpopulation relative to others were identified and ranked based on effect size statistics.

Two complementary strategies were implemented:

- Response-shared regulons: regulons consistently upregulated across subpopulations belonging to the same response category were identified by intersecting significant regulons across the corresponding subpopulations. This approach aimed to capture regulatory programs commonly associated with a shared biological response, independent of cell-type identity.
- Subpopulation-specific regulons: regulons preferentially enriched in individual subpopulations were identified by comparing each subpopulation against related subpopulations within the same lineage. Regulons uniquely enriched in a given subpopulation were defined as those significantly upregulated in that subpopulation and not enriched in others. This strategy was designed to highlight regulatory programs underlying subtype-specific identity or state transitions.

Cell-Cell Interaction Analysis

Cell-cell communication analysis was performed using the LIANA framework[43] to infer putative ligand-receptor interactions between annotated glial subpopulations. We applied the rank_aggregate method, which integrates multiple ligand-receptor resources into a consensus score to provide robust interaction estimates. LIANA was run on the full single-cell glia and non-neuronal dataset using cell subpopulation annotations, the consensus resource, a minimum expression proportion threshold of 0.3 (expr_prop = 0.3), and a minimum of 100 cells per interacting group (min_cells = 100). Differential expression was assessed using the Wilcoxon rank-sum test.

The resulting interaction table provides ligand-receptor pairs with associated interaction strength (LR score) and specificity rank. For downstream analyses, we specifically focused on bidirectional communication between the AR2 astrocyte subpopulation and the M1 microglial subpopulation. Interactions were therefore restricted to those in which AR2 acted as sender and M1 as receiver, or vice versa, preserving signaling directionality. To obtain robust estimates, interaction scores were aggregated across observations to compute mean LR scores and mean specificity ranks for each ligand-receptor pair. To prioritize high-confidence and biologically meaningful interactions, we applied stringent filtering criteria, retaining only interactions with high mean specificity rank and high mean LR score. These filtered interactions were subsequently used for visualization and interpretation of asymmetric signaling patterns between AR2 and M1 reactive glial states.

UPR Signaling Analysis

To characterize the activation status of the Unfolded Protein Response (UPR) across cell subpopulations, we performed a dot plot analysis using the Scanpy library. We examined the expression of specific marker genes representing the three canonical UPR branches: the IRE1 arm (*XBP1, TRAF2, MAPK8, MAPK14*), the ATF6 arm (*ATF6, MBTPS1, MBTPS2*), and the PERK arm (*EIF2AK3, EIF2S1, ATF4*). This analysis was conducted across eleven identified subpopulations: A0, AR1, AR2, MH, MH_HSP, M1, MOL-A, PDAO-1, PDAO-2, OPCs-A, and PDAOPCs. In the visualization, the dot size represents the fraction of cells within each subpopulation expressing the gene of interest, while the color intensity corresponds to the mean expression level within the expressing fraction.

Braak Lewy Body Staging Analysis

To assess changes in cellular composition across Braak Lewy Body (LB) stages while accounting for the compositional nature of single-cell data, we applied a centered log-ratio (CLR) transformation at the subject level. For each subject, cells were first grouped by subpopulation and raw counts were converted into a composition vector representing the relative abundance of each subpopulation. A pseudocount of 1 was added to avoid undefined logarithms for zero counts. The CLR transformation was then computed by dividing each subpopulation count by the geometric mean of all subpopulation counts within the same subject and taking the natural logarithm. This approach normalizes each subject's cellular composition relative to its overall cellular landscape, thereby mitigating biases introduced by differences in total cell numbers and ensuring that subpopulation abundances are interpreted in relation to one another rather than independently.

Braak LB-stage-level summaries were obtained by averaging subject-level CLR values within each stage. To avoid spurious effects driven by single donors, subpopulation-stage combinations represented by fewer than two subjects were excluded from stage-level summaries. For visualization, CLR values were optionally standardized (z-scored) across Braak LB stages for each subpopulation to facilitate comparison of relative enrichment or depletion trends. This compositional framework enables detection of subpopulation-specific increases or decreases across Braak LB stage progression while appropriately accounting for interdependence among cell-type proportions.

Correlations between glial subpopulations and Lewy Body quantifications

To examine the relationship between glial subpopulation abundance and α-synuclein aggregations, for this analysis we restricted the data to the subset of donors for whom quantitative immunohistochemical measures of LB density (LBs/Area) were available, as previously reported in Barba-Reyes *et al*[14]. Analyses were performed separately for Pu and CN, and donors contributing fewer than 50 nuclei in a given region were excluded to ensure reliable compositional estimates.

For each remaining donor, subpopulation counts were computed and converted to proportions of the total nuclei recovered from that region. These proportions were subsequently CLR-transformed as described above to account for the compositional structure of the data. Spearman rank correlations were then calculated between the

CLR-transformed abundance of each subpopulation and the corresponding regional LB density, independently for Pu and CN. A predefined set of disease-relevant subpopulations was selected for this analysis: A0, AR1, AR2, MH, MH-HSP, M1, DAM, OPCs-A, PDAOPCs, MOL-A, PDAO-1, PDAO-2, and PDAO-3.

Donor stratification based on spatial analysis' priors

To investigate how cellular composition varies across the cohort, we performed patient stratification based on the proportional representation of specific astrocyte subpopulations. The selection of subpopulations used for stratification (AR1 and AR2) was informed by our prior sample representation analysis done using only the grey matter profiled by the Xenium datasets, which identified these clusters as key indicators of pathological diversity. Stratification was performed by calculating the relative abundance of each subpopulation within individual samples. SVZCs were not considered when computing relative abundance as they were found to be specific to the lateral ventricle. Patients were classified into distinct clinical groups using a hierarchical thresholding approach where samples were first evaluated for their AR1 (Unfolded Protein Response-related) astrocyte population. Any sample where AR1 exceeded 10% of the total astrocyte composition was assigned to the UPR group. For the remaining samples, those where the AR2 (Reactive) astrocyte population exceeded 10% were classified as Reactive. Samples that did not meet the minimum 10% threshold for either AR1 or AR2 were categorized as Homeostatic. This stratification allowed us to correlate specific transcriptomic states identified in the single-cell data with broader patient-level pathological profiles.

Differential expression analysis and comparison between donor groups and PD

To evaluate to which extent differentially expressed genes in PD were driven by donor groups' multicellular programs, we performed differential expression analysis between groups for each cell type annotated. Differential expression testing was conducted using scanpy's sc.tl.rank_genes_groups function, employing the Wilcoxon rank-sum test.

Two distinct analytical frameworks were employed. First, state-specific comparison where donors representing UPR and Reactive donor groups were tested against a baseline of homeostatic donors, intentionally excluding cells from the reciprocal PD-associated donor group from the subset to maintain reference purity. In addition, we performed differential

expression analysis between cells obtained from donors with PD and healthy controls. Significant differentially expressed genes (DEGs) were defined by an adjusted p-value of less than 0.05 and a minimum expression prevalence of 10% (pts > 0.1). To characterize the magnitude of transcriptional changes, these genes were categorized into four mutually exclusive tiers based on the absolute value of their log2 fold-change (LFC): Tier 1 (LFC ≥ 2.0), Tier 2 (1.0 ≤ LFC < 2.0), Tier 3 (0.5 ≤ LFC < 1.0), and Tier 4 (0.25 ≤ LFC < 0.5). The distribution and directionality of these genes were visualized using stacked bar charts, with up-regulated and down-regulated genes plotted on opposing y-axes and color-coded by tier.

To assess transcriptional overlap between cellular states and disease conditions, three-way Venn diagrams were generated for each cell type using the matplotlib-venn library. Potential pseudogenes and non-coding transcripts, identified by prefixes such as AC, AL, LINC, AP, or AF, were filtered out prior to analysis. A dual-threshold strategy was employed to identify shared signatures: a candidate universe of genes was first established using a strict threshold (e.g., $|\log_2\text{fold-change}| \geq 1.0$ and $P_{adj} < 0.05$) in at least one condition, and their presence in the remaining conditions was evaluated using a relaxed threshold (e.g., $|\log_2\text{fold-change}| \geq 0.5$ and $P_{adj} < 0.05$). This methodology allowed for the identification of genes with consistent directionality across groups even when the magnitude of change varied.

To evaluate gene sharing across different cell types for each condition, UpSet plots were generated using the upsetplot library. This analysis utilized a the same logic used for identified shared DEG between multicellular programs and PD, where a candidate universe of genes was first established for each comparison (UPR, Reactive, or PD) using a strict threshold ($|\log_2\text{fold-change}| \geq 1.0$ and $P_{adj} < 0.05$). The presence of these candidate genes was then cross-referenced across all other cell types using a relaxed threshold ($|\log_2\text{fold-change}| \geq 0.25$ and $P_{adj} < 0.05$). In plots, only intersections containing more than 10 genes were visualized.

Functional Enrichment Analysis

To characterize the biological functions associated with unique and shared gene sets across donor groups, we performed gene set enrichment analysis (GSEA) using the GSEApy (v1.1+) library. For each cell type, we previously partitioned differentially expressed genes into seven distinct overlap categories: genes unique to PD, Reactive, or UPR states, and genes shared between specific combinations (e.g., PD + Reactive, PD + UPR, and those

common to all three). This partitioning was achieved by intersecting gene sets defined by our previously established strict and relaxed thresholds.

Functional enrichment was conducted using the GO Biological Process 2023 database. For each category containing at least five genes, the top three most significant terms (based on adjusted p-values) were selected to define a master pathway list for each cell type and visualized using comparative dotplots, where the dot size represents the gene ratio (proportion of the gene set overlapping with the GO term) and the color intensity reflects the significance level expressed as -log10(Adjusted p-value).

Spatial transcriptomics (Xenium) data generation

Spatial transcriptomics platform

The Xenium datasets analyzed in this study included both previously published datasets[14,45] and newly generated datasets. For the newly generated datasets, spatial transcriptomic data were obtained using the Xenium in situ platform (10X Genomics), enabling subcellular-resolution characterization of RNA within tissue sections, consistent with the approach described in Garma *et al*.[45] and Barba-Reyes *et al*[14]

Gene panel design

The Xenium technology uses oligonucleotide probes to measure gene expression from a predefined panel. In this study, we employed a gene panel consisting of 266 genes from the Xenium Human Brain Gene Expression Panel. An additional 100 genes were selected based on our snRNA-seq dataset, resulting in a custom panel (Xenium Custom Gene Expression Panel 51–100, Z3DREH, PN-1000561, 10X Genomics).

Experimental workflow

Tissue blocks from human subjects (N = 4; including putamen and caudate nucleus) were retrieved from −80 °C storage and transported on dry ice to a cryostat (CryoStar NX70, Thermo Scientific). Samples were mounted on the specimen holder using Tissue Tek O.C.T. Compound (4583, Sakura) and equilibrated to −20 °C within the cryostat chamber for 5 minutes. Tissue sections of 10 µm thickness were collected and placed directly into the imaging region of precooled Xenium slides (12×24 mm, PN-3000941, 10X Genomics).

Section adherence was facilitated by briefly warming the reverse side of the slides with gentle pressure, followed by immediate refreezing on the cryobar. Slides with mounted tissue were kept in the cryostat during sectioning and subsequently stored at −80 °C.

Downstream processing (including probe hybridization, ligation, and rolling circle amplification) was performed at the in situ Sequencing Infrastructure Unit (Science for Life Laboratory, Stockholm) according to the manufacturer's protocol (CG000582 Rev E, 10X Genomics), with chemical quenching applied to minimize background fluorescence. Tissue sections were imaged using the Xenium Analyser (10X Genomics), which also performed signal decoding and data acquisition. This same protocol was used to generate previously published datasets included in [14,45].

Spatial transcriptomics (Xenium) data analysis

Segmentation, data preprocessing and cell type identification

Xenium experiments provide spatial positions for all decoded reads. Therefore, the first step in processing these datasets was to segment individual cells and determine their transcriptomic composition. In this study, cells were defined using the default nuclear Xenium segmentation, a conservative approach that minimizes the risk of misse[23]ention21. The segmented cells were preprocessed using Scanpy[56]. Preprocessing involved filtering out low-quality cells, removing those with fewer than 50 total counts or fewer than 5 detected genes. The data were subsequently normalized to total counts, log-transformed, and scaled. We performed PCA and constructed a neighborhood graph (n_neighbors=10, n_pcs=30) to generate a UMAP embedding for visualization. Leiden clustering at a resolution of 2.0 was applied to identify distinct cell populations, which were then manually annotated using an external reference based on marker gene expression and spatial position. For subpopulation identification, each population was subclustered and manually annotated based (Code availability).

Gene module analysis using Hotspot

To identify spatially or transcriptionally coherent gene modules in the Xenium datasets, as we did in snRNA-seq, we employed the Hotspot algorithm. Analysis was initiated using a Depth-Adjusted Negative Binomial (DANB) model to account for technical variation and library size differences, using the total counts per cells for UMI normalization. A K-Nearest

Neighbors (KNN) graph was constructed using the top 20 neighbors in the PCA latent space to define the local cellular environment.

We evaluated the significance of gene expression patterns by calculating local autocorrelations (Geary's C) across the KNN graph. Genes showing non-random spatial or local distribution were filtered using a False Discovery Rate (FDR) threshold of 0.05. To group these informative genes, a local correlation matrix was computed, capturing pair-wise gene relationships within local neighborhoods.

Modules were subsequently defined using a minimum threshold of 5 genes per module and a clustering FDR of 0.01. For each identified module, we calculated per-cell scores to represent the aggregate local expression of the module's gene members. These scores were integrated into the dataset to facilitate downstream analysis of biological programs across the identified sample regions. To facilitate their interpretation, manual annotation of the gene modules was done based on the exploration of the module's composition and scores across cells

Niche identification

NicheCompass[25] was applied to delineate cellular domains by integrating spatial transcriptomics data across all samples. A latent graph embedding was generated using a graph convolutional network (GCN) model, incorporating categorical covariates such as sample replicates. The model was trained for 400 epochs with regularization to enhance ligand–receptor–based niche identification. Clustering of the latent embeddings was then performed using the Leiden algorithm (with a resolution of 0.2), and the resulting niches were annotated according to their spatial distribution and cellular composition.

Identification of spatially-variable genes

To identify spatially variable genes (SVGs), we performed a sample-wise spatial autocorrelation analysis using the Squidpy framework[58]. Since we focused on the grey matter regions, for each sample, we kept only cells identified as part of the grey matter during domain analysis. Next, spatial connectivity was modeled via Delaunay triangulation to define cell neighborhoods. Within each sample, we calculated Moran's I statistics to quantify global spatial patterns, assessing significance through 100 permutations per gene. To ensure robust estimation, analysis was restricted to samples with at least 50 observations. The resulting Moran's I scores and p-values were aggregated across all replicates, enabling

a comparative assessment of spatial transcriptomic signatures across experimental conditions.

Sample representation of spatial datasets

To analyze high-level variation across donors and identify distinct disease endotypes in the Xenium samples, we performed sample-level representation learning using the patpy[38] implementation of the GloScope[37] method. For this, we selected only cells identified within the striatal gray matter domain and we excluded samples which were found a posterior to present a hybrid molecular profile, being classified as neurological controls, but presenting a Braak stage > 0. Before representation, we consider sample filtering for those samples containing less than 500 cells, with no samples excluded. Sample representations were generated using the GloScope algorithm, which models each donor as a distribution of cells within the X_{pca} latent space. We calculated a sample-to-sample distance matrix by estimating the divergence between these cell-state distributions using a k-nearest neighbor (k=6) approach, resulting in an embedding where samples with similar cellular compositions cluster together.

The resulting distance matrix was used to construct a sample-level neighbor graph, which was visualized via UMAP with a minimum distance of 0.02 to preserve local structure. Donor subgroups, or endotypes, were identified using Leiden clustering at a resolution of 0.9. After group annotation based on molecular and cell type composition, we integrated our analysis with complementary comprehensive clinical and technical metadata, including Braak and Thal stages, Post-Mortem Interval (PMI), Age, and Sex, while technical variables such as median nucleus area and total counts per sample were monitored for potential batch effects.

Code availability

All code corresponding to the analysis of single-nuclei RNAseq dataset is available at figshare and the code corresponding to spatial transcriptomics (Xenium) datasets is available at https://github.com/Moldia/PD_striatal_xenium.

Data availability

Raw and normalized counts from single-nuclei RNA-seq data are available at figshare. Processed and annotated cells from Xenium experiments, in the form of AnnData, as well as a KaroSpace viewer can be downloaded from the following Zenodo repository. These data will be publicly available as of the date of publication.

Acknowledgements

The authors acknowledge the Massachusetts Alzheimer's Disease Research Center (especially Patrick Dooley and Tessa Connors-Stewart), the Parkinson's UK Brain Bank at Imperial funded by Parkinson's UK (a charity registered in England and Wales, 258197, and in Scotland, SC037554), and the NIH NeuroBioBank (NIH Ref-1851, Requestor: Professor Ernest Arenas, R.I.P.), for the supply of tissue samples and associated clinical and neuropathological data. The authors also want to thank the National Genomics Infrastructure in Stockholm funded by Science for Life Laboratory and SNIC/Uppsala Multidisciplinary Center for Advanced Computational Science for assistance with massively parallel sequencing and access to the UPPMAX computational infrastructure. Further thanks go to Katarina Tiklova and Chika Yokota from the *In Situ* Sequencing Infrastructure Unit at the Science for Life Laboratory, Stockholm.

We would like to thank Dr. Marco Grillo for his insightful comments on the Xenium analysis. We would also like to thank Vladimir Shitov for his suggestions regarding sample-representation analysis as well as all members from the Theis lab. Finally, we are extremely grateful to the brain donors and their families who have made this study possible.

Funding

The authors acknowledge support from grants PID2019-109046GA-I00, PID2022-136526OB-I00 by MICIU/AEI/10.13039/501100011033 and ERDF/EU (to A.B.M.-M. and 2019-FPI to J.M.B.-R.), RyC program RYC-2017–22594 and

CNS2024-154925 by MICIU/AEI/10.13039/501100011033 ESF Investing in your future (to A.B.M.-M.), the Swedish Foundation for Strategic Research FFL 18–0314 (A.B.M.-M.), the Swedish Research Council 2017–03349 (to A.B.M.-M.), the Plan Propio of University of Cádiz (2023-046 / PU / EPIF-FPI-CT / CP to G.G-U), the Swedish Research Council (2021-03293 and 2024-02533) (to MN), the NIH/NIA R01AG089349 and R21AG087072 (to AS-P) and the US National Institute on Aging P30AG062421 (to B.T.H. and A.S.-P.).

Authors contributions

Concept and design: JMBR, SMS, MN, ABMM

Tissue acquisition and processing: LH, ABMM

Sequencing: LH, ABMM

Data analysis: JMBR, SMS, GGU, MC, NR

Interpretation of the data: JMBR, SMS, AS-P, ABMM

Supervision: MN, ABMM

Resources: FJT, MN, BTH,ASP, ABMM

Writing-original draft: JMBR, SMS, ABMM

Writing-review & editing: all authors

Competing interests

B.T.H owns stock in Novartis; he serves on the SAB of Dewpoint and has an option for stock. He serves on a scientific advisory board or is a consultant for AbbVie,Alexion, Ambagon, Aprinoia Therapeutics, Arvinas, Avrobio, AstraZenica, Biogen, Bioinsights, BMS, Cure Alz Fund, Cell Signaling, Dewpoint, Latus, Merck, Novartis, Pfizer, Sanofi, Sofinnova, Takeda, TD Cowen, Vigil, Violet, Voyager,

WaveBreak. His laboratory is supported by research grants from the National Institutes of Health, Cure Alzheimer's Fund, Tau Consortium, and the JPB Foundation – and a sponsored research agreement from Abbvie and Sanofi. He has a collaborative project with Biogen.

A.S.-P. is supported by research grants from the National Institutes of Health and the Alzheimer's Association, has received research funds from Abbvie, inc., and has a Material Transfer Agreement with Ionis Pharmaceuticals, Inc.

S.M.S. is a co-founder of Spatialist AB, a consulting company focused on spatial transcriptomics data analysis.

F.J.T. consults for Immunai, CytoReason, BioTuring, Genbio and Valinor Industries, and has ownership interest in RN.AI Therapeutics, Dermagnostix, and Cellarity. R.K.R. advised iuvando GmbH and consults for RN.AI Therapeutics.

The rest of the authors declare no competing interests.

References

1. Stocchi, F., Bravi, D., Emmi, A. & Antonini, A. Parkinson disease therapy: current strategies and future research priorities. *Nat. Rev. Neurol.* **20**, 695–707 (2024).

2. Obeso, J. A. *et al.* Past, present, and future of Parkinson's disease: A special essay on the 200th Anniversary of the Shaking Palsy. *Mov. Disord. Off. J. Mov. Disord. Soc.* **32**, 1264–1310 (2017).

3. Spillantini, M. G. *et al.* Alpha-synuclein in Lewy bodies. *Nature* **388**, 839–840 (1997).

4. Horsager, J. & Borghammer, P. Brain-first vs. body-first Parkinson's disease: An update on recent evidence. *Parkinsonism Relat. Disord.* **122**, 106101 (2024).

5. Braak, H. *et al.* Staging of brain pathology related to sporadic Parkinson's disease. *Neurobiol. Aging* **24**, 197–211 (2003).

6. Clarence, T. *et al.* A Transcriptomic Roadmap of Parkinson's Disease Progression at Single Cell Resolution. 2025.07.30.25332436 Preprint at https://doi.org/10.1101/2025.07.30.25332436 (2025).

7. Gerfen, C. R. & Surmeier, D. J. Modulation of striatal projection systems by dopamine. *Annu. Rev. Neurosci.* **34**, 441–466 (2011).

8. Hornykiewicz, O. Chemical neuroanatomy of the basal ganglia — normal and in Parkinson's disease. *J. Chem. Neuroanat.* **22**, 3–12 (2001).

9. Kordower, J. H. *et al.* Disease duration and the integrity of the nigrostriatal system in Parkinson's disease. *Brain* **136**, 2419–2431 (2013).

10. Zhang, X., Zhang, R., Nisa Awan, M. U. & Bai, J. The Mechanism and Function of Glia in Parkinson's Disease. *Front. Cell. Neurosci.* **16**, 903469 (2022).

11. Smajić, S. *et al.* Single-cell sequencing of human midbrain reveals glial activation and a Parkinson-specific neuronal state. *Brain J. Neurol.* **145**, 964–978 (2022).

12. Martirosyan, A. *et al.* Unravelling cell type-specific responses to Parkinson's Disease at single cell resolution. *Mol. Neurodegener.* **19**, 7 (2024).

13. Kam, T.-I., Hinkle, J. T., Dawson, T. M. & Dawson, V. L. Microglia and astrocyte dysfunction in parkinson's disease. *Neurobiol. Dis.* **144**, 105028 (2020).

14. Barba-Reyes, J. M. *et al.* Oligodendroglia vulnerability in the human dorsal striatum in Parkinson's disease. *Acta Neuropathol. (Berl.)* **149**, 46 (2025).

15. Fiorini, M. R., Dilliott, A. A., Thomas, R. A. & Farhan, S. M. K. Transcriptomics of Human Brain Tissue in Parkinson's Disease: a Comparison of Bulk and Single-cell RNA Sequencing. *Mol. Neurobiol.* **61**, 8996–9015 (2024).

16. Pande, R. *et al.* Single Cell Atlas of Human Putamen Reveals Disease Specific Changes in Synucleinopathies: Parkinson's Disease and Multiple System Atrophy. 2021.05.06.442950 Preprint at https://doi.org/10.1101/2021.05.06.442950 (2021).

17. Uriarte Huarte, O. *et al.* Single-Cell Transcriptomics and In Situ Morphological Analyses Reveal Microglia Heterogeneity Across the Nigrostriatal Pathway. *Front. Immunol.* **12**, (2021).

18. Bryois, J. *et al.* Genetic identification of cell types underlying brain complex traits yields insights into the etiology of Parkinson's disease. *Nat. Genet.* **52**, 482–493 (2020).

19. Lind-Holm Mogensen, F., Seibler, P., Grünewald, A. & Michelucci, A. Microglial dynamics and neuroinflammation in prodromal and early Parkinson's disease. *J. Neuroinflammation* **22**, 136 (2025).

20. Xu, K. *et al.* Neuroinflammation in Parkinson's disease: focus on the relationship between miRNAs and microglia. *Front. Cell. Neurosci.* **18**, 1429977 (2024).

21. Salazar Campos, J. M., Burbulla, L. F. & Jäkel, S. Are oligodendrocytes bystanders or drivers of Parkinson's disease pathology? *PLOS Biol.* **23**, e3002977 (2025).

22. Paul, G. & Elabi, O. F. Microvascular Changes in Parkinson's Disease- Focus on the Neurovascular Unit. *Front. Aging Neurosci.* **14**, (2022).

23. Marco Salas, S. *et al.* Optimizing Xenium In Situ data utility by quality assessment and best-practice analysis workflows. *Nat. Methods* **22**, 813–823 (2025).

24. DeTomaso, D. & Yosef, N. Hotspot identifies informative gene modules across modalities of single-cell genomics. *Cell Syst.* **12**, 446-456.e9 (2021).

25. Birk, S. *et al.* Quantitative characterization of cell niches in spatially resolved omics data. *Nat. Genet.* **57**, 897–909 (2025).

26. Scelsi, C. L. *et al.* The Lateral Ventricles: A Detailed Review of Anatomy, Development, and Anatomic Variations. *Am. J. Neuroradiol.* https://doi.org/10.3174/ajnr.A6456 (2020) doi:10.3174/ajnr.A6456.

27. Chidambaram, S. B. *et al.* Superoxide dismutase and neurological disorders. *IBRO Neurosci. Rep.* **16**, 373–394 (2024).

28. Kanehisa, M. & Goto, S. KEGG: Kyoto Encyclopedia of Genes and Genomes. *Nucleic Acids Res.* **28**, 27–30 (2000).

29. Bocchi, R. *et al.* Astrocyte heterogeneity reveals region-specific astrogenesis in the white matter. *Nat. Neurosci.* **28**, 457–469 (2025).

30. Liu, Y. *et al.* CD44 expression identifies astrocyte-restricted precursor cells. *Dev. Biol.* **276**, 31–46 (2004).

31. Obernier, K. & Alvarez-Buylla, A. Neural stem cells: origin, heterogeneity and regulation in the adult mammalian brain. *Development* **146**, dev156059 (2019).

32. Trainor, A. R., MacDonald, D. S. & Penney, J. Microglia: roles and genetic risk in Parkinson's disease. *Front. Neurosci.* **18**, 1506358 (2024).

33. Cheng, Y.-H. & Ho, M. S. Disease-associated microglia in neurodegenerative diseases: Friend or foe? *PLOS Biol.* **23**, e3003426 (2025).

34. Tansey, M. G. *et al.* Inflammation and immune dysfunction in Parkinson disease. *Nat. Rev. Immunol.* **22**, 657–673 (2022).

35. Mestre, T. A. *et al.* Parkinson's Disease Subtypes: Critical Appraisal and Recommendations. *J. Park. Dis.* **11**, 395–404 (2021).

36. Berg, D. *et al.* Prodromal Parkinson disease subtypes — key to understanding heterogeneity. *Nat. Rev. Neurol.* **17**, 349–361 (2021).

37. Wang, H., Torous, W., Gong, B. & Purdom, E. Visualizing scRNA-Seq data at population scale with GloScope. *Genome Biol.* **25**, 259 (2024).

38. Shitov, V., Dehkordi, M. M. & Luecken, M. D. Benchmarking Sample Representations from Single-Cell Data: Metrics for Biologically Meaningful Embeddings. in (2025).

39. Sundaram, A., Appathurai, S., Plumb, R. & Mariappan, M. Dynamic changes in complexes of IRE1α, PERK, and ATF6α during endoplasmic reticulum stress. *Mol. Biol. Cell* **29**, 1376–1388 (2018).

40. Damisah, E. C. *et al.* Astrocytes and microglia play orchestrated roles and respect phagocytic territories during neuronal corpse removal in vivo. *Sci. Adv.* **6**, eaba3239 (2020).

41. Park, J.-S. *et al.* Blocking microglial activation of reactive astrocytes is neuroprotective in models of Alzheimer's disease. *Acta Neuropathol. Commun.* **9**, 78 (2021).

42. Dimitrov, D. *et al.* Comparison of methods and resources for cell-cell communication inference from single-cell RNA-Seq data. *Nat. Commun.* **13**, 3224 (2022).

43. Dimitrov, D. *et al.* LIANA+ provides an all-in-one framework for cell–cell communication inference. *Nat. Cell Biol.* **26**, 1613–1622 (2024).

44. Savani, M. *et al.* TMET-32. Cell-intrinsic pyrimidine synthesis pathway choice in human brain and glioma. *Neuro-Oncol.* **27**, v435 (2025).

45. Garma, L. D. *et al.* Interneuron diversity in the human dorsal striatum. *Nat. Commun.* **15**, 6164 (2024).

46. N. M., P. *et al.* A multi-region single nucleus transcriptomic atlas of Parkinson's disease. *Sci. Data* **11**, 1274 (2024).

47. Xu, J. *et al.* Human striatal glia differentially contribute to AD- and PD-specific neurodegeneration. *Nat. Aging* **3**, 346–365 (2023).

48. Pande, R. *et al.* Single Cell Atlas of Human Putamen Reveals Disease Specific Changes in Synucleinopathies: Parkinson's Disease and Multiple System Atrophy. 2021.05.06.442950 Preprint at https://doi.org/10.1101/2021.05.06.442950 (2021).

49. Han, J. *et al.* The roles of microglia and astrocytes in neuroinflammation of Alzheimer's disease. *Front. Neurosci.* **19**, 1575453 (2025).

50. Single-cell transcriptomic and proteomic analysis of Parkinson's disease brains | Science Translational Medicine. https://www.science.org/doi/10.1126/scitranslmed.abo1997.

51. Prasad, V. Transmission of unfolded protein response—a regulator of disease progression, severity, and spread in virus infections. *mBio* **16**, e03522-24 (2025).

52. van Ziel, A. M. & Scheper, W. The UPR in Neurodegenerative Disease: Not Just an Inside Job. *Biomolecules* **10**, 1090 (2020).

53. Cicero, C. E. *et al.* Sex differences in the severity of non-motor symptoms in Parkinson's disease: a systematic review and meta-analysis. *Npj Park. Dis.* https://doi.org/10.1038/s41531-026-01323-w (2026) doi:10.1038/s41531-026-01323-w.

54. Cattaneo, C. & Pagonabarraga, J. Sex Differences in Parkinson's Disease: A Narrative Review. *Neurol. Ther.* **14**, 57–70 (2025).

55. Wolock, S. L., Lopez, R. & Klein, A. M. Scrublet: Computational Identification of Cell Doublets in Single-Cell Transcriptomic Data. *Cell Syst.* **8**, 281-291.e9 (2019).

56. Wolf, F. A., Angerer, P. & Theis, F. J. SCANPY: large-scale single-cell gene expression data analysis. *Genome Biol.* **19**, 15 (2018).

57. Aibar, S. *et al.* SCENIC: single-cell regulatory network inference and clustering. *Nat. Methods* **14**, 1083–1086 (2017).

58. Palla, G. *et al.* Squidpy: a scalable framework for spatial omics analysis. *Nat. Methods* **19**, 171–178 (2022).

Main Figures

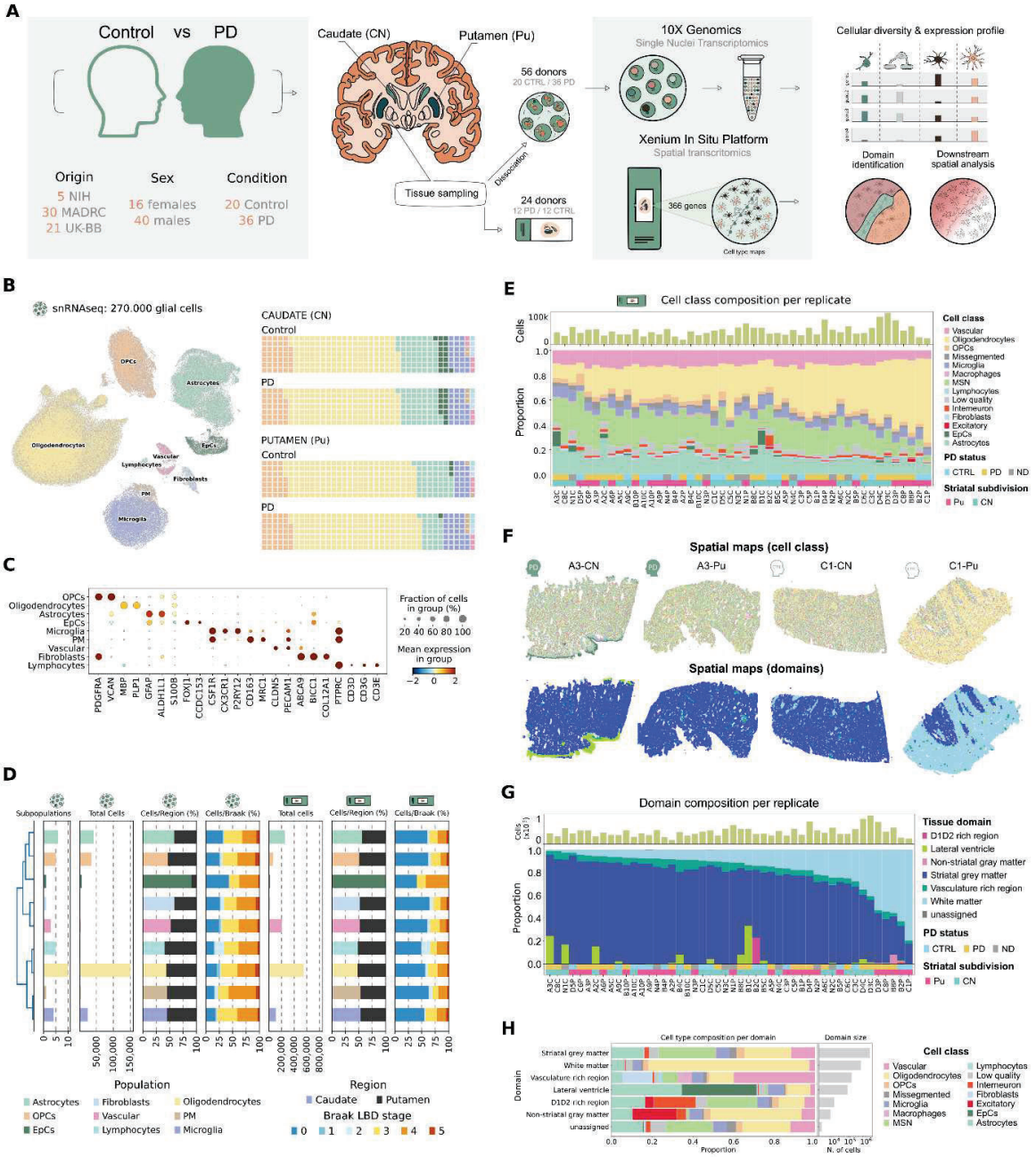

Figure 1. Study design and cellular diversity identified in the striatum

A. Schematic representation of the experimental workflow followed to profile striatal samples using both snRNA-seq and spatial transcriptomics (Xenium)

B. Glial diversity identified in the striatum using the snRNA-seq data, represented in the UMAP (left), with cellular frequencies of each cell type across PD status (PD, Controls) and regions profiled (Putamen, Caudate) (right).

C. Markers for each population visualized in a dotplot. The size of the dot represents the % of cells expressing that gene in each cell type, and the colormap the mean expression in that group.

D. Summary barplots for each identified cell population, showing from left to right: the number of subpopulations resolved within each major class; total cell counts retained after quality control in the snRNA-seq dataset; regional breakdown by CN and Pu; percentages of cells across Braak stages; total cell counts in the spatial transcriptomics dataset; regional breakdown in spatial data; and Braak stage distribution in spatial data.

E. Cellular composition across Xenium-profiled samples. The stacked bar plot displays relative cell type proportions, while the upper bar plot indicates total cell counts per sample. Metadata, including PD status and anatomical region, are annotated below.

F. Representative spatial maps of cells profiled using Xenium are shown, with cells colored by cell class (top) and by assigned domain (bottom). Cell class colors correspond to the palette shown in panel C. Four representative samples are displayed: two PD samples (caudate and putamen) and two control samples (caudate and putamen).

G. Domain across Xenium-profiled samples. The stacked bar plot displays relative domain proportions, while the upper bar plot indicates total cell counts per sample. Metadata, including PD status and anatomical region, are annotated below.

H. Compositional analysis of Xenium-defined tissue domains. Relative cell type frequencies are shown via stacked bar plot (left), with corresponding total cell yields per domain illustrated by the adjacent bar plot (right).

*Icons used throughout the figures: the snRNA-seq gem miniplot indicates data derived from the single-nucleus RNA sequencing dataset; the tissue slide icon indicates data derived from the spatial transcriptomics dataset.

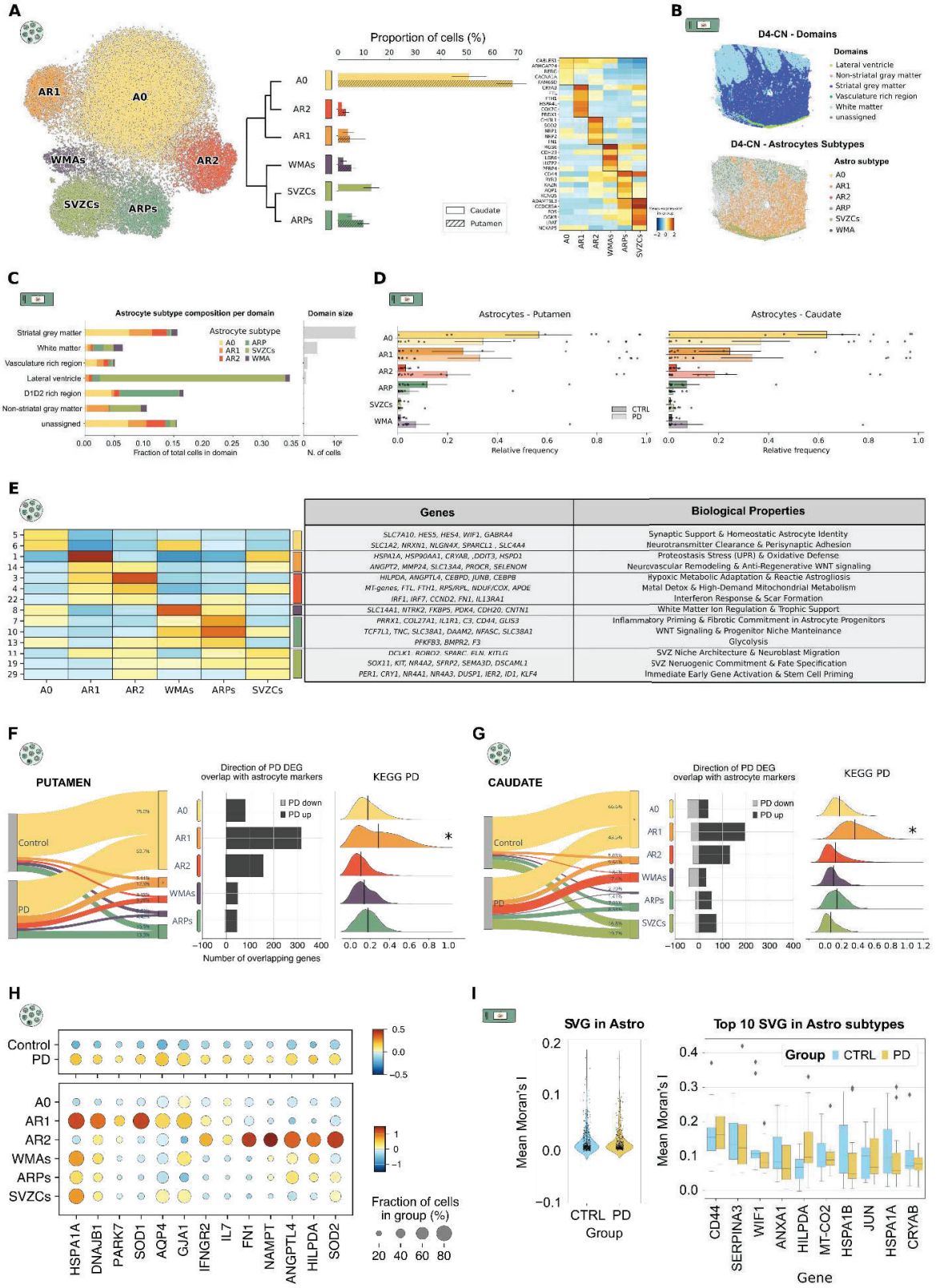

1222 **Figure 2. Analysis of astrocytic diversity in the striatum reveals two PD-associated**

subtypes

A. Molecular and spatial characterization of astrocytes. The UMAP (left) visualizes astrocyte subtype clustering, while the middle bar plot shows their relative distribution in CN and Pu. The heatmap (right) highlights the expression profiles of the top five marker genes for each subtype, with the colormap representing the mean expression in each subpopulation.

B. Comparative spatial mapping of a representative Xenium sample. The sample is visualized twice: first to show the tissue domain architecture (top) and second to highlight astrocyte subtype diversity (bottom). In the latter, astrocytes are color-coded by subtype against a background of gray-scaled "other" cell types.

C. Stacked barplots showing frequencies of each subpopulation per domain identified in spatial data with corresponding total cells per domain illustrated by the adjacent bar plot (right).

D. Compositional analysis of astrocytes clusters per condition in Xenium defined GM. Relative subpopulation frequencies in each condition are shown via barplots in both Pu (left) and CN (right).

E. Subtype-specific enrichment of Hotspot modules in astrocytes subpopulations. This heatmap illustrates the average activity (module scores) of gene programs identified in astrocytes. Only modules showing enrichment in specific subtypes are shown, supplemented by a list of lead genes and their corresponding biological functions.

F-G. Independent analysis of PD-associated astrocyte subpopulations in Pu (F) and CN (G). Each panel includes a river plot showing the relative abundance of each subtype across PD and Control groups (left), a stacked bar plot illustrating the overlap of PD differentially expressed genes (DEGs) with each subtype (middle), and the distribution of KEGG Parkinson's Disease pathway scores across identified groups (right).

H. Dotplot highlighting genes from DEA analysis overexpressed in PD that overlap with specific astrocytic subpopulations.

I. Spatial gene expression variability in striatal gray matter astrocytes. Violin plots display the mean Moran's I scores for all profiled genes, stratified by PD condition (left). This is complemented by a boxplot illustrating the distribution of scores for the top 10 genes with the highest mean Moran's I values, grouped by clinical status (right).

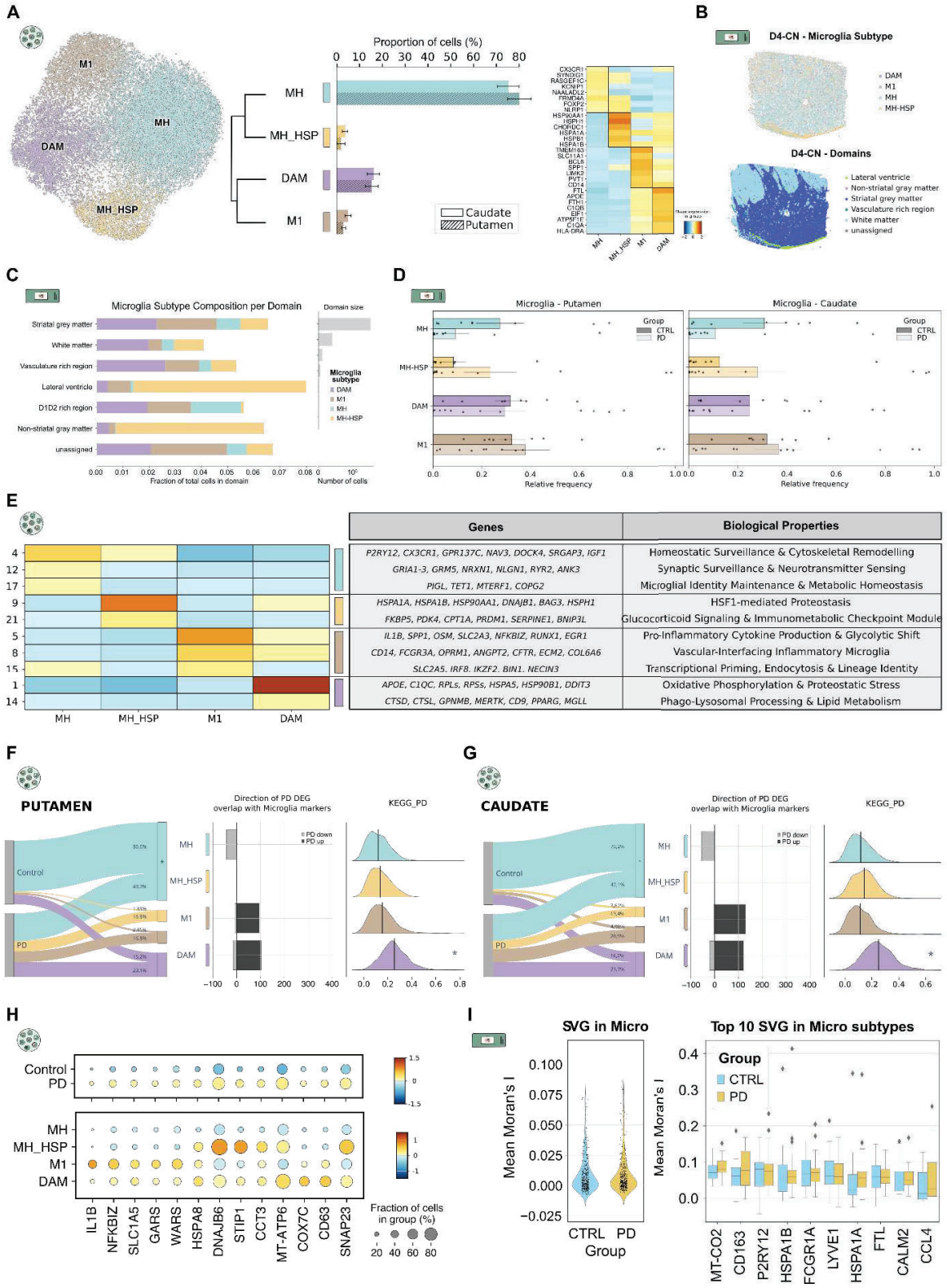

1253 **Figure 3. Analysis of microglial diversity in the striatum reveals two PD-associated**

subtypes

A. Molecular and spatial characterization of microglia. The heatmap (right) highlights the expression profiles of the top five marker genes for each subtype, while the middle bar plot shows their relative distribution in CN and Pu. The UMAP (left) visualizes microglial subtype clustering.

B. Comparative spatial mapping of a representative Xenium sample. The sample is visualized twice: first to show the tissue domain architecture (top) and second to highlight microglial subtype diversity (bottom). In the latter, microglia are color-coded by subtype against a background of gray-scaled "other" cell types.

C. Stacked bar plots showing the relative abundance of each microglial subpopulation within each spatially defined tissue domain. Total cell counts per domain are shown in the adjacent bar plot.

D. Relative abundance of microglial subpopulations in control and PD conditions, restricted to gray matter as defined by Xenium spatial data, shown separately for Pu (left) and CN (right).

E. Subtype-specific enrichment of Hotspot modules in microglia. This heatmap illustrates the average activity (module scores) of gene programs identified in microglia. Only modules showing enrichment in specific subtypes are shown, supplemented by a list of lead genes and their corresponding biological functions.

F-G. Independent analysis of PD-associated microglial subpopulations in the Putamen (F) and Caudate (G). Each panel includes a river plot showing the relative abundance of each subtype across PD and Control groups (left), a stacked bar plot illustrating the overlap of PD differentially expressed genes (DEGs) with each subtype (middle), and the distribution of KEGG Parkinson's Disease pathway scores across identified groups (right).

H. Dotplot showing PD-associated differentially expressed genes with enriched expression in specific microglial subpopulations.

I. Spatial gene expression variability in striatal gray matter microglia. Violin plots display the mean Moran's I scores for all profiled genes, stratified by PD condition (left). This is complemented by a boxplot illustrating the distribution of scores for the top 10 genes with the highest mean Moran's I values, grouped by clinical status (right).

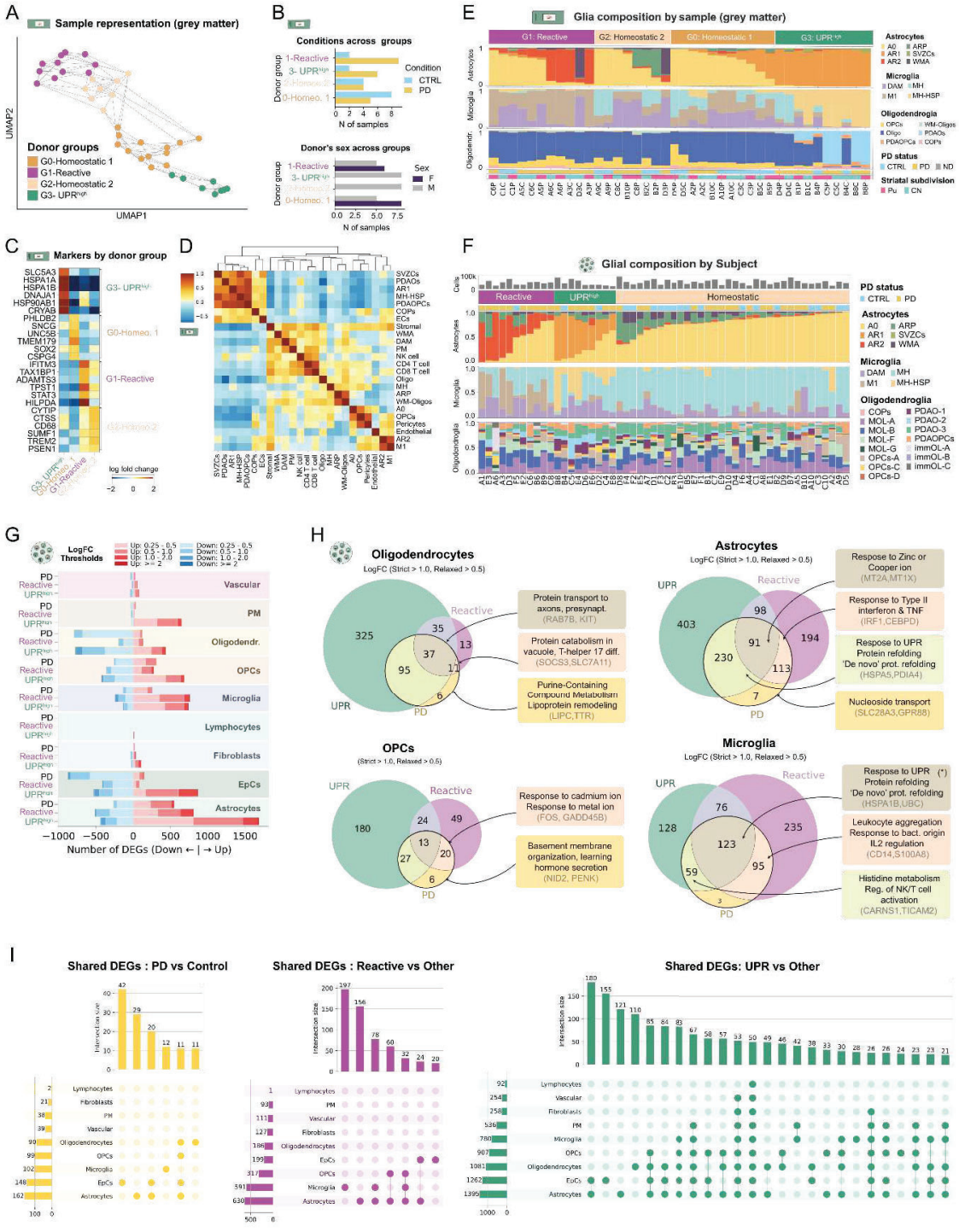

1284 **Figure 4. PD-associated multicellular programs identified by compositional analysis of**

glial subpopulations in striatum.

A. Spatial representation of Xenium datasets. The map includes only cells identified within the striatal gray matter domain, with individual cells color-coded by their assigned donor group.

B. Sample composition by donor group. The upper bar plot illustrates the distribution of samples based on PD status (top), while the lower bar plot provides a breakdown by donor sex (bottom).

C. Differential expression across patient groups. This heatmap displays the mean expression levels for the top six differentially expressed genes (DEGs) identified for each donor group, compared across all cohorts.

D. Correlation of cellular architecture in the striatal gray matter. The heatmap illustrates the Pearson correlation of pairwise cell subtype abundances across all Xenium samples, restricted to cells within the gray matter domain.

E. Cell type-specific subtype composition in the striatal gray matter. The stacked bar plot illustrates the relative proportions of astrocyte, microglia, and oligodendroglia subtypes across Xenium samples. To provide context for each sample, the total cell count is indicated in the upper bar plot (top), while corresponding metadata, including PD status and donor group, are annotated directly above the compositional data.

F. Cell type-specific subtype composition in snRNA-seq samples. The stacked bar plot illustrates the relative proportions of astrocyte, microglia, and oligodendroglia subtypes across snRNA-seq samples. The total cell count for each sample is indicated in the upper bar plot (top), while corresponding metadata, including PD status and donor group, are annotated directly above the compositional data.

G. Differential gene expression (DGE) analysis across PD-associated states. The stacked bar plot illustrates the count of upregulated and downregulated genes across each cell type for three comparisons: PD vs. Control, UPR^{high}, vs. homeostatic, and Reactive vs. homeostatic. Significance is defined by an adjusted p-value < 0.05 and $|\log_{2}FC| > 0.25$. Genes within each bar are further stratified by their specific fold-change magnitude.

H. Transcriptional overlap across disease states. Venn diagrams depict shared and unique DEGs between PD, UPR^{high}, and Reactive groups for astrocytes (top, left), OPCs (top, right),

oligodendrocytes (bottom, left), and microglia (bottom, right). Annotations highlight significant enriched pathways and representative genes within key intersections.

I. Differential expressed genes shared across cell types. Upset plots illustrate the number of differentially expressed genes (both upregulated and downregulated) shared among cell types when comparing PD vs. Control (right=, UPR^{high}, vs. homeostatic (middle), and Reactive vs. homeostatic (right). Only intersections containing more than 10 genes were visualized

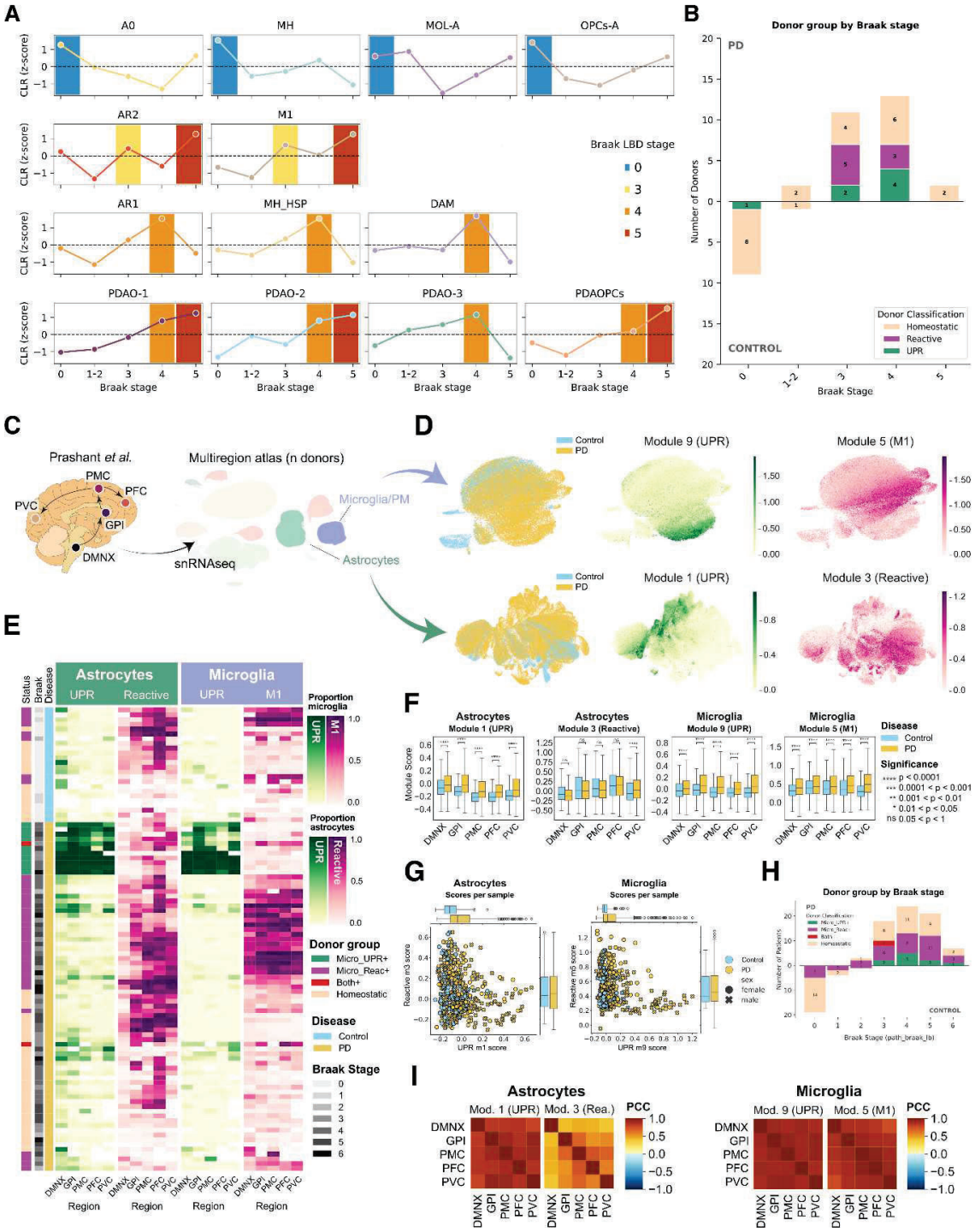

1322 **Figure 5. Braak stage-dependent dynamics and regional distribution of glial**

molecular programs in Parkinson's disease

A. Lineplots showing CLR-transformed abundance of each subpopulation across Braak stages, grouped by the molecular program to which each subpopulation belongs.

B. Barplots showing the number of donors at each Braak stage, stratified by molecular program and condition (PD, upper panels; controls, lower panels).

C-D. Glial subtype signatures in the multiregional PD atlas. Overview of the multiregion atlas (Prashant *et al.*) highlighting the isolation of microglia and astrocytes (C). Accompanying UMAP plots visualize subpopulations by disease status, UPR activation, and reactive/M1 signatures (D).

E. Distribution of disease-associated glial phenotypes across donors and brain regions. Heatmap depicting the frequency of microglial and astrocytic subtypes within each profiled region per donor. Rows represent individual donors, annotated by clinical metadata (Braak stage, PD status, and donor group) on the left sidebar.

F. Enrichment of PD-associated signatures by disease status. Box plots illustrate the distribution of module scores across microglial and astrocytic subtypes, stratified by PD status. Quantifications for all signature modules are presented for each profiled anatomical region.

G. Correlation between UPR and reactive signatures in microglia. Scatter plot illustrating the relationship between mean UPR^{high} (x-axis) and Reactive/m1 (y-axis) microglial (right) and astrocytic (left) signature scores across all samples from Prashant et al. Individual data points are colored by donor sex and shaped by PD status (e.g., circles for Control, triangles for PD).

H. Barplots showing the number of donors at each Braak stage, stratified by molecular program and condition (PD, upper panels; controls, lower panels).

I. Regional correlation of cell-type signature scores. Heatmap displaying pairwise Pearson correlations of mean signature scores across all donor samples for Astrocytes (left) and Microglia (right).

Supplementary Files

This is a list of supplementary files associated with this preprint. Click to download.

- SupplementaryTablesLegend.pdf
- SupplementaryFigures.pdf
- UnifiedExtendedDataTables.xlsx